Deposition of nanocrystalline diamond films by MW plasma CVD & Gas-phase diagnostics using *in-situ* molecular-beam mass spectrometry and emission spectroscopy

Oliver James Louis Fox

University of
BRISTOL

A dissertation submitted to the University of Bristol in accordance with the requirements of the degree of Doctor of Philosophy in the Faculty of Science, School of Chemistry

Abstract

This thesis aims to address some contemporary issues concerning both the fundamental science underpinning diamond synthesis by chemical vapour deposition (CVD) and, at the other extreme, the application of this knowledge to a range of diamond applications covering a fairly broad range of research disciplines. In highlighting how our understanding of the complex mechanisms and processes involved in diamond formation can be transferred into different diamond technologies and applications, it is hoped that many diverse research fields will come to benefit from the impressive range of physical properties which this material possesses. A wide range of different gas mixtures and process conditions are investigated through both diamond growth, looking at the rate of deposition and the crystalline morphology, and spectroscopic diagnostics, with absorption and emission techniques of the microwave-activated plasma discharge. Empirical results are complemented by comparisons with a self-consistent 2D computational model developed by Dr. Yu. A. Mankelevich at Moscow State University.

We describe the progress in construction and commissioning of an *in-situ* molecular-beam mass spectrometer (MBMS) which will provide information on the chemical environment just above the surface on which diamond is being deposited, and will supplement data from spectroscopic studies which run concurrently. Although not yet reaching a completely satisfactory and effective working state, the MBMS system has been improved so that quantitative measurement of stable species within the plasma is possible through modification of the sampling and vacuum apparatus and the software analysis system. These developments have resulted in an increase in the instrument sensitivity and improvement in the detection limit.

Nanofocusing of high-energy X-ray radiation using refractive optics is often difficult due to the small refractive decrement in most materials. Combined with the drive to get as close as possible to the diffractive limit using smaller focal spot sizes is the requirement that any optics must be able to withstand the high energy flux and accompanied heating associated with the latest generation of synchrotron accelerators. Diamond has been proposed as a material for refractive optics as it exhibits low absorption of radiation and high thermal conductivity to cope with such conditions.

Novel fabrication methods combine our successful film seeding method and a high-quality, sacrificial Si template on which nanocrystalline diamond is deposited and has resulted in lenses with impressive nanofocusing capabilities. Testing at the STFC Diamond Light Source synchrotron facility has indicated that 11 keV X-ray radiation can be focused onto a spot size of 400 nm and lenses which focus to smaller sizes are currently in fabrication.

I declare that the work in this dissertation was carried out in accordance with the Regulations of the University of Bristol. The work is original, except where indicated by special reference in the text, and no part of the dissertation has been submitted for any other academic award. Any views expressed in the dissertation are those of the author.

SIGNED: .... DATE:..........................

Acknowledgements

There has hardly been a moment throughout this project that I have been without the crucial, hard-working support of a MSc or BSc project student to help with, amongst other things, troublesome apparatus and seemingly endless processing of data from the mass spectrometer. Their work has undoubtedly contributed to the advancement of both MBMS system and the knowledge of diamond CVD discussed in this thesis and for this, and their friendly company, I am extremely grateful to all of them. Neil Chadda worked on deposition of NCD films in different inert gases and proved a very able analyst of Raman data obtained when characterizing the range of diamond that was grown. The often unrewarding development of different seeding methods was conducted with tireless help from James Holloway who also grew diamond with addition of N_2 to the plasma with detailed characterization of the plasma by emission spectroscopy and the films using Raman and powder-XRD. This deposition chemistry was balanced with important improvements in the MBMS system beam-to-background ratio by various hardware modifications that were installed and tested with James's assistance. Tom Davies helped with many other modifications of the MBMS apparatus and a large amount of testing of the time-gating system in addition to depositing the first X-ray lens substrates to be tested at the synchrotron beamline. The calibration of the MBMS system for stable species in the plasma such as C_2H_2 and CH_4 and initial testing of the beam with a plasma was carried out with help from Tom and, later, James Comboni. Returning to fundamental processes, Beccie Whittaker investigated the presence of large carbon particles landing on un-seeded substrates, subsequent growth on these substrates and properties of the diamond colloid used for seeding. Her work also involved ongoing improvement of the MBMS system and important modifications. Most recently, Nick Thorne has been involved with deposition of the latest, and most successful, batch of NCD X-ray lenses as well as testing of the new MBMS sampling orifice and subsequent plasma analysis.

In development of the electrospray apparatus thanks must be paid to Prof. Anke Krüger (University of Würzburg, Germany) and Dr. Masaki Ozawa (Meijo University, Japan) for kindly supplying samples of their BASD nanodiamond in various liquids and to Dr. Nicolaie Moldovan (ADT, Ltd.) for growth, and characterization, of UNCD films.

Working closely with Adnan Malik, at the STFC Micro & Nanotechnology Centre, on diamond lens fabrication and with Lucia Alianelli and Kawal Sawhney, from the Diamond Light Source synchrotron facility, has been very rewarding. Only the diamond deposition was carried out by the Bristol Diamond Group and was a small part of an intricate process located between lens design/Si substrate fabrication and Si removal/beamline testing. As such, any supplementary work, in addition to the diamond growth, described as part of this thesis is wholly down to them and full acknowledgment should be paid for the extensive and detailed contribution to the overall project. In particular, I would like to thank Adnan Malik for supplying the SEM images of the lens after Si substrate removal and Lucia Alianelli for providing the data from the beamline testing as well as a wealth of other information essential to this work.

Engineering new hardware for the MWCVD reactor and the MBMS instrument has been achieved with expert help from Keith Rosser, Dr. James Smith and the School of Chemistry Mechanical workshop. The project has also benefitted from input and support from the rest of the diamond group and in particular Dr. Gareth Fuge, Dr. Jie Ma, James Richley and Ben Truscott. Overall, I am greatly indebted to Prof. Paul May and Prof. Mike Ashfold for supervising the project, offering astute advice and supporting the various avenues of this research.

Contents

Nomenclature used in this document:

One of the crucial factors in this area of chemistry is the gas composition of the plasma which is, obviously, heavily dependent on the mixture of gases which flow into the reactor. As will become apparent, the various gases are controlled as flow rates with units of standard cm^3 per minute (sccm). However, as the total flow rate can fluctuate depending on the experiment it is often more straightforward to quote these flows values as mole fractions of the total rate, $\chi_0(X)$, where the subscript zero indicates a fraction of gas X in the inlet mixture rather than in the plasma, which is likely to be different as a result of the reactions occurring there. Consequently, values referred to as $\chi(X)$ will be the mole fraction of species X within the plasma, or at some, specified distance from the substrate, which has been either determined experimentally from one of the analytical techniques or inferred from a computational model. It has sometimes been easier to quote $\chi_0(X)$ not as true mole fractions but as a percentage or part per million (ppm) of the total flow rate due to the number of decimal places required.

1.0 Introduction

1.1 Diamond: introduction

1.1.1 Natural carbon

Carbon occurs naturally both as a free element, in the form of graphite or diamond, and combined with other elements in a multitude of compounds. Many of these carbon-containing substances are fundamental to life on Earth and form the basis of an entire branch of science known as organic chemistry. In an anthropological sense, carbon materials have been known since prehistory in the form of charcoal, soot and even diamond, used as a polishing abrasive *circa* 2500 BC (Lu *et al.*, 2005). Diamond has been held in special regard throughout history with many early records deriving from Indochina around the 4th to the 2nd centuries BC. Categorization of carbon as an element came in the late-18th century with Antoine Lavoisier using the name *carbone* from the Latin *carbo*, meaning charcoal, while the term diamond was first proposed at the same time, combining the Greek words for transparent (δίαφαυής or *diaphanes*) and invincible or unbreakable (αδαμας or *adámas*). The fact that diamond was an allotrope of carbon was proven by both Lavoisier in France and Smithson Tennant in England by burning the material and weighing the CO_2 produced (Tennant, 1797).

Natural diamond is formed in a band of molten rock in the upper part of the Earth's mantle, known as the asthenosphere, located between 100 and 200 km below the surface. Material from this region occasionally gets transported closer to the Earth's surface during volcanic eruptions and forms distinct pipes of rock when it eventually cools. Mining of these ancient volcanic pipes of rock, termed kimberlite (after the discovery of diamond containing rock near the South African town of Kimberley in 1870), yields a large proportion of the natural diamonds globally, although they are also found in sedimentary rocks and alluvial deposits as a result of natural erosion of the kimberlite pipes (Hazen, 1999). With some notable exceptions, the majority of mined, natural diamonds are not of gemstone quality but find uses in industrial applications including polishing abrasives and cutting tools (Greenwood & Earnshaw, 2001). This inherent natural scarcity and the considerable efforts required in the extraction and refinement processes combine to make natural diamond a highly desirable and expensive commodity and synthetic diamond an indispensable alternative.

In the sections which follow we examine the structural characteristics of different carbon allotropes (section 1.1.2) and the resultant physical properties (section 1.1.3) before introducing various forms of synthetic diamond (section 1.2) and methods for fabricating them (section 1.3). Formation of diamond films in microwave chemical vapour deposition (MWCVD) is given more in depth discussion as it forms the basis of the following thesis. Various aspects of MWCVD chemistry are addressed (section 1.3.4) before describing the present understanding of the reaction mechanisms contributing to diamond deposition and the contribution from computation modelling of the growth environment (section 1.4). We finish this introductory chapter by looking at two other important areas for diamond deposition: i) the introduction of different elements or compounds to alter either the properties of the diamond film or the plasma deposition environment (section 1.5) and ii) the way in which diamond films nucleate on different substrates (section 1.6).

1.1.2 Solid carbon structures

In addition to the fullerenes (molecular carbon), there are at least six crystalline forms of carbon, including diamond, α-graphite, β-graphite, Lonsdaleite (hexagonal diamond), chaoite, and carbon(VI), with hexagonal α-graphite being the most thermodynamically stable allotrope under ambient conditions ($\Delta H_{\text{transformation}}$ = 1.9 kJ mol^{-1}) (Greenwood & Earnshaw, 2001). In the graphite allotrope sp^2 hybridized carbon atoms are covalently bonded to three nearest neighbours in hexagonal arrays, which form comparatively weakly-bound layers stacked on top of each other and held together by van der Waals forces. Conversely, sp^3 hybridized carbon atoms in diamond are bonded to four equidistant neighbours in a high-density, σ-bonded lattice with a cubic unit cell, a_0 = 356.68 pm and interatomic distance of 154.5 pm. In fact, the diamond lattice is made up of two interpenetrating, close-packed face-centred-cubic lattices which are offset along the body diagonal. Natural diamonds are classified according to the amount of nitrogen atoms (N) they contain as this determines some of the physical properties. Type Ia contain 0.05-0.25% N as the most abundant impurity within the crystal whereas type Ib contain higher N fractions up to 1%.

A minority of films contain negligible amounts of N (IIa) but some do contain boron (IIb) giving them a, highly sought after, blue colour.

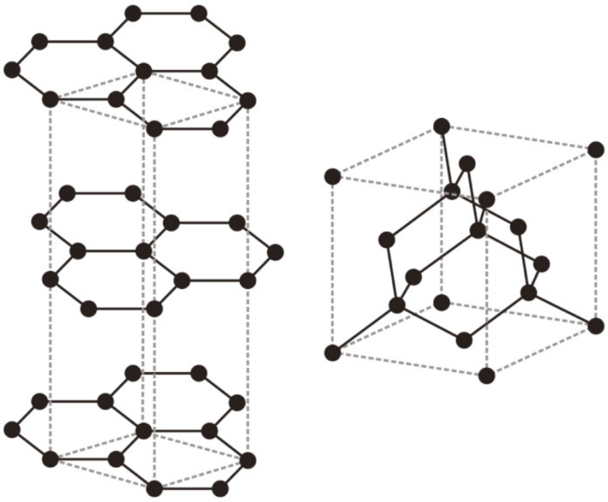

Figure 1.1: Simplified sketches of the graphite (left) and diamond (right) structures.

1.1.3 Diamond Properties

Diamond is well known to be the hardest of all minerals but it also displays a large array of other extreme properties which are summarised in the following table:

Criteria	*Properties of diamond*
Structural	Extreme mechanic hardness (~ 90 GPa) and wear resistance
	Low compressibility (8.3×10^{-3} m^2 N^{-1})
	High bulk modulus (1.2×10^{12} N m^{-2})
	High thermal conductivity (2×10^3 W m^{-1} K^{-1}, at room temperature (RT))
	Low thermal expansion coefficient (1×10^{-6} K^{-1} at RT)
Electronic	High electrical resistivity (~10^{16} Ω m, but 10^{-1}-10^4 Ω m for doped material)
	Wide intrinsic band gap (indirect gap = 5.4 eV, but lower for doped material)
	Surfaces exhibit a low or even negative electron affinity
Chemical	Chemically and biologically inert
	Resistant to corrosion
Optical	Transparent over broad range of wavelengths from deep-UV to far IR
	Highly resistant to damage from irradiation

Table 1: Some of the extreme properties of natural diamond (Field, 1992, May, 2000).

Optical brilliance in transparency and refractive index make it highly prized as a gemstone and its fine array of exemplary properties, ultimately derived from the stability of the tetrahedral covalent network of carbon atoms, lends itself to a great many applications. In many respects the controlled formation of low-defect synthetic diamonds produces superior material for optical and electrical uses.

1.2 Synthetic diamond

1.2.1 Single crystal diamond (SCD)

Synthetically produced diamond comes in many different sizes and morphologies. At one extreme the small diamond seed crystals can be grown epitaxially into large, single crystal materials through gradual deposition of carbon. Development of CVD methods has allowed growth rates of 165 μm h^{-1} by working at high pressures around 350 Torr that lead to large SCD deposits up to 18 mm in size (Liang *et al.*, 2009). These homoepitaxial processes are extensively studied with particular attention paid the growth rate and the evolution of different crystal planes but are not used as part of this project.

1.2.2 Microcrystalline diamond (MCD)

CVD diamond does not, in general, form into a single-crystal structure but is instead composed of small diamond crystallites which are, often, surrounded by non-sp^3 material at the boundaries between the individual grains (we use the terms crystallites and grains interchangeably). Diamond layers can be fabricated from a continuum of different grain sizes from macroscopic near-SCD crystals to nanocrystalline diamond (NCD) morphologies (section 1.2.3). Between these extremes is a material known as microcrystalline diamond (MCD, or sometimes PCD: polycrystalline diamond) where grain sizes range from 100-10000 nm. In cross-section MCD films show a columnar structure with individual crystals getting larger with deposition time/film thickness.

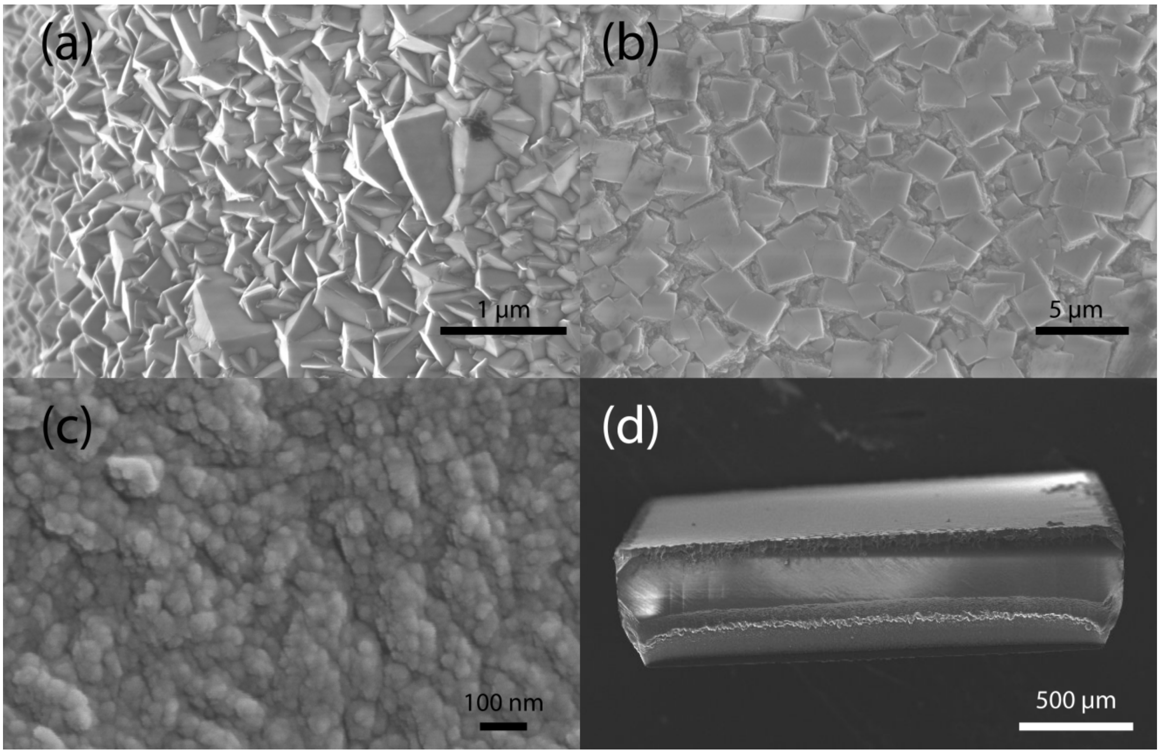

Figure 1.2: A range of different synthetic diamond morphologies from large single crystals (d, shown from one end) through <111> (a) and <100> facetted microcrystalline films to nanocrystalline diamond (c). (a) to (c) were grown and (d) was coated using MWCVD at the University of Bristol.

Like most crystalline solids, diamond can be described by different planes which exist periodically throughout the lattice and, as a diamond crystal grows, one of these planes is often favoured and propagates through the structure, leaving this surface exposed at the end of the deposition. In diamond, the three dominant crystal planes are defined by the Miller indices <111>, <110> and <100>. Generally, synthetic diamond surfaces, or natural diamonds cleaved along a particular plane, show distinct properties due to the arrangement of atoms and, for MCD, the differences are apparent when comparing the surface morphology of <111> and <100> facetted samples (Figure 1.2a & b). We see that the <111> dominated morphology is comprised of diamond grains which have a pyramidal structure and, roughly, triangular facets whereas, the <100> sample contains square facets corresponding to this crystal plane. Obviously, in SCD the topographical preference is transferred through the growing sample from the seed particle and, hence, it is not immediately apparent which crystal face is being deposited on as they all look flat. An understanding of the structure of these different crystal faces is important as the deposition mechanics and energetics will vary depending on the arrangement of atoms and interatomic distances on each surface (see section 1.4.2). Overall, the morphology is determined by the different mechanisms of diamond deposition which, in turn, result from the varied plasma chemistry.

1.2.3 Nanocrystalline diamond (NCD)

Compared with MCD, NCD films exhibit smoother surfaces but, as they contain a greater proportion of sp^2 carbon, are sometimes said to be poorer quality diamond, although they often display similar, and sometimes better, physical properties. It is obvious that as the grain size is reduced the surface area of all the grains in the film increases and this results in an increase in the non-diamond content of the structure. Grain sizes in NCD films range from 5 to 100 nm with the lowest ranges (<10 nm) fashionably referred to as ultrananocrystalline diamond (UNCD) although the material is essentially identical albeit with smaller crystallite sizes. At the lower limit the surface smoothness of NCD films becomes comparable with single crystal diamond with average roughness measures of a few nm and is, therefore, desirable for many diverse applications. Rougher films typically form as a result of clustering of individual diamond grains into larger structures such as the spherical shapes, termed ballas diamond, and these can be observed as distinct islands on the substrate surface if the deposition is stopped before the film becomes continuous Figure 1.2c. What makes NCD distinct from MCD is that the surface roughness is independent of film thickness as renucleation of the crystals occurs throughout the deposition (Krauss *et al.*, 2001, Williams *et al.*, 2006). X-ray diffraction (XRD) and near-edge X-ray absorption fine structure (NEXAFS) studies have attempted to quantify the sp^2 carbon material present in the grain boundaries (Gruen *et al.*, 1996, Zhou *et al.*, 1998a).

The diamond morphology is strongly dependent on the conditions in which it is deposited and is discussed in detail in section 1.3.4.

1.2.4 Applications of synthetic diamond

As a result of the exemplary properties of natural stones (see Table 1) which are augmented in synthetic materials, diamond has found a vast range of applications over and above its reputation as a sought-after gemstone. The range of uses of thin diamond films has been extensively reviewed (Gicquel *et al.*, 2001, May, 2000, Yarbrough, 1991) with special attention given to electrical properties (Railkar *et al.*, 2000, Williams *et al.*, 2005), optical properties (Koidl & Klages, 1992), tribological properties (Erdemir *et al.*, 1996), biological capabilities (Williams *et al.*, 2007b) and uses as biological (Nebel *et al.*, 2007) or radiation sensors (Bergonzo *et al.*, 2001) or micro-electronic mechanic devices (Auciello *et al.*, 2004, Huff *et al.*, 2006, Krauss *et al.*, 2001). It is clear that diamond offers unparalleled opportunity for applications too numerous to go into any depth here.

At present there are many situations in which diamond would seem like the ideal material but is not utilized because of a lack in the knowledge of transferring designs from research lab to industrial-scale fabrication or the high cost, making applications currently unaffordable.

1.3 Diamond Synthesis

1.3.1 High-pressure/High-temperature diamond

It was initially thought that the considerable activation barrier separating the two allotropes of carbon could be overcome by exerting a large pressure on graphite to form the slightly more thermodynamically stable diamond allotrope in the laboratory. However, the increase in this activation barrier with pressure requires additional heating, and thus the high pressure and high temperature (HPHT) method was developed at General Electric to obtain diamond (Bundy *et al.*, 1955). Typical conditions emulate those occurring in the Earth's crust where diamonds are formed naturally at values of p ~ 150 kbar and T ~ 2000 °C. These values can be reduced slightly by using transition-metal catalysts, such as Fe, Co and Ti, which dissolve carbon and allow the diamond crystals to precipitate when the p and T are satisfied at a boundary known as the Berman-Simon line on the carbon phase diagram. Modern press designs incorporate large anvils and copper heating coils in which mixtures of metal catalyst, graphite and diamond seed particles are finely tuned to achieve a certain crystal size depending on the application. A key parameter in this process is the temperature gradient across the carbon/catalyst mixture where the graphite is heated more than the diamond seed. Carbon dissolves into the metal and deposits on the seed but the temperature gradient ensures that it cannot redisperse into the catalyst allowing the seed to grow (www.e6.com/en/education/synthesisofdiamondusinghpht).

There are a vast number of applications of these HPHT diamonds, and fabrication plants owned by companies such as Du Pont and Element Six routinely produce diamond on an industrial scale. Despite the success of this method the product is slightly limited in size with the largest HPHT diamonds only measuring ~2 mm across although this has not prevented their production accounting for 90% of all industrial diamonds.

1.3.2 Diamond growth: CVD

While industrial HPHT diamonds are important for numerous applications, there are many other situations where this material does not meet the required criteria. Employing chemical vapour deposition (CVD) technologies to form thin films of diamond across large areas and different substrate types has taken diamond research in many diverse directions. CVD processes take many forms but all rely on the deposition of activated gaseous precursors onto a solid substrate. The diamond CVD process uses the gas-phase kinetics to trap the metastable diamond structure in a non-equilibrium system (Matsumoto *et al.*, 1982, Spitsyn *et al.*, 1981). Typically, this involves a low pressure (~10–200 Torr) and high substrate temperature (~700–1200 K) environment consisting of an activated gas-phase mixture that contains some hydrocarbon precursor species which react and deposit onto the substrate. Either thermal or plasma discharges are commonly used to activate the carbon-containing mixture which invariably contains some hydrogen which dissociates to form reactive H atoms. In environments rich in H atoms the etch rate of sp^2 carbon (graphite) is between 10 and 100 times faster than that of sp^3 diamond and produces a situation in which, the thermodynamically metastable carbon allotrope (diamond) is kinetically favoured (Angus *et al.*, 1968).

Modern diamond CVD techniques have evolved over the last 20 years into many different formats but with two main reactor-types dominating the field: Hot-filament activated CVD (HFCVD) and microwave-activated CVD (MWCVD). The latter technique has been referred to as MPCVD, MW plasma-enhanced CVD (MWPECVD) or MW plasma-activated CVD (MWPACVD or MPACVD) but all are synonymous and we will stick with MWCVD.

The HFCVD and MWCVD methods are discussed below with the emphasis on microwave activation as the following thesis is devoted to this topic. Deposition in DC-arc jet reactors is not treated here but has been discussed in various papers (Dandy & Coltrin, 1995, Konov *et al.*, 1995, Ohtake & Yoshikawa, 1990).

1.3.3 HFCVD

Activation of the carbon-containing gas mixture in HFCVD reactors is achieved thermally using a metallic filament, usually tantalum, tungsten or rhenium, which is resistively heated (Matsumoto *et al.*, 1982). Although reactor dependent, diamond deposition typically occurs at T_{filament} ~2300-2700 K and at low pressures of ~20 Torr. The substrate must be positioned fairly close (~4 mm) to the filament in order to be sufficiently heated and subjected to high enough fluxes of H atoms and hydrocarbon growth species although additional heating is often supplied using a secondary substrate heater to raise the growth rate. Diamond is deposited on the substrate at a rate of ~1-10 μm h^{-1} although this is obviously dependent on the process conditions. The HFCVD systems are slightly limited as some reactant species can oxidise or corrode the filaments and the filaments, themselves, can also be the source of contamination of the diamond films. However, these reactors have the advantage that arrays of filaments can be used to deposit diamond over fairly large areas.

As it forms the core of the research dissertation which follows the MWCVD system is discussed in greater detail in the following section.

1.3.4 MWCVD

A mixture of hydrocarbon species and hydrogen can be efficiently activated using a microwave discharge that produces a reactive mixture of neutral, ionic and radical species (Kamo *et al.*, 1983).

1.3.4.1 CVD plasmas

Plasmas comprise a physical state in which a certain percentage of atoms or molecules have been ionized to form a system where electrons, ions and neutral species co-exist as a very reactive medium. The existence of separate charged species within the plasma gives it many distinct properties and allows the system to be influenced by electric and magnetic fields. In the MWCVD system the plasma is controlled by centring the electrical field maximum in the middle of a moderate pressure discharge tube or reactor vessel directly above the CVD substrate. The substrate is heated to ~1000 K by the plasma and exposed to the array of reactive species in the discharge.

The first MWCVD reactor for diamond deposition consisted of a quartz tube inserted into the rectangular MW waveguide so that the electric field maximum lay at the centre of the tube and formed a discharge in a gas mixture of 1-3% CH_4 in H_2 (Kamo *et al.*, 1983). Another reactor system employs an antenna to couple MW into a water-cooled chamber through a quartz window in an ASTEX design, named after Applied Science and Technology, Inc., who commercialized the reactor. This system has become widely used and is the design upon which the reactor used in this thesis is based. It uses an antenna at the top of the reactor to bend the MW from the rectangular TE_{10} mode into the circular TM_{01} mode around which the cylindrical vessel is designed. The dimensions of the reactor means that it contains only one radial mode of the MW which results in a maximum amplitude forming at two positions, one above and one below the quartz window. This causes a plasma to form at the node in the low pressure side situated just above the substrate. The dimensions of this reactor mean that large areas can be coated (<10 cm diameter) and high power densities (with input power up to 6 kW and pressure to 200 Torr) applied to achieve fast growth rates. Large reactors have been used deposit on substrates up to 75 mm in diameter using $P \sim 5$ kW and $F_T = 1000$ sccm (Ralchenko *et al.*, 1997).

1.3.4.2 The plasma discharge

In the plasma driven by absorption of electromagnetic (EM) radiation the input energy is transferred most efficiently to the lightest species, the free electrons and protons, and the energy is then transferred to larger and neutral entities through secondary interactions. This results in an energy partition between the electrons, with a temperature, T_e, measured in electron volts, and the neutral gas species which are in thermal equilibrium at a particular gas temperature, T_{gas}. A plasma state is initiated by coupling the electric field and the small fraction of free electrons in the gas until a spontaneous discharge forms. The MWCVD reactor is designed so that a standing-wave forms between the antenna and the substrate which contains only one maximum node above the substrate. Energy is transferred to the system as the electrons are continuously accelerated and decelerated in this wave leading to the exchange of some of this energy gain with the neutral background gas.

Below ~15 Torr (~ 20 mbar) EM-driven plasmas are characterized by a T_e which is solely determined by the frequency, ω, and amplitude, E, of the electric field. At higher pressures the T_e is influenced by the scattering due to background species and can be related to the T_{gas} and the reduced electric field E/n, where n is the number density (Hagelaar *et al.*, 2004). This means that these discharges cannot be ignited above 20 Torr as the free electrons do not experience enough oscillations in the field before being quenched through collision. Once stable, however, the pressure can be increased as the heating will result in a decrease in n. At this point the augmented density of charged species means there is greater absorption of the power from the EM field. However, at higher densities the plasmas become more conductive and the microwave energy cannot penetrate as far leading to a contraction in plasma volume at higher pressure. The chamber pressure, p, and the input MW power, P, can be combined to give a power density, Q which will vary throughout the system.

Ultimately, it is the power density in the plasma (or the distance between the hot filament and the substrate) that determines the substrate temperature in systems where no additional substrate heating is applied. A window of temperatures exists for optimum deposition of diamond by MWCVD which is centred at $T_{sub} \sim 1000$ K ± 250 K. Above this range only graphitic or amorphous carbon films are found, while below ~ 750 K no diamond is deposited. This limits the type of materials which can be used as substrates, because they must be able to withstand the harsh environment in the MW reactor. Therefore, it is an aim of modern diamond CVD research to enable deposition at lower T_{sub}. One such method demonstrated diamond deposition at substrate temperatures as low as 650 K using halogenated precursor species and aluminium (T_{m} = 933 K) substrate although deposition onto zinc (T_{m} = 692 K) was less successful (Schmidt & Benndorf, 2001).

1.3.4.3 Chemistry of the diamond CVD environment

The last two decades have seen a number of major advances in our understanding of the chemistry and composition of activated gas mixtures used to deposit diamond films. In particular, the changes in composition with spatial location in the reactor and with various process conditions have been studied for the first time (Butler *et al.*, 2009, Hassouni *et al.*, 2010).

a) Hydrogen

The presence of atomic hydrogen (H) is essential in both HF- and MWCVD techniques driving the deposition mechanism (section 1.4.2) and allowing the metastable diamond allotrope to form preferentially over the thermodynamically favoured graphite by etching sp^2 carbon adducts back into the gas phase. Fully terminating a growing diamond surface with H atoms also favours formation of the tetrahedral sp^3 lattice by hindering C-C cross-linking reactions on the surface. Even in the gas phase, atomic H serves to fragment any long-chain hydrocarbons which may form and disrupt the depositing film, and indicates why plasmas where H_2 is not a major component at the inlet contain, generally, more sooty, non-diamond contaminants.

For MW activated systems, hydrogen also forms stable, chemically active plasmas across a wide range of chamber pressures and MW powers, dominating the interactions between neutral species and the gas-surface chemistry. At the typical T_{gas} ~ 3000 K that MWCVD discharges achieve (Gicquel *et al.*, 1994, Kaminsky & Ewart, 1997, Lombardi *et al.*, 2005b) around one third of the H_2 will be dissociated into atomic H and $\chi(H_2) \sim \chi(H)$. The gas-phase reactions driven by atomic H will be addressed in section 1.4.3.

b) Hydrocarbons

In many diamond deposition environments, including our MWCVD reactor, typical MCD deposition conditions consist of a hydrocarbon source gas (often methane, CH_4, for solely economic reasons) diluted with hydrogen. The hydrocarbon gas is rapidly converted into C_2H_2 under the prevalent plasma conditions as well as lower concentrations of other C_1 and C_2 radicals in the plasma centre. In the production of MCD films the hydrocarbon fraction depends moderately on the method of gas activation, with MWCVD systems requiring ~5% CH_4 in H_2 whereas only ~1% is necessary in HFCVD reactors to achieve analogous morphologies. For both systems an increase in the hydrocarbon mole fraction, $\chi_0(C_xH_y)$, results in a change in morphology from MCD to NCD (see section 3.2) and then at higher $\chi_0(C_xH_y)$ non-diamond amorphous carbon (a-C) deposits (May & Mankelevich, 2008).

Many experimental studies have shown that the identity of the hydrocarbon in the feed gas mixture is irrelevant and that the key factors are the H:C ratio and the concentration of the CH_x (x = 0-3) growth species above the substrate surface. The role of these growth species is to transport carbon from the plasma core to the substrate surface where they are incorporated into the lattice. The methyl radical is favoured as the growth species as many studies have shown that it is present above the substrate in concentrations higher than most other hydrocarbon radicals and that surface reactions have favourable activation barriers. Further evidence is provided by the use of molecular beams containing CH_3 which deposit diamond at a fast rate (Lee *et al.*, 1994, Loh *et al.*, 1996).

c) Argon & other noble gases

There has been much interest in the addition of inert gases to the standard H_2/CH_4 mixture, with the detailed studies of the involvement of both noble gas (*e.g.* argon) and nitrogen in diamond deposition. The latter is also an important impurity in natural and synthetic diamond films and will be discussed in section 1.5.3. Argon (and, to a lesser extent, the other noble gases) has been added to process-gas mixtures in small amounts since the early MWCVD experiments as its presence has both helped initiate or stabilize the plasma (Zhu *et al.*, 1990) and enabled actinometric measurements (Gicquel *et al.*, 1994). Addition of Ar has also been shown to increase the diamond deposition rate although this can be at the expense of film quality with a greater sp^2 content being observed (Han *et al.*, 1997, Zhou *et al.*, 1997). Larger mole fractions of Ar in the gas mixture during MWCVD can have a strong influence on the film morphology inducing NCD deposition above a certain threshold (Gruen, 1999, Zhou *et al.*, 1998b). At these limits the Ar-rich plasmas become unstable, reaching a limit at $\chi_0(Ar) \sim 0.97$. This is due to the ion recombination mechanisms in Ar being less efficient than in H_2 systems where the additional rovibrational degrees of freedom disperse the electronic binding energy. Instead, Ar ions react with H_2 to form ArH^+ which can accept an electron and form neutral fragments.

d) Oxygen

The addition of oxygen to diamond CVD reactors, most commonly as CO or CO_2, has become an important and well-studied field offering novel ways of producing different morphologies often at lower substrate temperatures – therefore, on a wider range of substrate materials – and with lower power consumption. The power efficiency is an important consideration for commercial applications where reactors may run for weeks to produce thick SCD layers and where the cost of electricity becomes significant.

Like atomic H, oxygen also serves to suppress sp^2 carbon during the deposition process improving the diamond quality (Kawato & Kondo, 1987) but also limits the amount of hydrogen incorporated into the sp^3 lattice (Tang *et al.*, 2004).

The combination of CO_2 and CH_4 has successfully produced diamond films at T_{sub} as low as 710 K. The negligible mole fractions of O, O_2, and OH in these systems at optimum growth conditions points towards the importance of CO (*cf.* the CN radical in section 1.5.3) in low-temperature growth of diamond (Petherbridge *et al.*, 2001b). This work also indicated that the window for diamond deposition occupies a small range between 50-52% CH_4 in CO_2. Simultaneous measurement of the CH_3 radical by mass spectrometry led to the conclusion that it was a key growth species as in H_2/CH_4 systems, to which comparisons were made. While sharing many similarities, the surface activation of the diamond-growing sites appears different in each gas mixture, with the H_2/CH_4 system being activated by addition and abstraction of H atoms. The CO moiety is believed to perform a similar role to the H atoms and is able to do so at a lower temperature (Petherbridge *et al.*, 2001b).

The CO_2/CH_4 system, both with and without additional H_2, is now widely used for deposition of diamond films at low T_{sub} due to the reduced activation barriers compared with the common H_2/CH_4 mixture.

e) Summary

The various components we have addressed, ignoring the inert Ar which acts in the manner of a catalyst, can be combined into a C-H-O phase diagram known as the *Bachmann Triangle* (Bachmann *et al.*, 1991). This empirically-derived phase diagram is segmented into regions of no deposition, diamond deposition and non-diamond carbon deposition and, thus, forms a useful tool for predicting the outcome for a specific gas mixture. It also shows that diamond deposition is, essentially, independent of the hydrocarbon precursor and activation method although, within the diamond deposition regime, the growth rate and sp^2 content can change considerably.

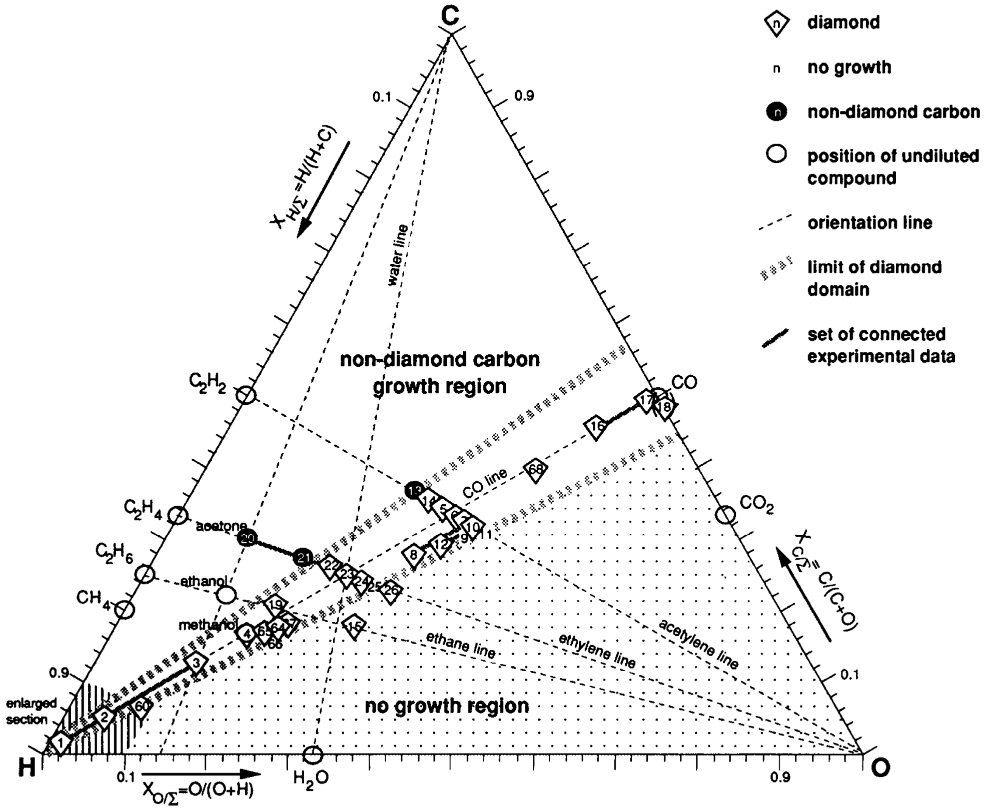

Figure 1.3: A C-H-O phase diagram summarising 70 experiments using different gas mixtures to deposit diamond by CVD (Bachmann *et al.*, 1991).

1.4 Modelling & mechanism of diamond CVD

1.4.1 Early kinetic modelling

Computational modelling of diamond-depositing environments has been extremely complementary to both ongoing gas-phase diagnostics and theories concerning reactions of growth species with diamond surfaces. Empirical results and observations can provide a framework onto which the complex set of chemical and physical processes is projected giving rise to theoretical outputs which can be tested experimentally. It is this synergetic relationship which has allowed models to become increasingly robust and experimental investigations to focus on key species.

Since the first CVD-type experiments, several generations of models have been created and enhanced, beginning with basic treatment of the kinetics of diamond deposition (Chauhan & Gardner, 1974, Chauhan *et al.*, 1976, Fedoseev & Varnin, 1983). The first approach was to combine experimental observations of different species within the chemical system (a method of flowing CH_4 and H_2 over heated diamond powder), and of the diamond film, to assign rate constants for some elementary processes. In particular, the theoretical kinetic model was compared with the observed increase in mass of the diamond powder after treatment showing a dependence of growth rate on the chemical reaction rates. The rate equations were found to be first-order in relation to $\chi_0(CH_4)$ in systems where the methane was diluted with H_2, hinting at the crucial role played by atomic H. It was suggested that the surface topography, *i.e.* which crystal face was being grown on, would also influence the kinetics.

It was these first kinetic models which allowed a rudimentary mechanism to be postulated by various groups (Harris, 1990, Tsuda *et al.*, 1986) and then augmented as advances were made in the experimental analysis of the CVD environment. New insights were provided by modifying the zero-dimensional kinetic approach (Harris *et al.*, 1988) to a one-dimensional system based upon an axis, z, defined as the distance from the substrate (Harris, 1989). The CVD system consisted of a H_2/CH_4 mixture at 0.5 Torr for which H, H_2 and hydrocarbons up to C_4H_6 were modelled using 25 reactions for which the kinetics were known from combustion studies (Kee *et al.*, 1985). This model allowed theoretical kinetics to suggest which species within the system could contribute to growth based on their measured abundance and the growth rate. Crucially, the model showed that only the dissociative reaction of CH_4 with another gas species to form CH_3 and H radicals was occurring at a high enough rate to sustain diamond deposition. Decomposition of methane is the initial stage in an expansive scheme of interconversion between hydrocarbons in the activated CVD environment.

1.4.2 Modelling the gas-surface chemistry

Modelling of the gas phase is, of course, important but offers deeper insights when combined with an understanding of the incorporation of carbon into the lattice and related surface kinetics. The most thorough of these gas-surface studies focused on HFCVD using H_2/CH_4 or $H_2/Ar/CH_4$ chemistry and modelled diffusion and convection processes as well as the gas-gas and gas-surface reactions (Frenklach & Wang, 1991). Improved accuracy was achieved by using a larger number of processes and involving a greater number of species with the final version consisting of 158 reactions, 50 species and the [111] diamond surface. The surface mechanisms involved addition of hydrocarbon species, including CH_3, C_2H_2, C_2H, C_2H_4, C_2H_3 and C_2H_6, to surface radical sites formed by H abstraction. It was concluded that the energetic barrier to incorporation of C_2H_2 was lower than the relatively slow reactions of CH_3 and the other radicals.

Interesting details about the substrate temperature were also conjectured: for example, showing that the increase in the growth rate with T_{sub} is due to the faster rate of H abstraction at higher temperatures as the activation barrier for loss of H is considerably higher than the reverse process. However, at higher T_{sub} the sp^3 carbon can become unstable and rearranges to form sp^2 material. Formation of aromatic species, for example, at high $\chi_0(CH_4)$, was shown to reduce the diamond quality by forming sp^2 networks in the gas phase and on the surface.

Modelling of the potential-energy landscape for individual reactions that occur on the growing diamond surface has also furthered our understanding of the deposition mechanism. Calculations have shown that diamond growth must occur *via* a specific, multi-step mechanism rather than random insertion of growth species into surface bonds which would, instead, produce a highly cross-linked network of hydrocarbon chains. Quantum-mechanical (QM) calculations were made for a CH_4/H_2 plasma using C_9H_{18} to represent the hydrogenated diamond [111] surface as it is small enough to allow an *ab initio* treatment (Tsuda *et al.*, 1986). A semi-empirical basis was used where MINDO/3 (Bingham *et al.*, 1975) molecular-orbital (MO) calculations determine the potential-energy surface and the lowest-energy mechanistic pathway which, generally, consists of reactions *via* transition states obtained by geometry optimization. From these calculations, mechanistic pathways were demonstrated for CH_3 addition to surface radical sites, insertion of growth species into surface bonds and subsequent rearrangement of dangling CH_3 groups into the diamond lattice. Some of the results indicated that ionic hydrocarbon fragments may play a role in the growth chemistry because the activation barriers for their reactions are often low.

In the early 1990's a new diamond CVD mechanism began to take shape based around the previous experimental and computational results and new calculations based on the growth of the hydrogen-terminated [100] surface by HFCVD (Chen, 1988, Harris, 1990, Harris *et al.*, 1991). Beyond HFCVD, the mechanism was quickly used to successfully make predictions for other diamond-deposition systems including those using plasma torch (Stalder & Sharpless, 1990) and combustion flame (Matsui *et al.*, 1990) activation. This mechanism, which would form a *standard growth model*, was based on modelling the [100] surface, rather than the [111] in the earlier study, with a C_9H_4 structure used to simulate the diamond lattice.

The proposed model relies on the excess of atomic H (*cf.* section 1.3.4.3) formed within the reactive plasma (or through thermal decomposition in the HFCVD reactor) which is continually added to and abstracted from the growing diamond surface. Diamond deposition occurs through a number of stepwise reactions beginning with abstraction of H by a gas-phase H atom leaving a surface-radical site. In the majority of cases another H atom will add back to this site but occasionally a carbon growth species, such as the CH_3 radical (Goodwin, 1991), will react to form a surface CH_3 group. This is only stabilized, however, if a surface-radical site becomes available on an adjacent lattice site and another CH_3 radical is added. At this point, further H abstraction leads to activation of one of these dangling CH_3 groups which then combine to propagate the diamond lattice. The result is net diamond deposition as *sp*^{2} adducts are etched back into the gas phase.

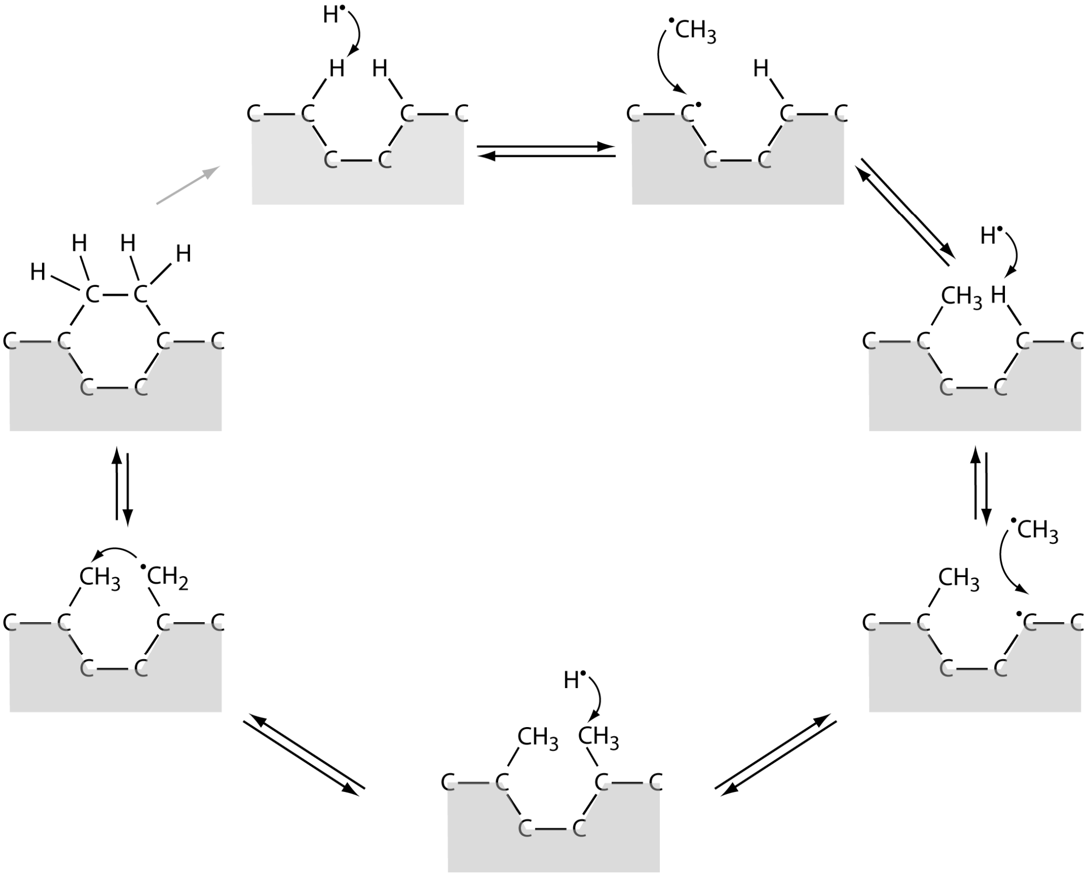

Figure 1.4: Simplified schematic diagram of the standard diamond-deposition model (Harris, 1990, May, 2000).

Experimental evidence for this model is derived from the first diagnostic analysis of diamond-deposition environments which used infrared-diode spectroscopy to detect CH_3, C_2H_4 and C_2H_2 in a HFCVD system where the source gas was methane (Celii *et al.*, 1988). Laser-induced fluorescence spectroscopy was then exploited to quantify the concentration of atomic H in similar systems (Meier *et al.*, 1990) and produced important values for use in kinetic models. At the same time, data from mass spectrometric residual gas analysis (see section 4.3.1) supported theories based around the growth of diamond from CH_3 species (Harris *et al.*, 1988).

While capturing the essence of diamond CVD, the standard model is fairly simplistic as it ignores many other processes such as surface migration and addition to different lattice sites, and thus introduces some errors when predicting trends in crystallite size or growth rate. Some inaccuracy also results from the small size of the diamond structure used in the calculations which, although allowing relatively fast results, was limited as sterically-induced stresses could not be dispersed into a full solid lattice. As well as explaining the mechanistic incorporation of CH_3 into the surface the model also looks at various pathways where diamond is not deposited, such as formation of CH_3CH_2 groups on the lattice surface.

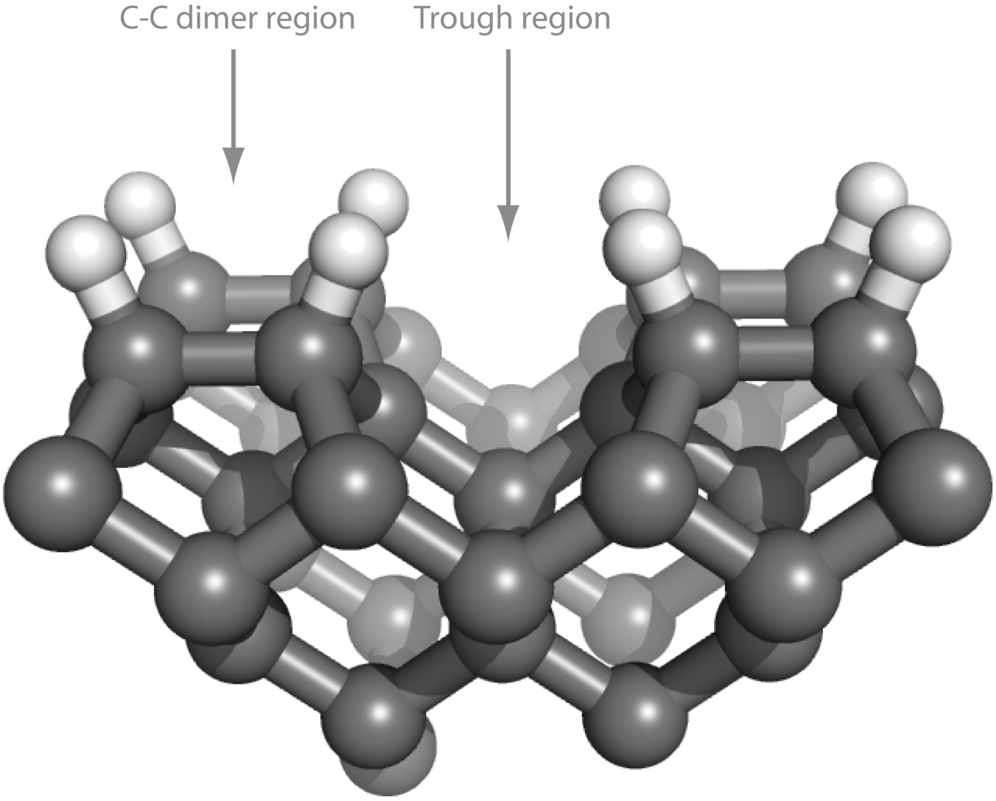

Figure 1.5: Part of the hydrogenated 2×1 reconstruction of the [100] diamond surface illustrating dimer and trough regions which behave differently in the kinetic models.

The mechanism was later expanded upon in an attempt to provide better predictions of the growth rates observed in experiment (Harris & Weiner, 1992). One of the major advances was to use a superior analogue of the diamond surface instead of the C_9H_4 structure which would model the stresses more exactly (Harris & Goodwin, 1993). The structure chosen consisted of a hydrogenated 2×1 reconstruction of the [100] surface made up of two carbon-dimer rows and resulting in a *dimer* region and a *trough* region which behave differently due to the variable interatomic geometries (Figure 1.5). In this formulation the trough regions are analogous with the C_9H_4 structure used previously but the dimer carbon atoms were not treated and required augmentation of the model using CH_3 addition to another radical site followed by structural isomerisation. The new model explained the relationship between the mechanisms occurring at *dimer* and *trough* sites which must occur in tandem for diamond deposition to proceed, and resulted in a much fuller understanding of the diamond CVD process. Mechanistic arguments were combined with reaction kinetics, calculations of steric influences in larger diamond structures and concentrations of growth species to provide rate equations which could accurately predict the diamond growth rate (Butler & Woodin, 1993, Goodwin & Butler, 1998).

1.4.3 Recent modelling of gas phase chemistry

Our current understanding of the gas-phase and gas-surface processes has been recently summarised by comparing new experimental data and computational models with the mechanistic picture we have just described, but with the emphasis on MWCVD (Butler *et al.*, 2009).

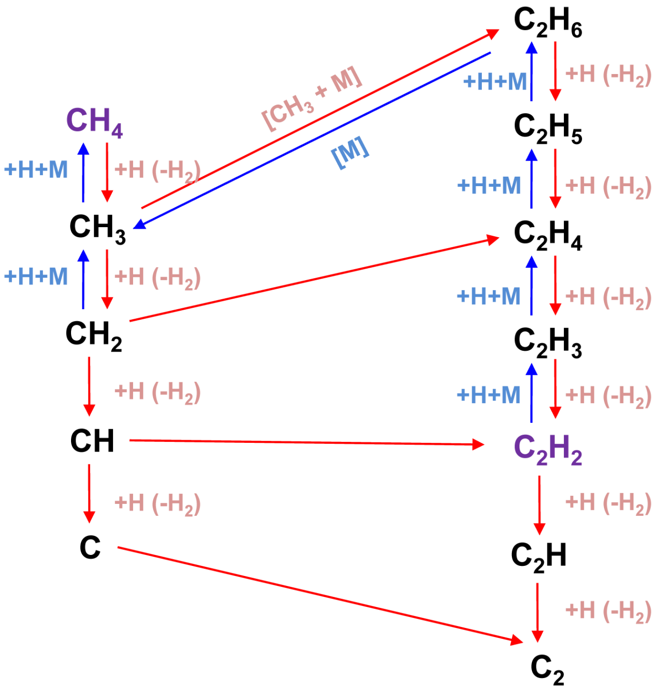

Figure 1.6: Interconversion between C_1 and C_2 hydrocarbons by H-shifting reactions. Arrows indicate the approximate position within the CVD plasma: '→' indicates high T_{gas} and high χ(H) at the plasma centre. '→' indicates reactions that occur further towards the periphery in regions characterized by lower T_{gas} but still high χ(H). Diagram is based on combustion analysis (Johnson *et al.*, 1992).

In the diamond CVD system the chemistry is dominated by a series of fast H-atom abstraction and addition reactions to C_1 and C_2 hydrocarbons, and governed by the local T_{gas} and χ(H), leading to thermodynamic distribution of different hydrocarbon species.

This gas-phase scheme shows that C_xH_y species with low y are favoured in the hotter plasma regions while saturated species are more abundant in the cooler periphery, and the conversions are made possible due to the high χ(H) throughout the system (Mankelevich & May, 2008). Combined with surface chemistry at the substrate and chamber walls, this treatment produces a complex medium to model computationally which has benefitted from improvements to *in-situ* plasma diagnostics.

Quantitative measurement of column densities, *i.e.* along the line-of-sight of the probe beam, of stable species, including CH_4, C_2H_2 and C_2H_6, as well as the CH_3 radical, within the CVD gas phase has been achieved using resonance-enhanced multi-photon ionization spectroscopy in the HFCVD system (Smith *et al.*, 2001) and IR laser absorption spectroscopy in the MWCVD system (Cheesman *et al.*, 2006, Hirmke *et al.*, 2007, Ma *et al.*, 2009a). These absorption measurements require well-characterized spectroscopic transitions and knowledge of the spectral changes with T_{gas} to produce a line-integrated absorption column-density, and in some, poorly characterized systems, the transition efficiencies must be calculated first. Predictably, the results show that radical species are concentrated at the plasma centre (T_{gas} > 2000 K) and they correlate well with the χ(H) and the temperature (Mankelevich *et al.*, 2008). It was found that C_2H_2 made up >97% of all the hydrocarbon species in the plasma mixture because of the high rate of conversion from CH_4 in the outer regions of the plasma away from the hotter core.

Radical species (CH, C_2 and H) were measured quantitatively in the MWCVD system using cavity ring-down absorption spectroscopy and showed peaks in their concentrations at the plasma centre correlating with the T_{gas} profile (Ma *et al.*, 2008). Identical results were also shown for both CH_4 and C_2H_2 source gases, showing the independence of the mechanism on the initial hydrocarbon. Excellent agreement was also achieved between experiment and computational modelling run in parallel with the experimental investigations.

The self-consistent 2-D model of the electric-field propagation, gas-phase chemistry and mass-transport processes in the MWCVD reactor used here has been developed by Dr. Yuri Mankelevich at the Skobel'tsyn Institute of Nuclear Physics, Moscow State University. From this, computer-modelling predictions of gas and electron temperatures and absolute hydrocarbon concentrations for the various molecules, radicals and ions can be made for a range of process conditions, as a function of height (z) above the substrate centre and radial distance from this axis (r). Many different plasma environments have been successfully described by the model including those for growth of NCD (May & Mankelevich, 2008), MCD (Ma *et al.*, 2008), and SCD (Mankelevich & May, 2008) (see Table 3).

For the plasma chemistry involving H_2/Ar/CH_4 mixtures that will be discussed later in the thesis, the model includes ~290 forward and reverse reactions involving neutral species (C, CH, $^3CH_2$, $^1CH_2$, CH_3, CH_4, $C_2(X)$, $C_2(a)$, C_2H, C_2H_2, C_2H_3, C_2H_4, C_2H_5, C_2H_6, C_3, C_3H, C_3H_2, C_4, C_4H,

C_4H_2, H, $H_2(v = 0, 1, 2)$, electronic excited levels $H(n = 2)$, $H(n = 3)$, H_2^*, Ar* (the lowest metastable levels) and Ar** (the lowest levels involved in resonance fluorescence)), and charged species (electrons, and the ions Ar^+, ArH^+, H^+, H_2^+, H_3^+, C^+, C_2^+, C_3^+, CH^+, C_2H^+, $C_2H_2^+$, $C_2H_3^+$, C_3H^+). Many of the plasma processes involve electron-particle reaction coefficients and are governed by the non-equilibrium electron-energy distribution function (eedf), $n_e(\varepsilon)$, which is calculated by solving the Boltzmann equation in a two-term approximation (Ma *et al.*, 2008, Mankelevich *et al.*, 2008). Calculation of the eedf, based on the absorbed MW power, can be used to determine the reduced electric field and electron temperature, T_e. Achieving a meaningful model output relies on numerically solving a set of non-stationary conservation equations for mass, momentum, energy and mole fractions, as a function of r and z, using a finite-difference method.

As the CVD plasma system is fairly complex, a number of simplifications have been necessary in this model including approximation of the electromagnetic field interactions in the treatment of the $CH_4/H_2/Ar$ system we have described. Alternative approaches have also produced interesting results but using a one-dimensional approximation for CH_4/H_2 (Hassouni *et al.*, 1998, Lombardi *et al.*, 2005a) and $CH_4/H_2/Ar$ gas (Lombardi *et al.*, 2004) mixtures. At present a full 2-D treatment of all physical processes has been restricted to simpler H_2-only discharges (Hassouni *et al.*, 1999, Yamada *et al.*, 2007). A review of these models falls outside the scope of this thesis, although a summary has been published (Hassouni *et al.*, 2010), and we instead concentrate on the Bristol-Moscow model which is relevant to this work.

The self-consistent model is divided into three parts which focus on the gas heating and mass transport, the gas-phase chemistry and eedf, and the gas-surface reactions, respectively. In the plasma phase the reactions between electrons and other species are governed by the eedf of the reduced electric field, E/n, where E = electric field amplitude and n = gas density. To simplify the model, the eedf, and the resultant electron temperature, T_e, distribution, are treated as being uniform throughout the plasma volume. The cylindrical plasma volume was determined not by the model but by experimental measurements (*e.g.* absorption studies). These assumptions mean that the eedf, T_e and related dissociation, ionization and excitation reactions can be described as a function of the input power. Calculation of the densities of radical and ionic species throughout the plasma then led to a full description of the complex gas-phase mechanisms using the ~290 reactions involving species described above. Computation of the large set of equations for each reaction is carried out for a number of small regions into which the reactor is divided, and the solutions reconstructed into a full model of the CVD environment. The program is iterated many times until steady state is achieved. Analysis of the modelling results shows how different species are formed and lost in the system, how material is transported around the reactor and how the input power is absorbed by different processes. A particular insight provided by the model is the presence and behaviour of ionic species in the plasma which was found to be dominated by H_3^+, formed from the reaction of excited H atoms and H_2, in H_2/Ar systems, and $C_2H_2^+$ when hydrocarbons are added (Mankelevich *et al.*, 2008).

Overall, however, it is the χ(H) and hydrocarbon interconversion system together with local T_{gas} which governs the gas-phase chemistry of the diamond CVD system. An understanding of the hydrocarbon interconversion leads to the relationship between the input carbon mole fraction (χ_0(C)) and the mole fraction of hydrocarbons in the plasma:

$$\chi(\mathrm{CH}_x) \sim (\chi_0(\mathrm{C}))^{\frac{1}{2}} \tag{1.1}$$

$$\chi(\mathrm{C_2H}_y) \sim \chi_0(\mathrm{C}) \tag{1.2}$$

The model shows that CH_3 is abundant near the substrate surface and uses this to calculate an upper limit for the growth rate:

$$\chi(\mathrm{CH_3}) \sim 5 \times 10^{-4}(\chi_0(\mathrm{C}))^{\frac{1}{2}} \tag{1.3}$$

$$G\left[\mu\mathrm{m\ h^{-1}}\right] \leq 0.15 \times p\ [\mathrm{Torr}] \times (\chi_0(\mathrm{C}))^{\frac{1}{2}} \tag{1.4}$$

While accurately predicting *G* for some systems this model produces less consistent results in more complicated environments such as the high χ(Ar) plasmas (Butler *et al.*, 2009).

1.4.4 Recent gas-surface modelling

The combination of gas-phase diagnostics and 2-D modelling has improved our understanding of the plasma chemistry, whilst developments concerning the gas-surface interactions have also been made. Rather than solely treating the straightforward addition of a growth species to a diamond lattice new models can describe the various stages in film deposition including formation of defects and faults. Calculations have shown that formation of a new layer of atoms on the lattice is a rate-limiting process during diamond CVD which consists of forming a four-carbon atom nucleus on the <111> surface (Butler & Oleynik, 2008). This nucleus is then used to grow the new diamond layer and also can be used to explain the growth-rate enhancement of certain species, such as CO and CN (see sections 1.3.4.3 and 1.5.3, respectively), as they are not etched back into the gas phase as readily as hydrocarbon adducts.

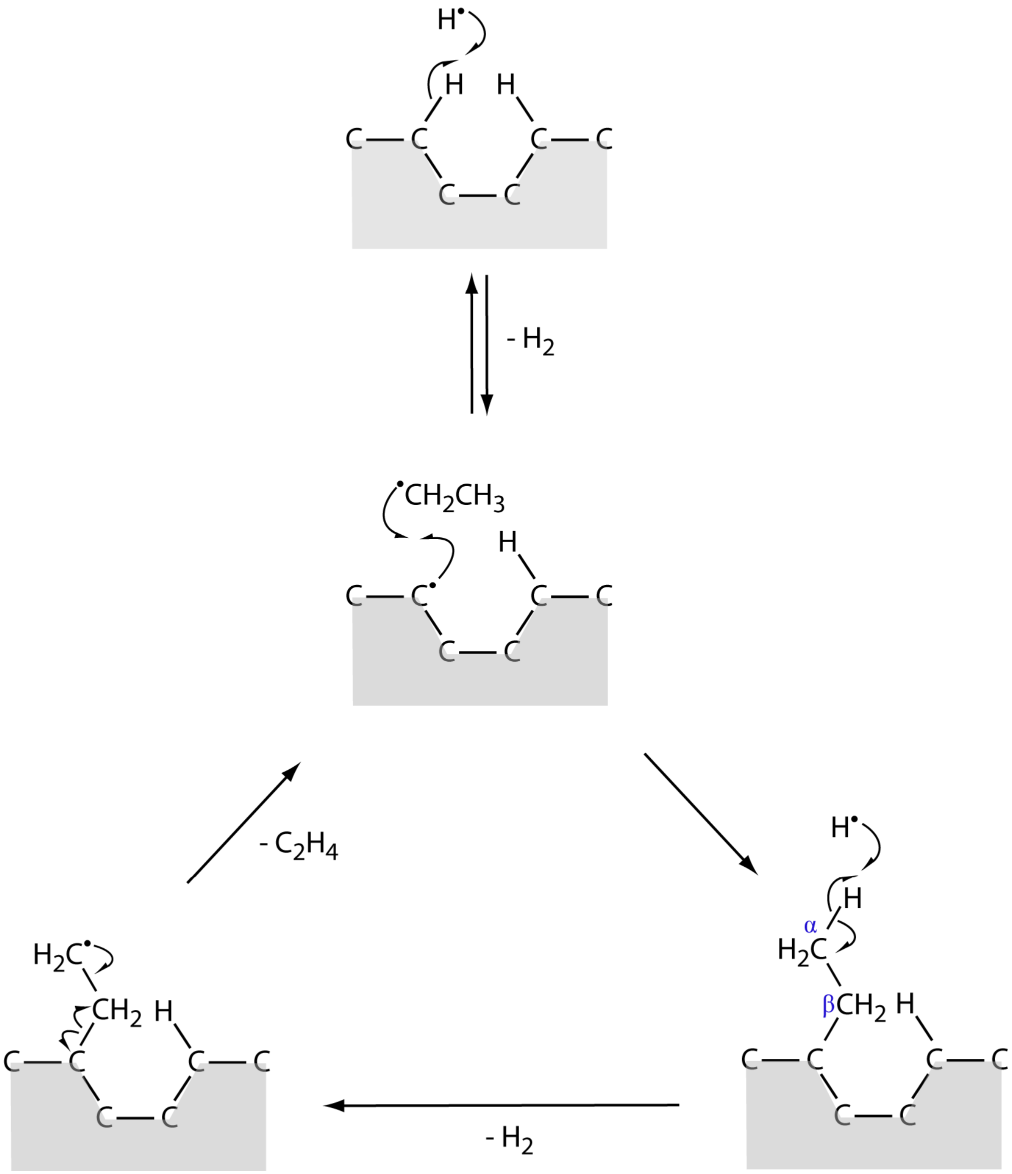

Figure 1.7: Mechanism for removal of large hydrocarbon adducts from the surface *via* the β-scission reaction leaving a surface-radical site.

Improved accuracy in surface-based calculations can be achieved by solving energy calculations for a certain number of atoms quantum mechanically (QM), within a larger framework which is treated only with a molecular mechanics (MM) approach. For these calculations the type of diamond surface used influences the results with studies concentrating on the <100> and <111> surface which are, nearly always, hydrogen terminated. In certain situations, for example when looking at surface migration, it is useful to investigate more complex surfaces containing step edges which are typically a few atoms high and are similar to defects commonly encountered in real diamond films. The QM/MM approach allows accurate modelling of the processes within a reasonable amount of computational time. Studied reactions include those relevant to addition of growth species to surface-radical sites (seen in Figure 1.4) but also more diverse processes such as insertion and rearrangement mechanisms. Solving the calculations provides information on which reactions and processes are likely to occur, and which are limited by an activation-energy barrier (Cheesman *et al.*, 2008). These QM/MM calculations show that growth of diamond can occur by insertion or incorporation of C_1H_x species (x = 0-3) into the diamond lattice and that C_2H_y species are more readily removed by a β-scission reaction during which H abstraction initiates an electronic rearrangement and breaking the carbon-carbon bond (Figure 1.7).

The potential-energy pathways for addition of growth species to dimer and trough sites on the reconstructed [100] surface were calculated using the QM/MM approach and showed a range of feasible reactions that could occur if some geometric requirements are fulfilled. Modelling of surface migration of species like CH_2 indicated the magnitude of any energy barriers involved and allowed a migration rate to be calculated (Cheesman *et al.*, 2008).

For MCD deposition the relative growth rates on the different crystal faces can be defined by a dimensionless factor called the 'alpha-parameter':

$$\alpha = \sqrt{3}\left(\frac{v_{100}}{v_{111}}\right) \tag{1.5}$$

where v_{100} and v_{111} are the growth rates on the [100] and the [111] surface, respectively (Wild *et al.*, 1990, Wild *et al.*, 1994). Similar parameters can be defined for other crystal faces and linked to the evolution of epitaxial diamond in CVD systems (Silva *et al.*, 2008). In theory, it would be a major triumph to link the deposition parameters, P, p and T_{sub}, to these morphology-specific growth parameters *via* the deposition chemistry we have discussed. Although yet to be achieved, a unified model of diamond CVD chemistry would combine the vast complexity of the plasma system, including a treatment of all the species and physical processes as a function of the experimental conditions, together with a detailed understanding of the gas-surface processes.

1.4.5 Kinetic Monte Carlo approach

Rather than treating the energetics of individual reactions using *ab initio* calculations that cannot be solved for large systems, new insights into diamond CVD have arisen from a statistical approach with mesoscale growth of the lattice dependent on the probabilities of a process occurring which is, in turn, based on predicted and measured rates. The CVD mechanisms of adsorption, desorption, migration and incorporation of growth species on solid surfaces are ideally suited to the Kinetic Monte Carlo (KMC) treatment. In simplifying the system and using a non-specific algorithm, much larger structures can be analysed providing details on diamond deposition across hundreds of atoms. Time dependent, pseudo-random events are proposed for each surface site with the probabilities of them occurring based on the pre-determined rates and other parameters such as the concentrations of growth species and the substrate temperature (Battaile & Srolovitz, 2002).

The first KMC modelling of diamond CVD was purely based on adsorption and could accurately predict growth rates by relating the incorporation of material as a function of the concentration of growth species above the substrate (Frenklach & Wang, 1991). Increasingly complex processes were included such as modelling some of the surface mechanisms (Battaile *et al.*, 1997), etching of species bonded to the substrate (Battaile *et al.*, 1999) and even surface migration in one of the latest, and most successful, proposals (Netto & Frenklach, 2005). Another KMC approach has also been gradually expanding from simple beginnings into a successful model based upon experimentally determined rates (May *et al.*, 2009, May *et al.*, 2010). This model was based on the standard growth model of addition of C_1 species to a [100] surface and included processes such as etching of different species, renucleation of crystals and migration of CH_2 on the surface. The model proved to be a good simulation of the CVD process and accurately predicted growth rates and diamond structures such as the formation of NCD by increasing the nucleation rate. This was achieved through formation of species on the surface which could not be etched back into the gas phase, simulating the presence of the four-carbon defect or CN adduct which acts as nucleus for a new diamond mono-layer (Butler & Oleynik, 2008). The influence of T_{sub} showed the complex relation between the various processes which occur during diamond CVD but also highlighted the limitations of the KMC approach which can produce un-physical results if the rates for certain processes are not accurately known.

Additional insights have arisen by treating diamond deposition at step edges with both molecular dynamics, to describe fast chemisorptions processes, and Metropolis Monte Carlo modelling, to examine other processes which occur on much longer time scales (Eckert *et al.*, 2010a). The results examined the mechanisms by which different growth species, such as CH_2, incorporate into step edges and how this is related to the formation of NCD morphologies (Eckert *et al.*, 2010b).

1.4.6 NCD deposition

This standard model for diamond deposition has been expanded to explain the entire distribution of crystallite sizes from single-crystal to ultrananocrystalline diamond. This is based on the competition for active sites on the growth surface by H atoms, CH_3 and other C_1 radicals (May *et al.*, 2006, May & Mankelevich, 2006, May & Mankelevich, 2008). The crucial factor influencing the crystallite size is thought to be the ratio of atomic H to all C_1 radical species at the deposition surface. This is due to the changing probability of renucleation, *i.e.* addition of new diamond nuclei or crystal twins on the surface, instead of etching of species back into the gas phase unless they add to certain, stable lattice sites. Experimental parameters – gas mixtures, temperatures and pressures – in the CVD reactor all combine to establish the ratio $\chi(\text{H}):\Sigma[\chi(\text{CH}_x)]$ (where x = 0-3) and which will ultimately determine the diamond grain size and film morphology. It is then obvious that the mole fraction of H_2 supplied to the reactor, and, therefore, the H atom density, will be critical in influencing the diamond grain size (Birrell *et al.*, 2006). Observations show that as $\chi_0(\text{H}_2)$ is decreased from conditions which would produce SCD or MCD the diamond grain size decreases towards a nanocrystalline state. Putting it another way, we see that as $\chi(\text{H}):\Sigma[\chi(\text{CH}_x)]$ decreases the film morphology changes from MCD to NCD and finally to UNCD or sp^2/a-C films depending on the T_{sub} (May *et al.*, 2007). Observations of NCD-depositing plasmas usually report high concentrations of soot particles and larger hydrocarbons which may prove important for the deposition mechanism. Attempts have been made to model these processes from the point of view of combustion chemistry (Mohasseb *et al.*, 2005), although their role in the deposition remains unclear.

Recent studies of the deposition of NCD films using inert-gas plasmas (where $\chi_0(\text{H}_2) < 0.5$) will be discussed in the experimental section, combined with the results from diamond growth and plasma diagnostics in section 3.3.

1.4.7 Other mechanisms

Of course, different growth species, other than the C_1 species of the standard model, have also been proposed as diamond precursors and the foremost of these are C_2H_2 and C_2. Incorporation of C_2H_2 into the diamond lattice was initially shown to have a low energy barrier (Frenklach & Wang, 1991) but the most likely outcome is that it is etched back into the gas phase *via* β-scission.

Intense emission from C_2 Swan bands in inert-gas-rich plasmas led to the proposal of a nanocrystalline-diamond growth mechanism based upon the C_2 radical species. This process relies on formation of C_2 from the abundant C_2H_2 (or from fragmentation of C_{60} fullerenes) sink within the reactor *via* thermal decomposition aided by efficient charge exchange from Ar^+ or by Penning ionization from the metastable Ar* species. A dissociative electron-ion recombination process would then involve ionization of C_2H_2 with Ar* and fragmentation of $C_2H_2^+$ into C_2 and H_2 on recombination with an electron. These mechanisms must be present and not hindered by a high activation barrier to achieve concentrations of C_2 at the substrate surface high enough to explain the observed growth rates (Gruen *et al.*, 1994a, Gruen *et al.*, 1994b, Gruen *et al.*, 1999, Zhou, *et al.*, 1998b).

Contrary experiments show that, while the decomposition of C_2H_2 to C_2 may occur in the hottest regions of the plasma, the concentration of the proposed growth species at the substrate surface is too low to explain the NCD growth rates (Fox *et al.*, 2009, May *et al.*, 2006, May & Mankelevich, 2006). As a result C_2 is now believed not to be a major contributor to diamond deposition and the growth of NCD films in inert-gas-dominated plasmas is still thought to proceed primarily *via* the addition of CH_x ($x = 0\text{-}3$) to the diamond lattice (section 1.4.2).

1.5 Trace additions, defects and doping

1.5.1 Diamond doping

Synthetic diamond deposition processes are amazingly adaptable, as testified by the range of different trace gases which have been added, through various means, to the CVD environment. The bulk of the ongoing research in this area is concerned with altering the naturally insulating nature of diamond and, in doing so, modify the electrical properties of the material. To produce semiconducting diamond requires introduction of dopant species which alter the band structure and reduce the band gap of the undoped or intrinsic material.

The large gap of 5.45 eV in intrinsic diamond makes excitation of electrons from the valence band into the conduction band unfavourable at room temperature or when exposed to radiation where $\lambda > 200$ nm, Figure 1.8.

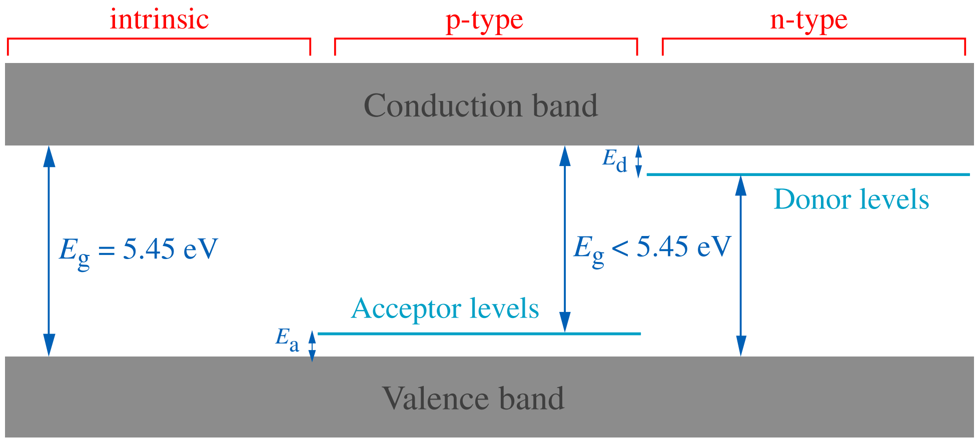

Figure 1.8: Introduction of acceptor or donor levels into the diamond band gap by doping the diamond results in semiconducting properties.

Introducing impurities with lower atomic number and fewer electrons than carbon produces acceptor levels by providing additional holes to remove electrons from the valence band and thereby reduce the effective band gap. Conversely, incorporation of atoms with higher atomic number than the diamond will supply extra electrons which occupy delocalised states just below the conduction band. In both instances the carrier density increases where the small binding energies, measured relative to either the valence or conduction bands, result in additional acceptor or donor levels and a contraction of the material's band gap (Ashcroft & Mermin, 1976). The resultant semiconductors are termed *p*- and *n*-type semiconductors, respectively, and are commonly combined into electronic devices, such as *p*-*n* junctions. Both forms of diamond doping have been achieved but formation of robust, reliable *n*-type material still remains a considerable problem for current diamond research. Devices which rely on semiconducting diamond include a wide range of sensors, such as X-ray (Bergonzo *et al.*, 2002) or particle (Bergonzo *et al.*, 2001) radiation detectors, and cold-cathode devices (Fink *et al.*, 1998). Making use of the negative electron affinity of diamond, the development of cold-cathode devices provides a route to forming new field-emission displays which require only very low applied fields to function (Talin *et al.*, 2001).

1.5.2 Boron

Fabrication of *p*-type diamond is generally performed by incorporating B atoms into the lattice as occurs in natural, type IIb diamonds which exhibit semiconducting properties. The acceptor levels are positioned close to the top of the valence band at $E_a = 0.37$ eV. Some of the earliest diamond deposition experiments involved B-containing gas mixtures (Spitsyn *et al.*, 1981) and use of reagents such as B_2H_6 (Shiomi *et al.*, 1990) has now become commonplace for growth of *p*-type material (Comerford *et al.*, 2006, Ramamurti *et al.*, 2008). In addition to these electrical properties, modifying the diamond lattice using substitutional B atoms manifests itself in both structural and optical changes to film (Locher *et al.*, 1995).

The concentration and position of B doping can be accurately controlled using particular gas-phase boron concentrations and other reactor parameters and, as such, the majority of *p*-type diamond will be B-doped. The important exception is *p*-type surface conduction on H-terminated surfaces in contact with air. Here there is an electron-transfer reaction between the H-terminated surface and the absorbed water layer which results in bending of the valence band towards the Fermi level and formation of a hole-accumulation layer (Ristein *et al.*, 2001).

Absorption spectroscopy has been used to probe the plasma-phase environment in B/H (Ma *et al.*, 2010a) and B/C/H (Ma *et al.*, 2010b) systems where B is added in ppm levels of B_2H_6.

1.5.3 Nitrogen

While boron doping is vitally important for current diamond device fabrication, nitrogen is the most frequent impurity, apart from hydrogen, found in both natural and synthetic diamonds. Unfortunately, the donor level formed when diamond is doped with N atoms lies too low (E_d = 1.7 eV below the conduction band) to be of any use for device applications, and so attention has turned to formation of *n*-type material using P atom dopants (see below). The intentional addition of trace amounts of N to diamond-depositing reactors has been extensively studied and has allowed both the growth rate and crystal morphology to be modified over wide ranges.

1.5.3.1 Nitrogen in the gas phase

Although not explicitly part of the Bachmann system of carbon, hydrogen and oxygen chemistry (see section 1.3.4.3e), the presence of nitrogen in diamond-growing environments is of considerable importance. Whether present as an impurity in the gaseous starting materials, as a result of inadequate vacuum apparatus or as an intentionally used additive, nitrogen is influential on many aspects of diamond CVD. These range from influencing the growth chemistry (altering the growth rates and the required input power) to changing the properties of the diamond film inducing different morphologies and electrical or doping characteristics.

The increase in growth rate, *G*, with N added to the source gases can be remarkable with observations of eightfold increases for just 100 ppm N_2 added to MWCVD reactors (Müller-Sebert *et al.*, 1996) although N is not incorporated into the film in large amounts (Locher *et al.*, 1994). The formation of {100} facets has also been shown to be favoured in the presence of trace (200 ppm) nitrogen (Cao *et al.*, 1996) and, as these are perpendicular to the growth axis, can be used to produce large, smooth diamond surfaces. It appears that the influence of N_2 on G and morphology is somewhat dependent on the activation method because growth using HFCVD is not altered as much as with MWCVD. Formation of stable nuclei on the growing diamond surface using the CN group has been a proposed mechanism for this enhancement in the rate of deposition because a rate-limiting step is overcome (Butler & Oleynik, 2008).

While not as effective a dopant as boron, incorporation of N into UNCD films to produce *n*-type conductivity has been demonstrated although conduction is thought to occur along grain boundaries rather than true doping of the bulk (Beloborodov *et al.*, 2006, Bhattacharyya *et al.*, 2001). Associated increases in sp^2 content with higher N content have been observed (Birrell *et al.*, 2003).

1.5.3.2 Nitrogen defects

Extensive investigation of the defects induced by diamond doping has been carried out using electron paramagnetic resonance (EPR) spectroscopy, which is foremost amongst other methods such as photoluminescence (PL) studies. Although many defects have been identified, some involve substitutional nitrogen next to a vacant diamond lattice site in so-called NV pairs and are often grown into the diamond during the CVD process. Two defects are particularly important and prevalent: the NV^0 centre (with an associated PL peak at 575 nm) and the NV^- defect (with a PL peak at 647 nm). These are of interest for diamond-based quantum computing as they can be identified within crystals and the associated spin determined or altered (Prawer & Greentree, 2008).

The presence of significant N in both natural and synthetic diamonds results in changes to the optical transparency and can give yellow or brown colouration to the crystal. It is sometimes possible to remove the majority of this unwanted optical absorption in CVD single crystal diamonds through annealing (Meng *et al.*, 2008).

Modelling diamond structures which contain N atoms on, or just below, the surface has been implemented using QM calculations which indicate different behaviour of different crystal surfaces. Substitution of different N-containing species at various sites in the lattice (Van Regemorter & Larsson, 2009a) and as co-absorbates on the surface (Van Regemorter & Larsson, 2008, Van Regemorter & Larsson, 2009b) has been shown to influence the growth mechanisms and, in most case, favour higher deposition rates.

1.5.4 Phosphorus

Like nitrogen, phosphorus has received special attention due to the possibility of *n*-doping synthetic diamond films (E_a = 0.56 eV, hence P is a shallow donor compared with N) and many different precursor species have been trialled as additives to CVD plasmas. The participation of phosphorus atoms and molecules added to CVD gas mixtures is even less well understood than the addition of nitrogen-containing species. However, considerable positive energy barriers when forming P-containing structures due to difference in atomic size, means that incorporation of phosphorus into the diamond lattice does not easily occur (Kajihara *et al.*, 1991). There have been a small number of successfully *n*-doped diamond films but these are not as reliable as the B-doped counterparts (Koizumi *et al.*, 1997, Nishimori *et al.*, 1997). More recently tertiarybutylphosphine (a less harmful reagent than phosphine) has been used to dope CVD grown films (Kociniewski *et al.*, 2006).

P-containing reagents do have an influence on the gas chemistry and the addition of phosphine in low concentrations has been shown to increase the growth rate and alter the diamond morphology. Like N, even ppm levels of phosphorus are supposed to participate in the gas-surface chemistry and influence the kinetics (Bohr *et al.*, 1995). An optimum concentration of 1500 ppm of PH_3 added to a HFCVD reactor induces a faster growth rate and a high quality diamond morphology (Tsang *et al.*, 1998).

Co-doping with N and P (from a solid $NH_4H_2PO_4$ source) was found to be particularly effective in HFCVD as, it was proposed, the incorporation of nitrogen disrupted the diamond lattice sufficiently to allow larger P atoms to find an appropriate doping site. Without this dilation of the lattice the difference in size between the diamond structure and the P atoms severely limits uptake of the dopant (Cao *et al.*, 1995a). The same study, using SIMS, also indicated greater incorporation of both N and P into the (111) surface compared with (100) and comparable concentrations of N and P in polycrystalline films (Cao *et al.*, 1995b).

1.5.5 Sulfur

Like phosphorus, the atomic size of sulfur means that the energy barrier for incorporation into the diamond lattice is high and doping only occurs with low efficiency. The addition of sulfur containing species (CS_2 & H_2S) to CVD source gases also results in a reduction in the diamond growth rate (Barber & Yarbrough, 1997, Sakaguchi *et al.*, 1999). This has been associated with an observed decrease in hydrocarbon growth species (such as CH_3) in MS analysis (Petherbridge *et al.*, 2002a). Inclusion of S into the diamond lattice was proposed to be *via* either the CS or HS species but the efficiency of doping was decreased by loss of solid sulfur to the chamber walls formed as HS diffuses to the cooler outer plasma and aggregates into clusters. Reported high conductivities for ‘S-doped’ diamond have been discounted (Kalish *et al.*, 2000) due to the co-incorporation of B into films: a process which may be favoured in the presence of co-doping S compounds (Garrido *et al.*, 2002).

1.5.6 Chlorine

The use of halogens and halogen-containing species, such as fluorocarbons, in the fabrication of semiconductor electronics has now become widespread for certain key processes. The addition of halogens to diamond-depositing gas mixtures has been studied to a lesser extent but with some important findings outlined below.

Early studies in a HF reactor showed that addition of HCl to standard gas chemistry resulted in a doubling of the observed growth rate (Pan *et al.*, 1994) possibly due to chloromethyl radicals adding efficiently to diamond surfaces. The presence of chlorine or chlorinated hydrocarbons also allows deposition at lower substrate temperatures, thus widening the range of possible substrates for diamond CVD (Chu & Hon, 1993). Chlorine was presumed to behave catalytically at the gas-substrate surface as only traces (1-2%) of Cl were observed on the diamond surface but not in the bulk material (Proffitt *et al.*, 2000, Tsang *et al.*, 1996).

1.6 Pre-treatment

1.6.1 Diamond nucleation & seeding

For many CVD processes nucleation is a crucial rate-determining step and, in most cases, before depositing a diamond film onto heterogeneous materials the substrate surface must be roughened or seeded. This is because spontaneous nucleation is unlikely on non-diamond surface, only achieving ~10^4-10^5 cm^{-2} on Si (although this is heavily dependent on the reactor type, gas activation and deposition parameters). Much higher nucleation densities are critical for producing continuous and uniform coatings or films (Ralchenko *et al.*, 2005), and nucleation is considered the most significant factor influencing surface roughness in NCD films (Lee *et al.*, 1999, Liu *et al.*, 2006, Williams *et al.*, 2007a). A seeding density of 10^8-10^{10} cm^{-2} is important to ensure the diamond grows with the required film properties such as grain size, orientation, transparency, adhesion and surface roughness (Cola *et al.*, 2008, Yang *et al.*, 1995). The nucleation density also determines the morphology of the reverse of the film and may be important for various applications where the substrate is used as a mould which is removed after deposition (see section 6.0). A detailed review of current nucleation methods has been undertaken recently (Das & Singh, 2007).

1.6.2 Mechanical treatment

The most basic, but very effective, nucleation of a heterogeneous substrate surface can be derived from mechanically scratching it to add imperfections, and for some materials, such as Si, to leave small particles embedded in the surface (Iijima *et al.*, 1990, Mitsuda *et al.*, 1987). Sufficient roughening of the surfaces to obtain a high enough nucleation is often achieved using mechanical abrasion with hard grit – SiC (Sawabe & Inuzuka, 1986), c-BN (Yarbrough, 1991) and Al_2O_3 have been investigated but diamond powder has proven most effective (Demuynck *et al.*, 1997, Morrish & Pehrsson, 1991). However, surface damage (microscopic defects and/or large scratches) is often not uniform and can give rise to low quality films making the process unsuitable for tribological/MEMS technologies. It is also limited to treating planar substrates and not applicable for complex and 3D shapes.

1.6.3 *Ex-situ* application of nanodiamond seed particles

Mechanical abrasion can be efficient at nucleating substrates for MCD deposition, but the low surface roughness of NCD and UNCD films often demands a less aggressive nucleation technique. A less vigorous approach is to apply nanodiamond (ND) seed particles, typically in the form of a colloid or slurry suspension in a suitable liquid, onto the substrate surface, where they may settle or become embedded depending on the process used. As will become apparent, the nanodiamond is often dispersed in water as its polarity suits the slight charged nature of the diamond surfaces. For less polar liquids the stability of the ND colloid becomes an issue.

1.6.3.1 Ultrasonic treatment

In this process substrates are treated by submersion in the ND suspension, and then ultrasonically agitated to apply or embed diamond seed particles in the surface and produce a high nucleation density (Smolin *et al.*, 1993). This method also damages or scratches the surface through cavitation or abrasion which will beneficially aid diamond nucleation as long as the film morphology is not influenced (Yugo *et al.*, 1996). Successful nucleation has been demonstrated using parameters such as an ultrasonically-agitated suspension of 4-6 nm ND in an alcohol for 15-30 min (Ralchenko *et al.*, 2005).

1.6.3.2 Spin-coating deposition

The ND colloid is added liberally onto a substrate and then rotated at ~2500 rpm for a set amount of time to achieve an even coating of seed particles by centrifugal force. Dispersing diamond seeds in a photoresist can also provide a route to forming patterned substrates using a photolithographic technique (Yang & Aslam, 1995). Despite its wide use in the semiconductor industry the technique is limited to planar substrates and other methods must be used for more intricate 3D shapes.

1.6.3.3 Electrostatic-spray (electrospray) deposition

The application of the seeding colloid onto the substrate is achieved by ionizing droplets of the dispersion emanating from a nozzle using a high voltage. The highly charged droplets repel each other, spreading out radially towards an earthed plate on which the substrate is mounted. This technique is widely used in industry for application of volatile suspensions of colloidal particles onto planar substrates, such as spray painting, and was developed for diamond seeding at the University of Bristol. The experimentation which resulted in the process is discussed in greater detail in section 2.5.5.

1.6.4 *In-situ* seeding: Bias-enhanced nucleation (BEN)

Adjustment of the growth parameters of a CVD reactor in the initial stages of diamond deposition can induce spontaneous nucleation on a previously untreated heterogeneous substrate surface. The determining factor is the ratio of hydrocarbon to hydrogen within the source-gas mixture which is chosen to induce implantation of carbon ions (and/or other species) into the substrate surface as a voltage bias is applied between the plasma and the substrate. The result is an epitaxial seed layer with very high nucleation density (Arnault *et al.*, 2008). Atomic force microscope (AFM) imaging has been useful in showing the effectiveness of this nucleation method (Chiang & Hon, 2001).

Successful implantation depends on the energy with which carbon species strike the substrate, requiring the first few atomic layers to be penetrated. This induces strain in the surface layers and may also contribute to nucleation of the diamond film (Lifshitz *et al.*, 1989). Three distinct models for nucleation by this method have been proposed for differing energy regimes:

1. Implantation model – nuclei form a thin surface layer by ion impact (Robertson, 1995, Stockel *et al.*, 1998)
2. Adatom mobility model – mobile carbon clusters form on the surface (Jiang & Klages, 1996, Jiang *et al.*, 1994).
3. Impact of larger carbon species results in direct diamond nucleation.

A bias of −70 V applied to the substrate has been shown to increase the nucleation density of diamond (Jiang *et al.*, 1993, Stoner & Glass, 1992, Yugo *et al.*, 1991) and seems to point to towards an implantation model. Indeed, successful nucleation has been shown for ion implantation into the substrate prior to diamond deposition (Gerber *et al.*, 1995, McGinnis *et al.*, 1995, Yugo *et al.*, 1993). Measurement of ion energies has failed to find consensus and provides a large range of readings between 10-100 eV depending on the analytical technique and the CVD reactor (Awakowicz *et al.*, 1997, Gerber *et al.*, 1994, Kulisch *et al.*, 1996). Sampling is challenging as the ions have to be extracted without altering their kinetic energy and only recently has mass spectrometry been applied (Kátai *et al.*, 1999a). The measurement of ions by mass spectrometry is discussed in section 4.3.7.

Although the use of BEN is fairly common it does have some drawbacks in requiring conductive substrates and not being easy to implement over large areas (Arnault, 2003).

1.6.5 Inter/Buffer layer

The final important nucleation process involves an additional layer between the substrate and the growing diamond film which allows higher nucleation densities and stronger adhesion between the film and the substrate. Carbon nitride (Karve *et al.*, 1996) and indium tin oxide (Musale *et al.*, 1999) buffer layers have been used to enhance diamond deposition. Ideally, materials for the buffer layer would share the diamond crystal structure (*e.g.* SiC). However, use of carbides may be undesirable due to the formation of an amorphous layer at the interface which may influence the electronic, thermal or optical properties of the film (Ralchenko *et al.*, 2005).

2.0 Experimental method

In this section we introduce the MW system which is based on an ASTex design with a process chamber purpose built by Element Six, Ltd. There are two, nearly identical, MWCVD reactors used in this research, one equipped with side arms for laser absorption measurements (section 2.6.2) and the other with a differentially pumped mass spectrometer system (see section 4.5). The latter setup is discussed here in detail as it is used for all the diamond deposition and MBMS experiments whereas the former system was only used for the absorption and some of the emission spectroscopic experiments and has been described in previous work (Cheesman, 2006, Ma *et al.*, 2008). After describing the deposition apparatus, the electrospray seeding method is introduced and followed by a description of the analytical techniques used to characterize the diamond films and the plasma discharges.

2.1 MW reactor

2.1.1 Microwave generator & waveguide

Activation of the gas mixture in the reaction vessel occurs by absorption of microwave radiation at 2.45 GHz generated by a 1.5 kW ASTeX magnetron (HS-1000) linked through a thermal load (CS-1000) and a directional coupler (DCS-1000). Excess power reflected back from the cavity is measured *via* a radio frequency (r.f.)-diode in the coupler, absorbed by the water-cooled thermal load and, therefore, protecting the magnetron. To convert from a preceding Bristol MW system design to the current one, a tapered adaptor is necessary to increase the bore of the waveguide to fit the three-stub tuner and antenna feedthrough. The antenna couples MW radiation through a right angle – from travelling horizontally to vertically down into the chamber – and tuning allows the cavity resonance to be optimized for a particular gas mixture or set of deposition parameters.

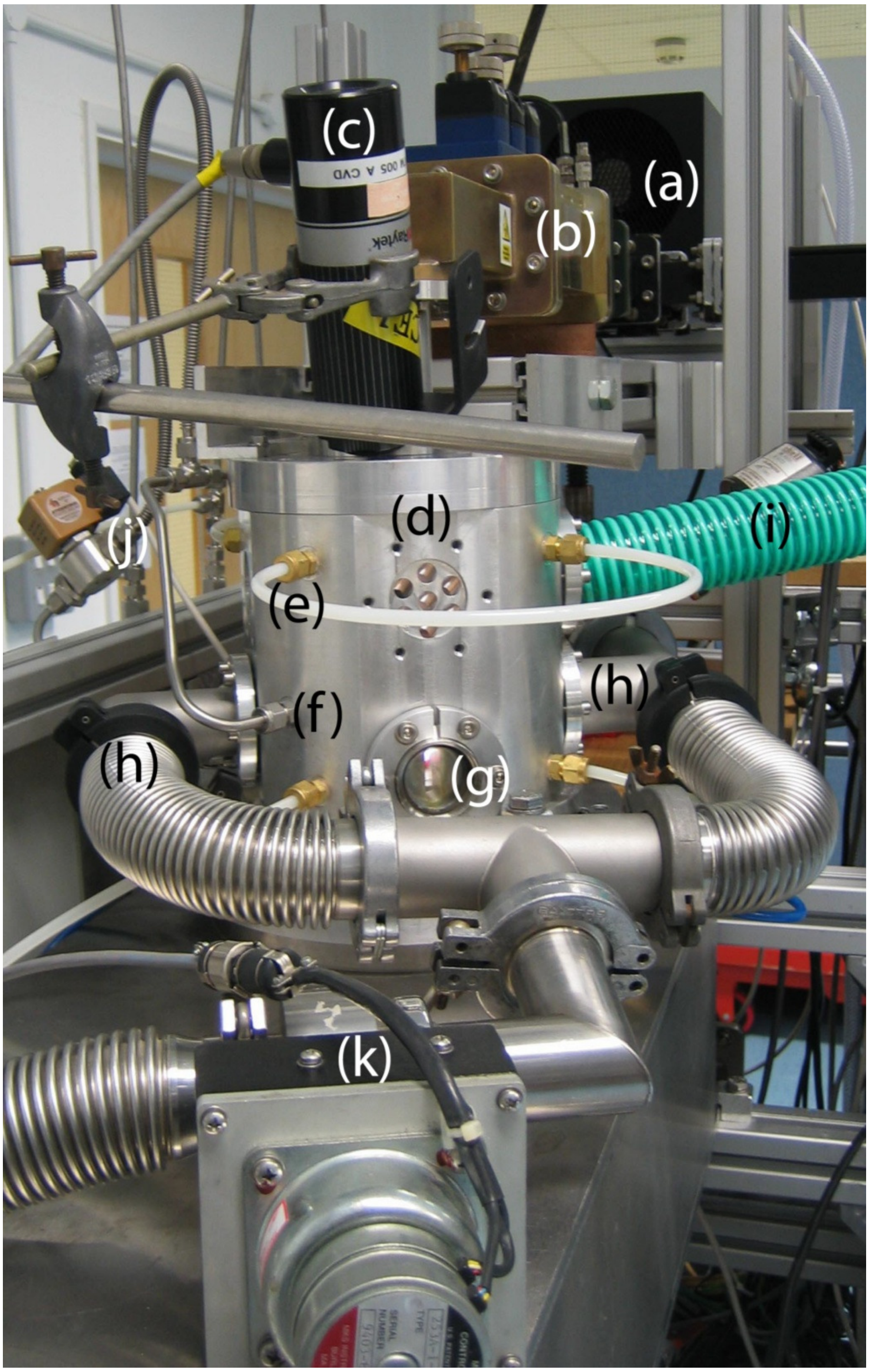

Figure 2.1: The MWCVD setup used for diamond deposition and MBMS experiments. Labelled parts include: (a) MW magnetron, (b) MW waveguide, (c) optical pyrometer, (d) reactor chamber, (e) cooling water circulation, (f) process gas inlet, (g) viewing window, (h) gas exhaust, (i) air cooling pipe, (j) solenoid valve and (k) pressure regulating butterfly valve.

2.1.2 Reaction chamber

2.1.2.1 Water-cooled reactor vessel

The Element-Six-designed plasma reactor (Cheesman, 2006) consists of a water-cooled aluminium cylinder (height = 175 mm, internal diameter = 120 mm) which is divided into two parts by a vacuum-sealed transparent 'quartz' window (which is actually made from fused-silica (Knight Optical UV Grade, 119.5 mm diameter × 7.4 mm thickness)). Above this partition is the atmospheric-pressure MW waveguide, and below it is the sub-atmospheric plasma CVD reactor with diametrically opposed gas inlets. Working pressures within the reactor are measured using a 1000 Torr (Chell MK861) capacitance manometer and the base pressure is monitored with a Pirani gauge (Edwards PRM10). The pressure is controlled with an automatic control unit (MKS252A) using a butterfly valve (MKS 253A-1-40-1) which throttles the exhaust from the chamber which is pumped by a rotary pump (Edwards E2M2). This works using a feedback from the chamber pressure gauge and controls the exhaust throttling accordingly, in effect altering the pumping speed. A blower is used to cool the quartz window by passing a stream of air across its top surface. To exchange samples and clean inside the reactor vessel the top section can be unbolted and jacked up vertically.

2.1.2.2 Substrate mount

The base of the reactor can be configured in two differing modes, with alternative inserts depending on the experiment. For growth of diamond films the MW reactor is isolated from the differential pumping stages and the mass spectrometer by sealing the joining flange with an Al platen and O-ring.

Deposition occurs on substrates of various sizes which can be located in recesses in Mo holders which are milled out to a depth which allows the substrate surface to lie flush with the upper surface of the holder. A number of different holders have been produced for use of different substrate shapes and thicknesses. To isolate the Mo holder (heated by the plasma to ~1000 K) from the water-cooled Al baseplate, it is placed onto a 250-µm-thick W wire ring as a thermal break. It may be important to note that no metallic paint has been used throughout any of the deposition experiments described here.

When conducting mass-spectrometry experiments, this plate is replaced with a Mo sampling insert which has the same dimensions as the combined Al platen/Mo holder configuration, but with an orifice in the centre (where the substrate would usually sit) to probe the plasma. The design of this sampling system will be discussed in more detail in section 4.5.

2.1.3 T_{sub} measurement with an optical pyrometer

It should come as no surprise that the substrate temperature plays a fundamental role in determining the nature of the diamond deposition. In the MWCVD setup this parameter is measured using a two-wavelength optical pyrometer (Raytek Thermalert SX) which is positioned above the reactor and focused onto the substrate and growing diamond film.

The emissivity coefficient of the surface being probed plays a large part in determining the value displayed by the pyrometer and must be set depending on the material being used. Emissivity, ε, is the relative ability of a surface to radiate energy compared to a blackbody ($\varepsilon = 1$) at the same temperature and, as such, the more reflective a material is the lower the emissivity. When calculating the substrate temperatures in the CVD reactor variations in the chosen value of emissivity between $\varepsilon = 0.1$-0.9 for a typical diamond on silicon film can cause a variation of ~500 K in the displayed T_{sub}, so ε must be set correctly. In addition, as the diamond film grows the emissivity of the surface will change slightly and the T_{sub} reading will become less accurate, often decreasing as a deposition run proceeds. For our work the emissivity was set to 0.6, which is the known emissivity of Si at 1000 K (Jain *et al.*, 1971), however, T_{sub} measurements should be interpreted with some degree of caution as variation in emissivity, position on sampled film and thermal adhesion with the Mo holder can result in deviations of ±50 K.

2.1.4 Substrate material

Substrates used in MWCVD were silicon (Si) or molybdenum (Mo) because the CVD process operates at high temperatures where many other materials have a propensity for deformation or for C atoms to dissolve into the substrate surface; the latter problem is particularly apparent in transition metals. Si also has a thermal linear expansion coefficient (4.68×10^{-6} K^{-1}) which is closer to that of diamond (1.18×10^{-6} K^{-1}) than most metals (typically $>1\times10^{-5}$ K^{-1}) which means that delamination of the deposited film as it cools is less of an issue than with metals such as Mo or Cu. Also in favour of Si is the formation of carbide interfacial layer which aids adhesion to the substrate. The influence of the substrate, and its pre-treatment, on the deposition of NCD films has been thoroughly investigated (Popov *et al.*, 2007). Research into lower T_{sub} diamond CVD is important for the expansion of the field into areas such as semiconductors and MEMS as it will allow a wider range of substrate materials to be used (Kohn *et al.*, 1999).

Polished silicon wafers (*p*-type, <100>, 0.3 mm thick) were diced into 1 cm squares (using a diamond wheel cutter, Department of Electrical & Electronic Engineering, University of Bristol) for the majority of this research.

2.2 Gas supply & flow control

2.2.1 Gas storage & delivery

Commonly used gases are stored in vented cabinets, with flammable ones (H_2 and CH_4) separate from oxidising or inert gases (O_2, Ar and N_2), and delivered to the various experiments throughout the laboratory with ¼”-inch Swagelok® pipework. Other gases which can be plumbed in for use on the system include He (also used for leak checking), Ne, Kr, C_2H_2, SF_6, NH_3 and dilutions of 10% N_2 in Ar, the latter two being in lecture-bottle size.

Gas	*Purity %*	*Supplier; Size*	*MFC manufacture; calibrated gas; size*	*Gas correction factor relative to N_2*
H_2	99.995	BOC; K (175 bar)	Tylan; H_2; 1000 sccm MKS; H_2; 50 sccm	1.01
Ar		BOC; W (230 bar)	Tylan; Ar; 2000 sccm MKS; N_2; 200 sccm	1.39
CH_4	‘100.00’	BOC (200 bar)	MKS; CH_4; 200 sccm	0.72
C_2H_2		BOC; M	MKS; CH_4; 200 sccm	0.72
N_2	O_2 free	BOC; W	Tylan; N_2, 10 sccm MKS; N_2; 200 sccm	1.00
N_2	10% in Ar	Argo	Tylan; N_2, 10 sccm	1.00
NH_3	99.98	Argo (8.2 bar/240 l)	Tylan; N_2, 10 sccm	0.73
He		BOC (100 bar)	Tylan; Ar; 2000 sccm	1.42
Ne	100.00	BOC; V (1000 l)	Tylan; Ar; 2000 sccm	1.46
Kr	100.00	BOC; V (250 l)	Tylan; Ar; 2000 sccm	1.54

Table 2: Gases used on the MW-CVD experiment together with details on their sources and flow rate control.

2.2.2 Controlling gas flow

The flow and mixing ratios of each gas are controlled using an electronic control box (MKS247C) which operates a gas manifold consisting of an array of six mass flow controllers (MFC) each with its own filter and bypass valves. The sizes of the various MFCs are indicated in the table above together with the relevant gas correction factor for using an MFC to control a gas other than the one for which it had been calibrated. After the MFC assembly all the gases are mixed into the same ¼" pipe before dividing into two and entering the reactor just below the quartz window.

Near the beginning of the experimentation and before starting the calibration experiments the MFC flow rates for their respective gases were compared with a newly calibrated controller, 2000 sccm H_2 in the first case and 200 sccm CH_4 in the latter. The calibration process consisted of measuring the pressure rise in the reaction vessel for a set flow rate, F_x, after the exhaust pumping had been closed off. This allowed any offset or non-linear behaviour to be identified and corrected.

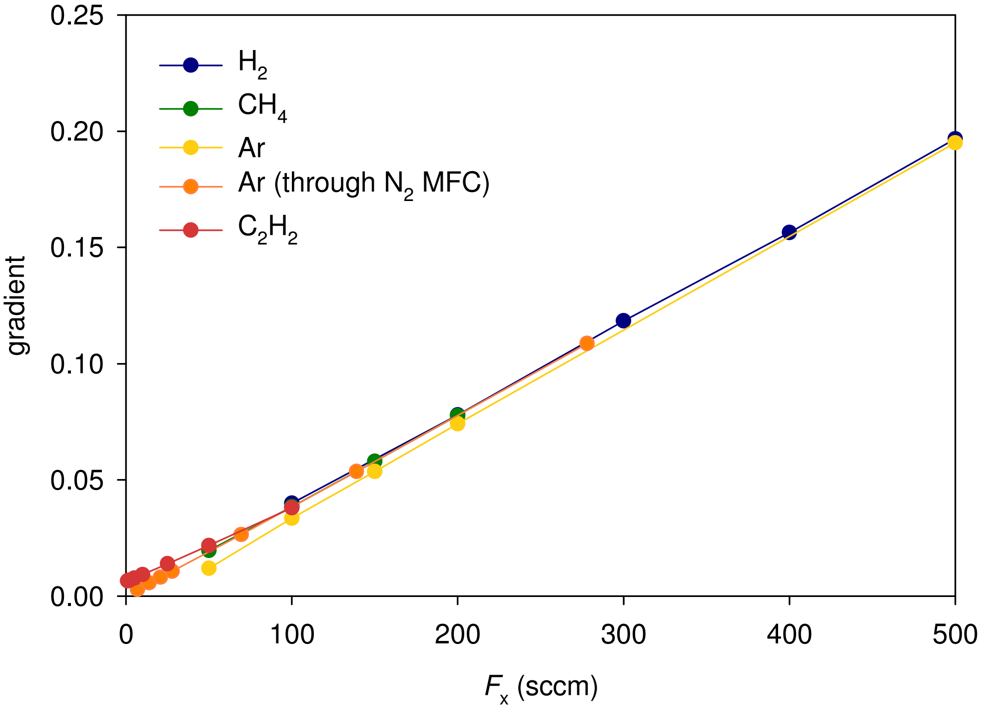

Figure 2.2: Calibration of MFCs against new H_2 flow regulator by measuring the pressure rise in a certain amount of time (gradient) against flow rate for each gas (F_x).

2.2.3 Standard gas mixtures

For our MWCVD system it is useful to define four standardized gas mixtures which result in different diamond film morphologies.

morphology	χ_0(X)			
	H_2	CH_4	Ar	N_2
MCD	0.885	0.044	0.071	0.0
NCD I	0.855	0.077	0.068	0.0
NCD II	0.951	0.047	0.0	0.002
'UNCD'	0.030	0.005	0.965	0.0

Table 3: Examples of standardized gas chemistry used to deposit various different diamond morphologies by MWCVD defined by the mole fractions of the constituent gases, X.

A standard operating procedure for running the reactor for diamond deposition is given in section 9.1.1.

2.3 Safety and Interlocking

Interlocking and monitoring of the system is important as any leak of air into the system or instability in the mainly-H_2 plasma could lead to a catastrophic explosion. The chamber pressure, the water-cooling flow rate and the power reflected back from the reactor are monitored by an interlock system (Rosemount Series 4001) which shuts down both the input power and the gas flow into the chamber if these parameters rise above a certain set point. The gas flow can be shut off quickly just by the inlet manifold with a solenoid valve. Pressure monitors in the mass spectrometer pressure stage also shut down the ion-source filaments should the pressure rise above 8×10^{-7} Torr (see section 4.1.3.1).

2.4 Pre-treatment of substrate

Section 1.6 described a range of techniques which can be used before the CVD process to nucleate heterogeneous substrates and significantly improve the rate and quality of the growing diamond films. This subject is extended in subsequent sections to describe specific experimental processes employed in the Bristol Diamond Group for treating substrates prior to growth in either

HF- or MWCVD reactors. The procedures were generally carried out on polished Si <100> substrates unless explicitly stated otherwise.

2.4.1 Substrate cleaning

Silicon substrates were cleaned before applying nucleation layers with the number of washes dependent on the quality of film required. Generally, the diced Si wafers were washed in dilute nitric acid and then any grease removed by rinsing in methanol before nucleation. After manual or ultrasonic abrasion the seeded substrates were washed in de-ionized water and dried with a N_2 flow. Larger, 2" diameter Si wafers (see section 2.5.5.4) were treated with dilute sulphuric acid, acetone and then methanol before seeding in the electrospray apparatus. Diamond substrates were treated with a nitric acid wash before hydrogenation to remove any metallic contamination (see section 7.1).

2.4.2 Manual abrasion

While not ideal for NCD deposition, the manual abrasion method offers a quick and reliable way of nucleating Si substrates. For this simple technique, the two polished surfaces of Si substrates are rubbed together with a small amount of 1-3 μm diamond powder between them. This roughens the surface and embeds some diamond sufficiently to nucleate continuous films in the CVD reactors. Excess diamond powder was removed from the surface by rinsing in methanol. If carried out evenly across the substrate a homogeneous seed layer can be obtained although this may only become apparent after the film has been grown.

2.4.3 Diamond suspensions & light scattering

Nanodiamond (ND) suspensions are often dispersed in water as the slight charging of the particles suits the polar solvent well, forming a homogenous colloid. For electrospray seeding it was necessary to disperse the ND in methanol and this meant either a solvent exchange or dispersion of solid particulate was required (see section 2.4.5.3). To determine the size distribution of particles in the colloid we used a dynamic light scattering apparatus (Malvern Zetasizer Nano) and showed that some aggregation was occurring on dispersal of the ND in methanol. Typically, particles formed aggregates around ~20-60 nm in size although this was dependent on concentration, source of the raw material and the amount of ultrasonic agitation the sample had received.

2.4.4 Ultrasonic abrasion & Spin-coating

Two methods were also used to seed samples although the success of the electrospray method meant they became redundant later in the project and so are only briefly described here.

Submersion of substrates in diamond colloidal suspensions and agitation using a high power ultrasonic probe (Bandelin Sonopuls HD2070, 3 mm microtip) should allow homogenous nucleation layers to be formed although this could not be achieved with our apparatus. Instead, the substrate was severely weakened and became brittle if too high a power was used, whereas no seeding was observed for low-power ultrasonic treatment. In addition, removing the film from the suspension resulted in poor uniformity which was still present after rinsing and drying.

In an attempt to achieve a dense nucleation layer a diamond colloidal suspension was spin-coated onto the surface using a spin coater (Laurell Technologies WS-650S-NPP-Lite) designed for coating wafers up to 6” diameter. Excellent uniformity was observed on substrates seeded in this way but they were much less densely coated than with the electrospray method and, therefore, required longer depositions to achieve continuous diamond films.

2.4.5 Electrospray method

2.4.5.1 Introduction

The development of the electrostatic spray deposition – ‘electrospray’ – apparatus for seeding substrates prior to diamond deposition included a number of trials and technical advances. These are described here as the topic does not easily fall neatly into any other section. While, strictly, this could be described as experimental testing and results, the main objective is to produce a repeatable and reliable *method* for pre-treating substrates which then underpins the majority of the growth studies covered in the rest of this work. We describe the optimization of some key factors, including the experimental spatial arrangement and colloidal properties, analyzing the seed layers by optical and electron microscopy, both before and after NCD deposition. The advantages and drawbacks of the electrospray method can then be determined in relation to other commonly used nucleation techniques.

To briefly recap, highly charged droplets of a colloidal suspension of diamond particles disperse from a nozzle, repel each other and are applied, evenly, to a substrate, thereby forming a nucleation layer. Deposition of NCD or MCD films after application of the seed layer by HF- or MWCVD offered the simplest test of success and allowed the method to be optimized.

2.4.5.2 Apparatus & Theory

In our method, 5 nm detonation nanodiamond is dispersed in a suitable medium and formed into an aerosol by application of a high potential (~35 kV) to a metallic capillary nozzle through which the colloid is pulled. This process forms particles of uniform size which repel each other as they radiate out preventing coalescence. Optimization of the technique allows application of a uniform coating of diamond colloidal particles onto an electrically grounded substrate located some distance away.

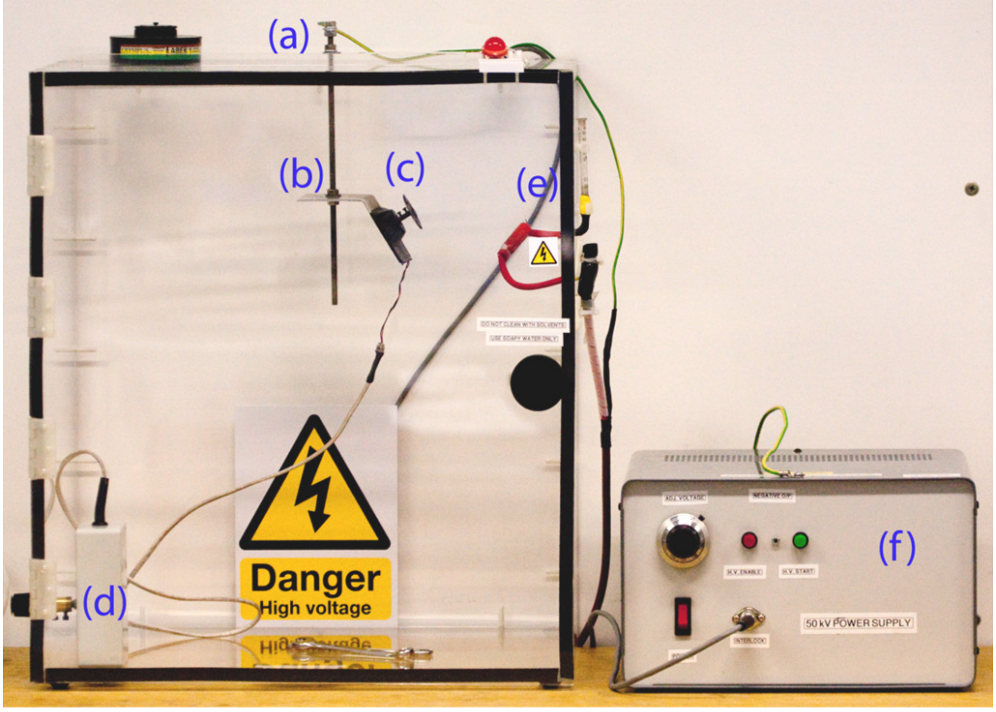

Figure 2.3: Photograph of the electrospray apparatus: (a) ground connection, (b) adjustable substrate mount, (c) substrate mounted on motorized wheel, (d) motor control, (e) capillary nozzle and (f) high voltage power supply.

The evaporation of the liquid from the aerosol droplet over the distance between the nozzle tip and the substrate determines the relative success of the technique, with the most uniform nucleation layers being produced when all, or a significant proportion, of the liquid evaporates from the aerosol in flight and results in application of only diamond seed particles to the substrate surface. If too much liquid remains in the droplet when it strikes the substrate splashing may occur which leaves marks on the surface and reduces the uniformity of the coverage.

Application of a strong electric field to droplets leaving the capillary causes further disintegration of the aerosol particles into a finely and uniformly dispersed colloid (Vonnegut & Neubauer, 1952). This was explained theoretically by the formation of a cone of liquid at the exit of the nozzle as a result of the hydrostatic balance between outward electrostatic pressure and inward pressure due to surface tension (Taylor, 1964). The electric field at the tip of this cone becomes highly concentrated, analogous to a corona discharge, and ionizes the gas around it forming charged droplets which repel each other (Meesters *et al.*, 1992). The formation of sub-micron aerosols from the tip of the cone has received continued attention, due to the wide range of possible applications, with new experimentation showing that the liquid must continually be supplied to the nozzle, thereby making the surface of variable pressure (Meesters *et al.*, 1990). The variation in the applied electric field and in the viscosity and conductivity of the colloidal liquid were found to be key parameters in determining the properties of the droplets dispersing from the nozzle (Smith, 1986).

A variation on the electrospray technique has already been employed successfully to seed silicon substrates prior to diamond CVD using diamond powders suspended in water (Malshe *et al.*, 1997, Malshe *et al.*, 1998). In this case, the particles were forced through drying media (removing the majority of the liquid) by application of 30 p.s.i. pressure into an electrostatic spray gun (with an ionizing electrode at 80 kV) where they became charged and were then applied to the substrate. Our setup differs in having *both* the dispersion medium and the diamond particles exit through the electrode nozzle and the volatile liquid surrounding the diamond particles then evaporating before reaching the substrate, resulting in a uniform but dense coating of diamond particles. The applied potential pulls the suspension through the capillary, removing the need to apply a pressure difference, while charging prevents the droplets coalescing. Testing the setup on 2 and 6 inch wafers, as well as complex three-dimensional substrates, has provided a novel means of seeding different surfaces prior to diamond deposition.

A schematic of the Bristol electrospray apparatus used for seeding substrates is shown in Figure 2.4.

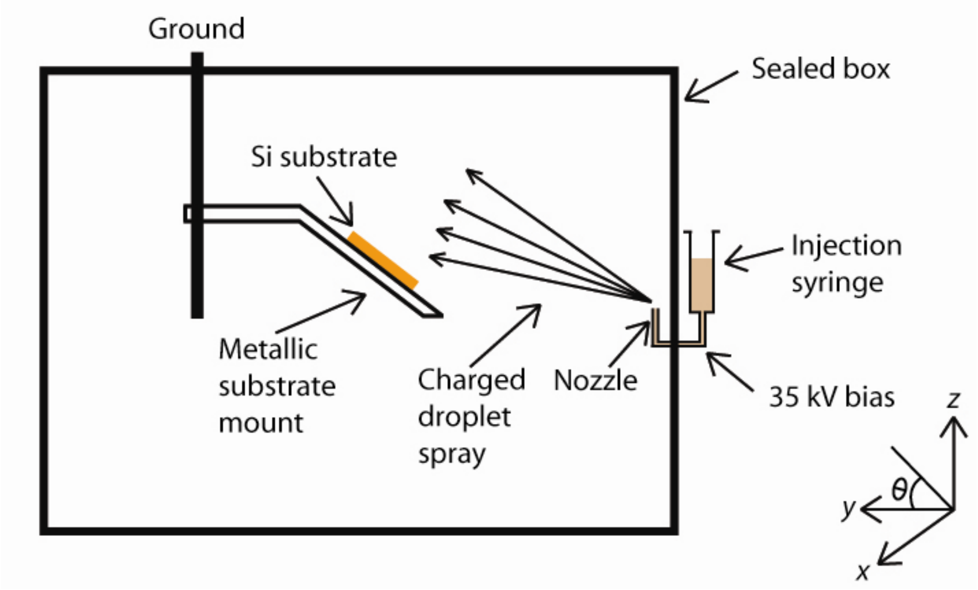

Figure 2.4: Schematic diagram detailing the electrostatic spray deposition apparatus. Coordinates are used to define the angle of the nozzle relative to the substrate.

In our method ~1 ml of a colloidal suspension of ND in the chosen dispersion medium was placed in a plastic syringe located on the outside of an insulating box (see Figure 2.4). A 21G syringe needle (outside diameter = 0.81 mm) passes through the wall of the box by turning through 90° and then bends upwards an angle of θ. The angle θ was optimized to achieve the best substrate coverage. Formation of a Taylor cone is guaranteed by choosing a small enough capillary tip to limit the size of the droplets and, therefore, the time-of-flight required for complete evaporation of the liquid medium.

A 35 kV bias applied to the metal syringe needle was sufficient to ionize the droplets without becoming unstable and arcing. The substrate (Si, unless otherwise stated) was positioned ~50 mm away from the nozzle tip on a moveable, conducting mount which could be adjusted through three axes of freedom. The mount was well grounded, ensuring that ionized aerosols emanating from the nozzle would be attracted along electric field lines towards the substrate.

For substrates with diameter >10 mm, further improvement in the seeding uniformity could be achieved by spinning them at up to 1500 r.p.m. using a small motor located on the angled mount. This has allowed successful seeding of circular Si substrates up to 6 inches in diameter. Application of the seed layer took just 3 minutes to complete and could be repeated to achieve thicker nucleation film, although this risked clustering seed particles on top of each other and depositing a less homogenous film.

2.4.5.3 Discussion & optimization of key parameters

On setting up the electrospray apparatus, it became apparent that two factors would exert most influence on the relative success of the process: the spatial alignment of the nozzle and substrate and the fluid properties of the diamond suspension. Optimization of these parameters is discussed below with assessment of the seed layer before and diamond film after deposition by optical and electron microscopy. Thorough characterization of the nucleation layer using atomic force microscopy has been carried out but falls outside the realms of this thesis (Vaz, 2011).

In the initial setup, two configurations for mounting substrates were employed depending on their size and shape. Substrates <10 mm in diameter could be mounted on the underside of a plate positioned in the *xy* plane (as defined in Figure 2.4) but ~20 mm higher along the *z*-axis than the nozzle tip. Larger substrates were found to benefit from simultaneous spin coating and were situated on a larger, angled mount as shown in Figure 2.4 with the surface to be coated at θ = 50°. For later work, all seeding was performed using the rotating mount as this facilitated coating of a small number (~4) of substrates in each batch, all with identical seeding density.

The orientation of the nozzle in relation to the substrate and mount was also a key factor in guaranteeing an even coating of ND particulate. Trial and error showed the optimal angle to be θ = 90°, *i.e.* the nozzle pointing along the *z* axis and, therefore, at 40° to the substrate surface. For angles θ <90°, residual 'splash marks' resulting from incomplete evaporation of the liquid (similar to those shown in Figure 2.5). At θ >90° insufficient ND was transported to the substrate to provide an acceptable nucleation layer.

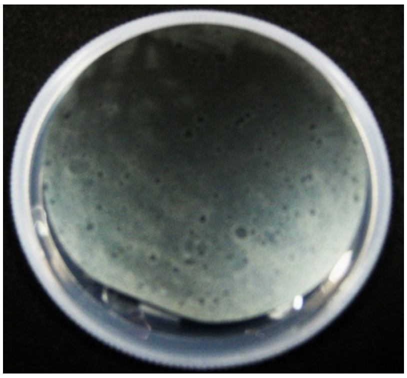

Figure 2.5: Example of 2" Si wafer (shown after deposition of a thin UNCD layer by HFCVD (courtesy of ADT, Inc.)) with poor seeding and 'splash marks' from incomplete evaporation of the liquid from the droplet.

Another variable, the nozzle-to-substrate distance, was similarly adjusted to be sufficiently large that all the liquid surrounding the ND particles evaporated from the droplets before reaching the substrates but still maintain the electrostatic attraction between droplets produced at the nozzle and the earthed mounting plate. When a new substrate size or shape was proposed for seeding and diamond deposition, fine tuning of these parameters was often necessary to achieve a suitably uniform nucleation layer.

Likewise, the physical properties, such as viscosity, dielectric constant and surface tension of the colloidal diamond suspension also have a large bearing on the homogeneity of the seed layer deposited. Studies with similar nozzles have shown that the primary droplets emanating from the tip are generally monodisperse with sizes in the order of 1 µm although this is strongly dependent on the flow rate through the nozzle. Increasing the concentration of the suspension had the effect of reducing the droplet size while also inducing agglomeration of particles. The presence of such agglomerates on the substrate increased the surface roughness of the subsequent film, especially those grown by HFCVD.

It is obvious that the suspension of diamond nanoparticles must have a narrow size distribution to ensure a homogenous coating of the substrates is obtained. This was made possible through treatment of both the raw detonation nanodiamond and the colloidal suspension before use in the electrospray apparatus. The nanodiamond used in this study was formed by detonation synthesis in an oxygen-deficient atmosphere and had the smallest sizes (4 to 5 nm) of all synthetic particulate diamond (Donnet *et al.*, 1997, Shenderova *et al.*, 2002). Due to the processes in which they form these nanodiamonds are often clustered into tightly bound agglomerates which increase the average particle size and must be broken down before dispersion into the ND colloid for electrospraying. The outer layers of the particles invariably consist of sp^2 carbon which must also be removed. This is often done by hydrogenation treatment and will be discussed in section 7.1 as it has a greater influence on other uses of ND particles such as bio-functionalisation or electrochemistry. For seeding of diamond films in a MWCVD reactor the presence of sp^2 layers is less problematic as they will most likely to be etched away in the early stages of diamond deposition.

Just considering the de-agglomeration of the secondary particles there have been a number of recent advances which have enabled the production of monodisperse nanodiamond colloids. Treatment of the ND samples used in the electrospray testing was carried out using a combination of stirred-media-milling with zirconia beads and high-power ultrasonication in a method termed bead-assisted sonic disintegration (BASD) at the Otto Diels Institut für Organische Chemie, Christian-Albrechts-Universität in Kiel, Germany (Ozawa *et al.*, 2007). The BASD technique is much quicker than previous milling processes, taking ~30 minutes to produce the required 5 nm particulate size.

The most important parameter in the electrospray technique is the nature of the liquid used to disperse the nanodiamond. The viscosity and boiling point of the liquid are crucial in determining how quickly it evaporates when travelling between the nozzle tip and the substrate. Low boiling point/low viscosity solvents, such as methanol, are therefore favoured, ensuring only the ND seeds are deposited onto the substrate. More viscous liquids, such as water and cyclohexane, tend to be partially transferred onto the substrate as well as the diamond leaving drying marks on the surface. We found that low-mass alcohols, such as methanol and ethanol, provide the most suitable dispersion media for the deagglomerated nanodiamond particles. The polarity of the OH bond allows formation of hydrogen bonds to the charged diamond particles thereby decreasing the propensity for spontaneous flocculation into large clusters, which was observed when using less polar liquids such as cyclohexane. Examples of the behaviour of similar densities of ND dispersed in different media is shown in Figure 2.6 where equal amounts of solid aggregated ND have been added to solvents and sonicated for ~10 min and allowed to rest before imaging. The flocculation in the non-polar cyclohexane (c) is immediately apparent when compared with the clear, non-aggregated water sample (a). Methanol (b) provides a fairly good colloid but takes more agitation to disperse the aggregates – as some material remains non-dispersed at the bottom of the vial.

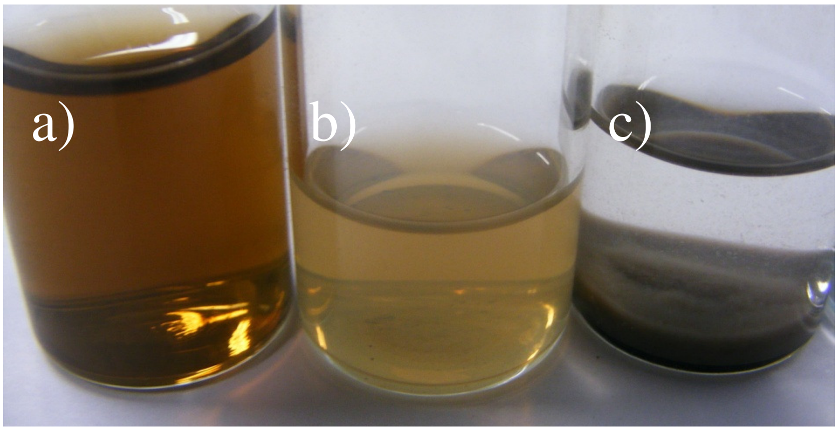

Figure 2.6: Nanodiamond colloids formed from dispersing small quantities of solid detonation diamond in three different liquids: a) water, b) methanol and c) cyclohexane showing the vast variation in behaviour from near-perfect dispersion in water to flocculation and precipitation from the cyclohexane.

As the de-agglomerated nanodiamond is supplied in a concentrated form dispersed in water, 0.5 ml was diluted in 20 ml of methanol for our application. Unfortunately this process causes a small degree of flocculation observed in dynamic light scattering experiments. To overcome the aggregation and stabilize the colloid in liquids less polar than water the 5 nm primary particles were coated with a polymer layer preventing their aggregation. Polyvinylpyrrolidone (PVP) is a polar surfactant which is sufficiently polar, due to the CO group on the pyrrole ring, to adsorb onto the charged ND surface. A steric layer is formed preventing neighbouring particles aggregating *via* van der Waals forces. This proved successful in dispersing the colloid in the majority of the liquids trialled with the exception of non-polar cyclohexane where significant flocculation was still observed. However, the use of PVP was abandoned following analysis of the seed layers by optical microscopy and the grown diamond films by electron microscopy. It was hoped that any polymer transferred to the substrate would be burnt away in the CVD plasma but it became apparent that the increased viscosity of the colloid meant that the methanol failed to evaporate before reaching the substrate. Subsequent drying of the polymer, liquid and ND phase on the substrate surface formed an undesirable cracked pattern in the nucleation layer and was still visible in the diamond film post-growth. This proved more problematic in the HFCVD grown films than those from the MW system but still were no longer as uniform as the films deposited without the polymer. Generally, the 1 ml aliquots of ND suspension were derived from a stock solution consisting of a 1:10 dilution of the BASD ND/H_2O in MeOH.

2.4.5.4 Diamond deposition at Bristol & ADT

To supplement the analysis of the electrospray seeding method carried out in our HF- and MW-CVD systems, UNCD deposition on larger substrates was carried out and compared with the Aqua 25 (1 µm) ultrasonic nucleation method by Dr. Nicolaie Moldovan, at Advanced Diamond Technologies, Inc. (ADT, www.thindiamond.com).

The problems caused when using the PVP surfactant became increasingly apparent as the crystal size decreased for the deposited film. When depositing MCD or NCD films by MWCVD any imperfections in the seed layer were not transferred to the film whereas UNCD films grown by HFCVD at ADT exhibited significant non-uniformity deriving from drying of the polymer and solvent mixture. This patterning can be observed in Figure 2.7 showing transfer of the drying pattern through to the UNCD film.

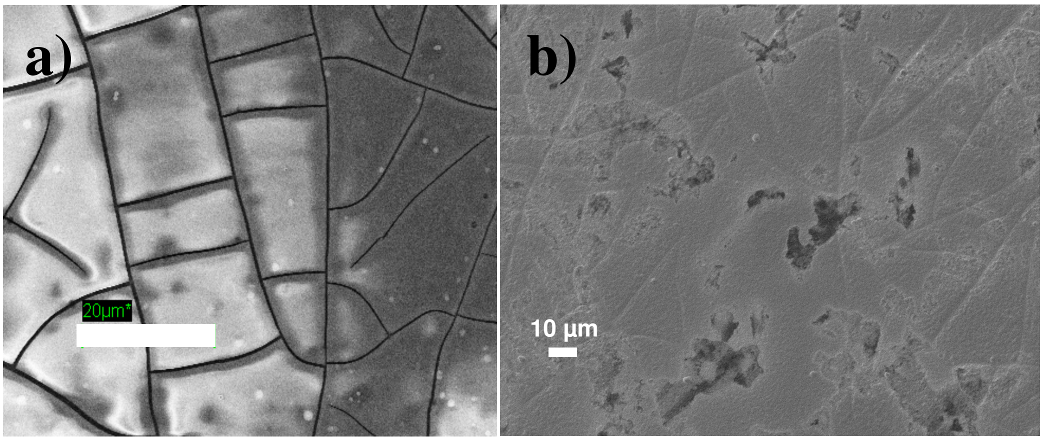

Figure 2.7: Patterning of substrates due to the PVP polymer drying and cracking, observed a) prior to and b) following HFCVD of a UNCD layer by electron microscopy (used with permission from ADT, Inc.).

There is also likely to be some disparity in the Bristol NCD films and the ADT UNCD films due, firstly, to the film thickness – the NCD films are ~5 μm thick and the UNCD are thinner being 1.15-1.25 μm. Inhomogeneities in the seed layer are therefore more likely to be observed in the UNCD film. Secondly, the higher growth rates, substrate temperatures and atomic hydrogen density in the MW system will reduce the influence of non-uniform areas of the seed layer and remove any remaining polymer. Analysis of the surface roughness of HFCVD-grown UNCD films using a stylus profilometer (2 μm tip over a 2 mm scan) shows higher roughness values for the electrospray seeded films (>100 nm) compared to the ADT seeding method (<10 nm) as expected from the poor uniformity observed in the nucleation layer. Raman analysis (not shown) confirms that the quality of the diamond (the ratio of sp^3-to-sp^2 carbon content) is not influenced by the nucleation method chosen, having similar spectra for both electrospray and ADT-seeded films.

The substrate patterning precludes the use of any stabilizing polymer, such as PVP, in the suspension and limits the types of liquids which can be used in our electrospray apparatus. The problem was eventually overcome by conducting the BASD process in methanol rather than water thereby removing the need to perform any solvent exchange which may induce particulate aggregation. We also note that the electrospray method, at present, cannot compete with ultrasonic nucleation of substrates prior to UNCD deposition by HFCVD. For deposition of MCD or NCD films in our MWCVD reactor – forming the bulk of the rest of this thesis – the electrospray method works very well.

After this trial-and-error development of the electrospray method we turned attention to coating larger substrate areas which are less successfully seeded by ultrasonic treatments. Working with

2-inch diameter circular Si substrates supplied by ADT we were able to optimize the nucleation process for large areas. An indication of the nucleation density and uniformity was obtained by growth of a thin UNCD layer on the film by HFCVD at ADT. With only slight adjustment of the position of the substrate mounting plate, moving it further back away from the nozzle, 2-inch substrates were successfully seeded in the electrospray apparatus.

Later testing also showed that electrospray apparatus was adept at coating 3D substrates as the entire structure is grounded and, hence, is attractive to the charged seed particles. This clearly offers advantages over nucleation by manual abrasion or spin coating which are limited to planar substrates. From initial testing with small silicon substrates we have shown successful nucleation on large wafers (up to 6” in diameter), 10×10×10 mm tungsten cubes and more complex structures such as those introduced in section 6.0.

An SOP for the electrospray seeding technique is given in section 9.1.2.

2.5 Spectroscopic analysis of the plasmas

2.5.1 Optical emission studies

Optical emission spectroscopy (OES) measures the intensity of radiation emanating from excited atoms and molecules as they relax to a lower energy configuration. In many diverse applications it forms a simple technique for obtaining information on relative and, sometimes, absolute densities of probed species as well as details of collisional and charge-transfer reactions and energy distributions within the sampled medium. Our understanding of the physics of low pressure plasmas has been greatly enhanced through information provided by emission spectroscopy experiments leading to breakthroughs in both fundamental science and the mainstream materials industry. Special care must be taken when analysing emission spectra to fully understand the physical processes occurring at the source, because measured intensities do not necessarily yield absolute species concentrations. It is also important to remember that it is only excited species which are being probed leaving many non-emitting or ground-state species undetected. Emission spectroscopy has proven very useful in furthering our understanding of diamond-depositing environments (Gicquel *et al.*, 1998, Ma *et al.*, 2009b). It has often been used in conjunction with other analytical methods, such as absorption spectroscopy or mass spectrometry.

In the Bristol Diamond Group OES spectra are collected through an optic fibre directed at the plasma centre through a quartz viewport in the chamber wall, and analysed using an Oriel Instaspec IV spectrometer consisting of a 25 cm monochromator and cooled (10 °C) charge-coupled device (CCD) detector. Some degree of spatial profiling is also possible by vertically translating an iris at the end of the optic fibre along the window at the side of the reactor. The light enters the monochromator and is dispersed by a grating onto the CCD, where it is digitised and displayed on a computer screen. After identifying the different transitions in the spectra, some of which will overlap with each other, their intensities were extracted by taking the background count rate away from the peak signal. As the background changes with wavelength the value of the background was interpolated for each peak separately. Typically exposures of ~20 ms were used and data averaged over ~1000 accumulations. The wavelength scale is calibrated using a mercury lamp for which the characteristic lines in the spectrum are well known.

Another correction is also applied to all the OES spectra in this thesis, due to the frequency dependent sensitivity of the detector and the response function of the diffraction grating. This was empirically determined and fitted with a power series function of the wavelength, λ.

2.5.2 Absorption spectroscopy

Important advances in the study of diamond-depositing systems have come about *via* the implementation of quantitative spectroscopic techniques for detecting selected gas-phase species in the activated gas mixture. One of the most sensitive techniques for probing plasma chemistry is cavity ring-down spectroscopy (CRDS) which can provide the line-integrated absorbance of a laser beam which is reflected through the cavity a large number of times using partially reflective mirrors (Ma *et al.*, 2008, Richley *et al.*, 2011, Wheeler *et al.*, 1998). As the absorbance is determined by the concentration of the absorbing species, according to the Beer-Lambert law, the density of this species in the column through which the beam passes can be calculated. This is possible if the probed transition and the temperature gradient in the column are well characterized and required spectroscopic constants known. A detailed methodology for calculating the column densities from the ring down coefficient and other parameters has been given elsewhere (Ma, 2008, Rabeau *et al.*, 2004). In the area of diamond CVD, CRDS has been used to quantify CH_3 (Wahl *et al.*, 1996), CH (Lommatzsch *et al.*, 2000) radicals in the gas phase of HF reactors as well as measuring concentrations of radicals such as CH, C_2 and atomic H in DC arc-jet (Rennick *et al.*, 2004, Wills *et al.*, 2002) and MW systems (John *et al.*, 2002, Ma *et al.*, 2008).

The apparatus for these CRDS measurements consists of two tubular arms which are attached either side of the second MWCVD reactor using flexible bellows assemblies. High-reflectivity

CRDS mirrors are mounted at the ends of these tubes forming a cavity through which the laser beam passes. The mirrors and mounts can be translated vertically relative to the MW chamber to allow spatial profiling of the plasma. A Nd:YAG-pumped dye laser (Continuum Surelite III with Spectra-Physics PDL-3) produces the beam at ~515 nm (C_2(a) radical), ~431 nm (CH(X) radical) and ~656 nm (H atom) dependent on the dye employed. Radiation exiting the cavity is measured with a photomultiplier tube and monitored using a custom-written LabView program and digital Oscilloscope (LeCroy Waverunner 64Xi, 600 MHz).

2.6 Characterization of deposited diamond films

2.6.1 Optical microscopy

The first analysis of a newly deposited diamond film is carried out using an optical microscope (Zeiss Axiolab) using magnification up to ×100 to determine the surface coverage, the uniformity across the film and the overall success of the deposition. This is particularly useful for making sure the nucleation layers are dense and homogenous enough to allow a thin film to grow. Ultimately, however, imaging the film with greater resolution is needed to ascertain the diamond morphology and this is provided by electron microscopy.

2.6.2 Scanning electron microscopy (SEM)

Throughout this study of diamond CVD the use of electron microscopy has frequently provided valuable analysis of the deposited films showing not only the surface morphology at high magnification, in terms of the average crystal size and preferred orientation, but also the film thickness, providing an accurate measure of the growth rate.

The majority of electron microscope images shown here are taken using either a JEOL JSM 5600LV or a JEOL JSM 6330F instrument, the latter employing a field-emission gun and operating at ultra-high vacuum to provide excellent resolution. Both microscopes operate using an electron beam, produced by thermionic emission in the JSM 5600LV and field emission in the JSM 6330F apparatus, which is focussed down to about 10 nm and accelerated to between 0.5-30 kV using electromagnetic fields. Magnetic fields are also used to raster the beam across the surface of the sample and produce an image by detecting the secondary electrons emitted from the surface. Imaging diamond can be difficult due to its high resistivity causing charge to build up on the sampled surfaces and producing intensely bright regions observed in some results. The standard method to reduce such charging is to coat the samples with a thin layer of evaporated metal (*e.g.* gold), but, in general, this was not done here since the diamond samples needed to be free of such coatings for subsequent analysis or applications.

Deposition growth rates were obtained by measuring the cross-sectional thickness of the films. The substrates were prepared by cleaving them (approximately a third of the way across the surface, but ensuring the most uniform part of the film was sampled) and mounting them on end to be viewed in cross-section in the SEM. For a particular sample, ~3 points were chosen along the exposed length of the film where the lower boundary, between the film and the Si substrate, could be easily seen and no damage/inhomogeneity was evident. The SEM images allowed an average film thickness to be obtained and combined with knowledge of the deposition time then yielded growth rates.

2.6.3 Atomic force microscopy (AFM)

Atomic force microscopy scans the sample using a sharp tip on the end of a cantilever which is deflected slightly according to Hooke's Law when in close proximity to the surface. The magnitude of this deflection is determined by the topography of the surface and the extent of the attractive force between the sample and the probe. A Bruker Multimode AFM instrument with Nanoscope V controller was used to analyse samples deposited by CVD using both contact and tapping modes. Atomic-scale resolution of micro- and nano-crystalline diamond films is not easy to achieve due to the rough topography and inherent hardness of the samples. However, a number of attempts were made taking care to prevent degradation of the sampling cantilever tip (Fox *et al.*, 2009). In other studies the use of tapping mode AFM has been favoured because the cantilever wear is not such a problem (Achatz *et al.*, 2007). A fuller investigation of the NCD films was also undertaken with these instruments, and others designed to make force measurements, and this is discussed in section 7.2.1.

2.6.4 Raman spectroscopy

Frequently, fast diagnostics of a recently deposited diamond sample can be obtained by using the analytical technique of solid-state Raman spectroscopy, whereby a characteristic spectrum can be produced arising from a particular solid-state composition. The relative signal from diamond and non-diamond deposits can quickly determine if the growth experiment has succeeded and provide instant comparison with previously deposited films.

Raman spectroscopy is based around analysis of the low-energy vibrational phonon modes of solid-state systems as they are excited to virtual energy states through interaction of the electron cloud and photons from a monochromatic laser source. On relaxation, these states can decay back to either the same vibration energy level they came from (elastic scattering) or, much less often, to different vibrational energy levels (inelastic scattering) when some, small amount of, energy is lost in nuclear displacement. Elastic or Rayleigh scattering emits a photon of the same energy as that absorbed and so does not contribute to the Raman spectrum. However, if the state relaxes to a vibrational energy level higher than the initial configuration then the emitted photon will be of lower than the excitation energy and is this is termed *Stokes scattering*. On the other hand, if the structure decays to a lower energy state than before the emitted photon will be higher in energy giving *anti-Stokes scattering*. Measurement of this inelastic scattering against the excitation energy provides detailed information on the phonon structure of the solid and, therefore, can be used to indentify different solid states within a sample. For solid-state samples at room temperature which are predominantly in the ground state, Stokes scattering dominates, and this is recorded as the Raman spectrum.

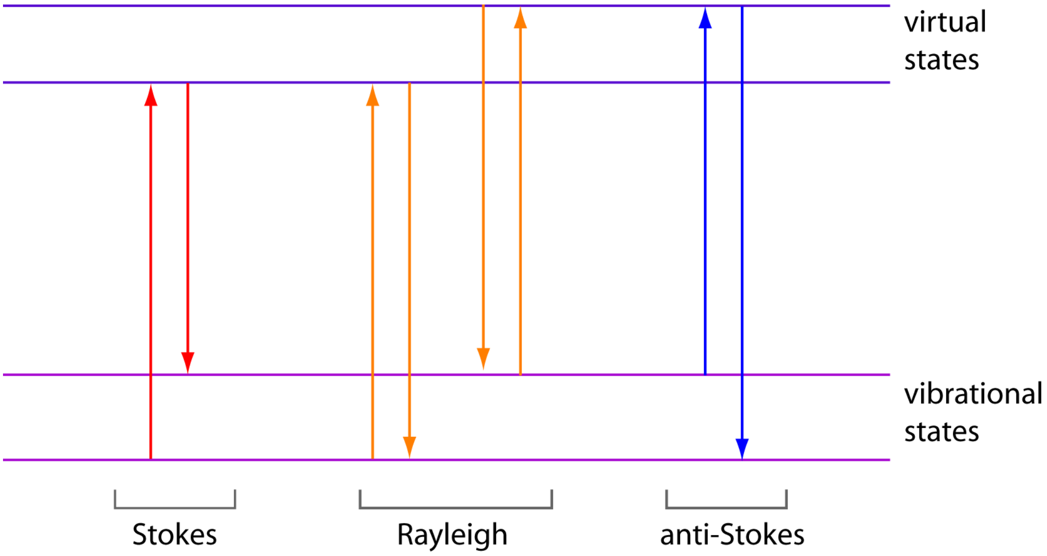

Figure 2.8: Categorization of elastic (Rayleigh) and inelastic (Stoke and anti-Stokes) scattering on relaxation of excited states to lower vibrational energy levels during Raman spectroscopy.

Of particular interest to us is the fact that Raman resonant bands are often strong for crystalline carbonaceous solids with distinct features corresponding to both sp^3 and sp^2 bonded structures. Pure diamond is easily identified by the peak at 1332 cm^{-1} indicative of the triply-degenerate (T_{2g}) first-order phonon of the sp^3 bonded lattice and its *Fd3m* space group (Knight & White, 1989, Prawer & Nemanich, 2004, Solin & Ramdas, 1970). Synthetic diamonds which are not formed from single crystals will also contain carbon in the form of graphitic sp^2 material and more amorphous structures (a-C). As we have seen before, the proportion of this non-diamond material within the MCD or NCD structure increases as the grain sizes get smaller. Graphitic carbon present in this material also contributes to the Raman spectrum due to two different stretching modes of the hexagonal sp^2 array. The Raman spectrum of single-crystal graphite, with the *P63/mmc* space group, consists of a single band at 1575 cm^{-1} (Tuinstra & Koenig, 1970) whereas in most sp^2-carbon-containing materials, including our polycrystalline diamond films, a second peak is also present at ~1360 cm^{-1} due a breakdown of the Raman, $k = 0$, selection rule in materials which are not perfectly crystalline. The two bands represent vibrational phonons which are either doubly degenerate (E_{2g}) stretching modes of the hexagonal lattice for the 1575 cm^{-1} band or singly degenerate (A_{1g}) breathing modes for the 1360 cm^{-1} band. The former transition is referred to as the G band (for crystalline **g**raphite) and the latter is termed the D band (after **d**isordered graphite). A small peak at ~1170 cm^{-1} is likely to be from long-chain hydrocarbons containing sp^2-carbon atom chains, polyacetylenes, which can occur at the grain boundaries of NCD films. It is sometimes referred to as the *UNCD* peak although its true identity has yet to be fully explained (Ferrari & Robertson, 2001). The exact position, intensity and line width of these four bands (1170, 1332, 1360 and 1575 cm^{-1}) in a Raman spectrum of MCD or NCD can tell us crucial information about the structure of the material, such as the build up of stress, disorder or influence of dopant atoms (Lespade *et al.*, 1984). The nomenclature for the intensities of these bands (I(G), and so on) used in the following discussion follows earlier, in-depth Raman studies of carbon materials (Ferrari & Robertson, 2004). In our analysis the positions of the D and G bands fall around 1380 and 1570 cm^{-1}, respectively.

In the Bristol Diamond Group, Raman spectroscopy is performed at room temperature using a Renishaw 2000 instrument and CCD detector. For maximum information on different samples, they can be illuminated by three different laser excitation wavelengths ranging from 325 nm (UV, He:Cd), 514 nm (green, Ar^+) and 785 nm (red, diode laser). Typical sampled areas are ~100 µm in diameter based on the focal spot size, and a penetration depth of around 100 nm (at $\lambda = 325$ nm) depending on the opacity of the deposited film.

Typical processing of spectra, using the Wire 2.0 programme (www.renishaw.com/en/wire-3-9450), involves removal of any background due to interference or photoluminescence and deconvolution of the various spectral peaks by fitting them with Gaussian functions. This allows the relative contributions from each sp^2 or sp^3 peak to be assessed independently as they often overlap in the spectrum. The relative intensities of the diamond and non-diamond bands allow us to infer the grain size in the sampled film (Klauser *et al.*, 2010). For an excitation wavelength of 325 nm, ratios between the intensity of the diamond peak and the G band ($I(sp^3)/I(\mathrm{G})$) greater than 5 tend to indicate large crystals are present and a MCD morphology while values <2 indicate much smaller diamond grain sizes and a NCD sample.

Additional information from the Raman system can be obtained from photoluminescence (PL) spectra which, in particular, can give information on the concentrations of different impurities within the diamond sample. As an example, the detection of nitrogen present in diamond films as a Nitrogen-Vacancy (NV) defect is an important use of PL spectroscopy as the dopant atoms produces a distinct resonance at 575 nm (see section 1.5.3).

To measure accurately some phonon active modes in certain materials requires cooling the sample down to temperatures approaching 0 K using liquid He, allowing thermal noise to be removed from the measurements. A series of PL experiments were carried out at these temperatures using a Renishaw InVia instrument (325 nm laser excitation) operated in the Department of Physics, University of Bristol, with help from Dr. Andrei Sarua.

2.6.5 Powder X-ray Diffraction (XRD) analysis

The various crystalline phases of our deposited films were analysed using X-ray diffraction using a Bruker-AXS D8 Advance powder diffractometer which illuminates the samples with monochromatic radiation producing a distinct scattering pattern measured using a goniometer. Different crystalline planes show characteristic dihedral angles and some of those useful for our analysis are shown in the following table.

It is possible to obtain values for crystallite size within microcrystalline diamond films using the width of the <111> peak although this has not been implemented with the data collected. Instead, small-angle X-ray scattering (SAXS) analysis, using synchrotron radiation at the Diamond Light Source facility, has been performed on the free-standing diamond samples grown for the lens project described in section 6.0.

Material & plane	*Dihedral angle* θ
Graphite:	
<002>	26.5
<100>	42.3
<004>	54.7
Diamond:	
<111>	43.9
<200>	51.2
<220>	75.3
<311>	91.5
Silicon:	
<111>	28.4
<220>	47.3
<311>	56.1
<400>	69.1
<331>	76.4

Table 4: Dihedral angles for common crystal planes in graphite, diamond and silicon solids from data in the Cambridge Structural database (www.ccdc.cam.ac.uk).

3.0 Diamond CVD Results

3.1 Introduction

Using the apparatus and method described in section 2.0, diamond films have been grown in order to characterize the MW system, investigate various gas mixtures not yet trialled at the University of Bristol and test newly developed techniques of film nucleation and high-growth-rate deposition. The CVD plasmas fall into a number of categories defined by the gas mixtures they employ. Firstly, the use of standard MCD growth conditions is discussed (section 3.2) and then extended to include NCD deposition by increasing χ_0(Ar) and other inert gases in section 3.3. Finally, the influence of nitrogen on the deposition plasma is explored for N_2 and NH_3 in section 3.4. Each part aims to determine the variation in plasma properties and describe the spectroscopic analysis that has been carried out before detailing the film properties in terms of their characterization by techniques including Raman spectroscopy, electron microscopy and diffraction studies. The analysis of these different gas mixtures by MBMS will not be discussed here but be retained for section 5.0.

3.2 Diamond deposition I: MCD

Microcrystalline diamond (MCD, see section 1.2.2) can typically be grown in the MW system by using a gas mixture of $\chi_0(H_2) = 0.885$ ($F(H_2) = 500$ sccm), $\chi_0(Ar) = 0.071$ ($F(Ar) = 40$ sccm) and $\chi_0(CH_4) = 0.044$ ($F(CH_4) = 25$ sccm), hence, we term these ‘standard’ MCD growth gas flows in the remainder of this work, with any deviation stated explicitly. Similar standards for NCD deposition are outlined in the following sections.

All of the initial diamond deposition in the MW reactor described in section 2.1 involved systematic deviation from these standard conditions as well as variation of the other plasma parameters, the MW input power, P, and the reaction vessel pressure, p. Films were grown on 14 × 14 mm Si substrates which were treated by manual abrasion using 1-3 µm diamond powder.

3.2.1 Plasma observations and spectroscopic studies

When using the standard mixture the plasma is very stable and can be operated over a wide range of input powers, from the upper limit of the apparatus at 1.5 kW to less than 0.6 kW at which point the plasma extinguishes, and pressures, ranging from 225 Torr down to ~75 Torr where the plasma becomes too large and heats the chamber walls and quartz window. The plasmas ignite around 60 Torr and with 200-300 W of forward power and typically contain fewer soot-like particulates compared with the high χ_0(Ar) systems discussed later.

Before adding any hydrocarbon the H_2/Ar plasma is dull purple in colour with the emission spectrum (360 to 600 nm) only containing the Balmer series transitions of atomic H: H-α at 656 nm ($n = 3 \rightarrow n = 2$), H-β at 486 nm ($n = 4 \rightarrow n = 2$), H-γ at 434 nm ($n = 5 \rightarrow n = 2$) and H-δ at 410 nm ($n = 6 \rightarrow n = 2$). There are some bands due to Ar in this range but, like the H-ε line, these are too weak to observe in our setup. Between 570 nm and 630 nm a number of weak transitions can be seen overlapping with the C_2 ($\Delta v = -2$) band and these are due to emission from excited H_2 ($^3\Sigma_u^+ \rightarrow {}^3\Sigma_g^+$). Addition of methane or acetylene results in a green colouration of the plasma due to the Swan band emission ($d^3\Pi_g \rightarrow a^3\Pi_u$) of the C_2(d) radical as seen in the spectrum in Figure 3.1.

This plasma system in an identical MWCVD reactor has been well characterized by laser absorption diagnostics using both cavity ring-down (Ma *et al.*, 2008) and quantum cascade laser absorption spectroscopy (Ma *et al.*, 2009a).

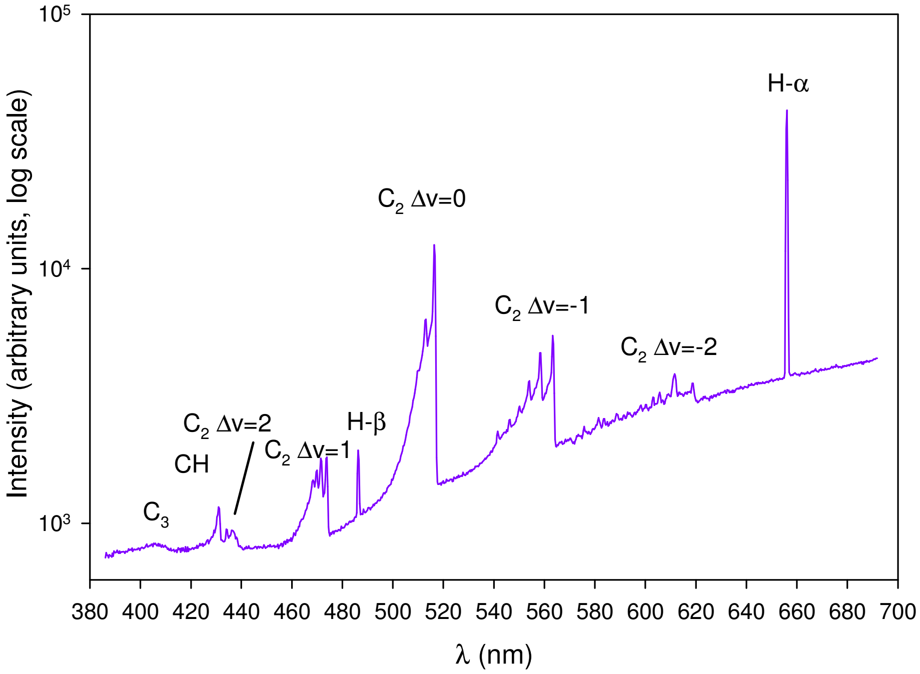

Figure 3.1: OES of a typical MCD-depositing plasma with the transitions due to atomic H and C_2, CH and C_3 radical species ($\Delta v = v' - v''$). These bands are discussed in more detail in section 3.3.

3.2.2 Experimental variation of plasma variables

Characterization of the deposition system was achieved by variation of the main parameters:

i) $F(CH_4) = 12.5\text{-}75.0$ sccm (corresponding to $\chi_0(CH_4) = 0.02\text{-}0.13$)

ii) $F(Ar) = 0\text{-}60$ sccm (corresponding to $\chi_0(Ar) = 0\text{-}0.1$)

iii) $p = 100\text{-}175$ Torr

iv) $P = 0.9\text{-}1.4$ kW

v) Further variation of multiple parameters to achieve highest growth rate.

We have already mentioned the instability in high P and low p plasmas which mark the boundaries for these variables. Similarly, at $\chi_0(CH_4) > 0.13$ the amount of soot and non-diamond particulate in the plasma is detrimental causing heating of the quartz window and reactor walls. Higher $\chi_0(Ar)$ will be addressed in section 3.3.

3.2.2.1 Increasing $\chi_0(CH_4)$

As methane is added to the H_2/Ar plasma the chemistry changes markedly as a mixture of neutral, ionic and radical hydrocarbon species are formed which cause a change in plasma colour from purple to green. The changes in the emission spectra when increasing the $\chi_0(CH_4)$ are shown in Figure 3.2 where we see the steady increase in the peaks due to carbon-containing species.

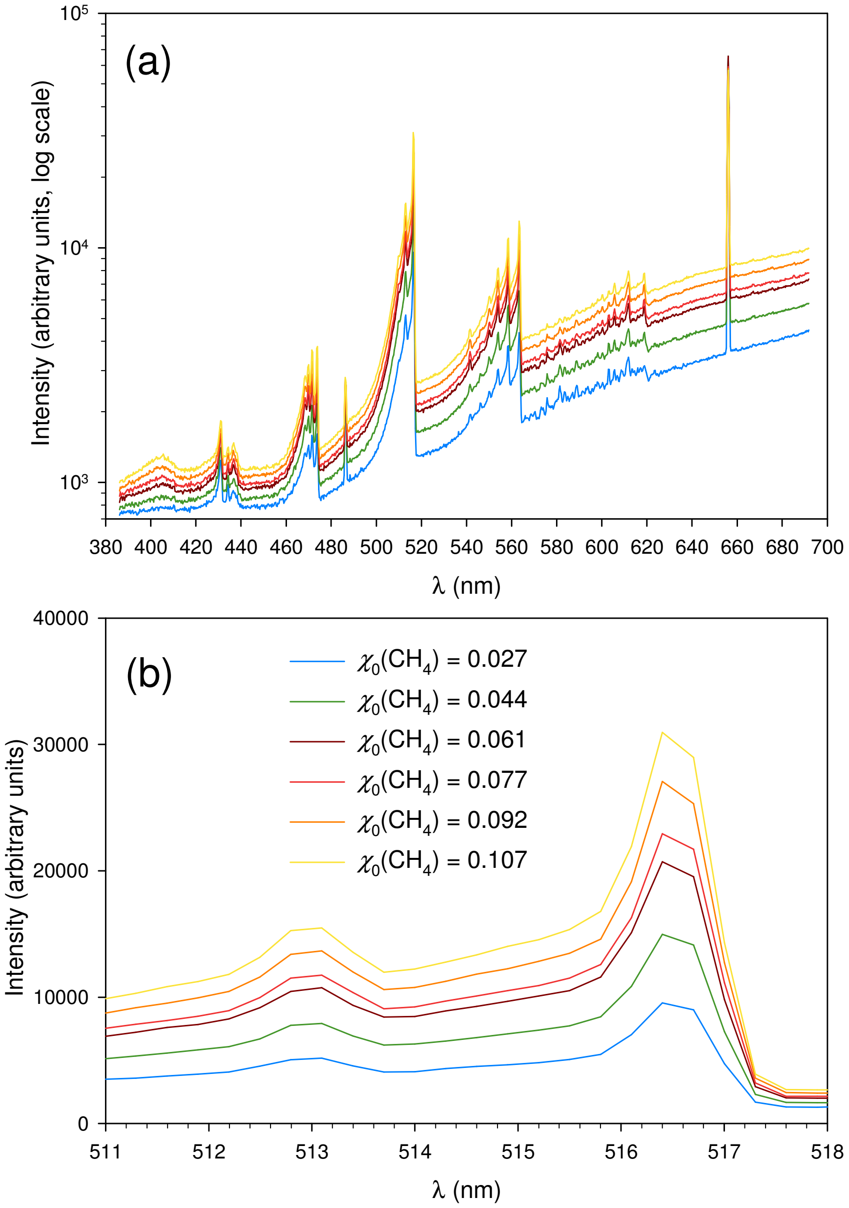

Figure 3.2: OES spectra for standard MCD conditions and constant p = 150 Torr and P = 1.2 kW but increasing $\chi_0(CH_4)$. (b) shows the increase in intensity of the $C_2(d \rightarrow a)$ peak at 516 nm with $\chi_0(CH_4)$. The spectra were measured at z ~ 10 mm, *i.e.* the plasma centre.

While we can see some trends in these spectra they become obvious when the normalized peak heights are plotted against the process variable (Figure 3.3). The $C_2(d \rightarrow a)$ peak increases linearly with $\chi_0(CH_4)$ while the $CH(A \rightarrow X)$ rises but less steeply. The H-α peak falls with increasing $\chi_0(CH_4)$, as observed in other experiments (Ma, 2008, Ma *et al.*, 2008, Richley *et al.*, 2011) as it is determined to a greater extent by T_e compared with the influence of T_{gas} on $CH(A \rightarrow X)$ and $C_2(d \rightarrow a)$.

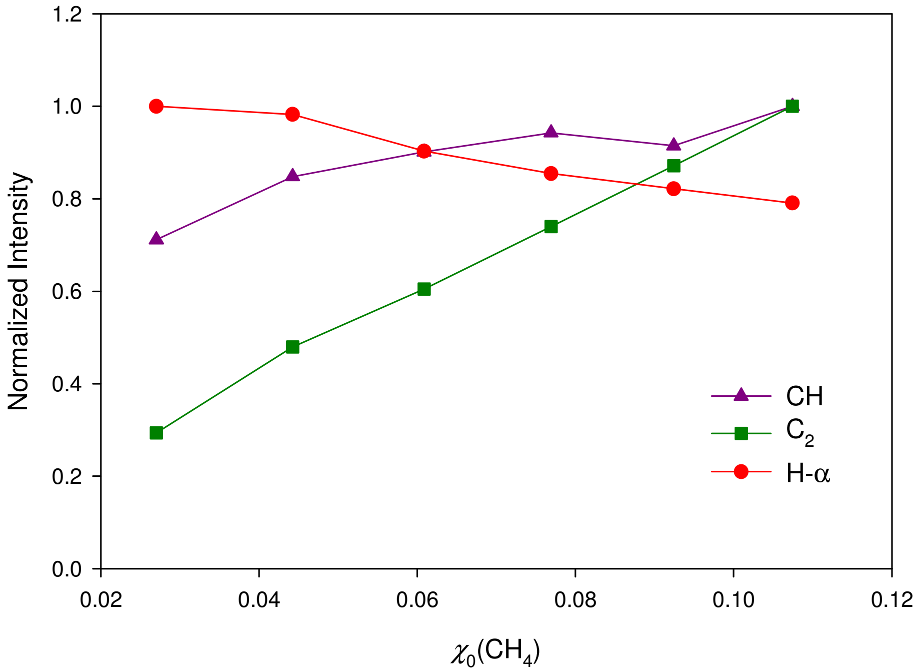

Figure 3.3: OES peak intensities for H-α (656 nm), C_2(d→a, 516 nm) and CH(A→X, 431 nm), normalized to their maximum value, against $\chi_0(CH_4)$.

The influence of $\chi_0(CH_4)$ on diamond CVD has been investigated extensively with observed morphological changes involving a decrease in the average crystal size with increasing hydrocarbon mole fraction (Kobashi *et al.*, 1988). An increase in $\chi_0(CH_4)$ in the standard gas mixture results in the grain size decreasing to tens of nm and the films being described as NCD.

Here we increased the $\chi_0(CH_4)$ from 0.02 to 0.13, whilst compensating with $\chi_0(H_2)$ and keeping $\chi_0(Ar)$ constant at 0.07, with $F_T = 565$ sccm. Similarly, the power density was kept constant by maintaining P and p at 1.2 kW and 150 Torr, respectively, and achieved a T_{sub} of 1120±50 K for the eight films deposited over 4 h (there was no discernable correlation between T_{sub} and $\chi_0(CH_4)$).

Inspection of the range of films grown showed no immediate switch between films exhibiting microcrystalline and nanocrystalline morphologies but rather a gradual continuum of decreasing grain size with increasing $\chi_0(CH_4)$. Films grown with $\chi_0(CH_4) < 0.1$ would still be classed as well-facetted MCD and only the film grown with $\chi_0(CH_4) = 0.122$ would be termed NCD, as shown in Figure 3.4 & Figure 3.5, indicating that the onset of nanocrystalline diamond may be at higher $\chi_0(CH_4)$ in our MW system than has previously observed in HFCVD reactors (May & Mankelevich, 2008).

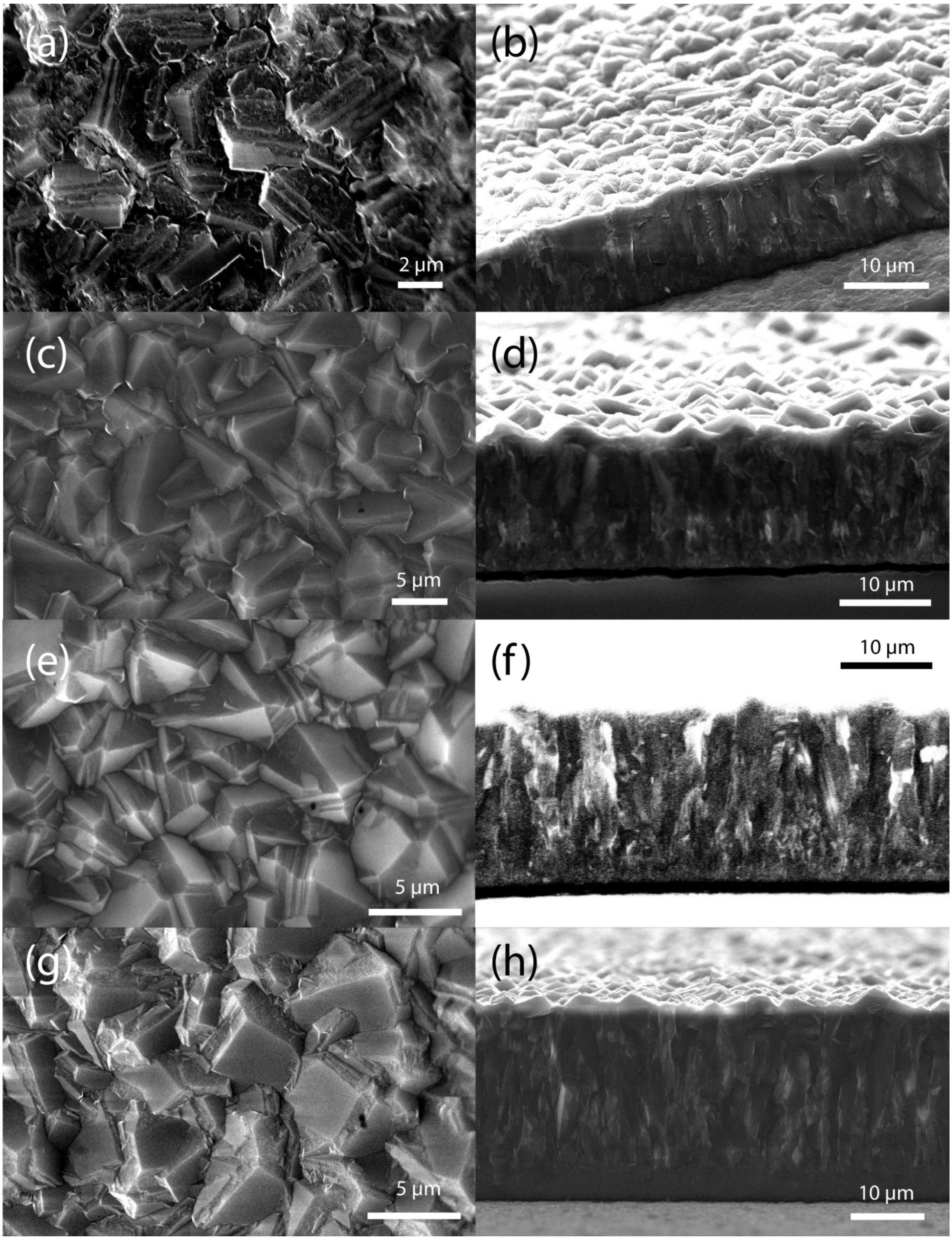

Figure 3.4: SEM images of MCD films grown with increasing methane mole fraction shown in both plan and cross-sectional views for $\chi_0(CH_4) = 0.023$ (a) & (b), 0.044 (c) & (d), 0.061 (e) & (f) and 0.085 (g) & (h).

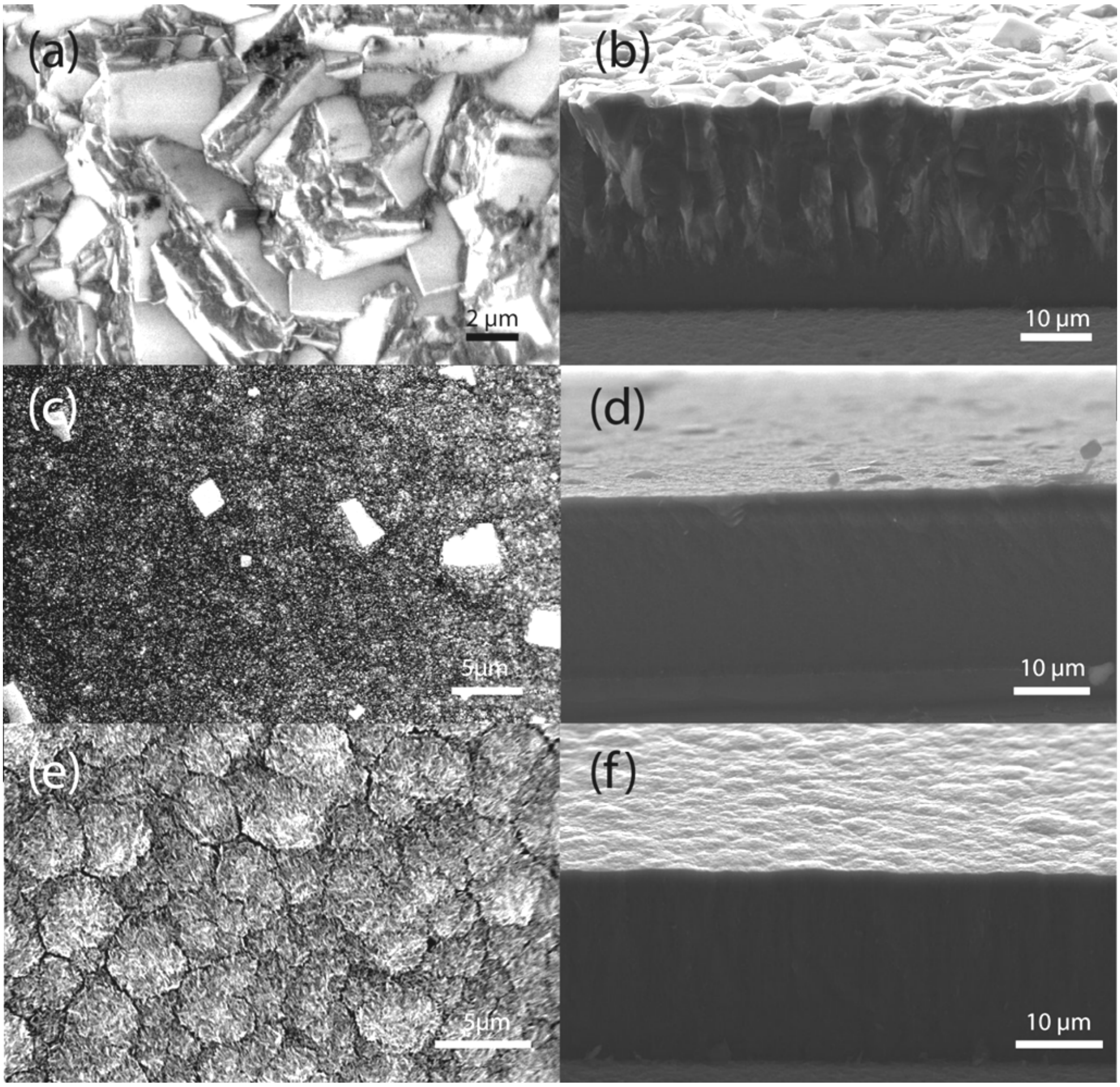

Figure 3.5: SEM images of MCD and NCD films grown with a further increase in methane mole fraction shown in both plan and cross-sectional views for $\chi_0(CH_4)$ = 0.100 (a) & (b), 0.112 (c) & (d) and 0.122 (e) & (f).

The observed onset of NCD morphology correlates well with the observed growth rates (Figure 3.6) as we see an initial increase in G from 10 to 30 µm h^{-1} with $\chi_0(CH_4)$ = 0.02-0.1 then followed by a decrease in G as $\chi_0(CH_4)$ is increased further. We might expect an increase in G as we add more hydrocarbon to the system and increase the growth species concentration, $\chi(CH_3)$ and this is true for MCD conditions. However, it is the ratio of atomic hydrogen to C_1 species, $\chi(H)/\chi(CH_x)$, where x = 0-3, which has been proposed as a more important factor and modelling has suggested that the ratio decreases from ~13 for MCD growth to ~3 for NCD deposition, albeit for HF systems (May & Mankelevich, 2008).

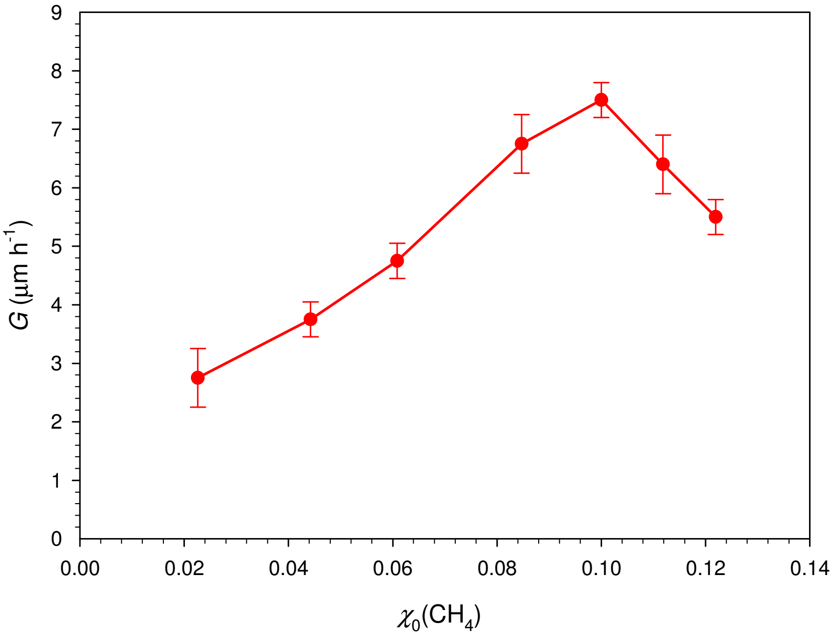

Figure 3.6: Dependence of growth rate, *G*, on $\chi_0(CH_4)$.

Further confirmation of the decrease in grain size with increasing $\chi_0(CH_4)$ comes from the UV-Raman analysis of this set of films where a marked reduction in the intensity of the diamond or *sp*^{3} peak (*I*(*sp*^{3})) with respect to that of the *sp*^{2} carbon D band (*I*(D)) is seen (Figure 3.7 & Figure 3.8).

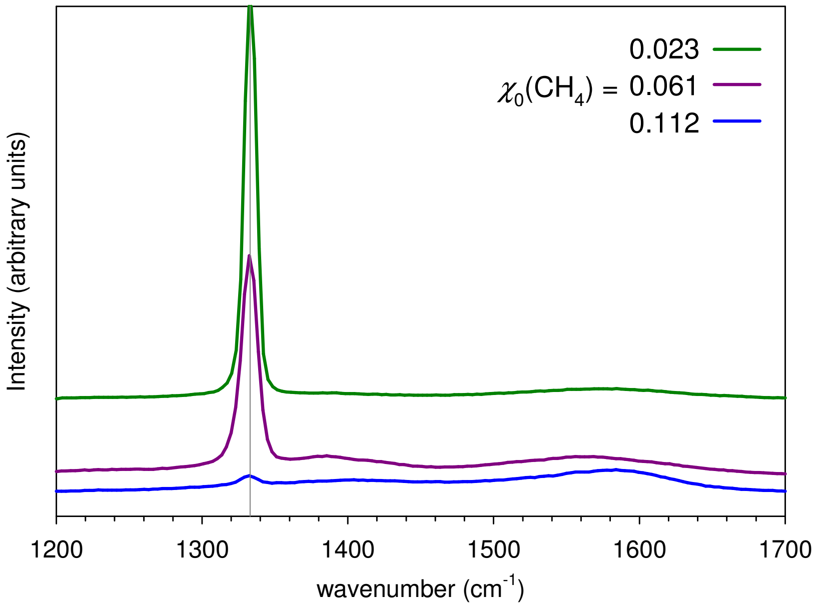

Figure 3.7: Three examples of UV-Raman spectra of diamond films grown with $\chi_0(CH_4) = 0.023$, 0.061 & 0.112. The change in morphology observed under the electron microscope is obvious again in these spectra.

Here, we see that where $I(sp^3)/I(\mathrm{D}) < 2$ the film exhibits a NCD morphology observed by SEM; an observation which will be useful when looking at films grown in Ar-rich or N_2-containing plasmas (sections 3.3 & 3.4).

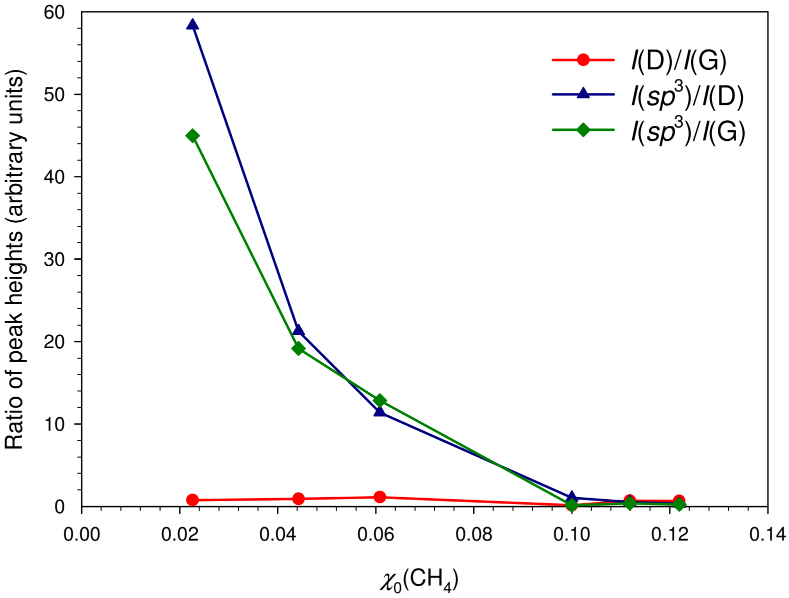

Figure 3.8: Relative peak intensities of sp^2 ($I(\mathrm{D})$ = 1380 cm^{-1} band, $I(\mathrm{G})$ = 1570 cm^{-1} band) and sp^3 ($I(sp^3)$) carbon with increasing hydrocarbon mole fraction, $\chi_0(CH_4)$.

3.2.2.2 Increasing χ_0(Ar)

The use of argon in diamond-depositing environments can be divided into two regimes; at $\chi_0(\mathrm{Ar}) < 0.5$ where MCD (or NCD with high $\chi_0(CH_4)$) deposition occurs, and $\chi_0(\mathrm{Ar}) > 0.5$ where NCD (or UNCD) films are produced. The latter situation is discussed in detail in section 3.3 but here we look at the influence of χ_0(Ar) on MCD-type plasmas.

Argon has been added to diamond depositing plasmas since the origins of the technique (Matsumoto *et al.*, 1985, Zhu *et al.*, 1990) as a way of increasing the T_{gas} and the growth rate of the diamond. This rise in temperature is obvious in the emission spectra (Figure 3.9) which show rising background signals (note that the spectra have similar background intensities at ~400 nm but widely different heights at ~680 nm due to increase in blackbody radiation). At this point we should mention that the background is, of course, subtracted from the intensities in Figure 3.10 which shows the increasing trends in all the radical-species emission intensities with χ_0(Ar).

The emission intensity trends all show increases with χ_0(Ar) which we can assign to a higher T_{gas}, which also manifests itself in the increase in T_{sub} (Figure 3.11), due to the inert gas transporting heat around the reactor efficiently through collisions with other gaseous species.

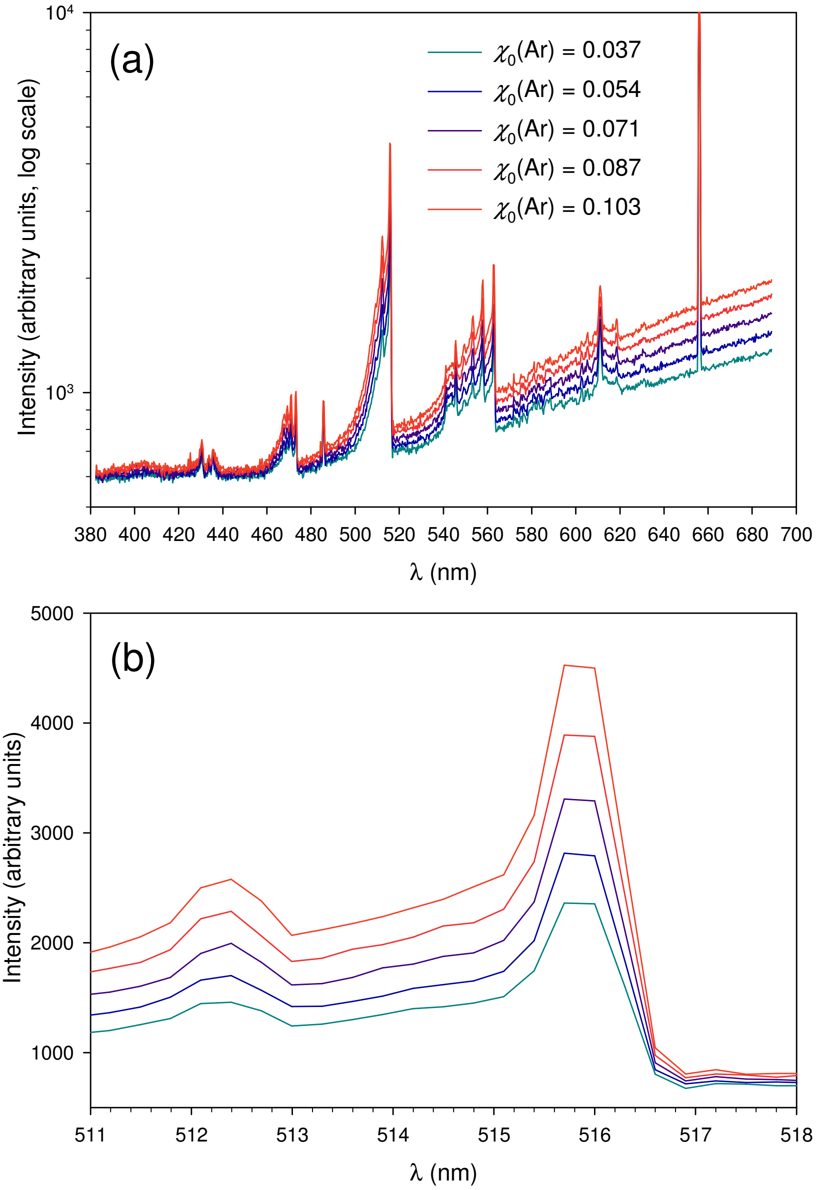

Figure 3.9: OES spectra for standard MCD conditions and constant p = 150 Torr and P = 1.2 kW but increasing χ_0(Ar). (b) shows the increase in intensity of the C_2(d→a) peak at 516 nm with χ_0(Ar). The spectra were measured at z ~ 10 mm, *i.e.* the plasma centre.

Diamond films were deposited as F(Ar) was varied between 0-60 sccm corresponding to χ_0(Ar) = 0-0.1, again balancing with $\chi_0(H_2)$ and at constant $\chi_0(CH_4)$ = 0.063, P = 1.2 kW and p = 150 Torr. Over this range of χ_0(Ar) the T_{sub} increased from 977-1137 K indicating the effect that even a small amount of argon can have on the plasma (Figure 3.11).

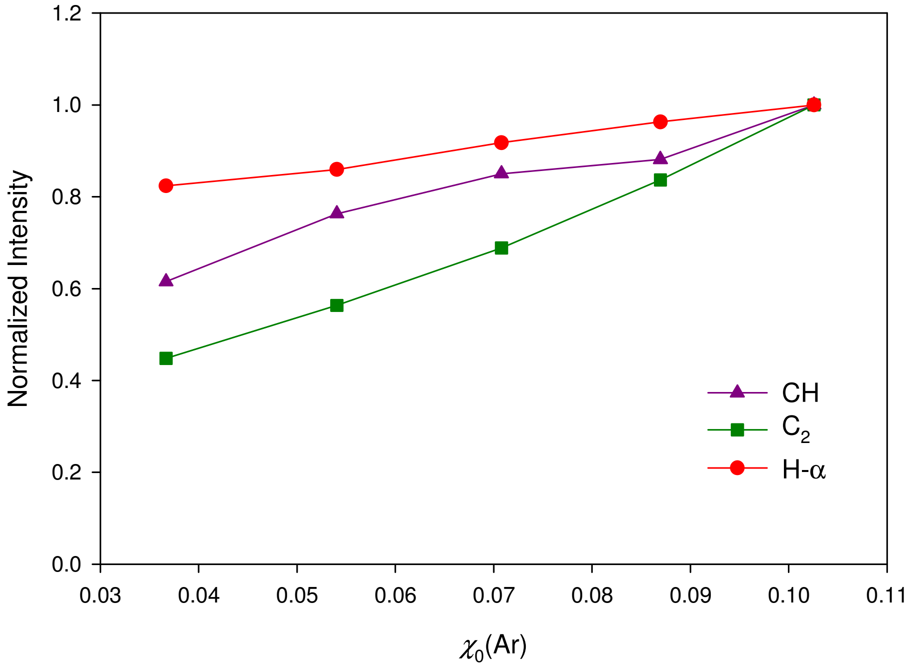

Figure 3.10: OES peak intensities for H-α (656 nm), C_2(d→a, 516 nm) and CH(A→X, 431 nm), normalized to their maximum value, against χ_0(Ar).

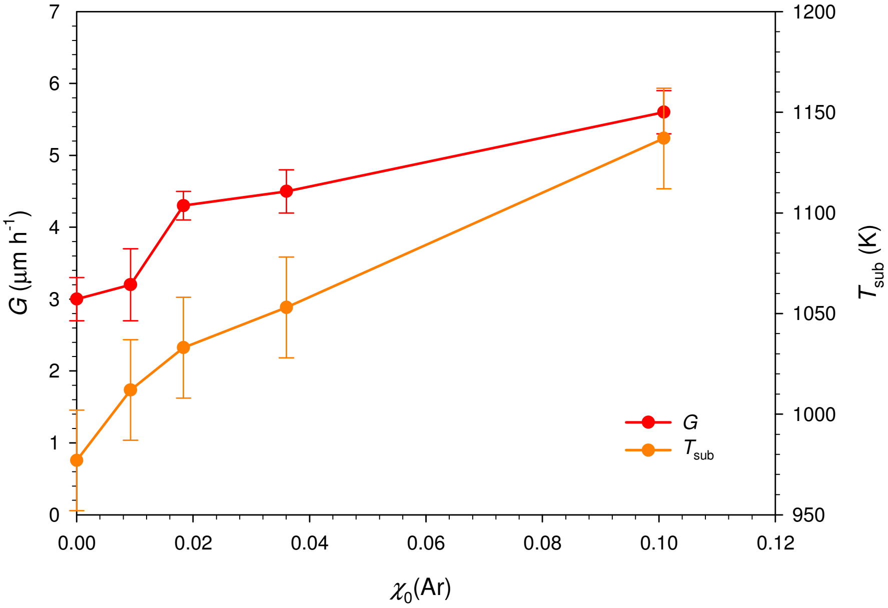

Figure 3.11: Dependence of growth rate, G, and substrate temperature, T_{sub}, on χ_0(Ar).

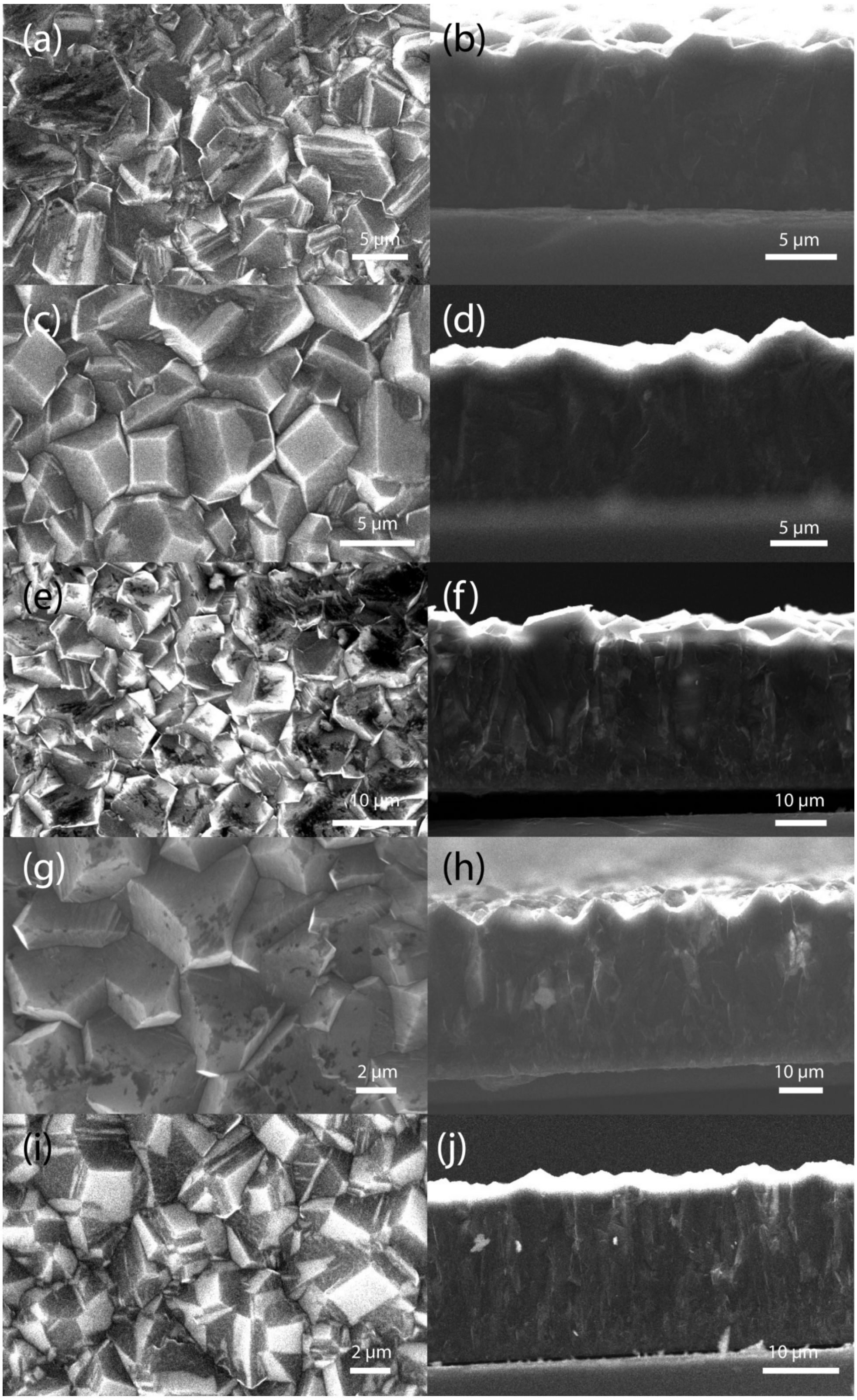

Figure 3.12: SEM images of MCD films grown with increasing argon mole fraction shown in both plan and cross-sectional views for χ_0(Ar) = 0.00 (a) & (b), 0.009 (c) & (d), 0.018 (e) & (f), 0.036 (g) & (h) and 0.101 (i) & (j).

SEM imaging of the films showed much less variation in the crystal size compared with the preceding methane experiments (Figure 3.12). The variation in T_{sub} can be correlated with the increase in *G* over the same range of χ_0(Ar) (Figure 3.11) and a slight but noticeable decrease in the film quality (the ratio of sp^3 to sp^2 bands) as measured by UV-Raman (Figure 3.13) which is in agreement with other studies that show more sp^2 content with higher χ_0(Ar) (Liu *et al.*, 2004).

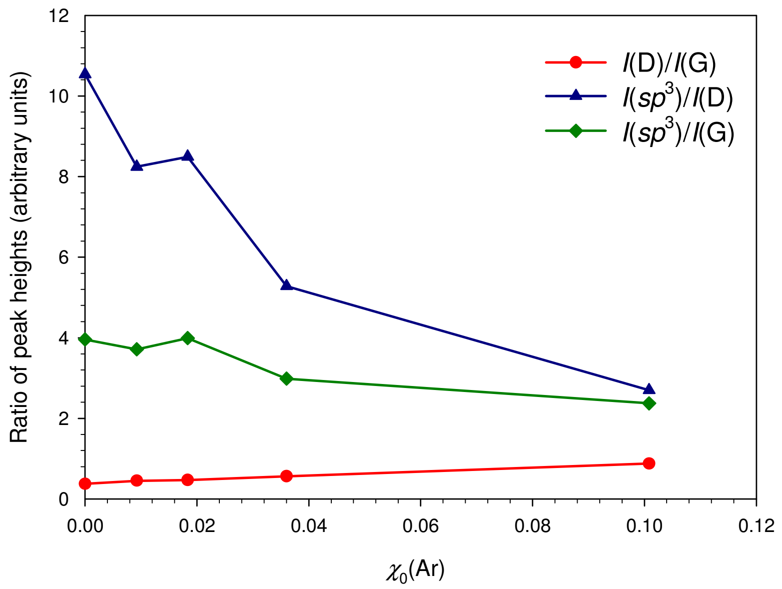

Figure 3.13: Relative peak intensities of sp^2 (*I*(D) = 1380 cm^{-1} band, *I*(G) = 1570 cm^{-1} band) and sp^3 (*I*(sp^3)) carbon with increasing argon fraction, χ_0(Ar).

3.2.2.3 Increasing power density

Raising either the input MW power, *P*, or the chamber pressure, *p*, has the result of increasing the power density in the plasma, the former by increasing the power density in a given volume of gas and the latter by reducing the volume for a set input power.

The emission spectra for increasing *P* (Figure 3.14) between 0.9 and 1.4 kW and for *p* between 90 and 180 Torr (Figure 3.15) provide evidence for rising T_{gas} because the curved blackbody background gets steeper at higher *P* and *p*. However, if we look at the background-corrected, normalized peak intensities we see slightly different behaviour for each discharge parameter. Emission from all three species rise in intensity with increasing *P* but while CH(A→X) and C_2(d→a) emission increases with *p* the peak height of H-α remains constant (as do those for H-β and H-γ). In contrast to previous analysis (Ma, 2008) no variation in the H-β/H-α ratio, an indicator of T_e (Gicquel *et al.*, 1996), was detected with either *P* or *p* and the three species show similar *sensitivity* or gradients as the power is increased. When increasing the chamber pressure, however, we see a difference between the emission from atomic H (whose production is dominated by the T_e) and that from C_2 and CH, which are dependent on T_{gas} and χ(H). While thermally dominated, the C_2(d→a) and CH(A→X) emission intensities increase with p (and T_{gas}) the H-atom intensity stays constant because the electron temperature is not altered (Ma, 2008). Indeed, the same slight rise in the H-intensity trend at ~100 Torr before peaking and slightly falling is mirrored in the earlier analysis and hints at more subtle and complex behaviour as T_{gas}, T_e, n_e and χ(H) change coincidently.

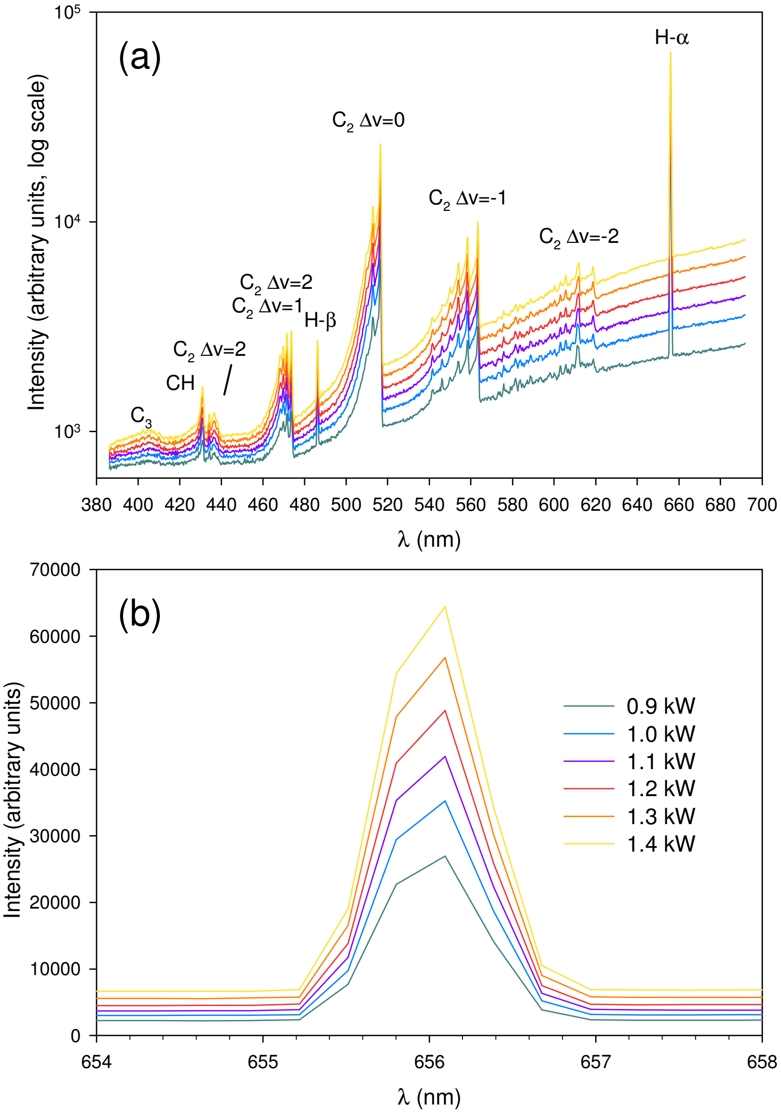

Figure 3.14: OES spectra for standard MCD conditions and constant p = 150 Torr but increasing input power, P. (b) shows the increase in intensity of the H-α peak with P although there is some increase in the baseline due the rise in blackbody radiation at higher T_{gas} ($\Delta v = v' - v''$).

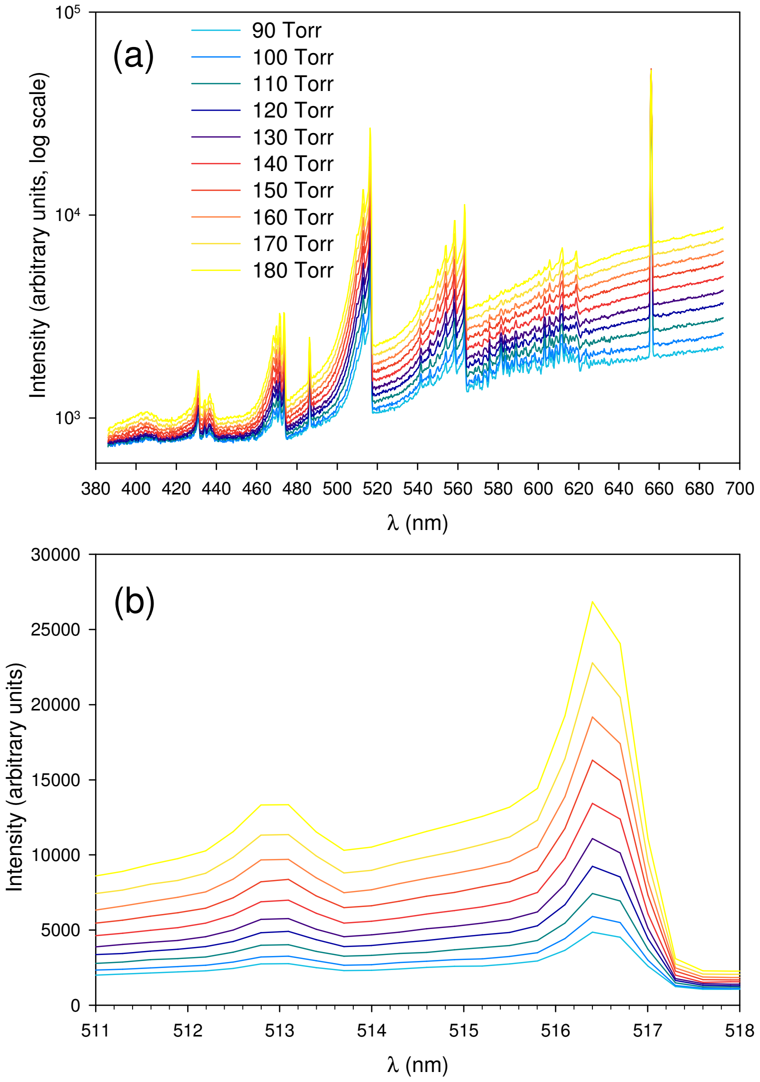

Figure 3.15: OES spectra for standard MCD conditions and constant P = 1.2 kW but increasing pressure, p. (b) shows the increase in intensity of the C_2(d⟶a) band with p although there is some increase in the baseline due the rise in blackbody radiation at higher T_{gas}.

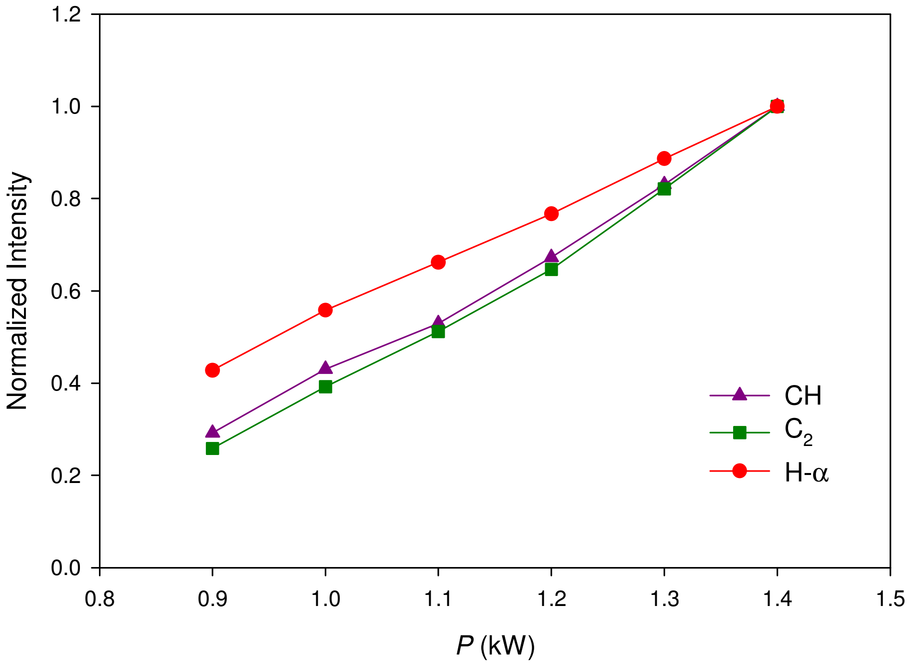

Figure 3.16: OES peak intensities for H-α (656 nm), C_2(d→a, 516 nm) and CH(A→X, 431 nm), normalized to their maximum value, against *P*.

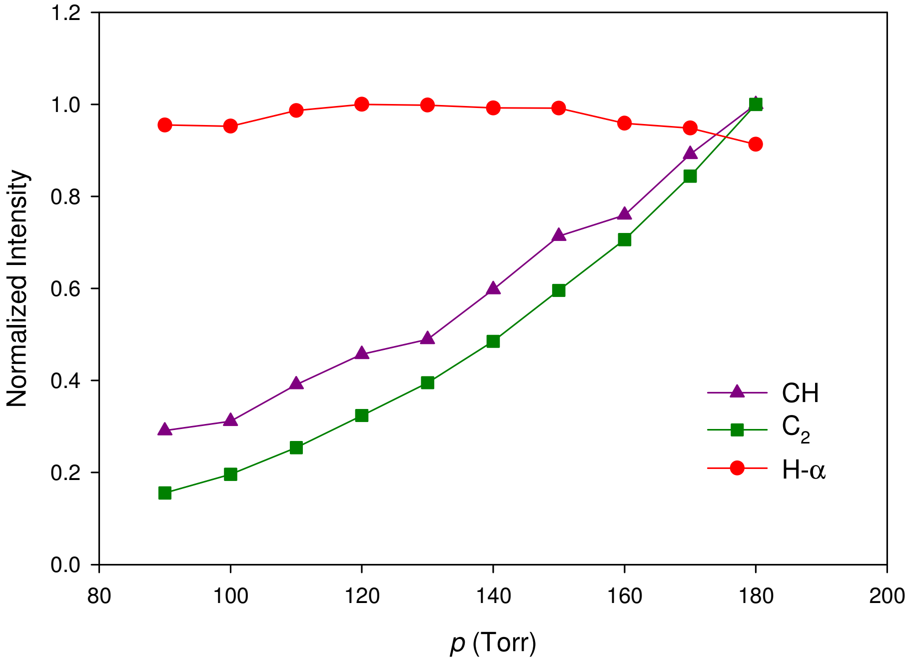

Figure 3.17: OES peak intensities for H-α (656 nm), C_2(d→a, 516 nm) and CH(A→X, 431 nm), normalized to their maximum value, against *p*.

Diamond films were grown in a mixture of $\chi_0(H_2)/\chi_0(Ar)/\chi_0(CH_4)$ = 0.87/0.07/0.06, F_T of 575 sccm and deposition time of 4 h, the input *P* was increased from 0.9-1.4 kW (for constant *p* = 150 Torr) and subsequently an increase in *p* from 100-175 Torr (for constant *P* = 1.2 kW). The effects of increasing the power density are seen as an increase in T_{sub} and G (Figure 3.18 & Figure 3.19) but, for a particular gas mixture, the variation in diamond morphology is negligible for different p and P, *i.e.* there is no discernable trend in the sp^3/sp^2 ratio measured by UV-Raman spectroscopy. To summarise, we see that increasing the power density, and thus T_{gas}, in these high $\chi_0(H_2)$ systems does not alter the diamond deposition mechanism significantly, within the bounds of our experiment, but primarily results in higher T_{sub} and growth rates.

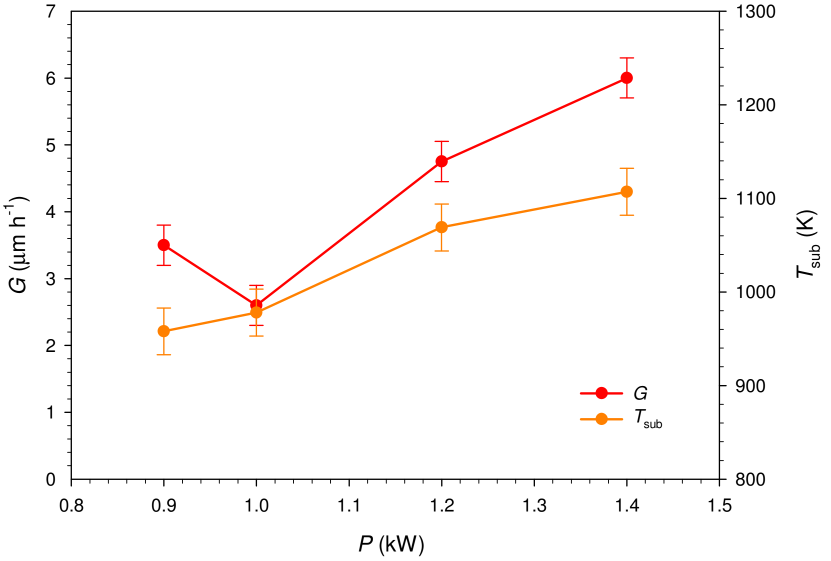

Figure 3.18: Dependence of growth rate, G, and substrate temperature, T_{sub}, on input power, P.

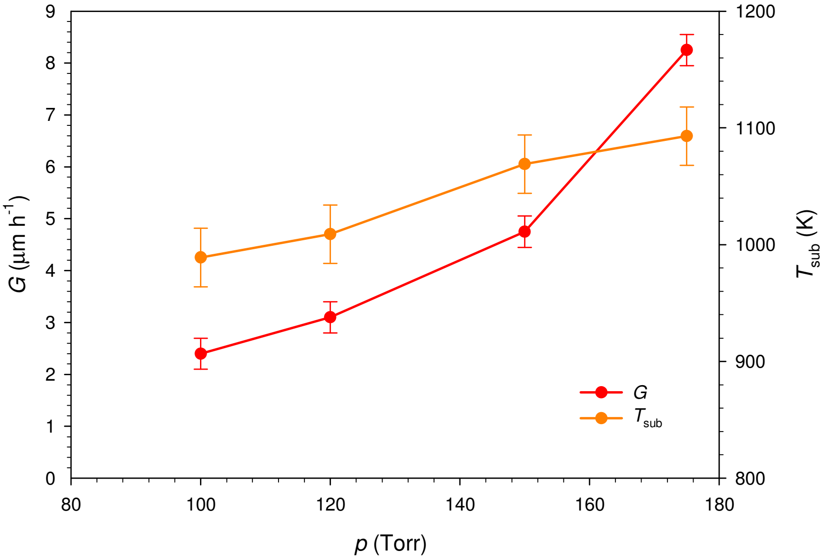

Figure 3.19: Dependence of growth rate, G, and substrate temperature, T_{sub}, on pressure, p.

3.2.2.4 Optimizing G & large area deposition

By systematically varying $\chi_0(CH_4)$, $\chi_0(Ar)$, P and p in turn it was possible to identify conditions which would lead to maximal growth rates, and in subsequent investigations these parameters were altered concurrently to achieve the highest G possible for MCD in the MW reactor. Often the optimum flow rates resulted in a higher T_{sub} and when combined together with higher power density a growth rate up to 9.3 μm h^{-1}. Care was taken to make sure that the quality of the diamond (sp^3/sp^2) was not compromised by the high T_{sub} and growth rates although the higher substrate temperatures meant that the films grown contain a higher sp^2 content. Using higher than usual $\chi_0(CH_4)$ ~ 0.085 (*i.e.* before the NCD threshold is reached) and higher P ~ 1.4 kW and p ~ 175 Torr a range of films were deposited at G = 7.4-9.3μm h^{-1} with an average T_{sub} = 1125 K.

As another ancillary experiment, a MCD film was deposited over a larger area than used in previous experiments using a 20×20 mm Mo holder. The film was extremely uniform except for the corners where the square substrate lay outside of the circular holder (which was slightly smaller). This showed that the plasma system can successfully deposit over these larger substrates as long as the holder is designed carefully so that the whole substrate lies within the recess.

3.2.3 Summary

Deposition experiments have shown the ranges of process parameters in which microcrystalline diamond thin films can be grown successfully allowing trends in crystal size (or sp^3/sp^2) to be determined using UV-Raman spectroscopy and SEM imaging. Some simple plasma diagnostics using emission spectroscopy have shown changes in the radical species concentrations as the mole fractions of methane, argon and hydrogen are altered. Combining these results has allowed high-rate deposition of MCD films. In the next section we will increase the $\chi_0(Ar)$ further and see marked changes in the plasma behaviour and the diamond morphology which is formed.

3.3 Diamond deposition II: NCD & noble gases

3.3.1 Introduction to inert-gas-rich plasmas

We have already discussed the recent interest in nanocrystalline diamond and its distinct qualities from facetted synthetic diamond in terms of both the physical properties of the material and the nature of the chemistry during its deposition (sections 1.2.3 & 1.3.4.3). An overarching feature of CVD diamond formation is the ability to tune the system to produce diamond crystals of different size through variation in some key plasma conditions. These typically involve changes in the proportions of the various gases which flow into the reactor as we saw in the discussion of the influence of $\chi_0(CH_4)$ and $\chi_0(Ar)$ on MCD deposition (section 3.2.2.1 & 3.2.2.2).

Increasing the $\chi_0(Ar)$ (or $\chi_0(X)$ when discussing generic inert or noble-gas plasmas where Ar was substituted for He, Ne or Kr) beyond 10% of the total gas flow (the limit in section 3.2.2.2) has interesting results for both the diamond deposited and the plasma chemistry. It is generally understood that increasing $\chi_0(Ar)$ (with a corresponding reduction in $\chi_0(H_2)$) from standard MCD conditions will result in a reduction in the diamond crystallite size and production of NCD films. The majority of research into NCD or UNCD deposition has been performed in plasmas consisting of a few percent of CH_4 in Ar with the addition of 1-2% H_2 to help stabilize the plasma (Kulisch & Popov, 2006, Xiao *et al.*, 2004).

Plasmas with $\chi_0(Ar) > 0.5$ have been investigated from a number of different viewpoints, including diamond film growth, absorption and emission spectroscopy, and resulted in a much fuller, although not yet complete, picture of the deposition chemistry. The deposition of thin NCD films using inert-gas plasmas at Bristol, together with some preliminary spectroscopic analysis, has been reported (Fox *et al.*, 2009) and followed up with a much more detailed CRDS and OES study which, with accurate computer modelling, summarised our current understanding of these inert-gas-rich systems (Richley *et al.*, 2011). The discussion which follows is mainly taken from these two papers and combined here with a few more experimental details which were omitted from the published work. The CRDS experiment and analysis were carried out by James Richley, whereas the OES measurements and related plasma diagnostics were undertaken by the author.

3.3.2 Plasma parameters & stability

In our discussion of the deposition of MCD in the MW reactor in section 3.2 we defined the key variables for deposition which were investigated. For high $\chi_0(Ar)$ plasmas each parameter is often limited to a smaller range because of the reduced stability of the system within the reactor. Here, instability is taken to mean any situation where the plasma i) heats some part of the apparatus, such as the quartz window or the substrate, to a dangerous or undesirable amount (Figure 3.20a & c), ii) no longer occupies a radially symmetric position within the vacuum chamber and/or forms intense secondary plasmas (Figure 3.20c & d) or iii) forms too much soot and particulate carbon in its periphery (Figure 3.20b & d). There is also a difference in severity in these issues on longer and shorter time scales. For example, the plasma can be run at a high power or particularly high χ_0(Ar) for a few minutes while a CRDS measurement is taken but, due to the increased heating of the quartz window, cannot be left for the timescales of several hours required for film deposition. As such, there are likely to be wider ranges in the fundamental plasma parameters for the spectroscopic testing than for the diamond deposition experiments. Lastly, due to the considerable differences in the physical properties of each inert gas tested, the MWCVD variables are likely to have dissimilar ranges. The required parameters for diamond deposition in He, Ne, Ar and Kr were determined experimentally and will be described in the section on film growth.

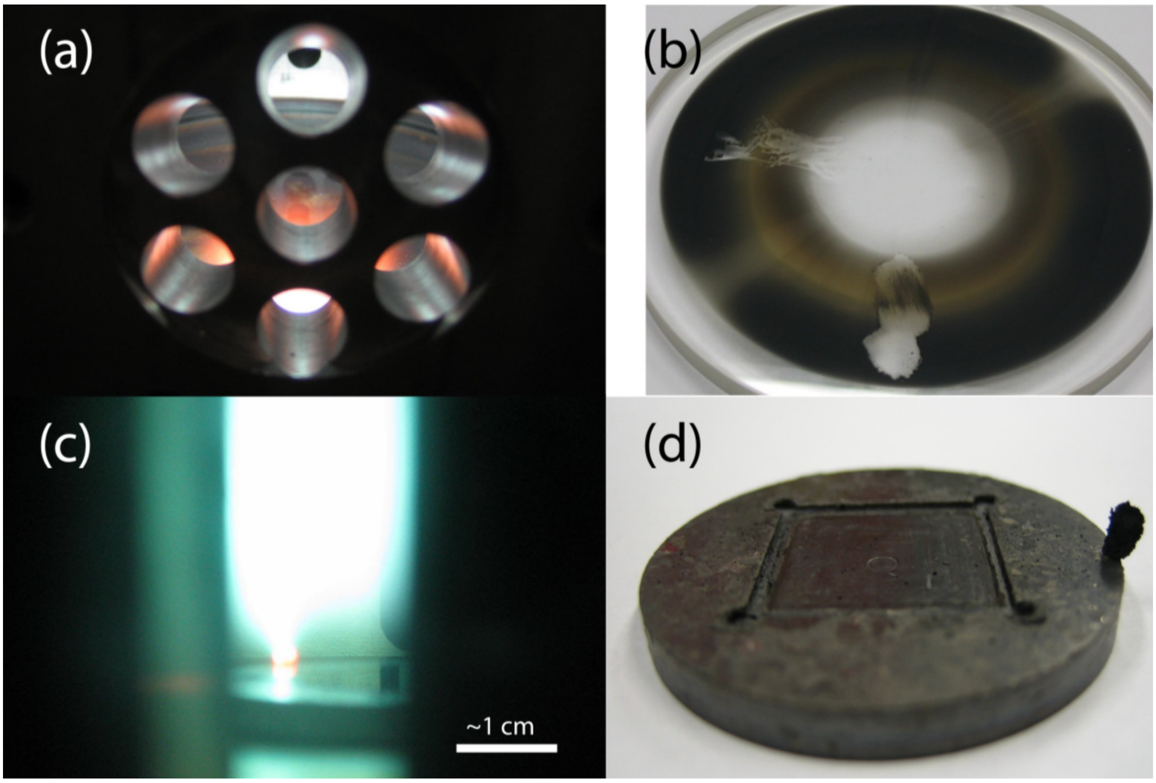

Figure 3.20: Two major forms of instability observed in the plasmas when running with high inert-gas fractions. (a) shows the plasma in contact with the quartz window at the top of the chamber when either the *p* is too low or the *P* too high. (b) shows the soot layer formed on the window when running these large plasmas for long deposition times (not actually the extreme case shown in (a) which is unsustainable). (c) shows the formation of a concentrated plasma on the edge of the substrate holder when the plasma is unstable, for example under too high a pressure and (d) the carbonaceous build-up which forms very quickly at this point.

The main CRDS experiment (section 3.3.9) was only performed using Ar rather than for each inert gas and the values for each variable are given below, however, it should be borne in mind that the full ranges stated may not, necessarily, produce diamond instead of graphitic or amorphous carbon deposits.

i) $\chi_0(H_2) = 0.1\text{-}0.5$ (*i.e.* $\chi_0(X) = 0.9\text{-}0.5$)

ii) $\chi_0(CH_4) = 0.0025\text{-}0.02$

iii) $p = 125\text{-}225$ Torr

iv) $P = 0.6\text{-}1.4$ kW

From these parameter values we see that the unstable plasmas generally correspond to low $\chi_0(H_2)$, low p or high $\chi_0(CH_4)$. There is some reactor dependency, with the deposition reactor being more stable at low $\chi_0(H_2)$ than the one used for CRDS measurements.

3.3.3 Diamond deposition with different inert gases

An important requirement for the proposed C_2 growth mechanism (section 1.4.7) is the formation of ionic or excited Ar species in the plasma which would undergo a charge-exchange reaction or Penning ionization, respectively, to form $C_2H_2^+$. This metastable species then dissociates to give C_2: previously believed to be a possible growth species. To determine the importance of the proposed Ar^+ charge-exchange and Ar* Penning reactions within high $\chi_0(Ar)$ plasmas, diamond was deposited in systems where Ar was replaced by one of the other readily available noble gases, including helium, neon and krypton. If diamond was deposited using these gases it would indicate that the energy-level-specific charge-transfer or Penning excitation reactions were not necessary, and that these C_2 forming mechanisms were unlikely to be dominant in the plasma system. Indeed, NCD deposition has been demonstrated a number of times before in both He-rich gas mixtures (Rabeau *et al.*, 2004) and a range of inert-gas/H_2/CH_4 systems (Griffin & Ray, 2006). Some plasma mechanisms of CH_4 interaction with Ne and Ar in gas mixtures of Ne/H_2/CH_4 and Ar/H_2/CH_4 have also been studied in detail (Tosi *et al.*, 1995).

Our experiments would be similar to the previous study (Griffin & Ray, 2006) but using a higher pressure regime for the MWCVD reactor outlined in the MCD work, whereas their work was conducted at 2.66 mbar (~2 Torr). The aim was to perform a systematic study of inert-gas-based plasmas, X/H_2/CH_4 where X = He, Ne, Ar or Kr at conditions indicative of most CVD diamond studies in ASTEX-type reactors: 100-150 Torr and ~1 kW MW power.

Although they share a number of remarkable properties which mark them out from the rest of the elements, as we descend down the group of inert gases from He to Kr (Xe being excluded from this study due to the prohibitively high cost of using large volumes of this gas) many plasma-influencing physical properties change significantly, as is apparent in Table 5.

X	*1st IP* eV	*Atomic mass* g mol^{-1}	*Thermal conductivity** mW m^{-1} K^{-1}	*Specific heat capacity*** J mol^{-1} K^{-1}
He	24.48	4.0	141.8	20.8
Ne	21.56	20.2	46.0	20.8
Ar	15.76	39.9	16.9	20.8
Kr	14.00	83.8	8.7	20.8

Table 5: Properties of some noble gases, * measured at 0 °C and 1 atm, ** at 25 °C (Hwang *et al.*, 2005). IP = ionization potential.

The way in which these physical attributes affect the plasma is likely to be complex but some general hypotheses can be made, mostly involving the efficiency of energy and momentum transfer between the inert-gas atoms and hydrogen. There will be efficient transfer of energy between species of similar mass, *i.e.* between hydrogen and helium, and thus mixtures of these gases will result in large diffuse plasmas where the power is evenly distributed. Conversely, the exchange of energy and momentum through collisions between hydrogen and krypton are likely to be less efficient and will cause the plasma to be more localised within the reactor. The behaviour of Ne and Ar will naturally fall somewhere between these two extremes. Similar arguments can be derived from the range of thermal conductivities which, basically, map the same trends in heat conduction through collision with neighbouring atoms. Larger thermal conductivities will cause more efficient spreading of the heat and more uniform, diffuse plasmas where energy is quickly transferred from the hot plasma centre to the periphery. Thus, we expected larger, cooler plasmas for the He/H_2 system and denser, hotter Kr/H_2 plasmas. As well as being larger in volume, He/H_2 plasmas were expected to be more stable due to the higher IP of He and to lack the propensity to form secondary plasmas or regions of instability at, for example, the substrate edge associated with low-IP Ar and Kr systems.

Diamond films were prepared in the 2.45 GHz MWCVD reactor used in the previous work with an inert-gas-rich mixture with $\chi_0(CH_4)$ ~ 0.07 and $\chi_0(H_2)$ ~ 0.01-0.03 to stabilize the system. The first films were grown with X = Ar making up between 0.93-0.98 (with a balance of H_2 at a constant F_T) of the gas composition flowing into the reactor. Argon was then substituted for the other inert gases in turn (He, Ne and Kr, all 99.99% pure). $F(CH_4)$ was kept constant at 5 sccm which corresponded to $\chi_0(CH_4)$ = 0.005-0.008 depending on the actual F_T used. As predicted, the physical properties of the inert gases manifested themselves in plasmas of markedly different size, shape and temperature. For constant p and P, a decrease in the size of the visible plasma ball was observed from He to Kr. Similar trends were reported for changes in plasma stability where He-based plasmas required little or no H_2 to be added in order to strike or maintain the discharge. Conversely, the Kr system required $\chi_0(H_2) \sim 0.03$ in order to initiate the plasma without formation of secondary plasmas around the chamber or becoming unstable. This has an immediate influence on diamond deposition because plasmas of varying volume (V_p) have different power densities ($Q \sim P/V_p$) and substrate temperatures (T_{sub}) for each inert-gas system. Consequently, the reactor pressure, p, and MW power, P, had to be located at values which resulted in suitable T_{gas} and T_{sub} to sustain diamond deposition. General trends can be seen in the following table which displays the ranges of parameters used to successfully deposit NCD films.

X	p Torr	P kW	T_{sub} K	$\chi_0(X)$	$\chi_0(H_2)$	$\chi_0(CH_4)$	G µm h^{-1}	$<d>$ nm
He	280-310	1.2-1.4	790-870	0.964-0.981	0.016-0.031	0.005	0.17	40-70
Ne	340-360	0.6-0.7	790-820	0.955-0.956	0.038	0.006-0.007	0.18	35-65
Ar	150-200	0.5-0.7	750-900	0.935-0.987	0.006-0.031	0.005-0.008	0.17-0.5	15-35
Kr	170	0.5	910-930	0.96-0.962	0.032	0.006-0.008	0.5-0.8	15-35

Table 6: Process conditions p, P, T_{sub} and gas composition as fraction of F_T which are suitable for forming NCD films by MWCVD. The observed growth rate, G, and average crystallite size, $<d>$, are also reported.

Some inconsistencies appear in the table of experimental details, including the higher-than-expected pressures of 340-360 Torr for the Ne plasmas due to the decision to only increase the MW power unless absolutely necessary. Therefore, P is similar for the three heavier inert gases, Ne, Ar, Kr, and only needed increasing for the He case where even at 300 Torr the plasma was still not heating the substrate enough for successful film deposition – necessitating the increase in P to between 1.2 and 1.4 kW. Conversely, these values would not be possible in the Ar or Kr systems as the plasma quickly become too large and unstable at higher P. It should be noted that T_{sub} values for all these plasmas are lower than observed in H_2-rich plasmas. While the lower P will have some influence on this, the substrate heating is generally less effective in the inert-gas plasmas compared with typical MCD-forming environments.

It should be noted that a greater number of films were grown using Ar and He as the main plasma constituent and a larger range of parameters was able to be tested. In particular, a broader range of $\chi_0(H_2)$ is expected for the Ne system where experiments were limited to variation in P and p. Also, due to the large and complex parameter space, where one variable often has an influence on another, it is possible that NCD deposition is possible outside the bounds listed in Table 6.

3.3.4 Film morphology & Growth rate

Within the ranges explored, NCD morphologies, where the average crystal size <100 nm, were obtained in all inert gases used with only slight variation in film texture displayed in SEM images taken of the deposited films (Figure 3.21). A noticeable reduction in crystallite size is apparent from these images working down the group from He to Kr while some longer range structure appears for the Ar and Kr grown films. In these cases, crystallites of the order ~20 nm diameter are arranged into elongated ellipsoidal domains with longest dimensions of ~100 nm. Aggregation into these domains has been observed previously in UNCD deposition although their formation mechanism remains unclear (Williams *et al.*, 2006, Williams *et al.*, 2008).

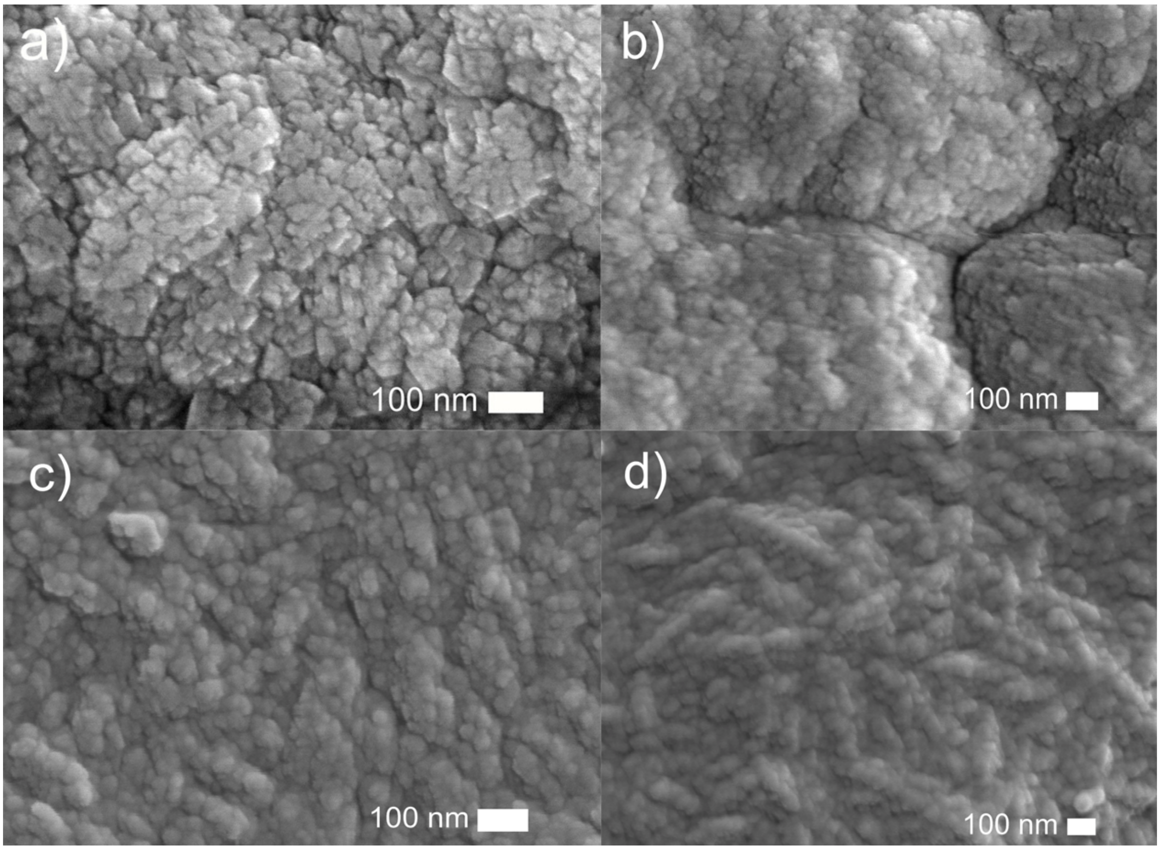

Figure 3.21: SEM images showing the surface morphology of NCD films grown in four different inert-gas mixtures: (a) He, (b) Ne, (c) Ar and (d) Kr using conditions described in Table 6.

Growth rates were determined by cleaving the samples and observing a cross-section of the film using SEM to provide an average film thickness. It is immediately apparent (Table 6) that growth rates, *G*, are an order of magnitude or more lower here than in the case of MCD deposition, with variation between slower deposition (~0.2 μm h^{-1}) in the larger, cooler He-based plasmas and more rapid growth in the hotter Kr plasmas (~0.6 μm h^{-1}). Overall, however, there is little variation in both morphology and deposition rate between all four inert gases used once the power/pressure ratio had been adjusted, indicating a shared diamond deposition mechanism. Any slight deviation is most likely due to the change in both T_{sub} and the rates of H-atom adsorption and recombination at the substrate surface because these will be the main source of substrate heating by the plasma (Yarbrough *et al.*, 1992).

3.3.5 Raman analysis of NCD films

Observed trends in diamond crystal size find correlation in UV-Raman spectra taken of films which show strong resonances due to the sp^2-carbon-related bands at ~1380 cm^{-1} and ~1570 cm^{-1}. Comparison should be made between these spectra and those made from MCD films in section 3.2 which are dominated by the sp^3 diamond peak. A decrease in the 1332 cm^{-1} sp^3 peak relative to the sp^2 bands was observed, corresponding to a reduction in the crystallite size and a parallel increase in the proportion of grain boundary material within the film (Figure 3.22).

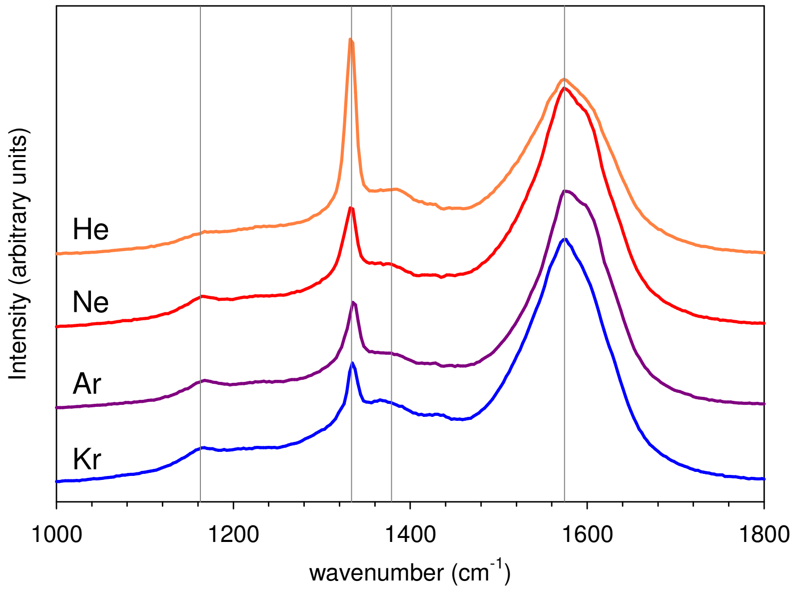

Figure 3.22: Laser Raman spectra (325 nm excitation) from films grown in X/H_2/CH_4, where X = He, Ne, Ar, Kr under process conditions listed in Table 6. The marked resonances are the 'UNCD' peak at ~1160 cm^{-1}, the sp^3 carbon peak at 1332 cm^{-1}, and the sp^2 carbon related D and G bands at ~1380 and ~1570 cm^{-1}, respectively. The spectra have been offset vertically for ease of display.

Deconvolution of the peaks in these spectra and comparison of the sp^2 and sp^3 carbon peak-height ratios (section 2.6.4) illustrates the change in crystal size even more starkly, with a significant drop in the $I(sp^3)/I(\mathrm{D})$ ratio moving down the group from He to Kr. Similarly, there is an increase in the $I(\mathrm{UNCD})/I(sp^3)$ ratio over the same range that would indicate an increase in grain boundary material associated with a smaller average crystallite size.

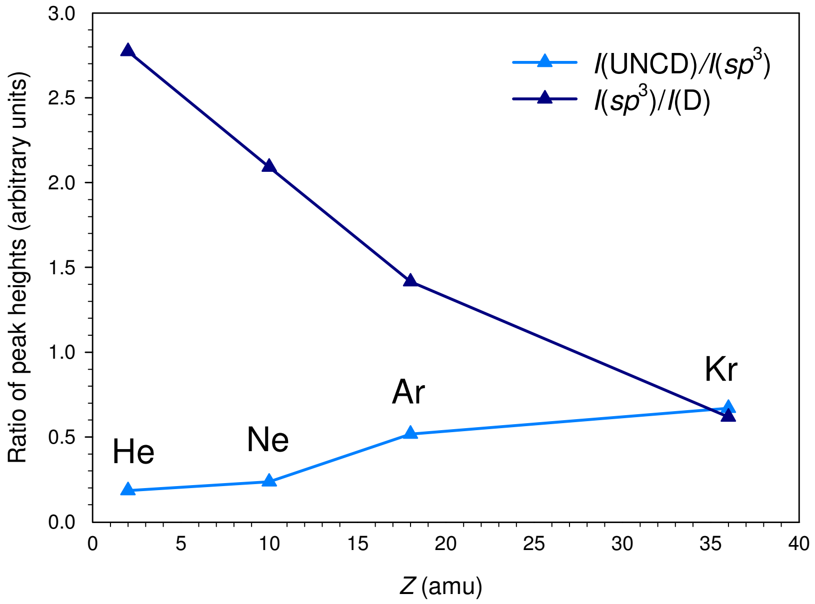

Figure 3.23: Ratios of selected peak intensities in UV-Raman spectra shown in Figure 3.22.

3.3.6 Optical appearance & Emission spectroscopy

As we have seen, the large increases in atomic mass and electron count down the group from He to Kr lead to differences in the plasmas because these parameters determine the diffusion, collisional quenching, electron excitation and heat transfer within the discharge. Visually, these are observed as changes in the size, colour and brightness of the plasma, but also in variation in T_{sub} and emission spectra. When a carbon source – CH_4 unless otherwise stated in this work – is present in the high $\chi_0(X)$ plasma it shows a characteristic intense bright green/white colouration, mainly due to the Swan emission bands of electronically excited C_2 radicals in the centre of the plasma. The band corresponds to the transition $d^3\Pi_g - a^3\Pi_u$ and is centred at 516 nm ($\Delta v = 0$) with additional vibrational structure visible at longer ($\Delta v = -1$ & $\Delta v = -2$) and shorter ($\Delta v = +1$ & $\Delta v = +2$) wavelengths (where $\Delta v = v' - v''$). Together these transitions roughly fill the entire visible spectrum of the emitting plasma, and with high power density or carbon fraction are often so intense that the plasma appears as a near-white continuum.

A rough indication of the plasma size and colour can be obtained from the colour photographs taken through the front window of the reactor in Figure 3.24. As expected from the arguments given, the He-based plasmas were more diffuse, cooler and exhibited weaker emission intensities for all species measured. He/H_2 discharges appeared to have a dull pink colour becoming greener with increasing $\chi_0(CH_4)$ whereas Kr/H_2 plasmas – with a thermal conductivity ~20 times lower –

were smaller, hotter and showed much more intense C_2 Swan-band emission with a bright white, green discharge.

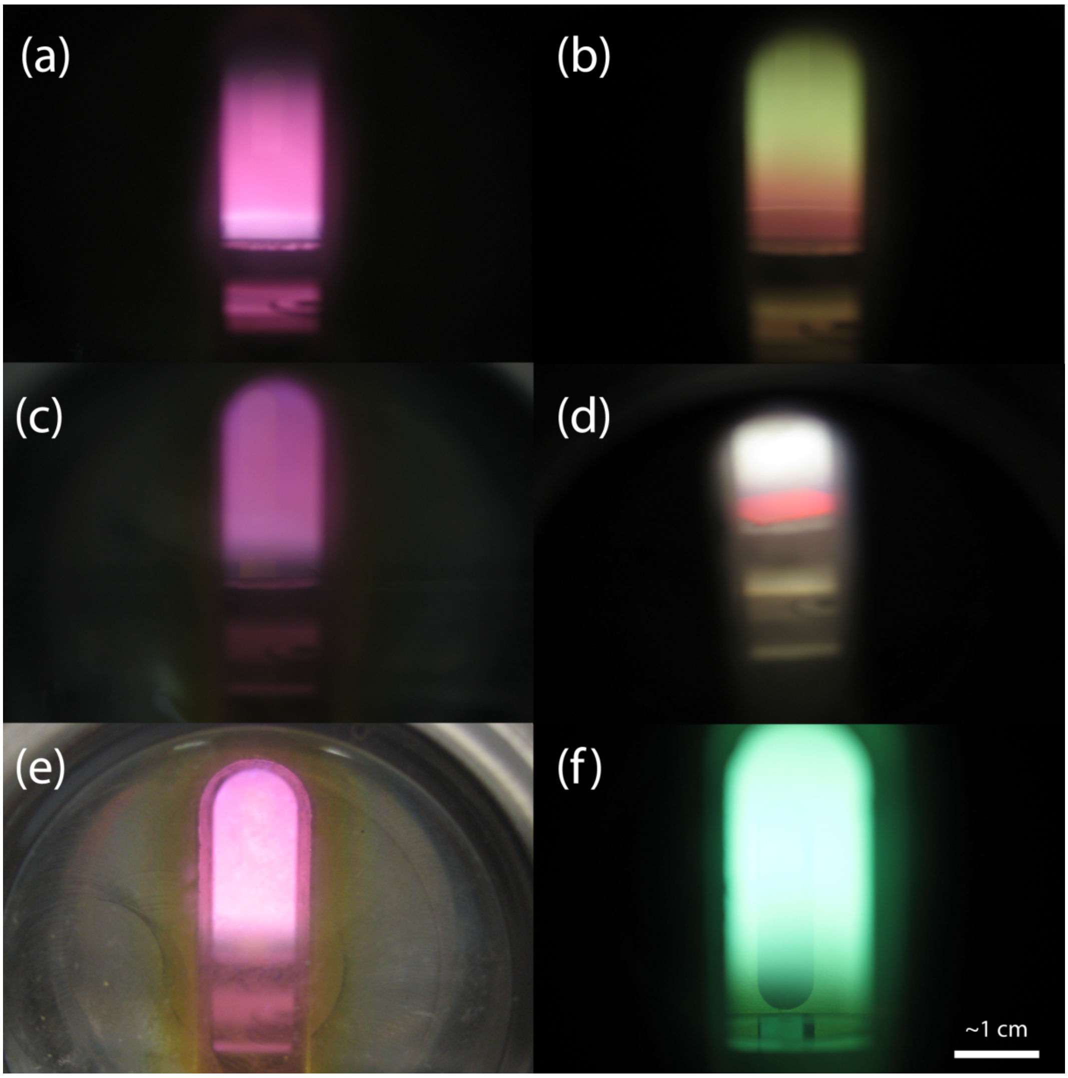

Figure 3.24: Digital photographic images of the plasma through the front viewport of the MWCVD reactor running with gas mixtures of (a) He/H_2, (b) $He/H_2/CH_4$, (c) Ne/H_2, (d) $Ne/H_2/CH_4$, (e) Ar/H_2, (f) $Ar/H_2/CH_4$.

A more detailed diagnosis of the plasma is derived from optical emission spectroscopy (see section 2.5.1) which can, in its simplest form, give us qualitative information on some of the different excited species in the plasma. To allow comparison between the inert-gas plasmas, a set of standard conditions, consisting of $P = 1$ kW, $p = 175$ Torr and $F_T = 520$ sccm, was used.

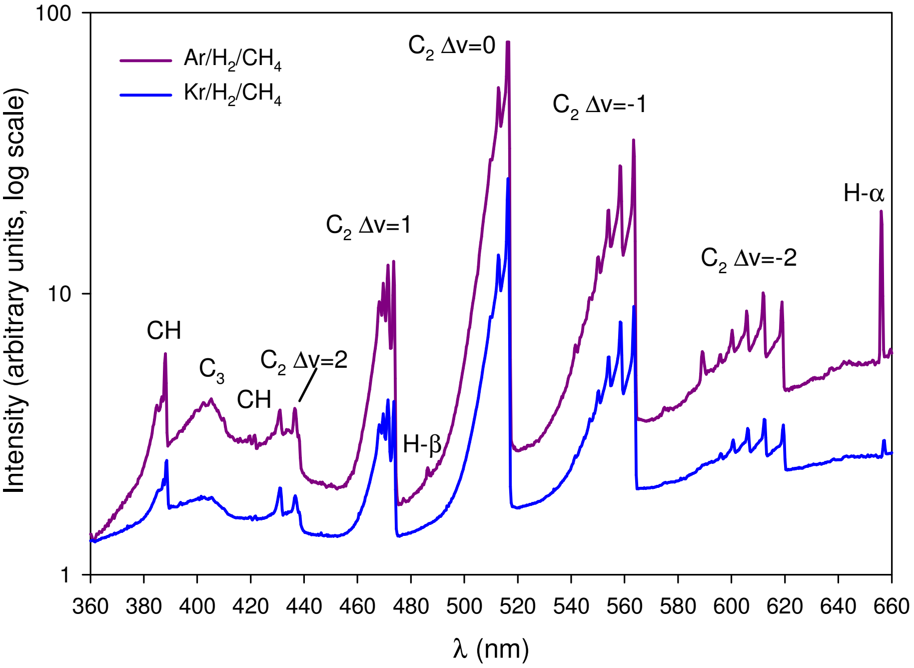

Figure 3.25: Typical OES spectra from Ar/H_2/CH_4 and Kr/H_2/CH_4 plasmas operating under standard conditions outlined in the text and comparisons should be made with the high $\chi_0(H_2)$ systems in Figure 3.1. Note that the intensities are plotted on a logarithmic scale ($\Delta v = v' - v''$).

It is possible to obtain an estimate of T_{gas} from fitting a curve to the rising baseline observed in the emission spectra based on a blackbody radiation equation (Elliott *et al.*, 2000). This background emission is attributed to solid soot particles that form in the plasma periphery and achieve local thermal equilibrium, emitting radiation as blackbodies (Hassouni *et al.*, 2006). For our set of standard conditions, P = 1 kW, p = 175 Torr, 91%X/4%CH_4/5%H_2, gas temperatures of T_{gas} = 1950 K for He, 2200 K for Ne, 2550 K for Ar and 2600 K for Kr discharges were estimated with ±100 K uncertainties due to fitting errors. This trend agrees well with the observed increase in T_{sub} between 800 K for He-based plasmas to 920 K for the Kr system. Gas temperatures at the centre of the plasma are likely to be higher than those determined from the OES spectra as will become apparent from the absorption experiments.

It is not surprising that the value of $\chi_0(CH_4)$ exerts a strong influence on the appearance of the emission spectra which are dominated by peaks from carbon-containing species labelled in the figure. The behaviour of three of these bands, C_2(d→a), C_3(A→X) and CH(A→X), to changes in $\chi_0(CH_4)$ is shown in Figure 3.26. Spectra were recorded for plasmas, at P = 1 kW, p = 175 Torr, with increasing $\chi_0(CH_4)$ = 0-0.04 and keeping a constant F_T, by corresponding reduction in $\chi_0(H_2)$. The relative intensities between the He- and Ar-dominated plasmas are in agreement with previous studies using a co-axial blade MWCVD reactor at p = 90 Torr, P = 2.1 kW (Rabeau *et al.*, 2004). Common behaviour is observed between the two studies which show higher C_2

intensities in the Ar/H_2/CH_4 system but higher atomic H emission in the He/H_2/CH_4. We will return to this issue after discussion of the absorption spectroscopy measurements of the absolute column density of H(n = 2).

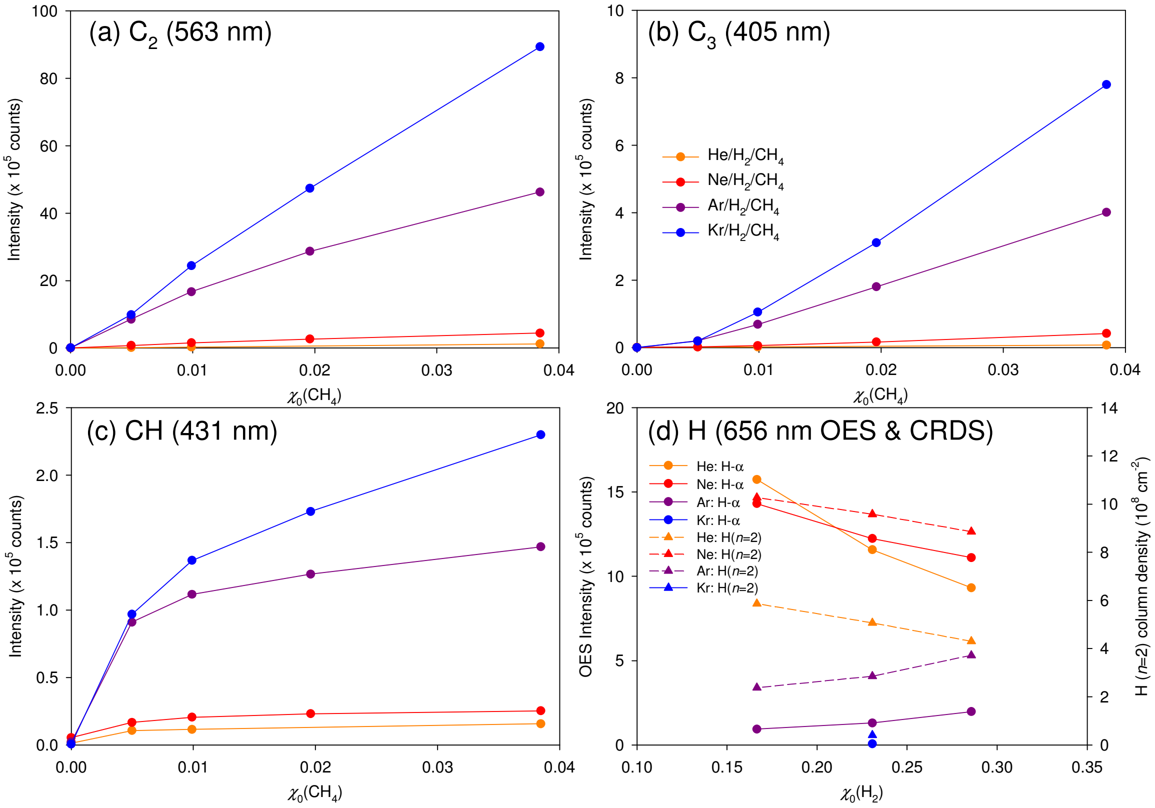

Figure 3.26: Dependence of (a) C_2(d→a, 563 nm), (b) C_3(A→X, 405 nm) and (c) CH(A→X, 431 nm) emissions on $\chi_0(CH_4)$ measured by OES for each inert-gas plasma at p = 150 Torr & P = 1 kW, using a gas mixture of $(93-x/2)\%X/(5-x/2)\%H_2/x\%CH_4$. (d) shows the excited H-atom densities in the plasma probed by two methods: (i) CRDS-measured H(n = 2) column densities (▲) and (ii) OES-measured H-α emission intensity (●) as a function of $\chi_0(H_2)$ for a similar plasma at p = 175 Torr & P = 1 kW. The balance for $\chi_0(H_2)$ is made up with χ_0(X) and $\chi_0(CH_4)$ was kept constant for the H-atom measurement.

Although not the strongest transition, the peak plotted for the C_2 radical is the $\Delta v = -1$ band head at 563 nm and shows a roughly linear proportionality, where $I_{C2} \sim \chi_0(CH_4)$. Slightly different dependency is exhibited by the CH(A→X) band (at 431 nm), which obeys the relationship $I_{CH} \sim (\chi_0(CH_4))^{0.5}$, and the C_3(A→X) band (centred at 405 nm), which rises as $I_{C3} \sim (\chi_0(CH_4))^{1.5}$. In each case I_X gives the intensity of the band in question but is not calibrated to any specific unit scale. These trends mirror those observed for the MCD depositing H_2-rich plasmas (Ma *et al.*, 2008, Mankelevich *et al.*, 2008) and are explained by the presence of C_2H_2 as the most abundant hydrocarbon species in much of the plasma apart from the hottest part of the core. Equilibrium between the various C_1H_x and C_2H_y hydrocarbon species and C_2H_2 gives rise to a linear dependency for C_2H_y fragments and a near square-root relationship for C_1H_x species, such as CH. Similar arguments can be made for the C_3 radical based on modelling which shows that the dominant production and loss mechanisms are:

$$\mathrm{C} + \mathrm{C_2H_2} \leftrightarrow \mathrm{C_3} + \mathrm{H_2} \tag{3.1}$$

$$\mathrm{C} + \mathrm{C_2H} \leftrightarrow \mathrm{C_3} + \mathrm{H} \tag{3.2}$$

$$\mathrm{C_2} + \mathrm{C_3} \leftrightarrow \mathrm{C_3} + 2\mathrm{C} \tag{3.3}$$

Combined in equilibrium these provide the $(\chi_0(\mathrm{CH_4}))^{1.5}$ dependence observed in the emission spectroscopy.

3.3.7 Absorption Spectroscopy I

Although emission studies can be very useful for qualitatively indicating relative changes in different species concentrations within the gas plasma, more detailed information on absolute values within the reactor can be obtained from absorption studies and cavity ring-down spectroscopy (CRDS) in particular (see section 2.6.2). The CRDS of inert-gas-rich plasmas was divided into two experiments, with the first consisting of H(n = 2) column-density measurements in plasmas using each of the four noble gases investigated in the emission and diamond deposition studies. Later studies concentrated just on Ar-based plasmas but measuring three important species in the plasma, CH, C_2 and H(n = 2), as well as covering a much larger parameter space, including variation in P, p, χ_0(X), and $\chi_0(\mathrm{CH_4})$. This in-depth study was carried out with James Richley in the Bristol Diamond Group and is discussed in section 3.3.9.

In the first experiment, the main variable was $\chi_0(\mathrm{H_2})$ which was varied between 0.17-0.28 balanced with the inert gas fraction, χ_0(X), and a constant $\chi_0(\mathrm{CH_4})$ = 0.005. To achieve these conditions, at the standard P = 1 kW, p = 175 Torr, there was a limit of $\chi_0(\mathrm{H_2})$ = 0.17 (*i.e.* χ_0(X) = 0.825) as the plasma became either too unstable within the reactor or too opaque to make accurate measurements. For comparative purposes, emission spectra were also taken at each point and the trends in the H-α line at 656 nm agree well with the H(n>1) results from CRDS.

Different behaviour is apparent for each of the noble-gas plasmas investigated with He- and Ne-rich mixtures showing similar trends. For these mixtures the H(n > 1) column densities (and H-α emission intensities) increase with χ_0(X), although more steeply for the Ne plasma. For the Ar-based system the opposite trend was observed in both absorption and emission. Oddly, only negligible excited H atoms could be detected in the Kr-based plasma, a result confirmed by the emission results which also show the H-α transition to be absent. To explain such behaviour requires some knowledge of the gas-phase reactions and will be discussed in conjunction with computation simulations in the next section.

3.3.8 Modelling of $Ar/H_2/CH_4$ and $He/H_2/CH_4$ plasmas

Computational modelling of two of the plasmas used in this study was performed by Yuri Mankelevich, Moscow State University, using the parameters described in section 1.4.3 for the Ar system and an analogous set of reactions for the He plasma. Much of the discussion which follows comes from dialogue between the Bristol-Moscow partnership.

It was important to focus on a set of standard plasma conditions for the simulation as it would be too computationally demanding to model the entire parameter space. As the regimes important for nanocrystalline diamond deposition in Ar or He systems are quite different two 'base' conditions were modelled: p = 170 Torr, P = 0.7 kW, T_{sub} = 873 K, F_{T} = 510 sccm for a $0.5\%CH_4/1\%H_2/98.5\%Ar$ mixture; and p = 300 Torr, P = 1.3 kW, T_{sub} = 873 K, F_{T} = 510 sccm for a $0.5\%CH_4/1\%H_2/98.5\%He$ mixture. These values were chosen as roughly average for NCD deposition in the MWCVD reactor in each inert gas. Another important factor is the size of the plasma ball which was determined by viewing through the various ports on the reactor and comparing the size with known dimensions within the chamber. Spatial OES measurements also provided information on the height of the cylindrical plasma region (h) as the peak in emission intensity would correspond to the plasma centre. While there is likely to be some error in these values, the diameter (d) and height (h) were taken as d ~ 90 mm and h ~ 50 mm for the Ar plasma and d ~ 70 mm and h ~ 35 mm for the He case with the plasma radially symmetric about a central axis. The smaller values for the He system are a result of the higher pressure compressing the plasma into a smaller volume – a requirement to achieve the T_{sub} necessary for diamond deposition.

In Figure 3.26d we see the different behaviour in the H(n = 2) column densities measured in different noble-gas-rich plasmas by CRDS. Understanding of how the excited levels of H atoms are populated can explain these trends. The concentration of excited-state H, [H(n > 1)], depends linearly on the concentration of ground state atoms, [H(n = 1)], and on electron density and temperature, n_{e} and T_{e}, respectively (Ma *et al.*, 2008):

$$[\mathrm{H}(n > 1)] \sim k_n n_e [\mathrm{H}(n = 1)] \tag{3.4}$$

The factor k_n is the excitation-rate coefficient which depends on the concentration of high energy electrons (ε > 10 eV) which constitute the 'tail' of the eedf curve. We can approximate the rate coefficient to be a function of the electron temperature, T_e and T^*, the 'temperature' or magnitude of the eedf tail (Shkurenkov *et al.*, 2008). If $\chi_0(H_2)$ is increased, for a given power density, $Q \sim P/V_p$, there will, naturally, be an increase in [H(n = 1)] but also a decrease in T_e due to the electron energy losses in low-threshold processes, such as vibrational and rotational excitation. These loss mechanisms are specific to molecular gases and will manifest themselves in a reduction in T_e if either $\chi_0(H_2)$ or $\chi_0(CH_4)$ is increased for a given plasma, assuming other parameters are constant. By the same arguments, inert-gas-rich plasmas will have higher T_e than those where H_2 makes up the major constituent of the gas mixture added to the reactor. The influence of $\chi_0(H_2)$ on T^* is more complex but is thought not to vary significantly given the electron densities required for absorption of the input MW power. If there was a large change in T^* with $\chi_0(H_2)$ then we might expect to see greater changes in the absorption and emission intensities in the interval studied (Figure 3.26).

The simulation produces electron, T_e, and maximum gas temperatures (*i.e.* at the plasma centre), $T_{gas,max}$ for each inert-gas plasma, with corresponding values for the H_2-dominated MCD system:

X	*mixture*	*p* Torr	*P* kW	T_e eV	$T_{gas,max}$ K
NCD:He	0.5%CH_4/1%H_2/He	300	1.3	**2.23**	**3220**
NCD:Ar	0.5%CH_4/1%H_2/Ar	170	0.7	**2.74**	**3550-3600**
MCD	4.4%CH_4/7%Ar/H_2	150	1.5	**1.28**	**2926**

Table 7: Model outputs for electron and gas temperatures for different inert-gas-based plasma systems and the MCD plasma (Ma *et al.*, 2008).

We see that these fundamental properties for the He plasma fall between the lower T_e and T_{gas} MCD plasma and the higher temperature Ar-rich plasma. In the He case, elastic collisions with the lightweight He atoms play an important function in the plasma energy balance, similar to the role of rovibrational excitation of H_2 in the MCD conditions. Despite the apparent similarities between the He and H_2 plasmas, delving further into the physics allows a much starker comparison to be made. The key is to recognize some degree of partitioning of various plasma processes within the reactor: we find that many are spatially dependent. In particular, important power absorption pathways were modelled at the substrate surface (z = 0.5 mm) and at the plasma centre for the He- and Ar-dominated gas mixtures allowing the partitioning of the input power to be estimated. Results show that the local power density, Q, is at a minimum in the plasma centre due to dissociation into atomic species and the resultant lack in molecular species. Conversely, Q is maximal at the substrate surface where the lower T_{gas} and surface reactions results in reformation of molecular species. Integrating over the entire plasma volume, the input power is partitioned into three main pathways:

X	*p* Torr	*P* kW	*1.Gas heating* %	*2. Radiation losses* %	*3.Chemical activation* %	*Chemical activation* W
NCD:He	300	1.3	**~88.5**	**~5.1**	**6.4**	**83**
NCD:Ar	170	0.7	**~61.3**	**~25.0**	**13.7**	**96**

Table 8: Model estimates of the partitioning of input power into different processes integrated over the plasma volume (Fox *et al.*, 2009).

Heating of the gas within the plasma can either be direct, through elastic losses, or indirect, through rovibrational relaxation. What we find is that the power expended in chemical activation – the part which is important for diamond deposition – is similar in both He and Ar plasmas (~83 W and 96 W, respectively) despite the difference in input power. It is for this reason that the optimization of P and p was necessary to locate the regime where diamond deposition was possible. Overall, at these optimized values, the He and Ar plasmas are more similar than first thought based on the T_e and T_{gas} outputs – at least in terms of diamond deposition. More detailed descriptions of the various plasma processes have been reported (Fox *et al.*, 2009).

Other aspects of the behaviour seen in the CRDS measured H(n = 2) results can be explained by the existence, or absence, of excited energy levels of the inert gas, X*, near the energy level of excited H atoms. Collisions between species with excited states at similar energies can induce changes in the eedf and the respective populations of these states.

X	*Excited states* eV
He	19.82 – 24.48
Ne	16.62 – 21.56
Ar	11.55 – 15.76
Kr	9.9 – 14.0
H(n = 2)	10.2
H(n = 3)	12.1

Table 9: Excited-state energy levels for the inert gases and atomic hydrogen.

From the data in the table we notice that only Kr has possible states which are close in energy to those of excited atomic H. This can explain the lack of the H Balmer series in the OES spectrum of Kr/H_2 plasmas, and that they are very weak once CH_4 is added. The decrease in H(n = 2) column density from He to Kr measured by CRDS will, mainly, be due to the increased collisional quenching of states similar in energy. Indeed, in the case of Kr plasmas, a number of reactions can be identified for which the energy mismatch, ΔE, is small between excited H species and ground-state Kr atoms:

$$\mathrm{H}(n=2)+\mathrm{Kr}(4p^6)\rightarrow\mathrm{H}(n=1)+\mathrm{Kr}(4p^5 5s^1)\quad \Delta E=-0.17\ \mathrm{eV} \tag{3.5}$$

$$\mathrm{H}(n=3)+\mathrm{Kr}(4p^6)\rightarrow\mathrm{H}(n=1)+\mathrm{Kr}(4p^5 5p^1)\quad \Delta E=0.01\ \mathrm{eV} \tag{3.6}$$

This series continues for H($n > 3$) and, together, will provide an efficient route for depopulating the excited states of H. Such pathways are not accessible to the lighter inert gases where their excited states fall too high in energy.

As well as providing important insights into the plasma physics, the model reports predicted concentrations of the various stable and radical species occurring at z = 0.5 mm above the substrate surface.

X	Ar	He
T_{gas} / K	1306	1193
Species	Number density / cm^{-3}	
X	1.23×10^{18}	2.38×10^{18}
H	3.42×10^{15}	2.57×10^{15}
H_2	1.99×10^{16}	4.03×10^{16}
CH_4	2.07×10^{11}	1.52×10^{13}
CH_3	1.27×10^{11}	3.06×10^{12}
CH_2	2.35×10^{9}	1.75×10^{10}
CH	1.54×10^{9}	3.32×10^{9}
C	4.69×10^{11}	1.11×10^{11}
C_2	1.21×10^{11}	1.25×10^{10}
C_2H	1.39×10^{12}	6.04×10^{11}
C_2H_2	2.17×10^{15}	5.43×10^{15}
C_3	4.39×10^{14}	2.95×10^{14}
C_3H_2	8.94×10^{13}	2.88×10^{14}
C_4H_2	1.26×10^{14}	2.44×10^{14}

Table 10: Calculated gas temperature T_{gas} and species concentrations at z = 0.5 mm above the centre of the substrate derived from 2-D modelling of a 0.5%CH_4/1%H_2/Ar plasma operating at p = 170 Torr, P = 0.7 kW and 0.5%CH_4/1%H_2/He plasma operating at p = 300 Torr, P = 1.3 kW. F_T = 510 sccm and T_{sub} = 873 K in both cases.

Further modelling after completion of the second CRDS experiments allowed comparison with the MCD conditions, while here the important concentrations are those of CH_3 and C which are expected to contribute to NCD deposition. However, these values should be treated with some caution as calculated growth rates due to these species – $G_C = 0.033$ μm h^{-1} and $G_{CH3} = 0.001$ μm h^{-1} for the Ar plasma & $G_C = 0.001$ μm h^{-1} and $G_{CH3} = 0.03$ μm h^{-1} for the He plasma – are nearly an order of magnitude lower than experimentally measured values, $G \sim 0.15$–0.5 μm h^{-1}. The growth rates quoted, based on reported algorithms (May & Mankelevich, 2008), do show a change in emphasis away from a CH_3 mechanism and an enhanced role for the C, although it is not certain how accurate this result is. A possible reason for this discrepancy may be the predicted abundance of C_3 (and higher) species which might be due to unreliable kinetic rate data leading to an overestimate of the conversion of C_1 species into C_3H_x and C_4H_x fragments. In each case, the sum of the concentration of C_1H_x (x = 0-3) species exceeds the C_2 density even if it is present at a higher density in these NCD depositing plasmas compared with standard MCD growing environments.

3.3.9 Absorption Spectroscopy II

So far CRDS had only been used to measure the H(n = 2) column densities while for high $\chi_0(H_2)$ systems CH(X, v = 0) and C_2(a, v = 0) radicals have also been probed (Ma *et al.*, 2008). Therefore, the next step was to apply this sensitive absorption method to inert-gas-rich plasmas and achieve spatially resolved column densities for a range of process parameters. Due to the amount of measurements which would need to be made (and our earlier findings which showed that diamond CVD did not differ between gases) it was decided to focus only on argon-based plasmas. In the next few sections we look deeper into the high-χ_0(Ar) plasmas and our understanding of the physics which underpins these thermally dominated discharges.

3.3.9.1 Trends with process conditions

Beginning with the optical appearance of the plasmas, we see distinct changes as Ar is substituted for H_2 as can be seen in the progression of digital photographs taken through the front viewport (*i.e.* perpendicular to the CRDS laser axis) in Figure 3.27 without methane and Figure 3.28 with methane. Both situations show the luminous part of the plasma increases in volume and intensity with increasing χ_0(Ar).

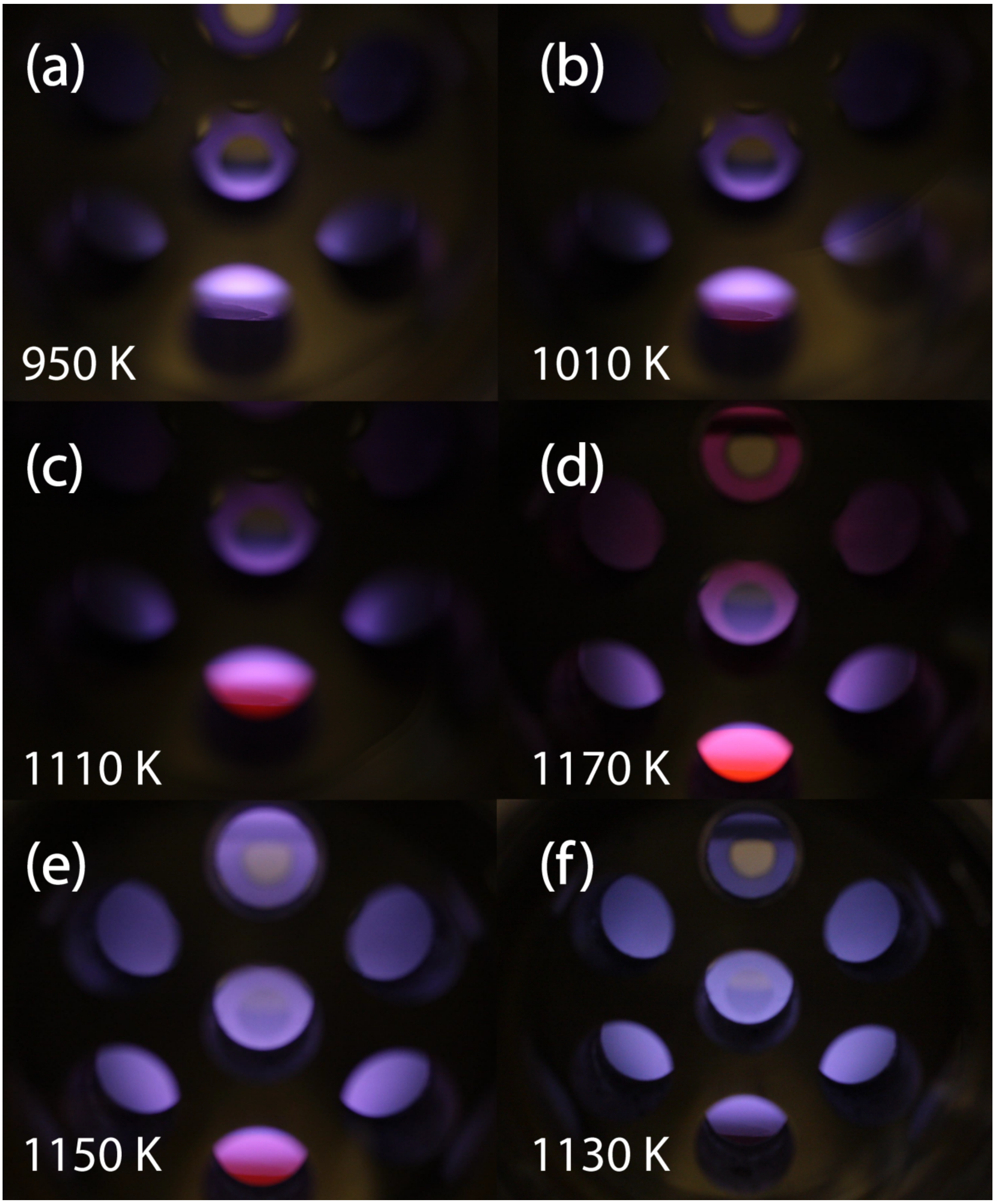

Figure 3.27: Digital photographs of H_2/Ar plasmas where $F(H_2)/F(Ar)$ = (a) 500/40, (b) 400/140, (c) 300/240, (d) 200/340, (e) 100/440, (f) 50/490 sccm and the T_{sub} recorded on the pyrometer is also shown. The expansion of the plasma volume is obvious in these images although some of the observed increase in intensity has been limited by the automatic exposure of the camera.

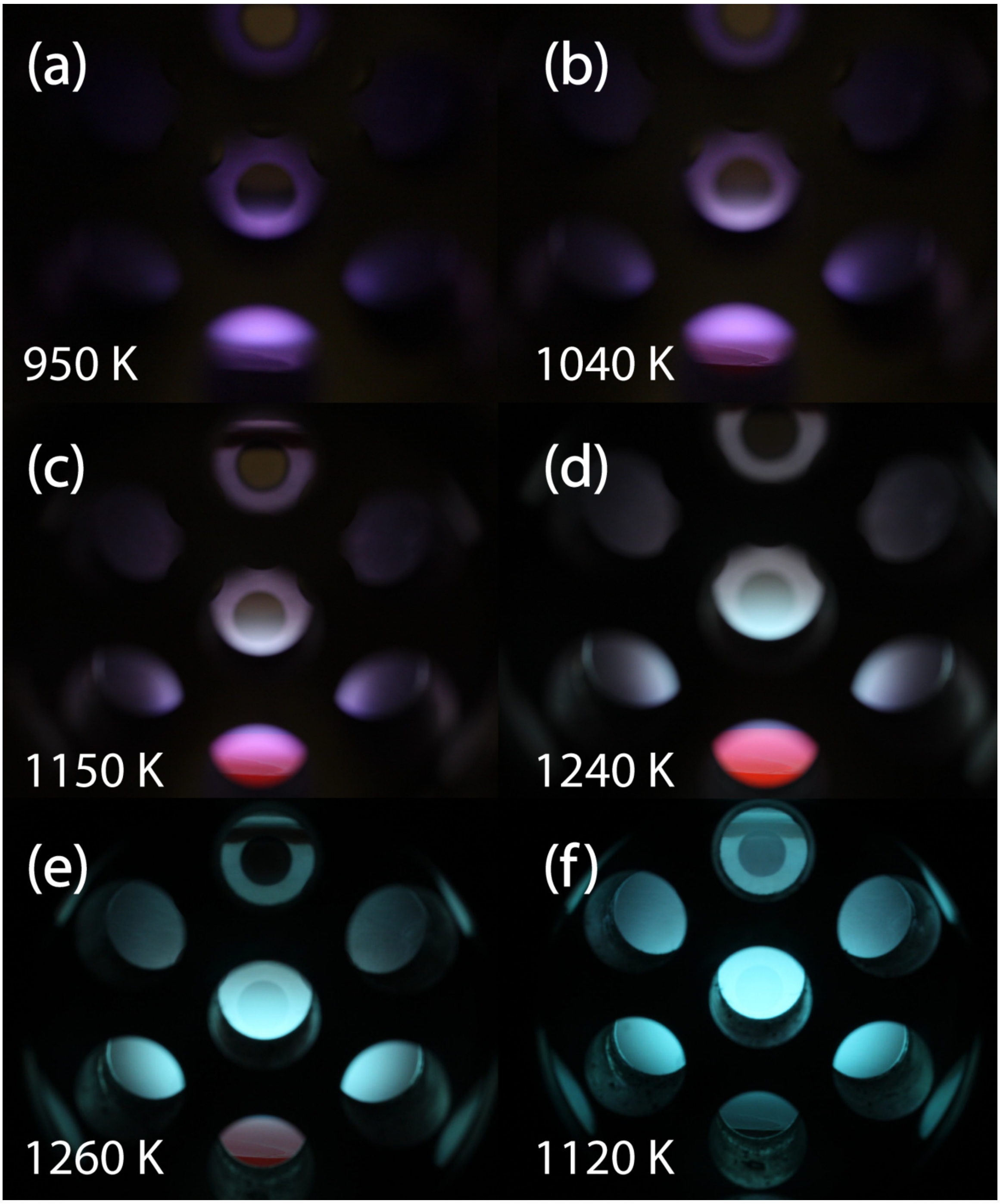

Figure 3.28: Digital photographs of $H_2/Ar/CH_4$ plasmas where $F(H_2)/F(Ar)$ = (a) 500/40, (b) 400/140, (c) 300/240, (d) 200/340, (e) 100/440, (f) 50/490 sccm, all with $F(CH_4)$ = 2.7 sccm ($\chi_0(CH_4)$ = 0.005). The T_{sub} is also recorded showing a maximum for the 100/440 mixture correlating with $T_{gas,max}$ in the computational model.

Even in the plasma where no CH_4 is added, some Swan-band C_2 emission is present at high χ_0(Ar) due to the efficient excitation of this radical in these systems and, possibly, the increased etching of carbon material from the chamber walls in the larger discharges. In the plasma with methane this C_2 emission becomes very intense (beyond the changes seen in the images as the camera uses automatic exposure settings which, naturally, become shorter) at high χ_0(Ar). Also recorded, using the pyrometer, is the substrate temperature which increases up to $\chi_0(\mathrm{Ar}) = 0.81$ before decreasing at higher values.

3.3.9.2 Emission Spectroscopy

As the previous OES experiment only looked at the changing emission intensities with increasing $\chi_0(CH_4)$, and to allow direct comparison between emission and absorption measurements, new spectra were taken simultaneously with the absorption experiment which follows. The following figure shows the trends in peaks attributed to CH(A→X), C_2(d→a) and C_3(A→X) radicals (at 431.4, 516.5 and 405 nm, respectively) and to H(n = 3 and 4) atoms (at 656.3 and 486.1 nm) with changes in $\chi_0(H_2)$, $\chi_0(CH_4)$, P and p. The intensities have been normalized to their highest value to aid the analysis. We see that H-α, H-β and CH(A→X) peaks rise to maximum values at $\chi_0(H_2)$ ~ 0.1 before decreasing to lower values, while C_2(d→a) and C_3(A→X) emission continues to increase with falling $\chi_0(H_2)$. While the I(H-β)/I(H-α) ratio does not vary significantly it does not follow that there is no change in T_e with this large change in $\chi_0(H_2)$ because several plasma parameters will be changing simultaneously. Indeed, the 2D computational model predicts a drop in T_e from 2.45 eV for $\chi_0(H_2) = 0.01$ to $T_e = 1.67$ eV when $\chi_0(H_2) = 0.25$.

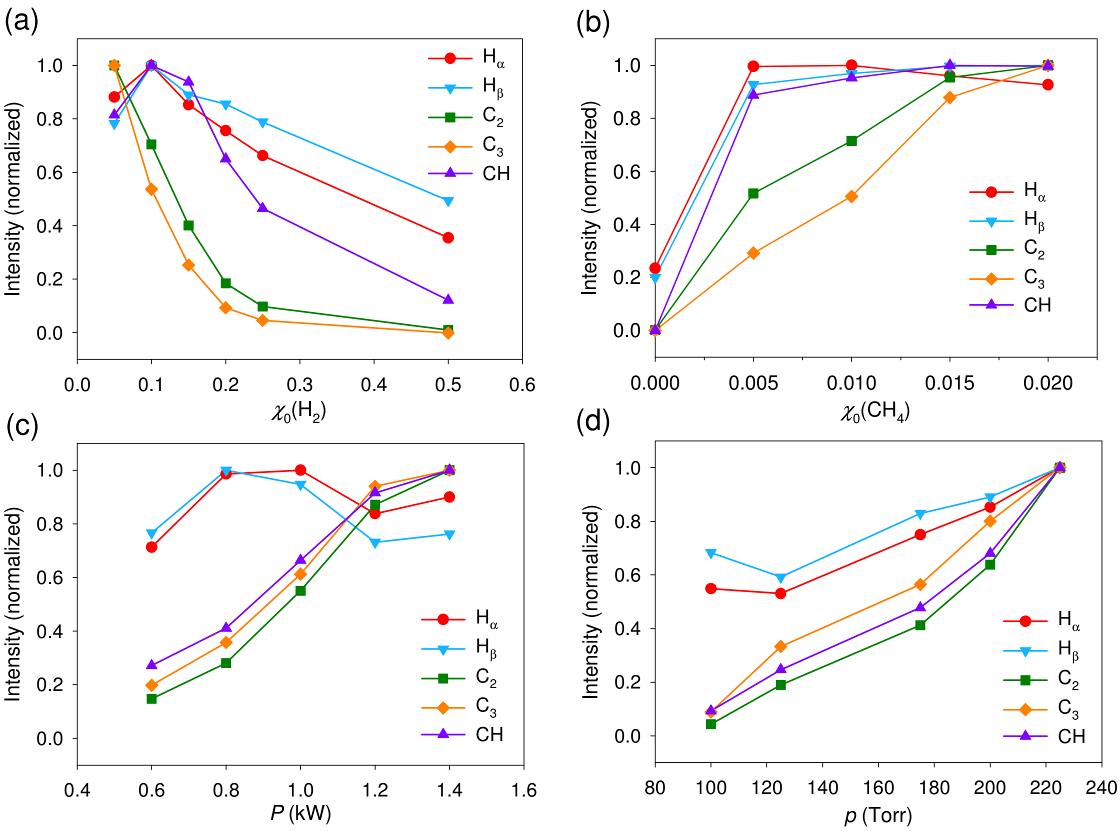

Figure 3.29: Normalized emission intensities for H-α, H-β, C_2(d→a), C_3(A→X) and CH(A→X) plotted against the experimental parameters: (a) $\chi_0(H_2)$, (b) $\chi_0(CH_4)$, (c) P and (d) p.

On addition of CH_4 a sharp rise in the H-α peak intensities is observed (Figure 3.29b) before falling away with higher $\chi_0(CH_4)$. This behaviour is explained by the complex changes in the T_e, n_e and densities of excited species, and is accurately predicted by the computational model (Ma *et al.*, 2008, Richley *et al.*, 2011). The various trends in the carbon-containing radicals correlate with our earlier findings and the explanations remain valid (section 3.3.6).

The increase in emission intensities for the C_2(d→a), CH(A→X) and C_3(A→X) peaks with P is also predicted because the higher power density will create more ground-state atomic H thereby driving the carbon-radical-formation reactions. Increasing the power density will also produce a higher n_e leading to a greater population in higher energy levels and, hence, more intense emission. Similar increases in the carbon-radical emission intensities are seen at higher p indicating their origin from thermally driven processes.

3.3.9.3 CRDS spectra & T_{gas} determinations

The CRDS spectrum of $C_2(d^3\Pi_g \leftarrow a^3\Pi_u)$ can be used to measure T_{gas} in the plasma centre by fitting the measured spectral line positions and intensities with simulations using the PGOPHER program (Western, 2011) and appropriate spectroscopic constants (Lloyd & Ewart, 1999). In Figure 3.30 comparisons can be made for part of the spectrum that depicts low-*J* R-branch transitions on the right-hand side and part of the P-branch (high-*J* transitions) on the left. The ratio of high-to-low-*J* line intensities gives us the C_2(a) rotational temperature, T_{rot}. Plotted are three experimental spectra for decreasing $\chi_0(H_2)$, or increasing $\chi_0(Ar)$ straddled by PGOPHER simulations of the same region at T_{rot} = 2000 and 3000 K.

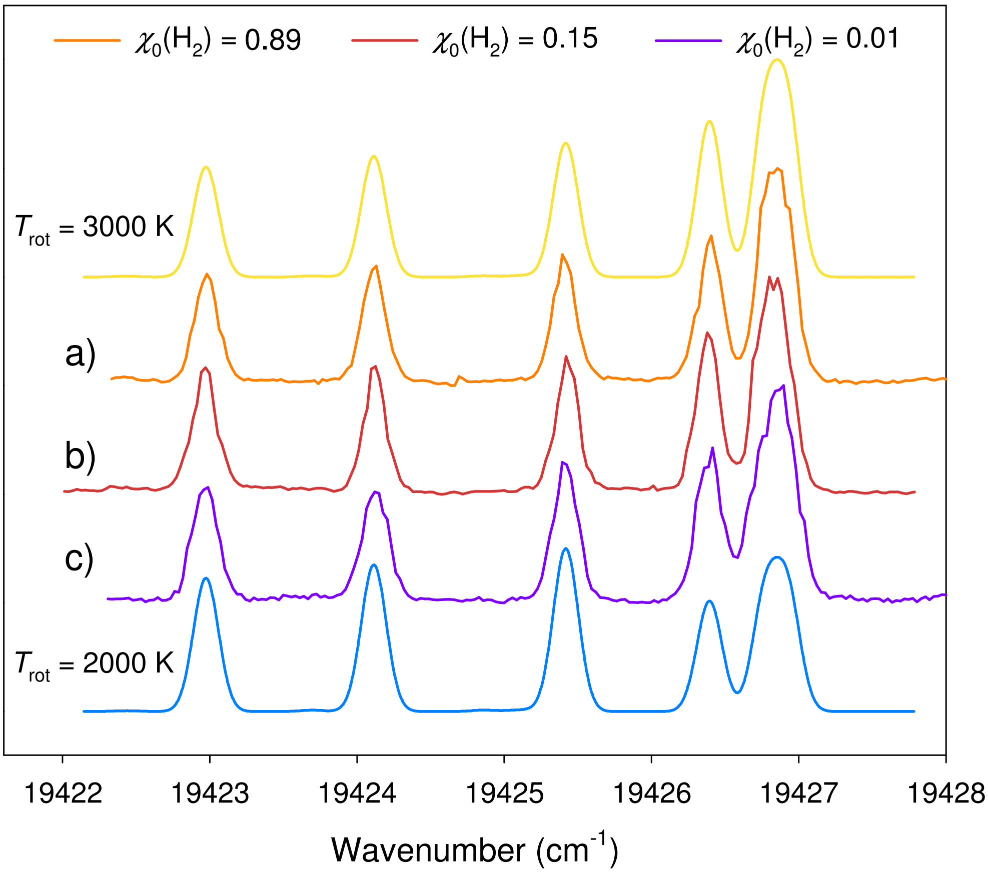

Figure 3.30: Part of the CRDS spectrum of C_2 ($d^3\Pi_g \leftarrow a^3\Pi_u$) band measured for (a) typical MCD deposition conditions (4.4%CH_4/88.6%H_2/7%Ar, p = 150 Torr, P = 1.5 kW), (b) the base conditions for the present study (0.5%CH_4/14.7%H_2/84.8%Ar, p = 150 Torr, P = 1.0 kW) and (c) UNCD deposition conditions (0.5%CH_4/1%H_2/98.5%Ar, p = 150 Torr, P = 0.5 kW). Either side of these experimentally derived results are PGOPHER simulations of same part of the spectrum at T_{rot} = 3000 K (above) and 2000 K (below).

It is obvious from these spectra that the T_{rot} does not appear to change much with increasing $\chi_0(Ar)$ and that all three empirical measurements are a better fit of the T_{rot} ~ 3000 K trace compared with the 2000 K simulation, agreeing with previous studies (Rabeau *et al.*, 2004). We can assume that T_{rot} is a good approximation for T_{gas} under these pressure conditions as the system will be in local thermodynamic equilibrium due to efficient rotational-translational energy-exchange processes. As the local T_{gas} varies greatly over the column sampled by CRDS, the high

T_{rot} values that we have measured imply that the radical species are concentrated in the plasma centre. Overall, these results show that the T_{gas} does not vary significantly with changes in the H_2/Ar ratio or plasma volume.

The CRDS-measured column densities for the atomic H (in the first excited state, H(n = 2)) and C_2 (in its first excited state, $a^3\Pi$) and CH (ground state, $X^2\Pi$) radicals are shown in Figure 3.31 as a function of process conditions together with the predicted values from computational calculations. The dramatic rise in C_2(a, v = 0) column density at lower $\chi_0(H_2)$ correlates previous experiments (Ma *et al.*, 2008) and the emission results. At $\chi_0(H_2) = 0.1$ the plasma became too large and unstable at P = 1 kW and a lower power density (P = 0.5 kW) was employed, but this still showed a steep rise in C_2(a) column density at $\chi_0(H_2)$ down to 0.01. The CH(X, v = 0) column density rises at first then reaches a maximum at $\chi_0(H_2) = 0.15$ before falling at lower $\chi_0(H_2)$ as seen in the OES results. Earlier CRDS measurements have shown rising C_2 column densities which reach a peak at $\chi_0(H_2) = 0.05$ although this could be due to the different MW reactor setup and discharge parameters (Rabeau *et al.*, 2004).

The trends with increasing $\chi_0(CH_4)$ mirror those seen in the emission experiment where the C_2(a) column density scales linearly with $\chi_0(CH_4)$ whereas the CH(X) column density rises less steeply. Similarly, the H(n = 2) column density shows a distinct rise when even small mole fractions of methane are added to the plasma. This is due to the change in the dominant ion in the plasma from H_3^+ in the H_2/Ar system to $C_2H_x^+$ (x = 2, 3) in H_2/Ar/CH_4 mixtures (and even C_3H^+ or $C_2H_x^+$ (x = 1-3) in very-low-$\chi_0(H_2)$ plasmas) which causes an increase in T_e.

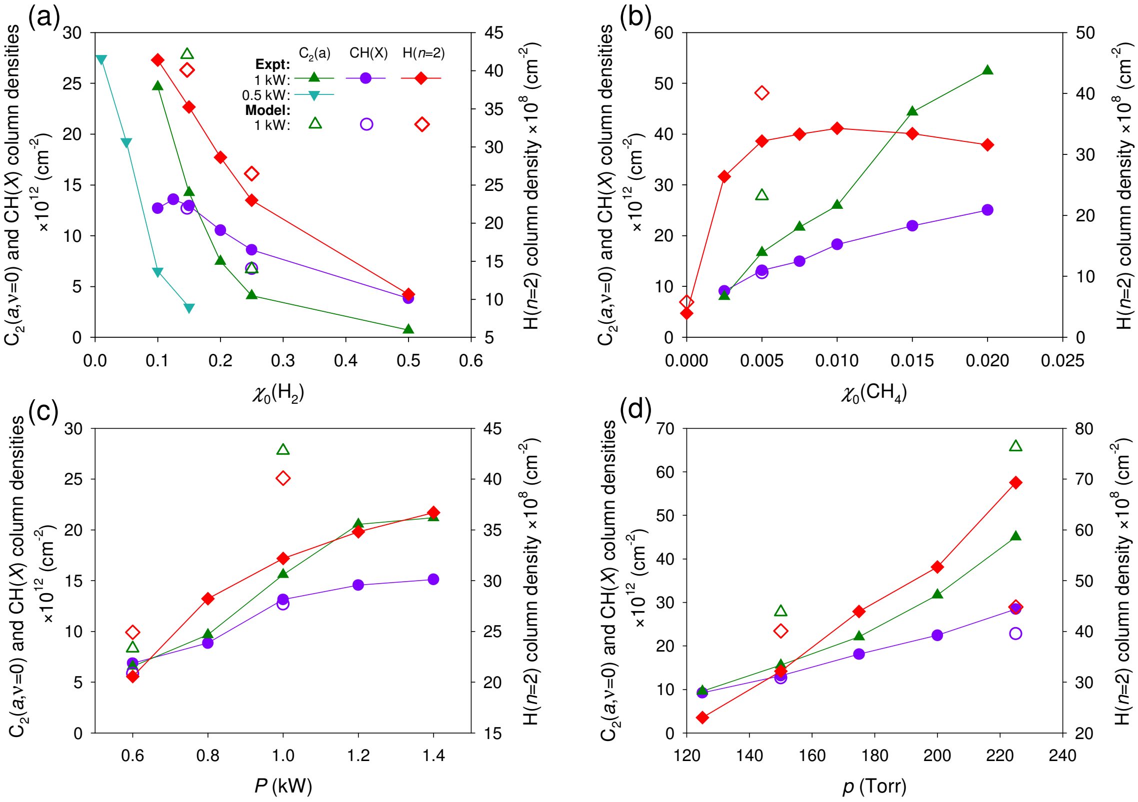

Figure 3.31: Column densities of C_2(a, v = 0) and CH(X, v = 0) radicals (left-hand scale, filled symbols) and H(n = 2) atoms (right-hand scale, filled symbols) measured at z = 9.5 mm as a function of (a) $\chi_0(H_2)$, (b) $\chi_0(CH_4)$, (c) P and (d) p. Also plotted are the corresponding quantities given by the 2D computational model (open symbols) (Richley *et al.*, 2011).

The CRDS results show increases in all the probed radical species as P and p increase and, in both cases, the rise in the C_2(a) column density is steeper relative to the other two species. The self-consistent model predictions shown in the figure, obtained by summing the number densities for the sampled column, agree well with the empirical results and in some cases overlap so they become hard to see. Only the dependence of the H(n = 2) column density on p is less well matched.

3.3.9.4 Spatial profiles

So far the column densities and emission intensities have been measured at the plasma centre (z = 9.5 mm) which tells us about the discharge chemistry but not necessarily about the species involved in diamond deposition. Spatial profiling, by translating the sampling CRDS laser or OES aperture vertically relative to the MW chamber, gives us an insight into the abundance of different species above the diamond growing surface. Figure 3.32 shows the emission intensity for C_2(d→a) and H-α measured against z for two different gas mixtures: $\chi_0(H_2) = 0.15$ and 0.01.

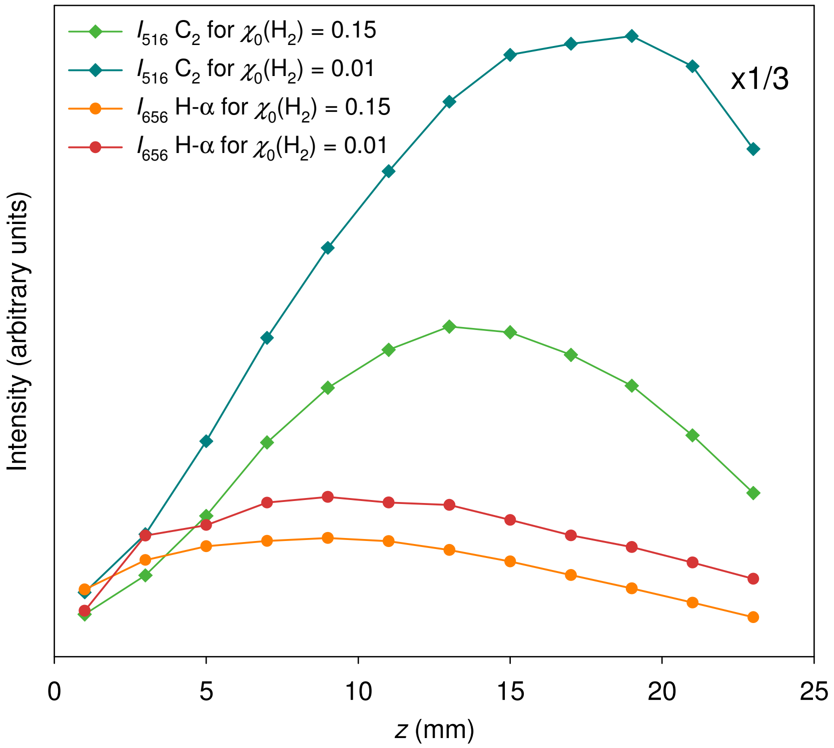

Figure 3.32: Vertical profiles of the optical emission intensity from C_2(A→X) (at 516 nm) and H-α (at 656 nm) measured using two different gas mixtures including the present base conditions (0.5%CH_4/14.7%H_2/84.8%Ar, p = 150 Torr, P = 1.0 kW) and a lower $\chi_0(H_2)$ (0.5%CH_4/1%H_2/98.5%Ar, p =150 Torr, P = 1.0 kW).

Both the H-α and C_2(d→a) profiles increase in intensity as $\chi_0(H_2)$ is lowered with a dramatic rise in the C_2-radical emission (the raw data is ×3 higher than the plotted profile) seen in the previous work. While the maximum column density of atomic-H remains at around z = 9 mm, the C_2 emission maximum shifts from z ~13 to z ~ 19 mm indicative of the increase in the luminous plasma volume. We also see the C_2(A→X) emission falling faster towards the substrate as the T_{gas} drops away and this is also observed in the absorption measurements in Figure 3.33.

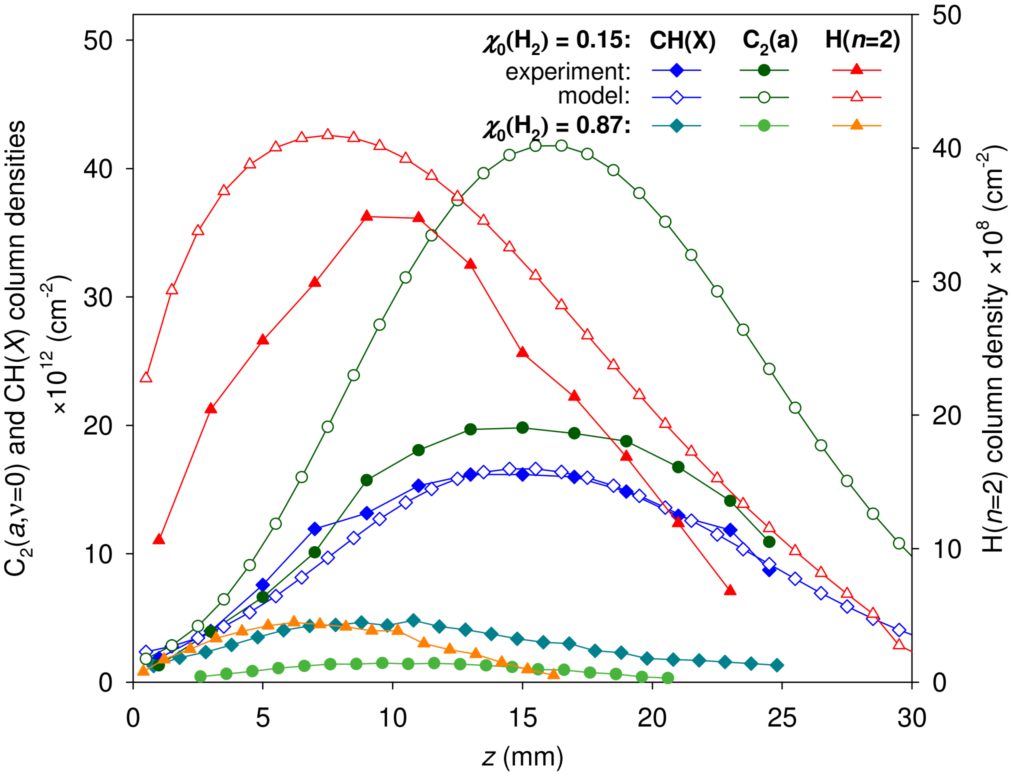

Figure 3.33: Vertical profiles of experimental CRDS-measured (filled symbols) and computational (open symbols) column densities of C_2(a, v = 0) and CH(X, v = 0) radicals (on the left-hand scale) and H(n = 2) atoms (on the right-hand scale) for the base conditions (0.5%CH_4/14.7%H_2/84.8%Ar, p =150 Torr, P = 1.0 kW). The CRDS profiles measured for the MCD base conditions (4.4%CH_4/88.6%H_2/7%Ar, p =150 Torr, P = 1.5 kW) are also shown (Ma *et al.*, 2008, Richley *et al.*, 2011).

This figure shows the column densities of C_2(a, v = 0), CH(X, v = 0) and H(n = 2) as a function of z for the representative base conditions for high-χ_0(Ar) plasmas as well as the modelling predictions and the MCD plasma conditions. Overall we have CRDS profiles for $\chi_0(H_2)$ ~ 0.87 (at higher P = 1.5 kW, Figure 3.33), CRDS and OES profiles for $\chi_0(H_2)$ ~ 0.15 and OES profiles for $\chi_0(H_2)$ ~ 0.01 (Figure 3.32), and across this range we observe emission intensities and column densities increasing and the visibly emitting plasma expand in size. The difference in the peak intensity for H(n = 2) is due to the dependence of this excited state on the local H(n = 1) concentration and T_e.

3.3.9.5 Modelling II

Using experimental observations we have discussed how the computation model was improved and used to make predictions shown in the figure, and to determine the spatial variation in plasma parameters such as T_{gas} and χ(H) as changes are made to the process conditions. Results show that increasing $\chi_0(H_2)$ from 0.01 to 0.15 only results in a doubling of χ(H) from ~0.02 to ~0.045.

In Figure 3.33 we show the 2D-model predictions which follow the experimental results for H(n = 2) and CH(X) but overestimate the C_2(a) column densities, although the peak positions are reproduced fairly well (Richley *et al.*, 2011). The model allows us to summarize some of the changes in the fundamental parameters of the CVD plasma as H_2 is replaced by Ar (Figure 3.34). The increase in plasma volume, V, is apparent together with the plasma centre (z_c) moving further from the substrate.

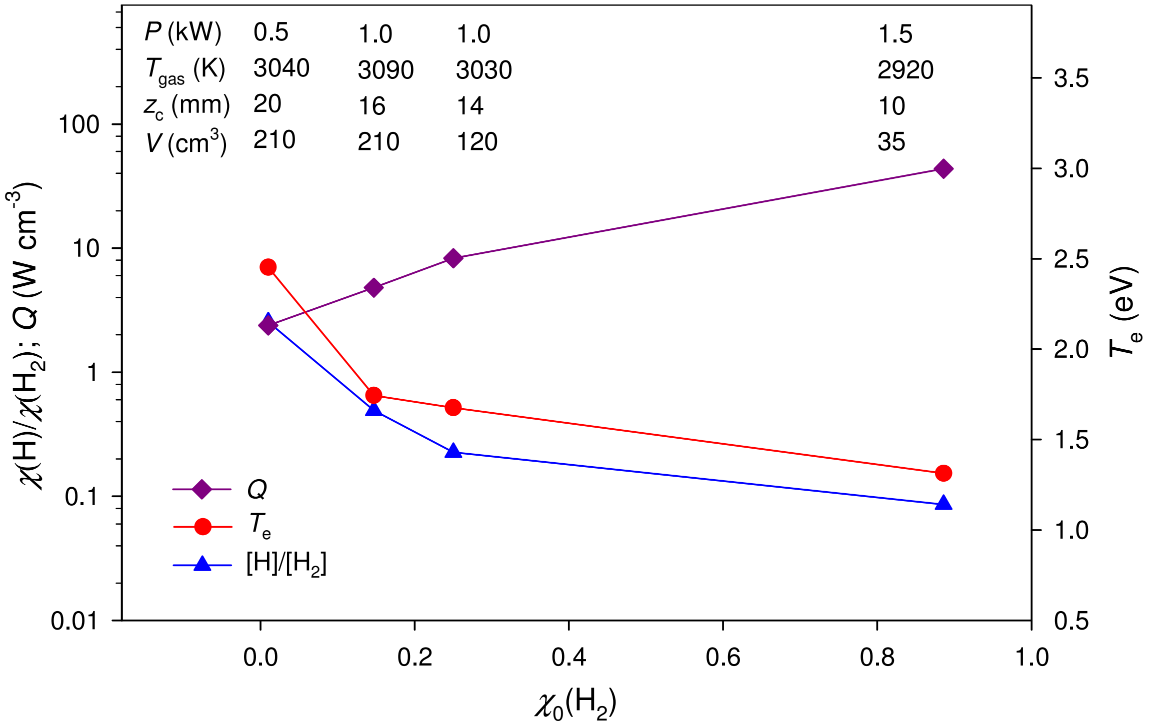

Figure 3.34: Model-predicted dependencies of the average electron temperature, T_e, average power density, Q, $\chi(H_2)/\chi(H_2)$, plasma volume, V, plasma centre position, z_c, and gas temperature, T_{gas} with changing $\chi_0(H_2)$ (Richley *et al.*, 2011).

We see that the decrease in power density, Q, at lower $\chi_0(H_2)$ is contrary to the increase in T_e. This is explained by the dominant absorption of P into H_2 rovibrational excitation in high-$\chi_0(H_2)$ plasmas and also the complex balance of ionization and recombination reactions (Richley *et al.*, 2011). In the low-$\chi_0(H_2)$ plasmas the input power goes not only into rovibrational excitation of H_2 and the hydrocarbons, but also into the elastic collisions of Ar and other species. At the same time the density of energy-dissipating states is lower in the Ar-rich system and so the absorbance capacity of these systems is lower and the plasmas must become larger for a given P. The trend in predicted T_{gas} shows good agreement with the evolution of experimentally measured T_{sub} (see section 3.3.9.1) first rising and then falling with increasing χ_0(Ar), and in doing so helps to validate the computational model. Predictions of the concentrations of C_1 growth species above the substrate surface show that, at low $\chi_0(H_2)$, the χ(C) is only one order of magnitude lower than

$\chi(CH_3)$ and this supports calculations which show that atomic C can add into surface CH bonds (Richley *et al.*, 2009), a mechanism which could explain the underestimation of G from purely CH_3 addition (May & Mankelevich, 2008).

3.3.10 Summary

Although different plasma conditions were necessary for successful diamond deposition all inert gas plasmas produced morphologically similar, homogeneous NCD films at roughly similar growth rates. Some variation was observed in the morphology using SEM imaging and Raman spectroscopy that showed a decrease in crystallite size down the group from He to Kr. Combining experimental data from OES and CRDS with detailed 2D(r, z) computational modelling has allowed some ideas about the plasma processes and the diamond deposition mechanism to be discussed. The results showed the increase in T_e and $\chi(H)/\chi(H_2)$ as H_2 is replaced with Ar and this correlates with increases in $C_2(a)$ and CH(X) radical column densities and emission intensities even though lower $\chi_0(CH_4)$ are used. Over the same range the T_{gas} does not vary significantly despite the differences in thermal conductivity between H_2 and Ar. The discussion supports the proposal that NCD deposition in high $\chi_0(Ar)$ plasmas can be explained using CH_x (x = 0-3) as the growth species.

3.4 Diamond deposition III: Nitrogen & NCD

3.4.1 Parameter space

In section 1.5.3 the addition of N_2 to the diamond-deposition environment was introduced as a way of modifying the morphology (Locher *et al.*, 1994) and the growth rate (Müller-Sebert *et al.*, 1996). To recreate these observations in our MWCVD system we planned to add N_2 in trace amounts and measure the changes in the gas-phase characteristics and diamond film. In the first experiments the deposition conditions consisted of:

$\chi_0(H_2) = 0.93$ ($F(H_2) = 500$ sccm)

$\chi_0(CH_4) = 0.065$ ($F(CH_4) = 35$ sccm)

$\chi_0(N_2) = 0\text{-}1866$ ppm ($F(N_2) = 0\text{-}1$ sccm)

while $P = 1$ kW and $p = 100$ or 150 Torr.

The set of films did not show the increase in G, which had already saturated at the lowest possible flow rate (0.25 sccm = 467 ppm), so a 10% dilution of N_2 in Ar was used to achieve mole fractions an order of magnitude lower. With parameters:

$\chi_0(H_2) = 0.93$ ($F(H_2) = 500$ sccm)

$\chi_0(CH_4) = 0.065$ ($F(CH_4) = 35$ sccm)

$\chi_0(N_2) = 0\text{-}187$ ppm ($F(N_2) = 0\text{-}0.1$ sccm)

while $P = 1$ kW and $p = 150$ Torr. It was assumed that the $F(Ar) = 0\text{-}0.9$ sccm would have negligible influence on the plasma.

Lastly high $\chi_0(N_2)$ plasmas were investigated using:

$\chi_0(H_2) = 0.1\text{-}0.98$ ($F(H_2) = 50\text{-}500$ sccm)

$\chi_0(CH_4) = 0\text{-}0.065$ ($F(CH_4) = 0\text{-}35$ sccm)

$\chi_0(N_2) = 0\text{-}0.9$ ($F(N_2) = 0\text{-}450$ sccm)

while $P = 1$ kW and $p = 80\text{-}150$ Torr.

3.4.2 Plasma observations and spectroscopic studies

Even at low concentrations the N_2 has an obvious influence on the emission spectrum of the plasma through the appearance of CN bands at ~388 and ~421 nm which are part of the $B^2\Sigma^+ \rightarrow X^2\Sigma^+$ system.

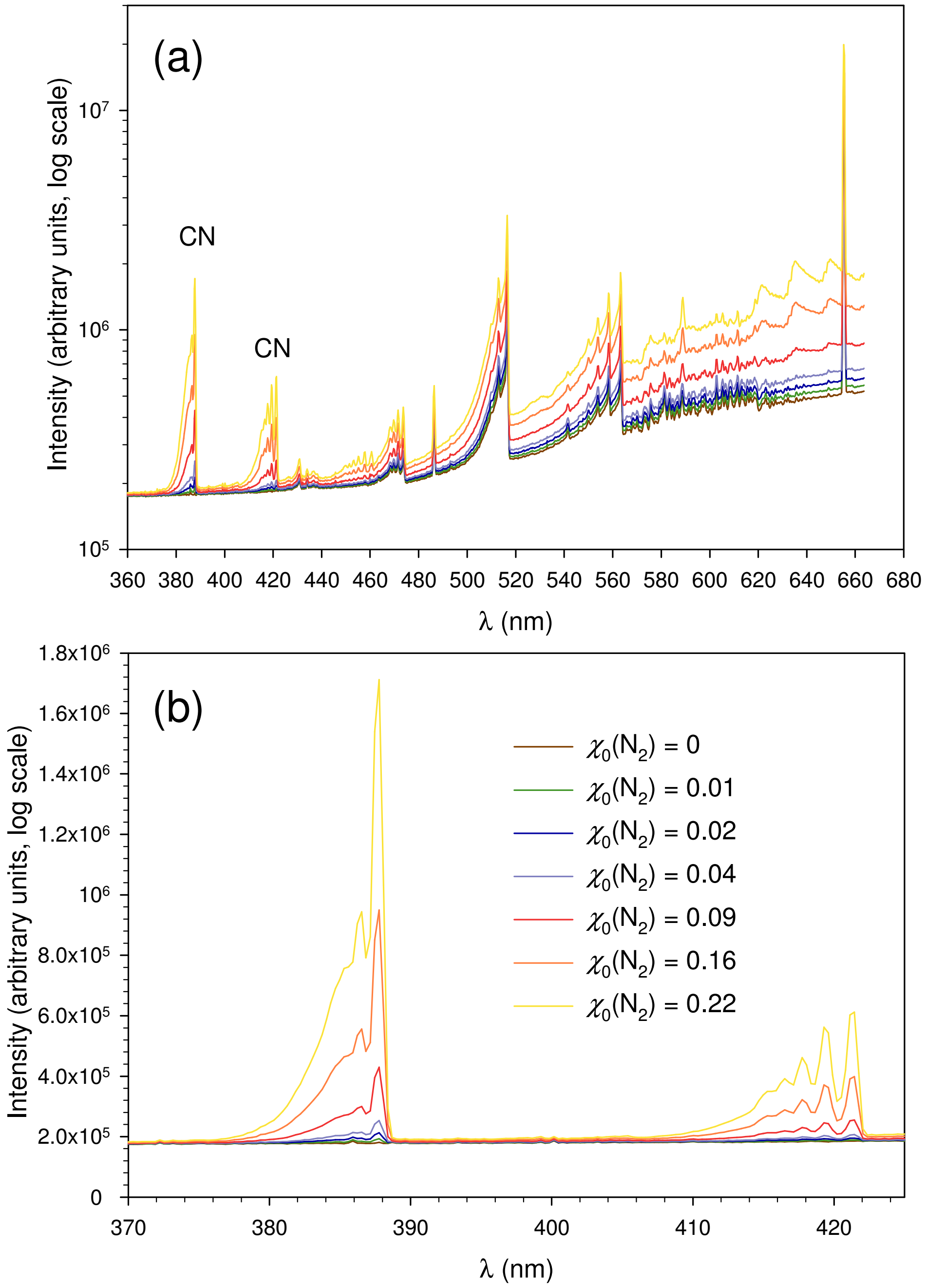

Figure 3.35: OES spectra for nitrogen-containing gas mixture and constant P = 1 kW and $\chi_0(CH_4)$ = 0.065 with $\chi_0(N_2)$ balanced with $\chi_0(H_2)$. (b) the increase in intensity of the CN(B→X) band with $\chi_0(N_2)$.

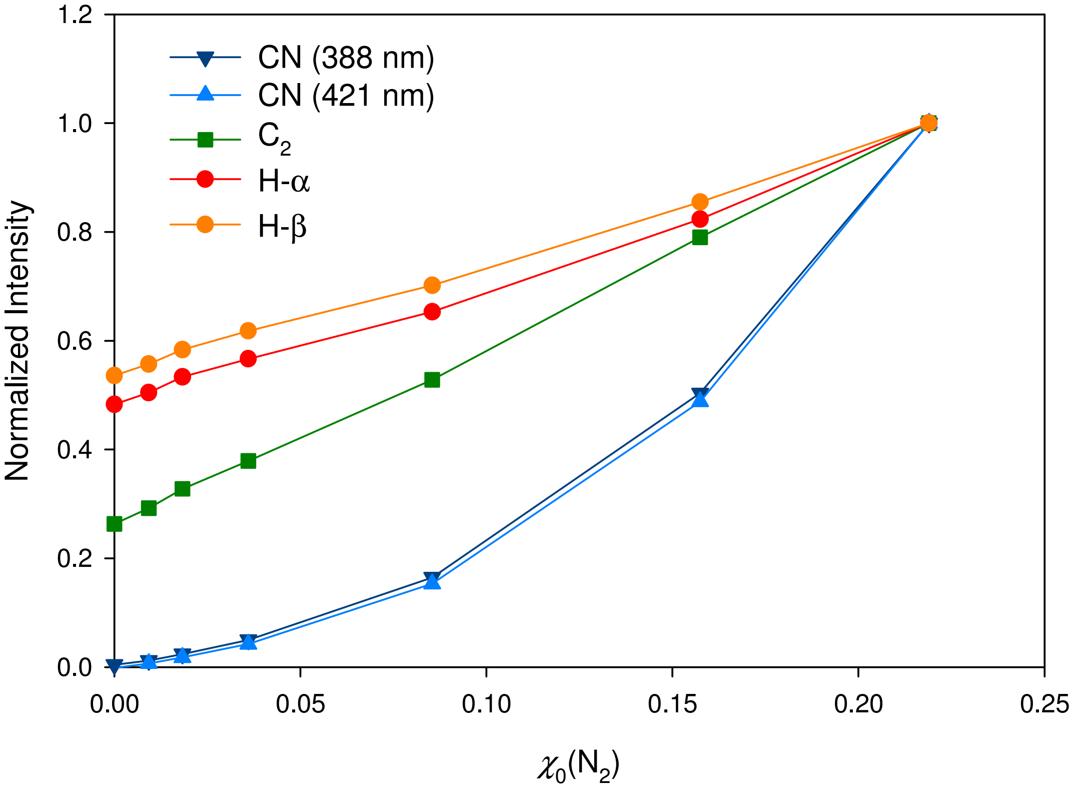

Figure 3.36: OES peak intensities for H-α (656 nm), H-β (486 nm) C_2(d→a, 516 nm) and CN(B→X, 388 and 421 nm), normalized to their maximum value, against $\chi_0(N_2)$.

We see roughly linear increases in C_2(d→a) and the H Balmer series while the CN(B→X) rises at a greater rate up to $\chi_0(N_2) = 0.2$. At higher $\chi_0(N_2)$ the T_{sub} rises as more N_2 is added to the system and, presumably, there is greater power absorption into the strong C-N and N-N bond-vibrations. The CN emission intensity continues to increase over this range although a rapid increase is seen at $\chi_0(N_2) > 0.6$.

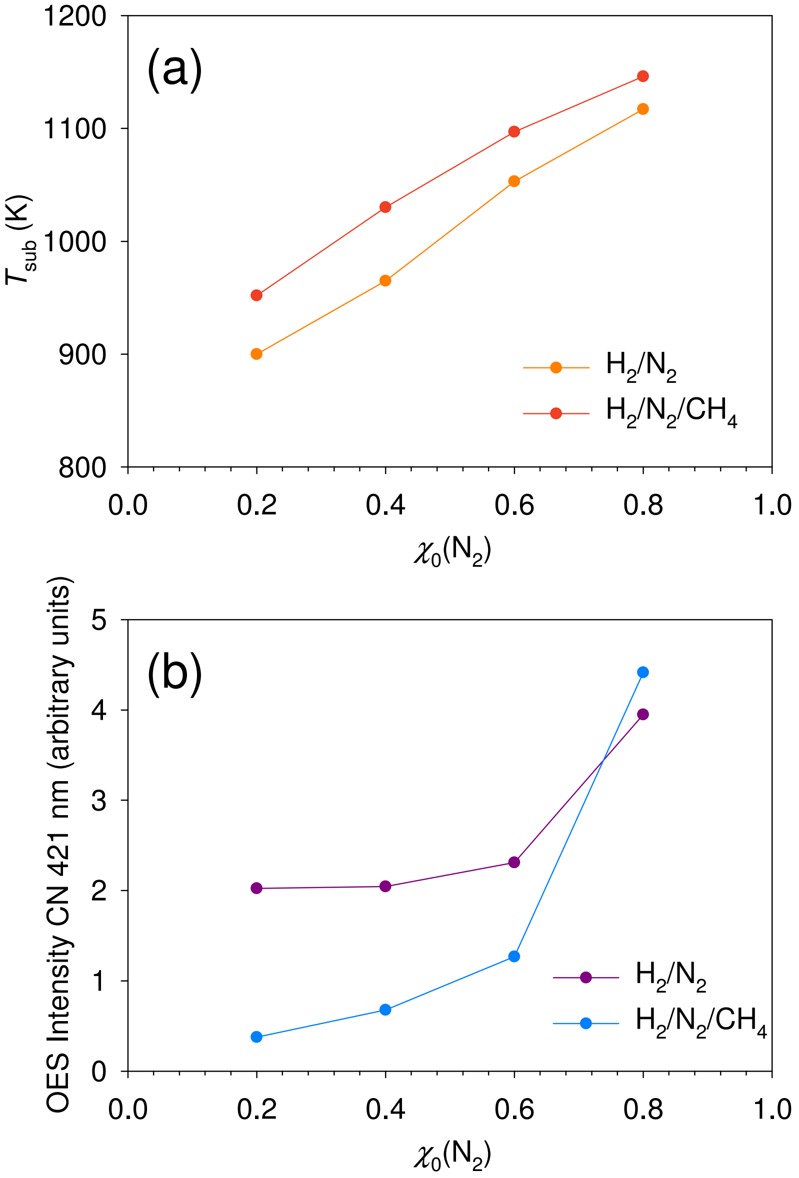

Figure 3.37: Increasing T_{sub} and CN(B→X) emission when replacing H_2 with N_2 in the plasma with and without CH_4 in the mixture. It will be seen that the increase in emission intensities seen in Figure 3.36 continues for $\chi_0(N_2) > 0.2$.

3.4.3 SEM analysis of diamond films

As expected, addition of N_2 induces significant transformations in the diamond morphology and, with increasing amounts of the N_2 the surface changes from large, facetted <111> crystallites for < 50 ppm N_2, to crystals becoming smaller, rougher, and then formation of twins before finally become nanocrystalline around 2000 ppm.

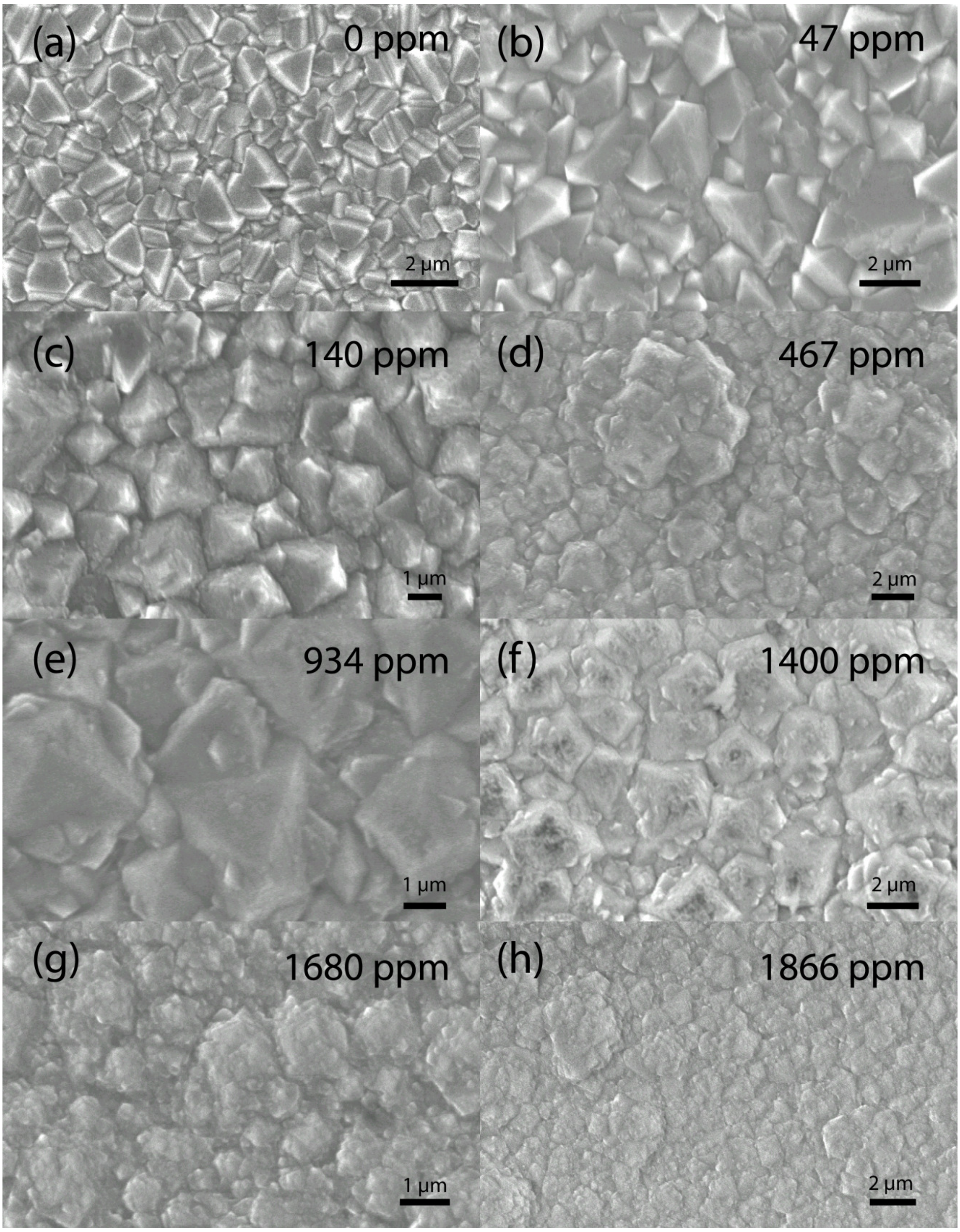

Figure 3.38: Changes in film morphology from MCD to NCD as $\chi_0(N_2)$ is increased from 0 to 1866 ppm.

Observing contact twins (stacking faults) mid-way through this transition (see Figure 3.38e) is important as it offers an explanation as to how nitrogen might be changing the growth rate and morphology. The formation of new crystal orientations can happen as any new layer is formed and it seems likely that the nitrogen or CN species is increasing the rate at which new diamond layers form and propagate. This is, essentially, a 'fast-tracked' renucleation process and continues until nucleation of new layers causes the formation of a nanocrystalline morphology (see Figure 3.38h). The proposed mechanism of this process, based on the stability of the CN adduct on the diamond surface, has been comprehensively described (Butler & Oleynik, 2008). Figure 3.39a shows a deposition experiment which has been stopped prematurely and shows the growth of individual diamond nuclei before the film becomes continuous. The change in morphology from MCD to NCD is also seen in the cross-sectional images where a pressure dependence is also apparent. At $\chi_0(N_2)$ = 47 ppm the film is obviously still MCD but at $\chi_0(N_2)$ = 467 ppm is MCD when grown at p = 150 Torr and NCD at p = 100 Torr. The increase in growth rate is also apparent increasing from G ~ 3.6 to 5.3 µm h^{-1} over the same range.

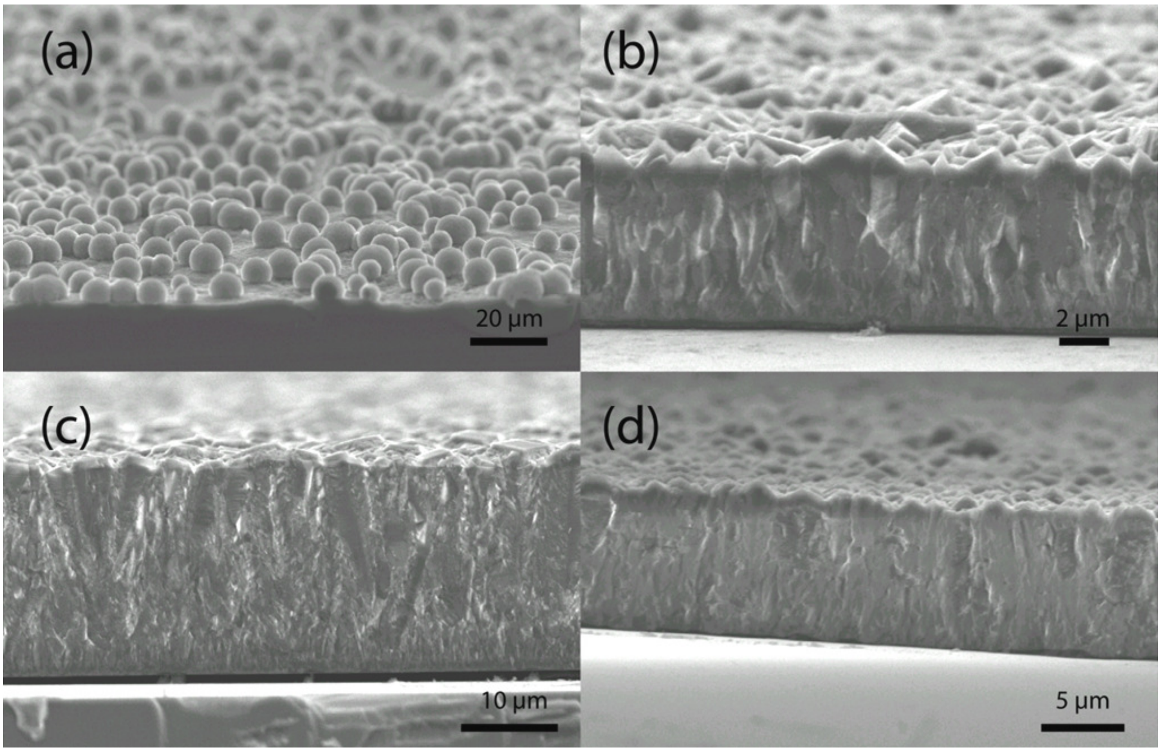

Figure 3.39: Different diamond morphologies obtained by using various $\chi_0(N_2)$ shown in cross-section. (a) shows a non-continuous film where the deposition has been stopped before completion of a complete diamond layer, (b) a MCD film grown with $\chi_0(N_2)$ = 47 ppm at 150 Torr (G ~ 3.6 µm h^{-1}). (c) and (d) show MCD films with small crystals sizes both grown with $\chi_0(N_2)$ = 467 ppm but at different pressures where (c) p = 150 Torr (G ~ 5.3 µm h^{-1}) and (d) p = 100 Torr (G ~ 3.4 µm h^{-1}).

3.4.4 Higher $\chi_0(N_2)$

Beyond $\chi_0(N_2)$ = 2000 ppm, the diamond crystal size decreases further and the films become smoother but the growth rate gradually begins to fall until, at $\chi_0(N_2)$ ~ 15%, no diamond is deposited. In the region $\chi_0(N_2)$ ~ 5-15% we see less diamond being deposited and non-continuous films begin to be grown (Figure 3.40a) while between 15 and 55% there is no deposition. In this region the N will have a large negative impact on the concentration of C_1 growth species, limiting deposition and also etching the seed layer. Above 55%, and becoming much denser for $\chi_0(N_2) >$ 80%, a number of large crystallites are rapidly produced on the substrates which are >10 μm in length after just 30 min deposition.

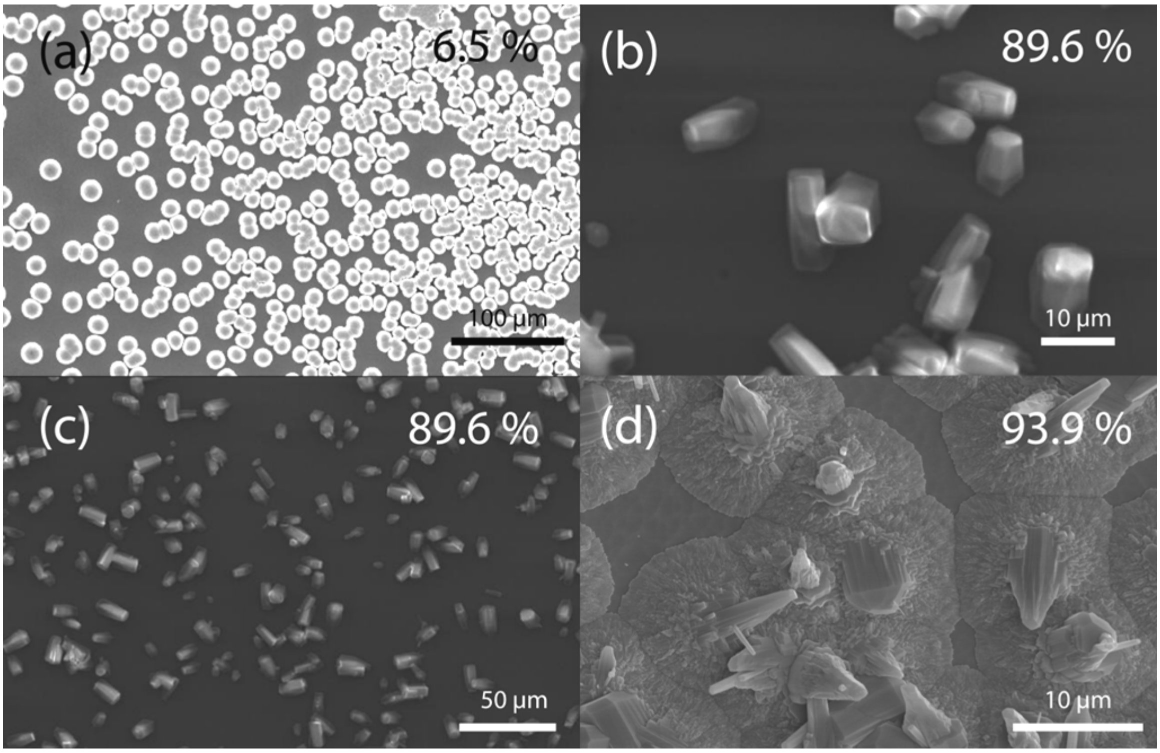

Figure 3.40: Examples of material deposited on Si substrates where $\chi_0(N_2) > 2000$ ppm showing formation of Si_3N_4 crystals above $\chi_0(N_2) = 0.55$ ((b) to (d)).

Fast growing, hexagonal crystals have been observed on substrates exposed to MWCVD plasmas that contain carbon and N_2 or NH_3 in high concentrations and has often led to misidentification as carbon nitride, C_3N_4. Further analysis, however, has correctly identified these as silicon nitride, Si_3N_4 (Badzian *et al.*, 1999, Chen *et al.*, 1996, Fu *et al.*, 2002). Silicon nitride exists in two forms, α-Si_3N_4 and β-Si_3N_4, and in some cases a small proportion of the Si atoms can be replaced with carbon to form silicon carbon nitride.

The mechanism of formation is proposed to be an etching process of the Si substrate using an activated N-containing molecule. This produces Si or SiN species in the gas phase which then deposit back on the substrate as Si_3N_4. Deposition experiments with and without methane show that carbon catalyses the deposition in all but the highest $\chi_0(N_2)$ plasmas (Figure 3.41). This observation implies that CN is an active species in these plasmas and one that is present in high concentrations (see the jump in emission intensity in Figure 3.37). Logically these crystals do not form when the same plasma is used with Mo substrates as there is no source of Si.

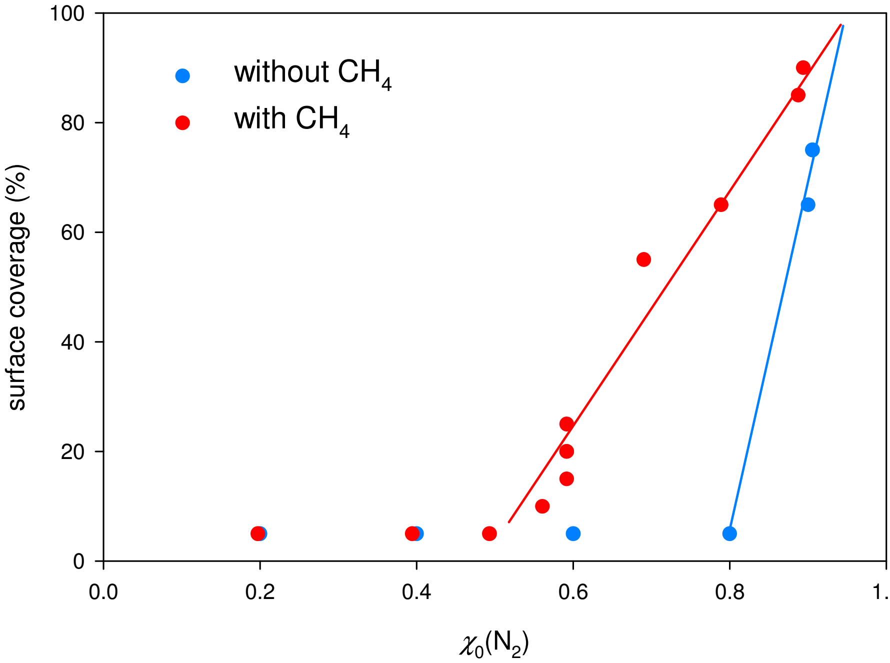

Figure 3.41: Surface coverage of Si substrates with Si_3N_4 crystals at different $\chi_0(N_2)$ both with and without CH_4 ($\chi_0(CH_4)$ ~ 0.014) added to the gas mixture. The balance is made up with $\chi_0(H_2)$.

Positive identification of our crystals came from three techniques. Firstly, low-temperature photoluminescence spectroscopy showed an intense emission (although this was not obvious using the Raman at room temperature) distinct from the usual NCD characteristics.

The SiN spectrum (Figure 3.42) consists of a very strong band centred at 2.0 eV and weaker bands between 2.5 and 3.5 eV. Also present are sharp phonon replica peaks (interaction between the bound exciton and vibrating lattice) around 3.4 eV that are visible due to cooling the sample to near 0 K. Although not conclusive, the 2.25 eV feature has in the past been attributed to quantum confinement luminescence from Si nanoparticles or quantum dots within the Si_3N_4 crystal (Cen *et al.*, 2009).

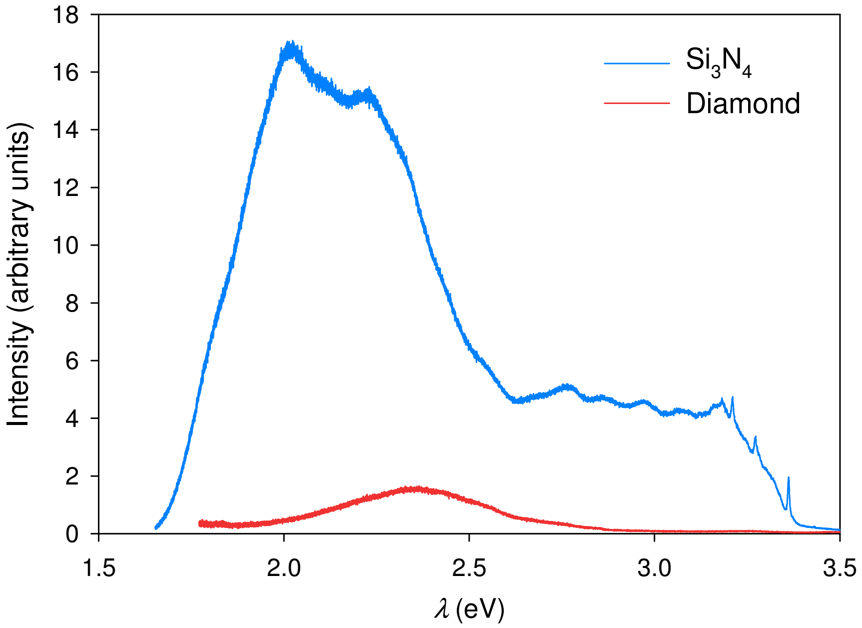

Figure 3.42: Low-temperature PL spectra of Si_3N_4 crystals grown in a $N_2/H_2/CH_4$ plasma and NCD film for comparison. Excitation at 325 nm and 83 K.

Like the PL spectra, the XRD pattern of Si_3N_4 crystals is characteristic enough to be distinct from any carbon material. One of the samples formed in the high $\chi_0(N_2)$ was subjected to powder-XRD diagnostics and the resulting pattern is shown in Figure 3.43. The output is fairly complex as the pattern indicates that the deposited crystals are made up of both the α- and β-phases of Si_3N_4, as well as a strong contribution from the Si substrate. The different crystalline phases can be differentiated as they correspond to different space groups where α-Si_3N_4 and β-Si_3N_4 are represented by *P31c* and *P63/m*, respectively.

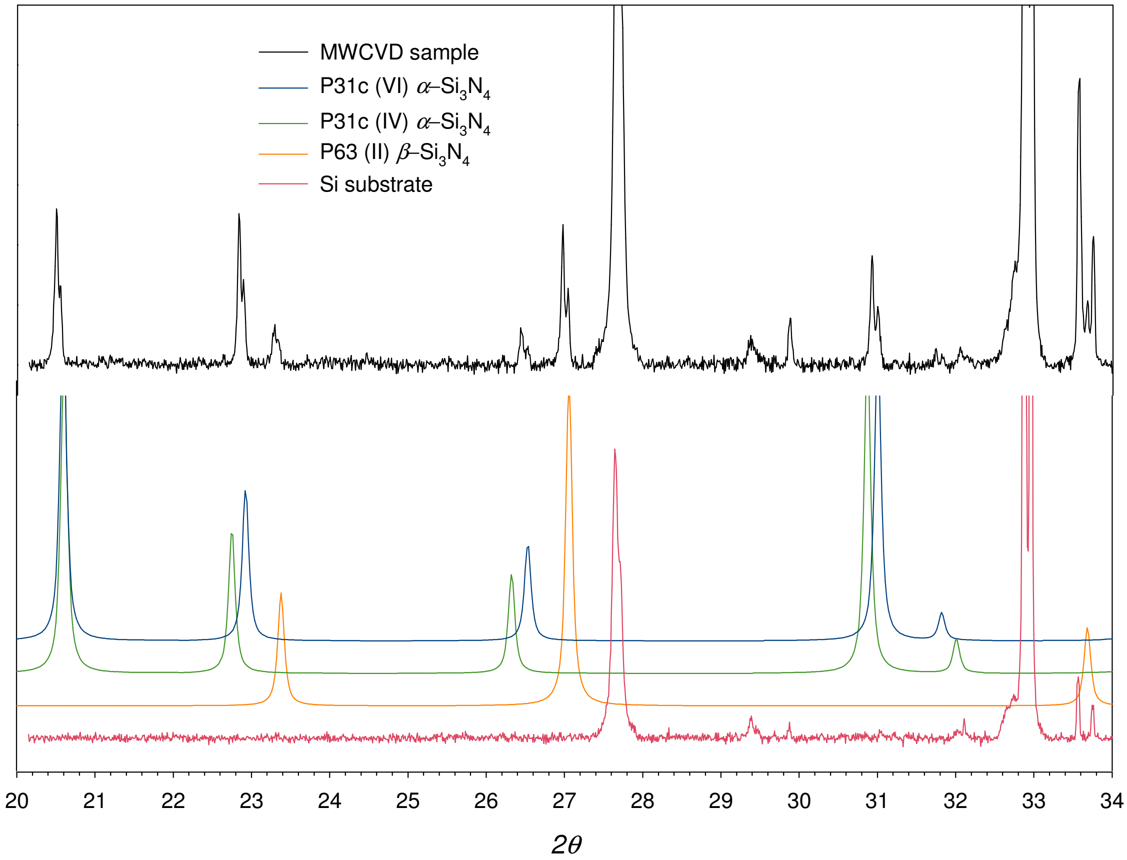

Figure 3.43: Powder X-ray diffraction pattern of MWCVD-grown crystals (above) and different crystal arrangements of Si_3N_4 and Si reference spectra (below).

Lastly, Auger electron spectroscopy, carried out on the samples at the Interface Analysis Centre, University of Bristol, showed that there was negligible (< 600 ppm) carbon incorporated into the crystals. Therefore, the crystals are completely Si_3N_4 in contrast to the silicon carbon nitride reported by other groups (Fu *et al.*, 2002).

3.4.5 Raman analysis of diamond films

Once again the observations made when looking at the film morphology under the electron microscope find corroboration in the relative ratios of the Raman resonant bands when the samples are illuminated with UV laser light (325 nm). As for the results when increasing $\chi_0(CH_4)$ in an MCD plasma, a decrease in both $I(sp^3)/I(\mathrm{D})$ and $I(sp^3)/I(G)$ is detected when increasing $\chi_0(N_2)$ from 467 to 1866 ppm. Similarly, the $I(\mathrm{D})/I(G)$ relationship is flat showing that the trends observed for the sp^3:sp^2 intensities are valid although they are not immediately apparent from the full spectra (Figure 3.45). The trends can be attributed to a decrease in the crystal size as $\chi_0(N_2)$ increases and is in agreement with the morphologies observed by SEM. The correlation lends further support to the theory of an increased renucleation rate as $\chi_0(N_2)$ increases (Butler & Oleynik, 2008).

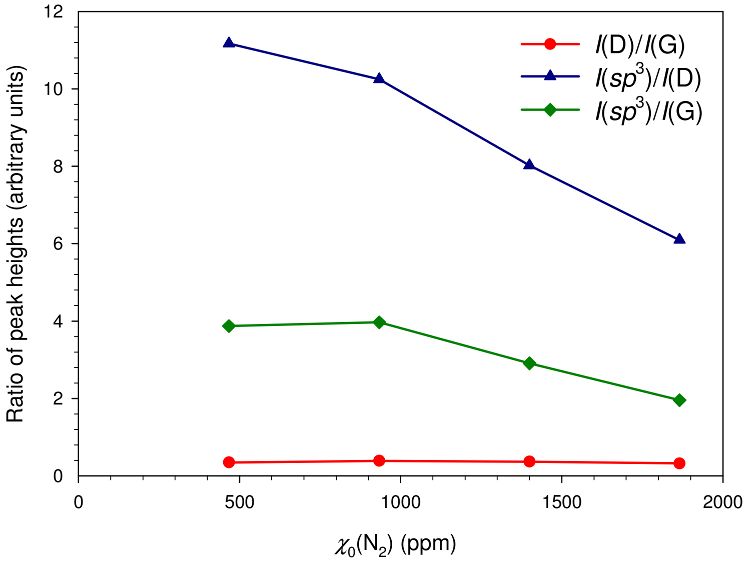

Figure 3.44: Supporting evidence for the reduction in crystal size observed in SEM imaging from UV-Raman spectra for films grown in a $H_2/N_2/CH_4$ plasma with increasing $\chi_0(N_2)$ at $p = 150$ Torr, $P = 1$ kW, $\chi_0(H_2) \sim 0.93$ and $\chi_0(CH_4) \sim 0.065$.

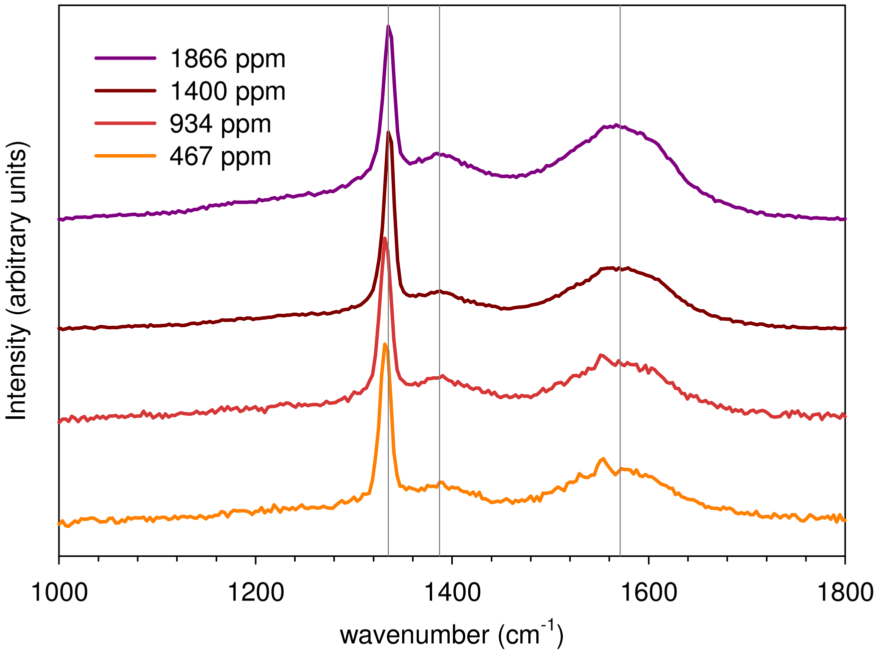

Figure 3.45: Raman spectra for four films grown with increasing $\chi_0(N_2)$. The slight shift in the 1332 cm^{-1} peak is more likely to be due to differences in experimental calibration rather than changes in the film.

Despite obtaining these results for four films grown with differing amounts of N_2 in the gas phase it must be pointed out that other series of diamond samples produced less correlation.

Specifically, working at the lower range of $\chi_0(N_2)$ ~ 50-200 ppm produced a number of similar MCD films (albeit at the enhanced growth rate discussed previously) and, because of this, no trends in the UV-Raman peaks could be deduced. Therefore, the transition to NCD morphologies must occur at $\chi_0(N_2) > 200$ ppm, as we have inferred from the SEM results. Any variation observed in the spectra (Figure 3.46) derives from differences in the morphology at the point where the Raman excitation was made. It is obvious that a wide range of different spectra can be obtained from the same diamond sample depending on whether an area is dominated either by large crystals or by grain boundaries – as such, the Raman spectra presented here should be taken as examples of parts of a diamond sample.

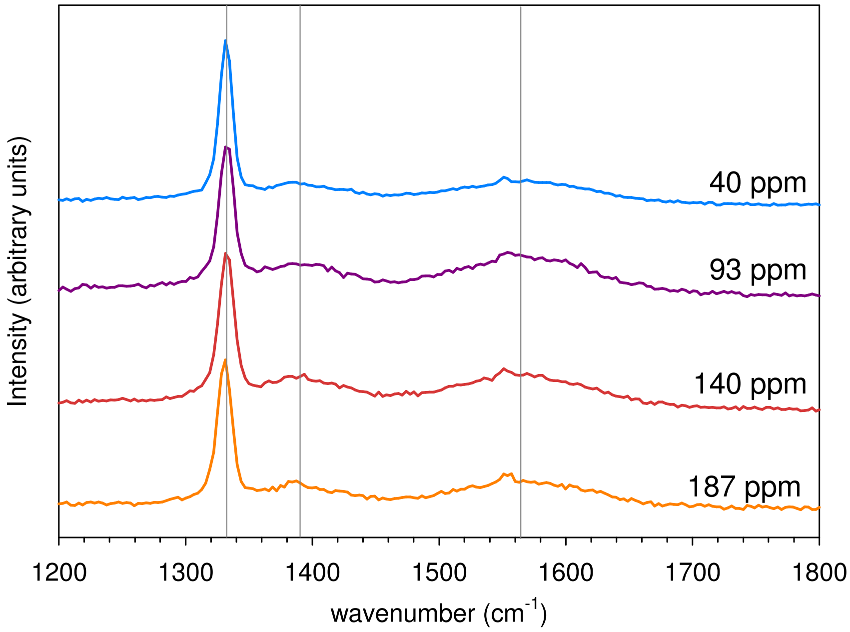

Figure 3.46: Raman spectra for four films grown with $\chi_0(N_2)$ = 40-187 ppm showing no apparent changes in morphology confirming observations of the SEM images.

3.4.6 XRD analysis

To complement the Raman analysis, powder XRD spectra were obtained for some of the deposited films to determine the diamond texture in the bulk phase. Spectra of films grown with $\chi_0(N_2)$ = 187 ppm are essentially identical to those of MCD samples from standard H_2/CH_4 plasmas. Moreover, there is no measured broadening or shift in the $2\theta = 43°$ <111> diamond peak which is sometimes predicted for films where N has been incorporated into the diamond lattice. The remaining unassigned peaks in the spectrum are from the <100> Si substrate.

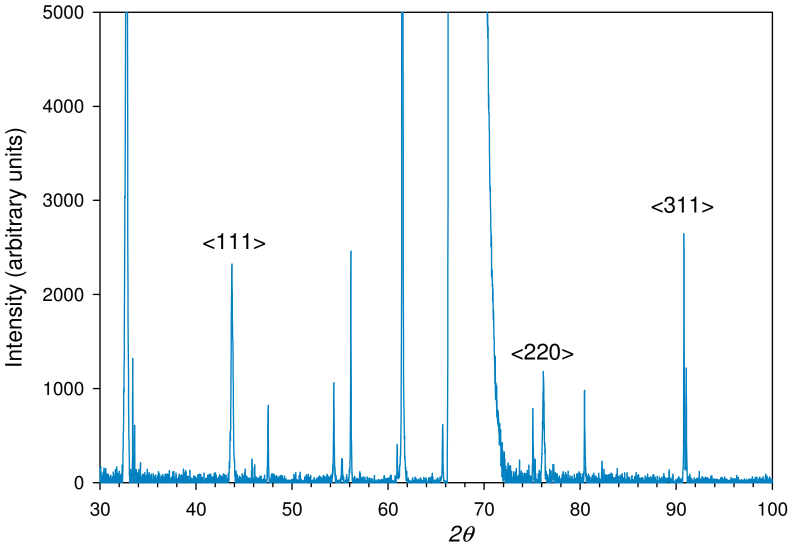

Figure 3.47: Powder XRD spectrum of MCD film grown in $H_2/N_2/CH_4$ plasma where $\chi_0(N_2)$ = 187 ppm. The majority of the (unlabelled) peaks derive from the <100> silicon substrate while the <111>, <220> and <311> Bragg reflexes of diamond are labelled.

3.4.7 Addition of NH_3 to diamond-depositing plasmas

As a significant proportion of the N_2 which is added to the reactor will end up as CN, or more likely the stable HCN analogue, the same results should be seen if different N-containing gases are added instead of N_2. Deposition of diamond by HFCVD has been demonstrated using NH_3, CH_3NH_2 and HCN (May *et al.*, 1996, Smith *et al.*, 2002).

We investigated deposition using $\chi_0(NH_3)$ = 0.0012-0.018 in H_2 (with $\chi_0(CH_4)$ = 0.065) at p = 150 Torr and P = 1 kW. Similar trends in diamond morphology (Figure 3.48) and growth rate were observed showing that the influence of N is not dependent on the nature in which the species is added to the MWCVD system, it is rapidly converted into HCN and CN.

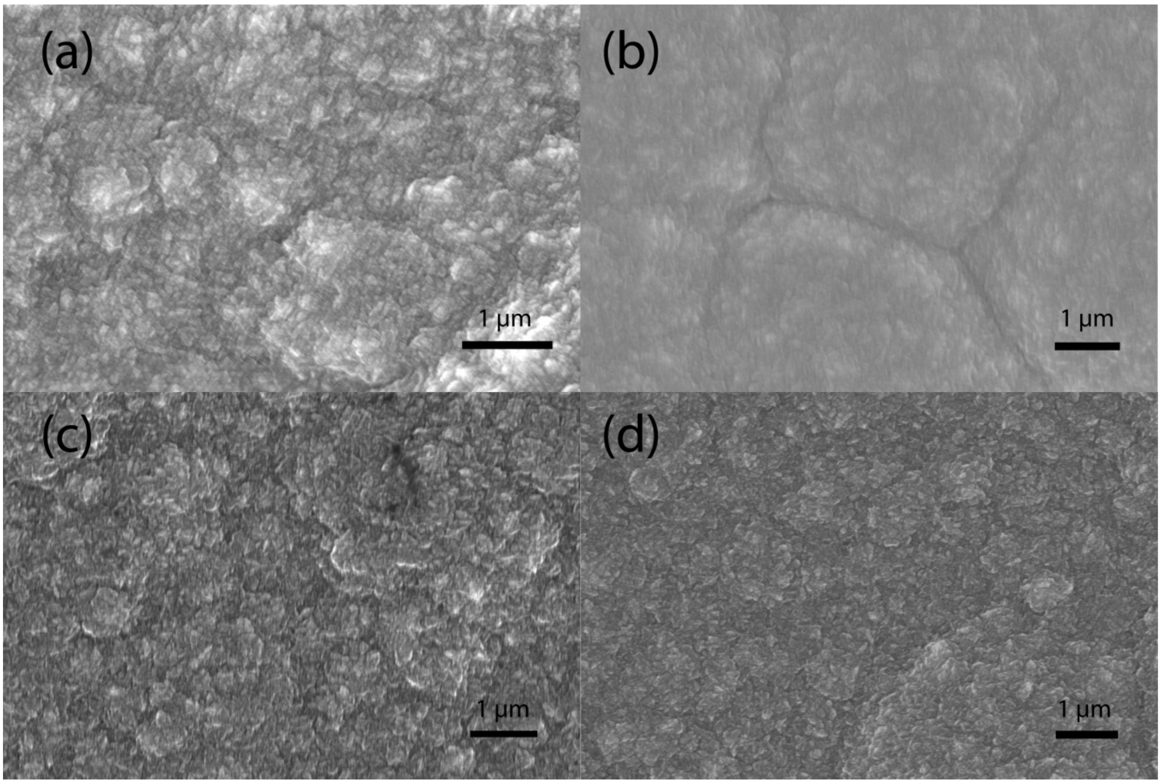

Figure 3.48: SEM images of NCD diamond films deposited with varying amounts of NH_3 in the gas mixture where $\chi_0(NH_3)$ = (a) 0.12%, (b) 0.23%, (c) 0.47% and (d) 1.38%.

3.4.8 Summary

Increases in growth rate and changes in diamond morphology have been measured as a function of $\chi_0(N)$ by adding N_2 and NH_3 to standard H_2/CH_4 plasmas. The diamond topography has been characterized by SEM imaging and UV-Raman analysis and the diamond plasmas probed with emission spectroscopy showing intense emission from CN(B→X) radicals. These species have been suggested as a possible catalyst for the observed morphology changes and the increase in deposition rate. At high $\chi_0(N_2)$ the formation of Si_3N_4 crystals from the etching of the Si substrates in the harsh plasmas has also been studied.

4.0 Molecular beam mass spectrometry (MBMS)

4.1 Mass spectrometry (MS)

4.1.1 Quadrupole mass spectrometry: Principles & Theory

Mass spectrometry (MS) occupies a unique niche in the field of analytical techniques and, because of its specific properties, has been employed in a wide range of forms covering much of modern science, from commercially-available residual-gas analysers and handheld tools for portable chemical detection, to bespoke hyphenated techniques at the cutting edge of biotechnology. At their heart, MS experiments share the same purpose of separating ions based on their relative mass (m) to charge (q) ratio. Spatial separation of ions is often achieved through application of electric ($\boldsymbol{E}$) or magnetic ($\boldsymbol{B}$) fields acting *via* the Lorentz Force Law:

$$F = q\boldsymbol{E} + q\boldsymbol{v} \times \boldsymbol{B} \tag{4.1}$$

Each field exerts a different influence on charged particles where $\boldsymbol{E}$ accelerates positive ions in the direction of the field vector but is not dependent on the initial velocity, $\boldsymbol{v}$, whereas, a magnetic field, $\boldsymbol{B}$, exerts a force perpendicular to the field vector and velocity. Consequently, the magnetic field will only act on ions with velocity components perpendicular to the field and separation can only occur by resolving different velocities by time-of-flight (TOF) analysis or positions by, for example, magnetic sector methods.

4.1.2 Quadrupole MS

Mass separation derived from the stability of ion trajectories in a solely electrostatic field was first proposed using an ion optic consisting of two pairs of electrodes onto which a.c. voltages of opposing polarities were applied (Paul & Steinwedel, 1953) and has, subsequently, developed into the modern field of quadrupole mass spectrometry (QMS). The arrangement of cylindrical electrodes and resultant four-fold symmetric hyperbolic field was shown to approach the ideal geometry, allowing the influence of the electrostatic field on the mass resolution to be mapped (Paul & Raether, 1955). Spatial separation of charged particles using time-dependent electrostatic potentials in such apparatus is achieved using a quadrupole mass filter (QMF) where the quadrupole field ($\Phi(x,y)$), of field strength Φ_0, is described by the saddle-point function:

$$\Phi(x,y) = -\frac{\Phi_0}{2}(x^2-y^2) \tag{4.2}$$

The quadrupole ion optic is shown in three complementary depictions in Figure 4.1.

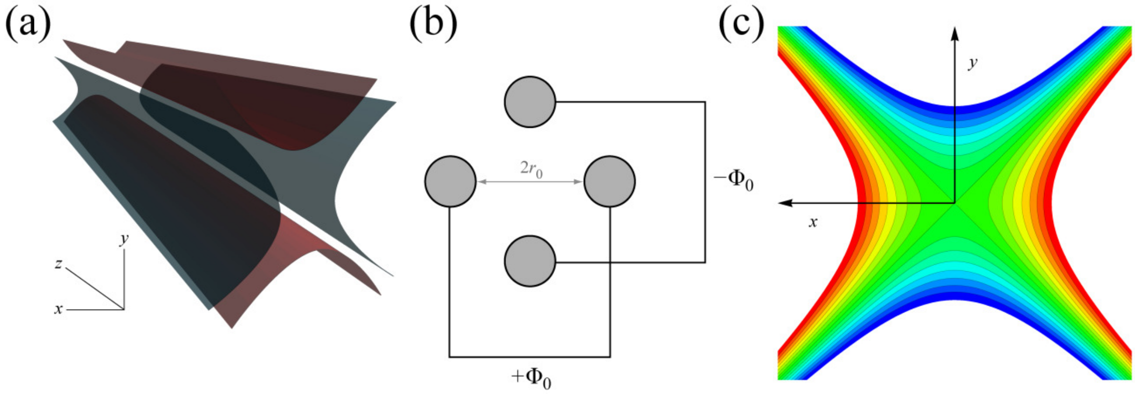

Figure 4.1: Theoretical quadrupole fields (a) & (c) and experimental quadrupole electrode arrangements (b). (a) the four electrodes as *ideal* hyperbolic cross-sections where ions are introduced centrally and are accelerated by the optic in the +z direction, (b) a schematic of a simple QMF arrangement of electrodes approximated as four cylindrical rods with opposing potentials applied, and (c) a contour plot of equipotentials on electrostatic saddle potential produced in such a device. x^2-y^2 potential plot courtesy of Ben Truscott, University of Bristol.

If we define the origin as the centre of the quadrupole (as shown in Figure 4.1) then a potential $+\Phi_0$ is applied to electrodes in the xz plane and an opposing potential of $-\Phi_0$ to those in the yz plane. Close to the z axis in an ideal QMF, where electrodes are placed at a distance r_0 from the origin, the potential is exactly parabolic and can be expressed by:

$$\phi(x,y) = \frac{x^2-y^2}{2r_0^2}\Phi_0 \tag{4.3}$$

An infinitesimal particle with formal charge Z and velocity in the z direction within the quadrupole field can be described by the following equations of motion (Paul & Raether, 1955):

$$\frac{d^2x}{dt^2} + \frac{Ze}{m}\frac{\partial\phi}{\partial x} = \frac{d^2x}{dt^2} + \frac{Ze}{m}\frac{2\Phi_0}{r_0^2}x = 0 \tag{4.4}$$

$$\frac{d^2y}{dt^2} + \frac{Ze}{m}\frac{\partial\phi}{\partial y} = \frac{d^2y}{dt^2} - \frac{Ze}{m}\frac{2\Phi_0}{r_0^2}y = 0 \tag{4.5}$$

$$\frac{d^2z}{dt^2} + \frac{Ze}{m}\frac{\partial\phi}{\partial z} = \frac{d^2z}{dt^2} = 0 \tag{4.6}$$

where e is the elementary charge and m is the mass of a singly charged ion.

Solutions to these differential equations for a charged particle entering the field centrally between the quadrupole electrodes (*i.e.* at the origin) and subject to a static field (constant Φ_0) are given by

$$x(t) = \frac{v_x}{\sqrt{k}}\sin\sqrt{k}t \tag{4.7}$$

$$y(t) = \frac{v_y}{\sqrt{k}}\sinh\sqrt{k}t \tag{4.8}$$

$$z(t) = v_z t \tag{4.9}$$

where v_i is the component of the ion's initial velocity parallel to the i axis and

$$k = \frac{Ze}{m}\frac{2\Phi_0}{r_0^2} \tag{4.10}$$

Thus, ion motion in the static field, Φ_0, is periodic in the xz plane and exponentially increasing in the yz plane causing it defocus or diverge. As a result, the transmittance of the field is zero as only the infinitesimal proportion of particles travelling exactly along the z-axis remains undeflected. The overwhelming majority of ions, where $v_x \neq 0$ and $v_y \neq 0$, follow altered trajectories after interaction with the field, and either collide with the electrodes or exit the field.

For a functioning mass filter the crucial modification, instigated by Paul *et al.*(1955), is to use a combination of static, $U = \Phi_0$, and periodic, $V = \Phi_0\cos(\omega t)$, potentials. While the static potential (d.c.) causes the ion trajectories to become unstable, the time-varying (t) component (a.c.) provides a periodic restoring force if the ions follow paths which are resonant with the oscillating field at an angular frequency ω. This is the case if ion trajectories correspond to certain, mass-dependent solutions of $\Phi(t)$ and produces a non-zero transmission for a given mass in the quadrupole field. The set of potentials is often generalised into the Mathieu form:

$$\Phi(t) = U - V\cos(\omega t) \tag{4.11}$$

where *U* and *V* correspond to the static, d.c., and periodic, a.c., components of the applied potential, respectively. We can then substitute this modified form into the Mathieu-type equations of motion:

$$\frac{d^2x}{dt^2} + \frac{Ze}{m}\frac{2(U - V\cos\omega t)}{r_0^2}x = 0 \tag{4.12}$$

$$\frac{d^2y}{dt^2} - \frac{Ze}{m}\frac{2(U - V\cos\omega t)}{r_0^2}y = 0 \tag{4.13}$$

which together provide the following canonical form:

$$\frac{d^2u}{d\xi^2} + (a - 2q\cos 2\xi)y = 0 \tag{4.14}$$

This expression recognizes the antisymmetric nature of the differential equations to define a single variable $u = x = -y$ and results in the following dimensionless quantities providing a range of periodic and stable solutions (de Hoffman & Stroobant, 2007):

$$a_u = a_x = -a_y = \frac{4}{\omega^2}\frac{Ze}{m}\frac{2U}{r_0^2} \tag{4.15}$$

$$q_u = q_x = -q_y = \frac{2}{\omega^2}\frac{Ze}{m}\frac{2V}{r_0^2} \tag{4.16}$$

$$\xi = \frac{\omega t}{2} \tag{4.17}$$

Solutions to the Mathieu differential equations involve an infinite number of regions of stability in (a,q) space but, for simplicity, we will only consider those close to the origin where ion pathways in both *xz* and *yz* planes are stable (bounded by the pink lines and the *q* axis in the figure below). This doubly-stable region has physical significance for the QMF as it indicates values of *a* and *q* for which an ion trajectory is oscillatory and bounded by the *x* ($a \geq 0$) or *y* ($a \leq 0$) axes. It is, therefore, obvious that a mass filter will, for a given *U*, *V* and *ω*, only transmit ions which have a mass and charge such that the pair of points (a_x,q_x) and (a_y,q_y) fall within this stable region (Paul & Raether, 1955). Close to the apex within the first Mathieu stability region the chosen values of *a* and *q* induce greater oscillations in the transmitted ion's motion and better mass resolution is achieved. In most cases the quadrupole is operated at a fixed a/q ratio close to this apex (at $a/q = 2.98$ or $U/V \sim 1.7$). To obtain a mass scan, *U* and *V* are scaled to shift the mass selected along a fixed a/q (shown in blue in Figure 4.2) where the mass of each ion is linearly proportional to the scaling of the voltages. This treatment assumes the ion has ideal initial velocity and position whereas, in reality, ions will enter the mass filter away from the origin and will be exposed to field imperfections from the non-hyperbolic electrodes.

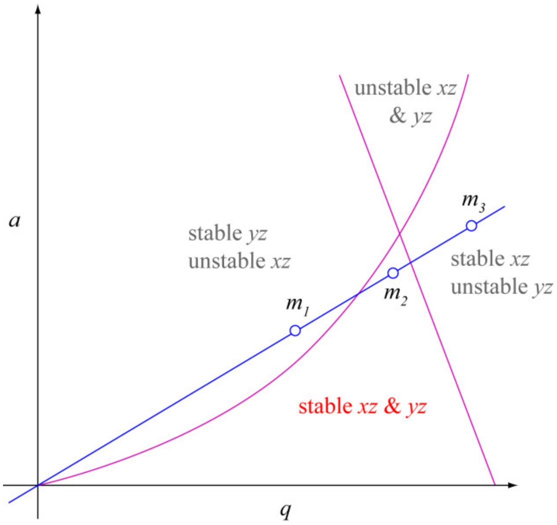

Figure 4.2: Stability diagram derived from solutions of the Mathieu differential equations as a function of a and q. In practical terms, the blue line corresponds to a particular set of operating conditions for which only one mass (m_2) falls within the stable region and will, therefore, display an oscillating trajectory with the mass filter while m_1 and m_3 will either leave the filter or collide with one of electrodes ($m_1 < m_2 < m_3$).

4.1.3 QMS apparatus

Although a multitude of variations exists, the main theme of quadrupole systems involves some key components which are discussed below with specific reference to the Bristol MBMS experiment.

4.1.3.1 Ion source

Unless the aim is to probe charged species with the mass spectrometer then the neutral species must be ionized before entering the mass filter. Ionization is achieved by a range of methods including sputtering, chemical ionization or photoionization, but, for volatile species, this is most commonly achieved by electron impact interactions. In the majority of systems the MS ionizer or ion source is located at the front end of the mass filter (Figure 4.3) and produces a collimated beam of ions, which is diagnostic of the sampled medium, before they enter the quadrupole. A monochromatic beam of electrons, typically at ~70 eV, is generated by thermionic emission from a heated filament and ionizes a portion of the gas sample on impact. In the Bristol MBMS experiment, the ionizing beam of electrons and the sample beam are orthogonal to each other in the cross-beam ion source. Cations generated in the interaction between these beams are extracted with a weak field perpendicular to both and accelerates them in the z-direction into the mass filter.

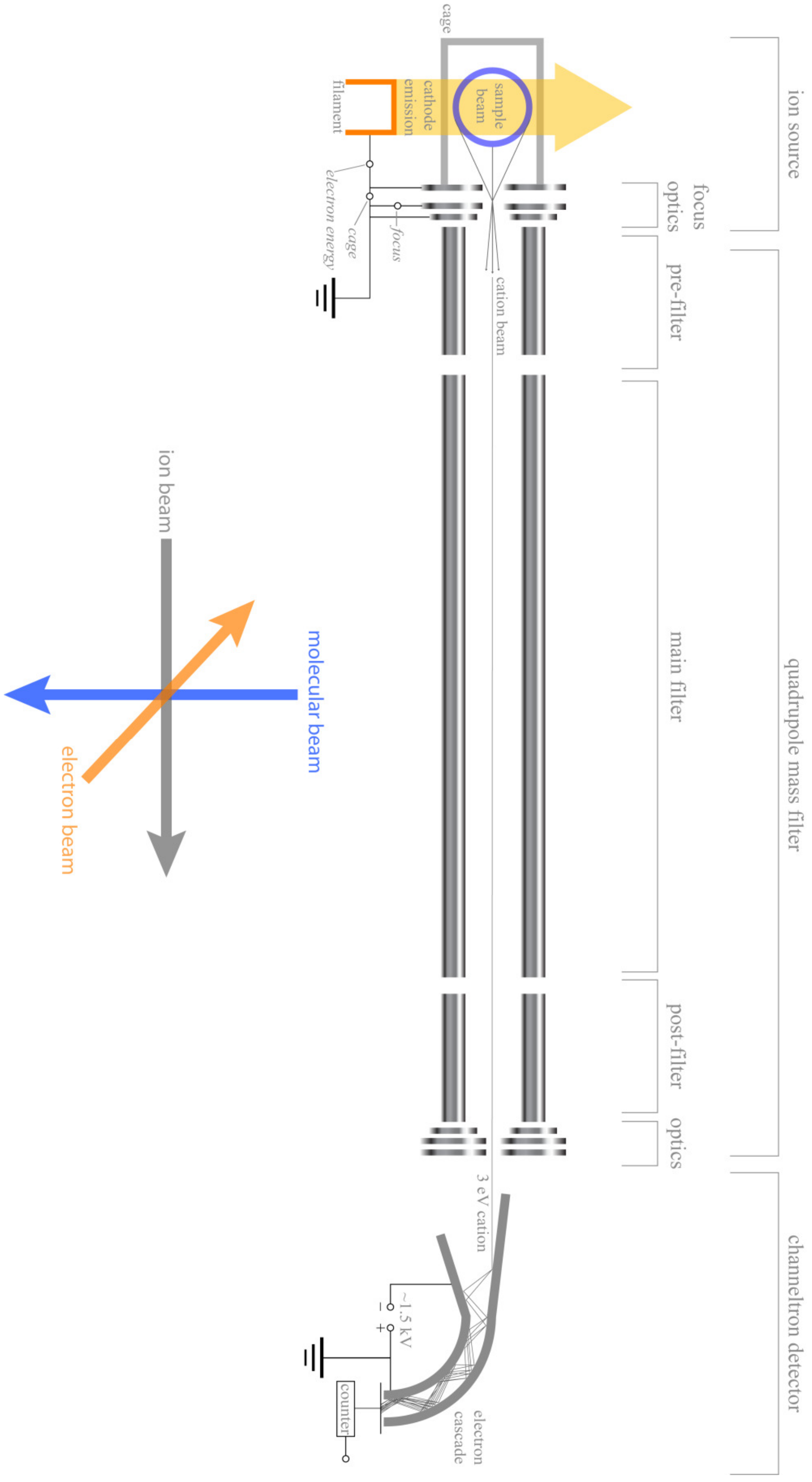

Figure 4.3: Schematic diagram of a typical quadrupole MS probe showing the composite parts: ion source, mass filter and ion detector (Hiden, 1993). Some of the operating variables are shown in *italics*.

4.1.3.2 Ion optics and mass filter

As previously described, the quadrupole mass filter consists of four cylindrical rods (two of which are shown in Figure 4.3) onto which the opposite d.c. and a.c. potentials are applied. In practice, a significant improvement in resolution can be achieved by increasing the number of radio frequency (r.f.) cycles acting on the charged species within the filter. This could be achieved in short filters by increasing the frequency or, more commonly, using longer quadrupole filters where ions typically have kinetic energy ~3 eV. To overcome the problem of the loss of these relatively low-energy ions to the low-pass filter (electrodes in the xz-plane), caused by the fringing fields at the extremes of the QMF, pre- and post-filters are employed. Operating only with r.f. fields, these provide a pathway through the Mathieu stability region with initial increase in q before the ions enter the main mass filter (Brubaker, 1968).

4.1.3.3 Ion detection

Ions which follow a trajectory directly through the mass filter are detected using a channeltron electron multiplier (CEM) to convert a single ion impact event into a cascade of electrons which can be measured as a current. Although not used exclusively, channeltron detectors are commonplace and are often constructed from lead silicate tubes which are coated with a semiconducting material. Incident ions are collected in the horn-shaped opening initiating an avalanche of electrons on subsequent impacts along a narrow, curved tube before being collected on an output electrode (see Figure 4.3). The collector is held at a potential around −2 kV which accelerates ions enough so that ~3 secondary electrons are emitted on each electron impact. A high gain is achieved, by holding the output electrode at 0 V, and after the cascade ~10^8 electrons are eventually produced from the original single ion impact event.

Detection gain is improved by operating in pulse-counting mode, allowing low signals to be measured, where the channeltron is run at saturation and the signal detected as a count rate. To improve the resolution, a discrimination level can also be set to remove noise from the measurement. Mounting the channeltron away from the z-axis and using a deflector plate is often required to reduce the noise derived from metastable species and photons produced in the ion source. Each channeltron will have a specific lifetime due to the damaging influence of high-energy ion impacts which limit the electron emission and, therefore, the gain. Attempts must be made to reduce the external factors, such as running at high pressures and contaminating the QMS with water or pump oils, so that the channeltron lifetime is extended as much as possible.

4.2 Molecular Beam MS

4.2.1 Beam formation and optics

Detection of radical species requires a method of preventing them reacting between the probed region and the detector. Formation of a molecular beam (MB) allows the extraction of a sampled gas into a much lower pressure environment so that the mean-free path becomes long enough that no quenching reactions can occur: their composition and gas temperature are essentially *frozen*. The beam, extracted under effusive conditions, can then be used to transfer the sample to the detector unperturbed and, in theory, the mole fractions measured in the ion source will be identical to those in the plasma. This effusive state is only possible if the orifice diameter is of the same order as the mean-free path in the plasma which is obviously impractical as the signal will be very small and the orifice will block in the CVD environment. However, many flow considerations are still valid if larger orifices, such as that used in this experiment, and non-effusive conditions are employed.

Degradation of the sampled beam is limited by stepping the pressure down through a number of stages reducing the shock experienced at each gas expansion and selecting only the unperturbed central section of the beam using skimmers. As the initial expansion from the plasma chamber at ~10^2 Torr through a sampling orifice to a chamber at ~10^{-3} Torr is a fairly large leak it will be non-effusive and supersonic, producing a shock-wave bounded by a Mach disk (Anderson, 1990). The dimensions of this shock-wave are dependent on the size of the orifice which also determines the flux of material into the next pressure stage. Beam skimmers act as the apertures between the next two pressure stages and are designed with a narrow tip and sharp leading edge to minimize scattering (Crichton, 2007) and collimate the beam so that it passes cleanly through the beam-modulating chopper and MS ion source. The first skimmer is located close to the sampling orifice, upstream of the Mach disk, to select only the gas for which the reactions have been halted, *i.e.* the isentropic region due to the reduction in the collision probability. Generally, the skimmer positioning becomes less of an issue if lower background pressures and stronger pumping are achieved. The divergent nature of the MBMS sampling orifice differs from many MB formation nozzles and may add further complexity to any calculations (Crichton, 2007).

4.2.2 Calculating beam properties

A relationship exists between the geometry of the molecular beam and the mean-free path which defines a dimensionless quantity known as the Knudsen number:

$$Kn = \frac{\lambda}{l} \tag{4.18}$$

where λ is the mean-free path of the sampled species (the average distance travelled without collision and, therefore, potential reaction) and l is a characteristic length scale of the instrument. In the MBMS experiment the crucial dimension is the diameter of the sampling orifice and in the first instrument for analysis of diamond deposition (see section 4.3.2) was calculated to have Kn = 0.1 (using an orifice diameter of 300 μm). This low value for an instrument means that collisions or recombination reactions between species after expansion are less likely and, thus, it should be possible to measure radical species before they are quenched. Thorough accounts of the composition distortions occurring during MBMS sampling have been given in the literature (Knuth, 1995, Singh *et al.*, 1999). In particular, analysis has shown that acceleration towards the non-effusive orifice results in an axial shift in the sampled region away from the substrate, by ~100 μm for a dilute mixture of Ar in H_2 at 100 Torr, while lighter species are influenced to a greater extent (Knuth, 1995, Swihart & Girshick, 1999).

Beam distortion caused by the large pressure gradients perpendicular to the beam results in radial diffusion of beam material and is one of the major sources of mass discrimination, addressed later. To calculate losses through reaction and the relaxation of the gas as it propagates, a 'zero'-dimensional model, where the calculated region has negligible volume but is still large on the molecular scale, was developed (Crichton, 2007). This model showed that $\chi(CH_3)$ and $\chi(H)$ drop in the beam due to losses through a CH_4-forming reaction between the two radicals rather between two CH_3 species.

4.2.3 Mass spectrometric sensitivity considerations

The intensity of the signal due to a certain fragment in the mass spectrometer can be given by:

$$I_{X^+} = i_e \sigma_X n_X \beta_{X^+} t_{X^+} \theta_{X^+} l_{cage} \tag{4.19}$$

where the measured count rate, I_{X+}, is the product of the emission current, i_e, the electron-energy-dependent ionization cross-section, σ_X, the number density of X in the ion source, n_X, the mass-dependent extraction efficiency of the ion optics, β_{X+}, the mass-dependent transmission efficiency of the quadrupole, t_{X+}, the mass-dependent detection efficiency of the channeltron, θ_{X+}, and the length of the ionization cage, l_{cage} (Singh *et al.*, 2000). This sensitivity is subsumed within a correction factor, a_{MS}, which can be calculated for different species.

4.2.4 Threshold ionization potential techniques

Detection and quantification of reactive radical species from the beam requires understanding that radical cations can be formed either by direct electron-impact ionization of the radical from the molecular beam or by dissociative ionization of some parent molecule.

Direct ionization: $$\mathrm{X} + \mathrm{e} \rightarrow \mathrm{X}^{+} + 2\mathrm{e} \tag{4.20}$$

Dissociative ionization: $$\mathrm{XY} + \mathrm{e} \rightarrow \mathrm{X}^{+} + \mathrm{Y} + 2\mathrm{e} \tag{4.21}$$

where Y could be a neutral, excited or even anionic species. The direct-ionization threshold ($\Delta E_i^{\mathrm{X}\rightarrow\mathrm{X}+}$) or ionization potential (IP) is typically > 2 eV below the dissociative-ionization onset ($\Delta E_a^{\mathrm{XY}\rightarrow\mathrm{X}+}$) or appearance potential (AP). The relative rates of these processes will depend ultimately on the energy of electrons formed in the ion source and, in practice, distinguishing between the two reaction pathways will involve setting the ion source to a electron energy (E_{e}) which only gives rise to direct ionization for a certain target species *i.e.* $\Delta E_i^{\mathrm{X}\rightarrow\mathrm{X}+} \leq E_{\mathrm{e}} \leq \Delta E_a^{\mathrm{XY}\rightarrow\mathrm{X}+}$ (Eltenton, 1947, Singh *et al.*, 2000).

Increasing the electron energy further than the AP can further complicate the analysis through formation of multiply charged species (observed at masses of m_{X}/n where n is the number of electronic charges). Deconvolution of these more complex spectra require knowledge of the cracking pattern of the molecules and often use modelling and statistical approaches (Kang *et al.*, 2002).

The use of threshold mass spectroscopy has been applied by the majority of the studies described in section 4.3 as well as many other plasma analytical fields (Agarwal *et al.*, 2004, Toyoda *et al.*, 1989, Tserepi *et al.*, 1997). Unfortunately, the technique has the slight disadvantage of providing relatively weak signals due to the small ionization cross-sections near the threshold potentials but is not reliant on complex deconvolution unless two species have masses which cannot be resolved by the quadrupole. Consideration should also be given to the internal energy of the species under analysis because hot molecules will fragment at lower energies and cause a significant spread in the observed AP for larger molecules with greater degrees of freedom.

One of the most difficult radicals to detect, the H atom, is also one of the most important for diamond-depositing systems. The main problem is the high partial pressures of H_2 which occur in all parts of the CVD and sampling system as it is commonly the most abundant gas added to CVD reactors. The count rate at 1 amu due to the H^+ cation can be produced from the two reactive pathways:

Direct ionization: $H + e \rightarrow H^+ + 2e$ (4.22)

Dissociative ionization: $H_2 + e \rightarrow H^+ + H + 2e$ (4.23)

Similarly, the other important radical for diamond deposition also suffers from interference from dissociative ionization:

Direct ionization: $CH_3 + e \rightarrow CH_3^+ + 2e$ (4.24)

Dissociative ionization: $CH_4 + e \rightarrow CH_3^+ + H^* + 2e$ (4.25)

Depending on the radical fragment in question there may be more than one possible parent species that may dissociate, further complicating the analysis. The energetics for each fragment and parent-species pair will depend heavily on the dissociative-reaction potential-energy surface which determines the distribution of energy between the reaction products and whether any of them are kinetically or electronically excited during the process. For the hydrogen system, above, the AP lies ~4 eV above the IP and corresponds well with the H_2 bond energy.

Experimentally, as long as the IP and AP are separated by a large enough energy gap, the calibration of the mass spectrometer is actually enhanced by observation of the onset of both reaction pathways for a certain molecular fragment. For the purposes of calibration, a count rate is measured with increasing electron energy for a certain mass fragment with 1) only the parent species in the molecular beam to measure the AP and then 2) a mixture of the fragment and the parent species in the beam to determine the IP. In the case of diamond studies this was first carried out by allowing the hydrocarbon/hydrogen gas mixture to form a molecular beam, first with the activating hot filament off (*i.e.* the cold gas) to measure the AP of CH_3 at 15 amu due to fragmentation of CH_4 as shown in Figure 4.4. Subsequent measurement of the count rate with the gas activated (hot filament on) produces signal due to direct ionization of CH_3 between the IP at 9.84 eV and AP at 14.3 eV and due to both direct and dissociative ionization above the AP.

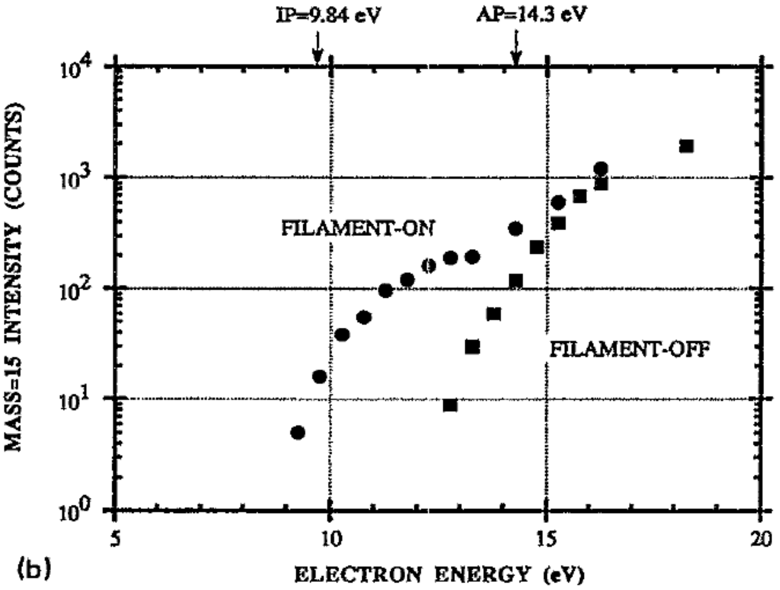

Figure 4.4: Example of a threshold mass spectroscopic study in a HFCVD reactor. CH_3 (15 amu) signal as a function of E_e when the hot filament is not heated (filament-off) and when heated to 2600 K (filament-on) as well as the locations of IP and AP indicated (Hsu & Tung, 1992).

4.2.5 Mass discrimination & correction factors

More accurate calibration of the instrument to a given target species, *X*, can be achieved by using the linear fits of the gradients of the count rate versus electron-energy plots near the threshold and using:

$$\frac{I_{\mathrm{X}^+}}{I_{\mathrm{R}^+}} = \left(\frac{\chi(\mathrm{X})}{\chi(\mathrm{R})}\right) a_{\mathrm{GD}} a_{\mathrm{MS}} \frac{\sigma_{\mathrm{X}}(E_{\mathrm{X}})}{\sigma_{\mathrm{R}}(E_{\mathrm{R}})} \tag{4.26}$$

where R is a standard gas, such as argon, of known mole fraction χ(R) in the system, a_{GD} is the relative mass-discrimination factor due to gas dynamics of the molecular-beam expansion, and a_{MS} is the relative mass-sensitivity factor for the mass spectrometer. For some radical species where the ionization cross-sections are not well known, it is possible to use the profile of a ‘similar’ species adjusted to the same threshold potential (Biordi, 1977).

The issue of mass discrimination by the MBMS instrument requires careful consideration as it is likely to always be present but can be corrected for if the factors a_{GD} are quantified accurately. It arises as the thermal speed is not constant with mass, leading to loss of lighter species from the beam. One method to counter this problem is to use an effusive leak of a standard, reference gas into the spectrometer to calculate the relative sensitivity factors using equation (4.1) to give:

$$a_{\mathrm{GD}}(\mathrm{X}) = \frac{\left(\frac{n_{\mathrm{X}}}{n_{\mathrm{R}}}\right)_{\mathrm{reactor}}}{\left(\frac{n_{\mathrm{X}}}{n_{\mathrm{R}}}\right)_{\mathrm{effusive}}} = \frac{\left(\frac{I_{\mathrm{X}}}{I_{\mathrm{R}}}\right)_{\mathrm{reactor}}}{\left(\frac{I_{\mathrm{X}}}{I_{\mathrm{R}}}\right)_{\mathrm{effusive}}} \tag{4.27}$$

$$a_{\mathrm{MS}}(\mathrm{X}^+) = \frac{\beta_{\mathrm{X}^+} t_{\mathrm{X}^+} \theta_{\mathrm{X}^+}}{\beta_{\mathrm{R}^+} t_{\mathrm{R}^+} \theta_{\mathrm{R}^+}} = \frac{\left(\frac{I_{\mathrm{X}}}{I_{\mathrm{R}}}\right)_{\mathrm{effusive}}}{\left(\frac{\sigma_{\mathrm{X}}}{\sigma_{\mathrm{R}}}\right)\left(\frac{\chi(\mathrm{X})}{\chi(\mathrm{R})}\right)_{\mathrm{known}}} \tag{4.28}$$

By using a range of gas standards the two sensitivity factors can be plotted as a function of mass and then species of unknown sensitivity can be estimated from these calibration curves. There should be little variation in a_{GD} with T_{gas} but this can be investigated for a given system and will vary for different gas mixtures being sampled. On the other hand, a_{MS} should be independent of both composition and temperature (Singh *et al.*, 2000). In our analysis this treatment is modified to provide a calibrating correction factor for measurements that are dependent on the prevailing gas mixture (see section 5.3.4).

This method gives the relative mole fractions of X and R and can be converted by dividing the definition of the mole fraction and dividing through by χ(R):

$$1 = \sum \chi(\mathrm{X}) \tag{4.29}$$

$$\frac{1}{\chi(\mathrm{R})} = \sum \frac{\chi(\mathrm{X})}{\chi(\mathrm{R})} + 1 \tag{4.30}$$

Converting to a number density requires knowledge of the local T_{gas} and the assumption that the sampled gas mixture obeys an equation of state.

4.3 MS applied to diamond growth studies

Ever since the first diamond films were produced by CVD technologies, mass spectrometry has been harnessed to provide the crucial analytical data used to establish and support mechanistic theory and computational modelling. MS experiments often have an advantage as they can measure a range of species simultaneously while many absorption-based studies tend to be set up to quantify just one. In this section the variety of *in-situ* instruments, and deposition reactors to which they are coupled, that have been developed in the field are examined in roughly chronological order with the emphasis on the gradual expansion of both the technical expertise and the analytical information with reference to the current theoretical arguments.

4.3.1 General Motors Research Laboratories, Warren, Michigan

Some of the earliest empirical data on the gas-phase chemistry occurring in diamond-depositing systems came from the coupling of a HFCVD reactor and a mass spectrometer *via* a quartz probe situated within the substrate to extract the gas mixture. The tube is maintained at 0.3 Torr with the HF reactor working at 20 Torr to allow quenching of neutral species. CH_4 and C_2H_2 were found to be the most abundant stable hydrocarbons and their respective mole fractions were measured as a function of the filament-to-substrate distance showing a rise in $\chi(CH_4)$ and drop in $\chi(C_2H_2)$ with increasing filament-substrate separation. Importantly, the analysis was allied with 1D flow calculations which suggested that only C_2H_2, C_2H_4, CH_4 and CH_3 were present in concentrations high enough to explain the observed growth rates (Harris *et al.*, 1988). While providing the first insights into diamond CVD chemistry, the setup was limited in only detecting stable species and, hence, offering only secondary data on the reaction mechanisms and no quantitative data on radical species.

Subsequent work with the same apparatus investigated the addition of oxygen to the reactor where it was found to reduce both $\chi(CH_4)$ and $\chi(C_2H_2)$ with a corresponding increase in $\chi(CO)$ also measured by MS. The kinetic models were augmented to include reactions involving oxygen using data from flame studies and produce fairly good predictions of $\chi(CH_4)$, $\chi(C_2H_2)$ and $\chi(CO)$. It was also suggested that the OH radical could etch pyrolytic carbon improving the quality of the diamond film and that the presence of CO aided deposition of diamond-like carbon at T_{sub} where only amorphous or sp^2 carbon would normally be grown (Harris & Weiner, 1989).

The $\chi_0(CH_4)$ in the input gas mixture was studied and, significantly, the $\chi(CH_3)$ was estimated by assuming that it undergoes a *self-scavenging* mechanism whereby two CH_3 radicals combine to form C_2H_6 and C_2H_4, the latter by rapid H-atom abstraction. This method assumed negligible loss of radicals to the probe/reactor walls and negligible concentration of both C_2H_6 and C_2H_4 in the sampling region. The detected $\chi(C_2H_4) + \chi(C_2H_6)$ signal was then calculated to be roughly half that of the CH_3 sampled, a result which was in good agreement with updated computation modelling. This method was extended to estimate $\chi(H)$ in the sampled region offering some insights into its pivotal role in the diamond growth mechanism (Harris & Weiner, 1990).

4.3.2 Sandia National Laboratories, Livermore, California

A key advancement in the instrumentation used to analyse diamond-depositing gas mixtures was the use of MBMS and this was first implemented coupled to a HF reactor (Hsu, 1991, Hsu & Tung, 1992, McMaster *et al.*, 1994). This essential modification allowed the quantitative detection of reactive species which had previously been quenched on collision with other molecules and the instrument walls. Combining MBMS with threshold ionization (see section 4.2.4) the analyses achieved a detection limit of 10 ppm for certain radical species with associated error of ±20% in calculated concentrations of all species.

The experiment initially was designed to sample a HFCVD reactor (typically operating at 20 Torr) through a 300 μm orifice situated in the substrate centre and into a 10^{-3} Torr chamber. The differential pumping – using 3 turbomolecular-pumped stages, separated by beam skimmers, to reduce the pressure down from 10^{-3} to 10^{-6} to 10^{-7} Torr in the QMS chamber – rapidly expanded the extracted gas increasing the mean-free path and impeding any further reaction. Further resolution was provided by using a tuning-fork beam-chopper (operating at 210 Hz) to allow subtraction of the background interference (Hsu & Tung, 1992). An instrument was thus constructed which was able to measure concentrations of stable species such as H_2, Ar, and C_2H_4 and some metastable radical species like CH_3 and H as functions of process conditions including $\chi_0(CH_4)$. Apart from C_2H_2, C_2H_4, CH_4 and CH_3 no other carbon-containing species were detected by this system leading to the assumption that the CH_3 radical must be a key diamond deposition species.

The MBMS apparatus proved robust enough on the HFCVD system that it was applied to a MWCVD reactor with comparisons between the two showing remarkable similarities (Hsu, 1992, McMaster *et al.*, 1995). It was shown that the plasma is dominated by thermal effects rather than ionic chemistry and allowed the proportionality of $\chi(CH_3) \propto \chi(CH_4)$ and $[\chi(CH_3)]^2 \propto \chi(C_2H_2)$ to be explained for HF systems through rapid interconversion between the hydrocarbon species as a function of T_{gas}. It was also concluded that H atoms were produced by thermal dissociation and electron bombardment at comparable rates. Evidence for filament *poisoning* at high methane concentration was also established as less atomic H is formed supporting similar studies (Celii & Butler, 1989, Hsu *et al.*, 1994).

The insensitivity of diamond-depositing plasmas to the input carbon source was also demonstrated by using C_2H_2 as the hydrocarbon precursor (McMaster *et al.*, 1995). Instead, the C/H ratio was much more important in determining the prevalent plasma chemistry, a fact that has been reiterated throughout mechanistic literature.

4.3.3 University of Massachusetts, Amherst

MBMS diagnostics of an r.f.-plasma-activated CVD reactor designed to deposit diamond-like carbon films in $H_2/Ar/CH_4$ plasmas at about 0.5 Torr were carried by sampling through a 800 μm orifice in the substrate. This apparatus was used to detect stable species such as CH_4, C_2H_2 and radicals such as H, but could not detect other species like CH_3 and CH_2. The MBMS results were compared with microprobe measurements that sampled into the plasma (Graff *et al.*, 1994).

4.3.4 University of Minnesota, Minneapolis

Two different MBMS instruments were constructed to detect species in thermal plasma CVD environments which operate at high powers of ~15 kW and up to atmospheric pressure. The first was designed to measure species through a 300 μm orifice in the substrate which extracts gas into a differentially pumped system and towards a mass spectrometer. A threshold-ionization technique was used to measure relative concentrations of CH_3, CH_4, C_2H_2, C_2H_4 and C_2H_6 and it was shown that the composition was independent of the feedstock hydrocarbon (Greuel *et al.*, 1995). A second design hoped to produce more accurate measurements of $Ar/H_2/CH_4$ plasmas running at 20-33 kPa (150-250 Torr) using a 75 μm orifice and shorter distances between beam optics. Again they applied the threshold-ionization method and produced a methodology for calculating mole fractions using Ar as an internal standard and determining transmission efficiencies for each species measured (Park *et al.*, 2004). This later instrument is of particular importance to our present study as the pressure range and T_{gas} are similar.

4.3.5 Physikalische Chemie I, Universität Bielefeld

Another MBMS experiment consisted of analysis of a diamond-depositing environment initiated using an oxyacetylene torch, made up of C_2H_2, O_2 and Ar, and combined MS with laser-induced fluorescence spectroscopy to detect various neutral and radical hydrocarbon species (Löwe *et al.*, 1999). Their use of time-of-flight MS is noteworthy as it allows better resolution of different species including those with the same m/z ratio. Not surprisingly for an instrument designed for and applied to measuring flame-like combustion CVD conditions through a 150 μm orifice, the experiment succeeded in measuring a large range of hydrocarbon species which were able to be quantified using calibration methods similar to our own (see section 5.3.4). Sampling was, again, achieved through a substrate which was able to translate closer to the torch allowing some spatial distributions to be mapped relative to a region of successful diamond deposition. The results led to the conclusion that diamond deposition in these systems was possible inside a narrow window of $\chi(CH_3)$ and $\chi(H)$ whilst the OH radical was found to inhibit deposition. Additional support to these results was provided by modelling the system using the CHEMKIN package (Kee *et al.*, 1985), updated to include new species found in these combustion flames. It was found that there was good correlation between experiment and prediction for the stable species (O_2, CO, C_2H_2) but less consistent for the radical species (CH_3, C_3H_3, C_4H_2) which required some linear scaling to match up (Kohse-Höinghaus *et al.*, 2000).

4.3.6 CNRS/Université d'Orléans, Orléans

Researchers at the Laboratoire de Combustion et Systèmes Réactifs focused their MBMS study purely on the CO_2/CH_4 MWCVD system typically at low pressures, p ~ 10-20 Torr. This system has special significance as a wider range of radical and neutral species were detected including many larger hydrocarbons, C_xH_y where $x > 3$, although this is likely to be due to the slightly different experimental conditions sampled (Aubry *et al.*, 2002). Specifically large-chain radicals, such as C_3H_5 and C_6H_5, and aromatic molecules, C_6H_6 and C_7H_8, were detected in the plasma system for the first time although their presence was theorized to be due to the formation of soot and a-C at the plasma periphery. It appears that they are more prominent in CO_2/CH_4 mixtures than in standard H_2/CH_4 plasma systems and, when present in high concentrations, can lead to deterioration of the diamond quality by forming sp^2-carbon deposits.

A variation in the mole fractions of most species within the plasma system was measured as the total flow rate of gas through the chamber was increased, leading to the conclusion that the residence time within the plasma led to differences in the chemical composition (Aubry *et al.*, 2004). It was proposed that some reactions which form species such as CO and C_2H_2 did not have time to reach an equilibrium state if shorter residence times/larger flow rates were utilized. Personally, this proposal seems fairly unlikely as the volume is large enough and reaction kinetics fast enough for CO and C_2H_2 reactions to occur to completion, although this could be fairly reactor specific especially at the low p used in this experiment.

Like other studies the input power and chamber pressure were shown to alter the plasma composition by influencing the T_{gas} and the reaction kinetics (Met *et al.*, 2006).

Most recently, the group has investigated the influence of $\chi_0(CH_4)$ in the apparatus coupled with more advanced theoretical predictions of mole fractions of a large range of species and, again, observations were attributed to the varying 'degree of conversion of the chemical system'. Despite some ambiguity in their discussion, the array of species detected by MBMS remains impressive and the correlation between theory and experiment is often good.

4.3.7 Department of Atomic Physics, TU Budapest

A different approach was taken at the TU Budapest to measure the ionic composition of a MWCVD plasma using a very similar method known as ion beam mass spectrometry (IBMS), where the beam enters the QMS without being ionized first leaving only charged species in the beam to be detected. Like the Orléans study, plasmas in the range of p = 1-35 Torr were studied producing interesting results concerning the density and energy distribution of ions within the CVD environment (Kátai *et al.*, 1999a). This was followed with a quantitative study which also addressed the issue of substrate biasing using a potential difference between 0 and 200 V as well as the ionic concentrations with $\chi(CH_4)$ ~ 0.0025-0.08 (Kátai *et al.*, 2000a). Working at a bias voltage of 200 V accelerates a range of ions towards the substrate, including C^+, CH^+, CH_2^+, C_2H^+, $C_2H_2^+$ and $C_2H_3^+$, all with energies between 50 and 80 eV. At a bias of 100 V the energy distribution had fallen to 30-40 eV, too low for implantation into the substrate surface and, therefore, not viable for successful nucleation. Further experiments concentrated on detailing the mechanisms of bias-enhanced nucleation with variation in applied voltage and hydrocarbon content (Kátai *et al.*, 1999b, Kátai *et al.*, 2000b). Moderate potentials placed on the substrate were also used to detect radicals such as CH_3 and C_2H which were overlooked in previous studies allowing comparisons between MBMS and IBMS to be made (Kováts & Deák, 2005). The detection of C_2H near the substrate and a correlation between its mole fraction and the growth rate has led to the proposal that it may play a role in the deposition process (Deák *et al.*, 2007).

Recently the IBMS apparatus has been applied to systems where argon has been added to the gas mixture to induce NCD deposition. Their results showed that a nanocrystalline morphology could be produced at lower $\chi(Ar)$ if a substrate bias was applied simultaneously and that the C_1 hydrocarbons (C, CH, CH_2 and CH_3) were likely to play a key role in the mechanism of NCD deposition (Csíkvari *et al.*, 2009).

4.3.8 Institut für Physik, Universität Augsburg

For completeness it is worth mentioning the analysis carried out in conjunction with OES studies of a MWCVD reactor with a gas mixture consisting of 1% CH_4 in H_2 to which was added between 130 and 8330 ppm of H_2S. Gas was extracted from the base of the reactor using a 0.15-mm-diameter capillary linked to a QMS system for measuring stable species. While being limited in the number of species which could be analysed, the results demonstrated the relative abundance of CS and H_2S and the reduction in stable hydrocarbons as the sulfur was added (Sternschulte *et al.*, 2002).

4.3.9 Summary

MS analysis has proven to be a very productive diagnostic tool for investigating the diamond CVD environment. Through its evolution the MBMS technique has become a more robust and reliable method for producing quantitative measurements of the mole fractions of not only stable species but also the more elusive radicals which are so important for diamond deposition. The MBMS apparatus has been applied to many different systems working under different conditions and provides a wide range of results which, combined with other experimental and computational methods, has revealed a more detailed understanding of the diamond growth mechanism. However, there are still problems of detecting radical species in higher *p* systems and ensuring that results are accurate by improving detection limits. After describing the development of the Bristol MBMS experiment through a number of different stages we focus on its latest incarnation (section 4.5) and testing (section 5.0).

4.4 MBMS studies at the University of Bristol

4.4.1 Diamond CVD analysis

In the Bristol diamond group, the MBMS concept was initially applied to a HFCVD reactor with gas sampled not through the substrate but using a 100 μm orifice at the end of a translatable, molybdenum probe projecting from the side of the reactor into the region heated by the filament. A beam was established by sampling the reactor chamber (~20 Torr) into a differentially pumped system reaching the QMS system at 10^{-6} Torr and modulated using a tuning-fork beam chopper (Tsang, 1997).

Early experimentation investigated the gaseous composition as a function of distance from the hot filament using a mixture of 1% CH_4 in H_2 which showed increases in $\chi(H)$, $\chi(CH_3)$ and $\chi(C_2H_2)$ closer to the filament (Rego *et al.*, 1994). Subsequent studies showed the influence of T_{filament} on the gas composition. It was also concluded that the diamond-deposition mechanism was independent of the hydrocarbon precursor employed with CH_4, C_2H_2, C_2H_4 & C_2H_6 source gases producing nearly identical compositions within the reactor (Rego *et al.*, 1995). It was also found that thermal-diffusion effects limited the diamond growth rate at T_{filament} higher than an optimum of ~2400 K while at lower temperatures a smaller proportion of the hydrocarbon precursor species were dissociated into radicals.

Following extensive study of the HFCVD system the MBMS apparatus was transferred on to a MWCVD reactor in a similar arrangement, sampling through the side of the reactor (Leeds, 1999) although there was found to be some perturbation of the plasma by the probe (Leeds *et al.*, 1999b). The results showed that the plasma composition was independent of the source hydrocarbon above $P = 0.7$ kW and that the $\chi(CH_3)$ near the substrate was higher than found in previous studies and computer modelling (Tsang *et al.*, 1999). It was demonstrated that probing the side of the plasma exerts a stronger influence at lower MW powers causing the discharge to deform and become asymmetrical and, thus, affects the MBMS analysis. Sampling the reactive plasma region also had its disadvantages where the orifice became blocked or detrimentally etched.

4.4.2 Addition of chlorine

The Bristol MBMS-HFCVD apparatus was the first MS system to investigate the behaviour of addition of other gas species to the diamond-deposition environment. First to be added was chlorine which was known to influence the deposition processes and enable diamond growth at lower substrate temperatures (Chu & Hon, 1993, Hong *et al.*, 1993). In the MBMS analysis both chlorinated methane ($CH_{4-n}Cl_n$, $n = 0\text{-}4$) and CH_4/Cl_2 mixtures were added to a HFCVD system with H_2 and showed similar deposition results and optimum T_{filament}. The research concluded that atomic Cl is mostly converted to HCl in the reactor and increases the growth rate by producing active sites on the diamond surface without being incorporated into the film (Rego *et al.*, 1996, Tsang *et al.*, 1996).

4.4.3 Addition of nitrogen

In sections 1.5.3 and 3.4 we saw how addition of nitrogen to diamond CVD systems can influence the growth rate and the crystalline morphology, and in the MBMS experiment a range of nitrogen-containing gas mixtures were analysed. These included mixtures of 0.5% CH_4 in H_2 to which 0.5% NH_3 or 0.25% N_2 was added, or 0.5% CH_3NH_2 in H_2 or, finally, 0.5% HCN in H_2, all of which maintain a 1:1 ratio between C and N (Tsang *et al.*, 1997). In all of these systems carbon was found to be present as HCN with, surprisingly, little C_2H_2 detected, and this is likely to be the reason for the slow growth rates and nanocrystalline morphology obtained. It was also proposed that the nitrogen could also limit the etching rate of sp^2 carbon by atomic H.

The findings of the HFCVD study were corroborated when similar gas chemistry was applied to the MWCVD-MBMS setup in that mechanisms did not depend on the identity of the N source and that large quantities of HCN were formed in the plasma (Leeds *et al.*, 1999a).

4.4.4 Addition of phosphorus

MBMS analysis of the HFCVD environment when PH_3 (up to 5000 ppm) is added to the gas phase showed presence of HCP (analogous to HCN) although it could not be quantified accurately and its role within the diamond mechanism was not determined. Diamond deposition results indicated an increase in the growth rate, as seen with nitrogen, that reached a maximum at 2000 ppm before decreasing (Tsang *et al.*, 1998).

4.4.5 Addition of sulfur

Sulfur doping was examined using species such as CS_2 and H_2S in the source gas mixture in both HF- and MWCVD systems which exhibited similar gas compositions but with a greater uptake (0.2%) of S in the MW grown films. As higher mole fractions of CS were detected in the MW reactor it was proposed that this species was important for doping of diamond with sulfur (Petherbridge *et al.*, 2002a, Petherbridge *et al.*, 2002b).

4.4.6 CO_2/CH_4 plasma analysis

The C-H-O system was investigated by film deposition, emission spectroscopy and MBMS analysis using $CH_4/CO_2/H_2$ mixtures and the same MWCVD apparatus as above with the aim of determining what mechanistic differences exist which allows film deposition at lower T_{sub} than standard H_2/CH_4 plasmas. Computational modelling indicated that the CO species may play an important role at the diamond surface, but CH_3 radicals are still likely to be the main growth species (Petherbridge *et al.*, 2001a). MBMS analysis showed negligible amounts of O, O_2 and OH within the plasma contrary to earlier theories of the role of oxygen in low-T diamond CVD. A maximum in the χ(CO) correlated with the gas mixture which produced the fastest growing, highest quality diamond films, indicating that CO plays an important role in the low-T chemistry. Some mechanistic pathways were suggested based upon adsorption of CO dangling bonds onto the diamond surface which can become involved in the carbon insertion (Petherbridge *et al.*, 2001b, Petherbridge *et al.*, 2001c).

4.5 New MBMS design

After the analysis of the CO_2/CH_4 system, the MBMS-MWCVD apparatus was completely redesigned to sample through the substrate in a new reactor chamber (Crichton, 2007). This would allow quantitative measurements of species in the critical region just above the substrate, something which was impossible with the previous experimental setup. Sampling in this way would also limit the perturbation of the plasma which had been so problematic when using a probe in the side of the reactor. Using a cross-beam ion source reduces the background noise experienced by the detector, while modulating the beam with a chopper improves the sensitivity to radical species. The setup is shown in Figure 4.5 with the direct line-of-sight between the plasma and the ion source clearly marked. Validation of the new MBMS design was achieved using a simple model (Crichton, 2007). The reactor is the same as used for the deposition experiments but with a sampling insert substituted for the Al plate at the base of the CVD chamber (see section 2.1 for details of MW reactor).

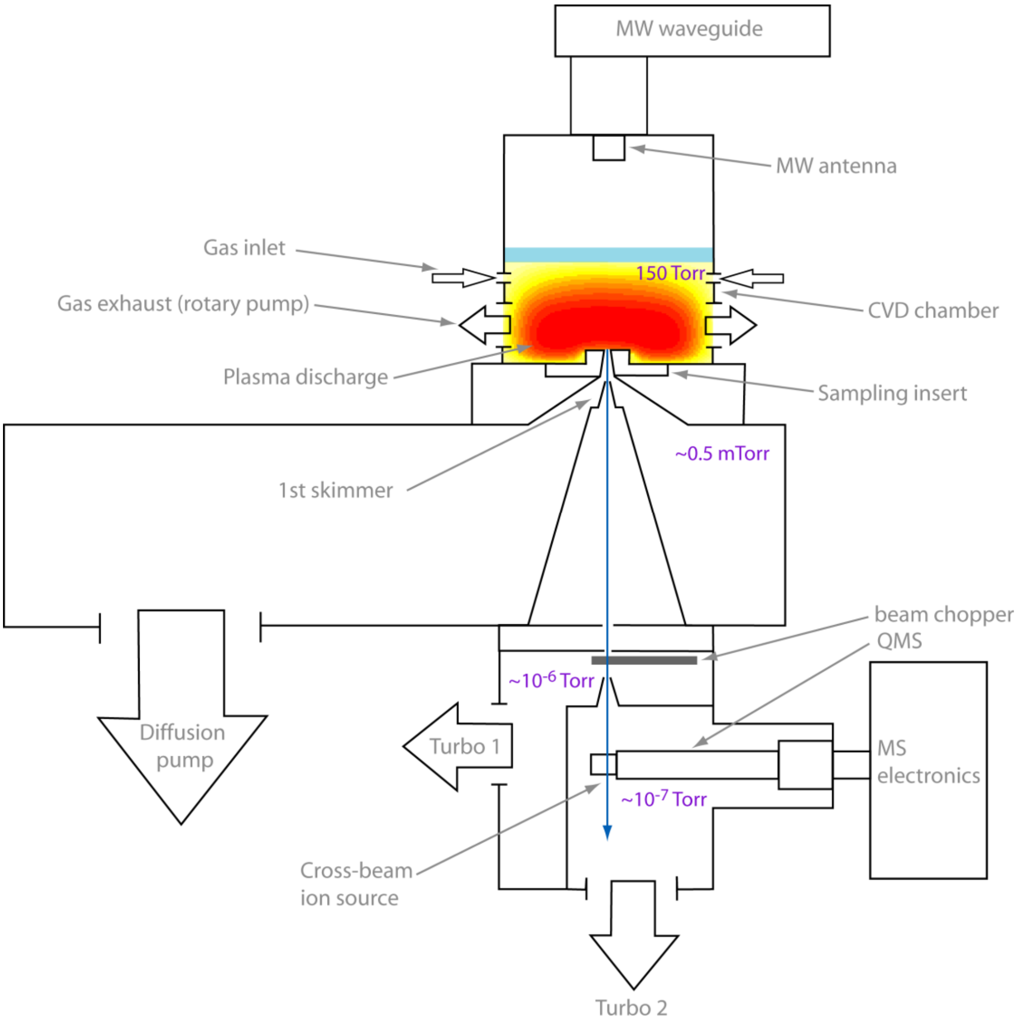

Figure 4.5: Diagram of the new Bristol MBMS-MWCVD experiment.

4.5.1.1 Sampling insert

Gas extraction from the plasma into the MBMS system uses an expansion orifice (SEM aperture, Agar Scientific A0909M) located precisely in the centre of a molybdenum plate which takes the place of the Al platen when running the plasma diagnostic or deposition experiments (see Figure 4.6). The orifice is made from chemically resistant molybdenum and brazed into position, after finding that silver conductive paint was not sufficient and would alter its properties on plasma treatment (Crichton, 2007). Thermal breaks are machined into the sampling annulus to control the axial heat flow and the Mo plate is sealed into the larger diameter, water-cooled, Al reactor base with an O-ring and secured with six countersunk M4 screws.

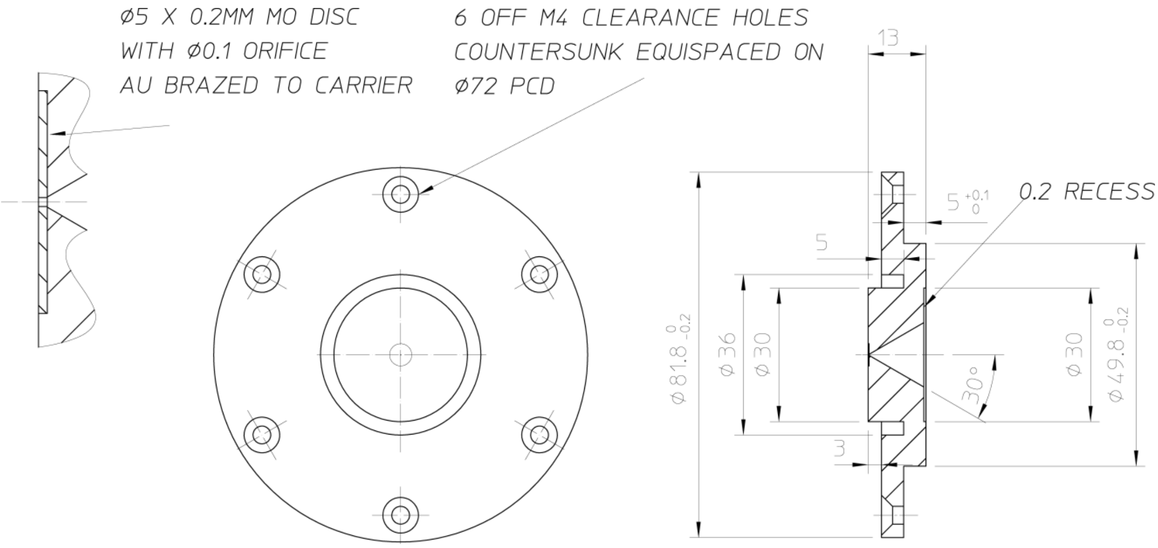

Figure 4.6: Orthographic projection of the molybdenum sampling insert.

4.5.1.2 Pumping stages

The first stage (termed the *box* stage with pressure, *p*(BOX)) of the differential pumping system forms the isentropic gas expansion and is evacuated using a 3000 l s^{-1} (H_2) cryo-cooled diffusion pump (Edwards 250M cryo-diffstak) which is backed by a rotary pump (Edwards E2M80). The pressure in this chamber (~0.1-1 mTorr) is monitored by a Pirani gauge (KJL 902006) and a Penning ionization gauge (Edwards CP25-K) and its large dimensions are a direct result of the large-diameter pump throat required for high conductance. The second (*mid*) and third (*MS*, with pressure *p*(MS)) stages are both pumped by 180 l s^{-1} (H_2) turbomolecular pumps (Edwards EXT 255) which are each backed by an oil-free scroll pump (ULVAC DIS-250). These high vacuum chambers are monitored using Penning ionization gauges (Edwards CP25-K), and the two backing pumps by Pirani gauges (Edwards PRM10) positioned between the primary and secondary pumping stages.

4.5.1.3 Beam optics and modulation

After the first orifice (Figure 4.7a) the beam is manipulated further using two skimmers and a rotating chopper wheel before reaching the ion source. The first skimmer (Figure 4.7b), with an orifice size of 0.3 mm, selects only the central part of the expanding gas plume ~15 mm below the sampling orifice to reduce the length in which the beam experiences background attenuation. The beam is skimmed once more (3 mm orifice) before entering the final, lowest pressure stage.

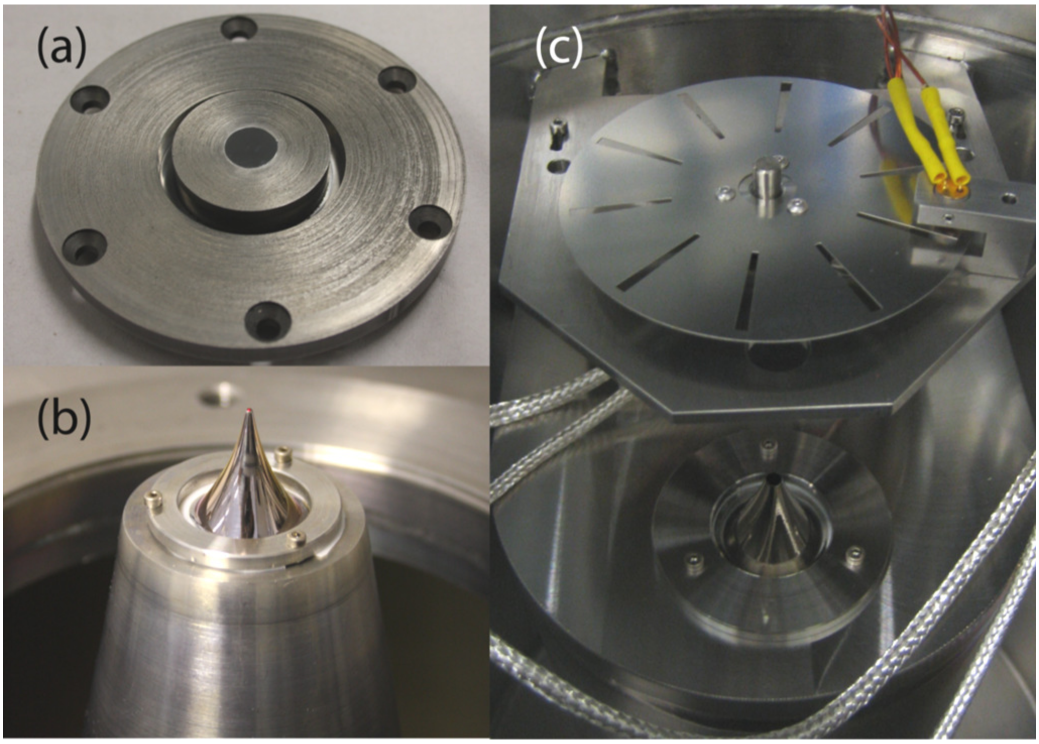

Figure 4.7: Photographs of the apparatus required to form the molecular beam: (a) the Mo sampling insert, (b) the first skimmer and (c) the beam chopper (above) and second skimmer (below).

The beam chopper, situated in the second pressure stage, consists of a wheel containing a number of slots (Figure 4.7c) which is rotated using a stepper motor (Arun Microelectronics Ltd.) and allows a beam-on (signal) and beam-off (background) measurement of the sampled mass within the ion source, hopefully improving the signal:noise ratio. The chopper frequency and phase are monitored on an oscilloscope (200 MHz LeCroy Wavesurfer) using a signal from a LED and photodiode mounted either side of the chopper wheel.

4.5.1.4 Quadrupole mass spectrometer

Located within the highest vacuum stage of the MBMS instrument is the Hiden Analytical positive-ion counter quadrupole mass spectrometer (HAL RC PIC101) which is mounted on a 4.5” CF flange perpendicular to the molecular beam intersecting with it at the ion source. The ion source contains two oxide-coated iridium filaments which emit an ionizing beam of electrons and rotates the ion trajectories through 90° into the QMS. The cross-beam mode of operation lowers the background by preventing high-energy radiation or ionic material in the beam from passing straight through the quadrupole and reaching the detector. In the current setup the beam passes through the ion source and is extracted by the second turbomolecular pump. The QMS feeds through to the RF head which contains electronics for running the system and returns an output signal to the mass spectrometer interface unit (MSIU) that acts as the computational control of the QMS system. Data analysis is provided by the Hiden MASsoft programme (www.hiden.co.uk/index.php/en/software-support/5-massoft) and a LabView 8.2 program developed in-house (see section 5.2). This data acquisition system was designed to an improved specification based, in part, on the shortcomings of the previous MBMS setup.

5.0 MBMS of MWCVD plasmas

5.1 Apparatus modifications and changes

The basic apparatus at the beginning of the project was able to take mass spectra, but neither the sensitivity nor the data collection processes were quite good enough to allow accurate quantitative information to be obtained. A number of modifications were made to improve the pumping efficiency, the quality of the vacuum, the beam alignment, the time-gated data collection and the control software. Throughout this ongoing project the most telling indicator of the state of the instrument is the signal (n_S) to background (n_B) ratio which is determined for some standard conditions to allow direct comparison with previous values and chart the improvements to the system. Following from previous work (Crichton, 2007), the standard test gas mixture consisted of 500 sccm H_2, 40 sccm Ar and 25 sccm CH_4 at room temperature and 100 Torr. To test the system the gas mixture was allowed to stabilize within each vacuum stage but with the chopper switched off. While recording the intensity of ^{40}Ar against time, the chopper was stepped manually so that the on and off positions were clearly visible as steps in the trace. The higher sections of this trace would then correspond to n_S+n_B and the lower regions equal to n_B. A measure of the sensitivity of the instrument can be determined from the ratio of n_S and n_B expressed as percentage.

5.1.1 Pumping and vacuum

Achieving the best vacuum possible in all the differentially pumped chambers is paramount for accurate working of the MBMS system, to ensure the beam is not distorted through collision with any residual gas and that the mass spectrometer is free from interference from background contamination. Lowering of the base vacuum – when the pumping chambers are sealed and no gas is flowing into the system – was achieved by removing background species from the residual gas. Typically, this background consists of air which leaks into the system, giving peaks at *m*/*z* = 28, 32, 44 amu, respectively, a large peak at 18 amu due to water retained within the reactor and adsorbed onto the metallic surfaces, and, lastly, a small quantity of hydrocarbon species at different masses. These three groups were dealt with using different steps, described below, and which, over the course of the project, resulted in a steady improvement in the high vacuum and a reduction in the background contamination.

5.1.1.1 Cold trapping

Removing water from the system is important due to the large peak it gives rise to at 18 amu which dominates the spectrum in this region and can even influence neighbouring peaks, with the possibility of interfering with the CH_4 peak at 16 amu or the Ne peak at 20 amu. For the higher vacuum stages the presence of water is more problematic and many UHV systems employ some kind of trap or cold finger to remove water and other unwanted background species (Aubry *et al.*, 2002). A simple cold trap was installed in the Bristol MBMS experiment by using a liquid N_2 coil situated in the final stage, directly below the mass spectrometer. The hardware consisted of a short cross-shaped chamber with two 6” CF flanges on the vertical faces and two 4.5” CF flanges on the horizontal axis. The larger flanges allowed the chamber to be attached to the MBMS apparatus between the MS chamber and the final-stage turbomolecular pump. On one of the smaller flanges a specially designed feed-through was manufactured to allow a feed and return ¼” Swagelok® pipe to pass into the UHV system. Inside the system this pipe was formed into a coil that filled the small chamber but situated symmetrically so it would not distort the beam passing from the ion source to the pump. Liquid nitrogen was added to the trap from a reservoir which required periodic refilling throughout the experiment. All the exposed metal surface and pipes outside the vacuum system were appropriately lagged to prevent the nitrogen boiling off prematurely.

The apparatus was tested by running a mass scan between 0 and 100 amu as the trap was cooled with liquid nitrogen and then allowed to warm up again. Observations showed a reduction (~37%) in the water peak as the trap cooled but, instead of being preferentially pumped away, as the trap warmed up, the peak returned to similar levels. Apart from the reduced water peak there appeared to be little change in any other background count rate with n_S:n_B ~ 5% As such, it was decided that the internal cold finger produced little gain in background reduction considering the amount of effort required to keep the N_2 coolant flowing (filling every 15 min) and the apparatus was removed from the MBMS experiment.

Throughout this period of vacuum improvement it was apparent that there was some degree of fluctuation in the signal from various hydrocarbon-based peaks between 40 and 70 amu. It was proposed that this could only come from back-streaming oil from the rotary backing pump which might reach the *box* stage of the apparatus when roughing out the chamber or when the diffusion pump is switched off. Any oil from the diffusion pump would give a different response in the mass spectrum as it is based on phenyl groups unlike the long-chain hydrocarbon oils which could, potentially, be mistaken for molecules originating in the CVD plasma. To prevent any stream of hydrocarbons and to remove other contaminants, an in-line cold trap was installed in the pumping line between the diffusion pump and the rotary backing pump. This consisted of two stainless steel pipes of different diameters welded together in such a way that the gas passes down the inner pipe and up the outer pipe before being pumped away. The whole assembly is placed in a dewar of liquid N_2 which cools all the metal surfaces to trap any oil, water or other molecules. After using this setup for a few weeks the vacuum substantially improved and the hydrocarbon background was nearly completely removed. It was obviously necessary to clean the trap occasionally to remove the collected contaminants and this was done by washing the trap through with ethanol and blow drying while extracting any gaseous species into a duct. Due to the improvements observed with the cold trap it was used for all subsequent experiments. In addition, the procedure for shutting the diffusion pump down was reviewed to ensure that there was no chance of any pressure gradients which would assist the back-streaming of pump oil.

5.1.1.2 Degassing

Compared with the contaminant removal performed by either cold-trap design, the reduction of background interference is more apparent when degassing the filaments. This procedure places a voltage across the ion-source filaments, but not the QMS, and results in the heating of the ion source and neighbouring metalwork so that water and other species desorb and are, hopefully, pumped away. The result is a much cleaner mass spectrum and a better n_S:n_B ratio which overall improves the sensitivity of the instrument. It also results in a reduction in any peak-intensity drift which is sometimes observed if the spectrometer has not been operated for some period of time.

As well as this routine degassing, performed for between 30 min and 1 h before beginning any experiment, the whole experimental apparatus was baked out using a resistively heated tape which surrounds the vacuum system. This was mandatory following opening of the system to air, for example when aligning the beam, and resulted in a large decrease in the background interference mostly due to loss of water but also through removal of N_2, O_2 and CO_2. Typically the system was heated to ~120 °C, lagged with insulating, metal foil and left to degas for a whole day and resulted in superior vacuum being achieved when the system cooled back down.

5.1.1.3 Vacuum improvement

Towards the beginning of the project it was observed that the diffusion pump was not pulling the best vacuum it could achieve. The pump operates on the principle of capturing gas, and other volatile contaminants, in a high-velocity jet of heated pump fluid, in our case Santovac 5 (a polyphenyl ether), as it condenses on approaching the water-cooled pump body. In doing so, the gases are compressed and are extracted to the next stage of the pump before, eventually, be removed through a backing-condenser to the rotary backing pump. With the aim to get closer to the stated working capacity (3000 l s^{-1} H_2) the cooling water circulation was modified. The pipework was diverted from its original course to achieve a higher flow rate through the pump cooling coil as it was observed that the pump was heating up when working at capacity. The pump fluid was also replaced as this had become discoloured with contamination from inside the pump. These alterations combined to allow a better and more stable vacuum to be achieved.

Throughout the project the vacuum was monitored using a leak-check method with a stream of helium directed around joints outside the instrument while the MS was set to measure an m/z of 4 amu and using an electron energy ~30 eV because of the high IP of He. Due to the small size of He atoms and the excellent detection limit when the MS is run in a base vacuum $\sim 5 \times 10^{-8}$ Torr any small leaks at insufficiently tightened joints were quickly identified and sealed.

5.1.2 Beam optics

Perhaps the most significant improvement in the spectrometer sensitivity was made by adjusting the alignment of the beam optics. It is obvious that precise positioning of the orifices and beam skimmers within the apparatus will allow a maximum flux of gas to pass through the ion source and result in the largest signal intensity possible. In doing this alignment any detrimental beam scattering from offline surfaces will also be minimized. However, accurate positioning of the sampling orifice, the two beam skimmers, the chopper aperture and the MS ion source is not straightforward and an experimental method was developed to achieve greater precision. This became absolutely necessary when attempting to align the smaller orifices and skimmers used later in the project.

To align the beam optics a He-Ne laser, adjusted through 3 degrees of freedom using 3 prisms, was used to provide a line-of-sight onto which the skimmers could be placed. A crucial modification was to use a photodiode and oscilloscope to provide a more accurate measurement of the brightness of the laser light passing through all the components rather than using the previous method of inferring the brightness by eye. For this method to work the chopper was run at low frequency and, thus, produced a pulse of light whose intensity could be measured.

At the outset the laser was aligned crudely with the widest diameter components at the top and bottom of the MBMS apparatus, *i.e.* passing the beam through the ion source, the second 3 mm-diameter skimmer and the sampling orifice. Next, the first skimmer (0.3 mm) was aligned with this beam by removing the sample extraction plate and carefully positioning and securing the skimmer in place. Further freedom was provided by using two PTFE seals between the skimmer itself and the clamp which holds it in place (see Figure 5.1a). Lastly, the sampling orifice and reactor base-plate were repositioned carefully above the skimmer and tightened incrementally, ensuring that the laser intensity remained at a maximum. At this stage the amount of light transmitted was hardly visible and the photodiode was, therefore, essential for the successful alignment.

A measure of the success of the alignment is gained from recording the change in the signal-to-background ratio for the standard test-gas mixture (see section 5.1) and results are shown in the following table.

test	n_S counts s^{-1}	n_B counts s^{-1}	n_S:n_B %
I	7256.94	5527.64	**23.8**
	Orifice alignment		
II	58555.77	26172.54	**55.3**
III	59187.17	25633.89	**56.7**
IV	78824.67	33109.03	**58.0**

Table 11: Improvement in signal-background ratio (n_S:n_B) of the m/z = 40 Ar peak after alignment of beam optics using sensitivity test and a gas mixture of $\chi_0(H_2) = 0.88$ ($F(H_2) = 500$ sccm), $\chi_0(Ar) = 0.07$ ($F(Ar) = 40$ sccm) & $\chi_0(CH_4) = 0.04$ ($F(CH_4) = 25$ sccm) at $p = 100$ Torr with no plasma ignited.

The improvement on alignment is stark with a doubling in the n_S:n_B ratio and an eightfold increase in the signal count rate. Further increases (between II and III) were achieved through improvement to the vacuum system through degassing and heating. The system will continue to be tested in this way to monitor the efficiency of the MB and pumping apparatus.

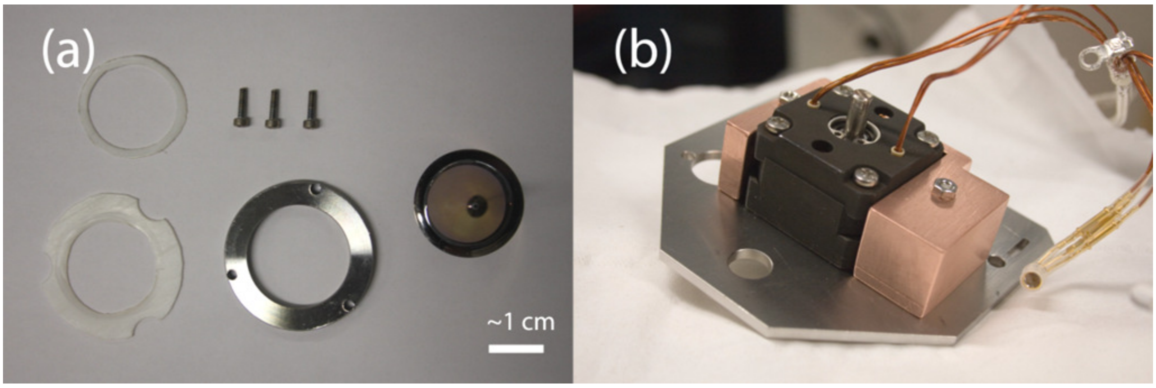

Figure 5.1: Two engineering problems addressed during testing of the MBMS apparatus. (a) the first skimmer (right) together with the new PTFE seals (left) and circular clamp (centre) which hold it in place. (b) the copper heat sink surrounding the chopper stepper motor.

5.1.3 Beam modulation

Modulation of the molecular beam produced by the beam optics was achieved using a rotating chopper mounted across the beam axis within the penultimate differentially pumped (MID) stage. The spectrometer is synchronized, on an 8 MHz timebase, with the chopper using an OPTO-IR circuit consisting of an LED and photodiode located either side of the rotating chopper wheel.

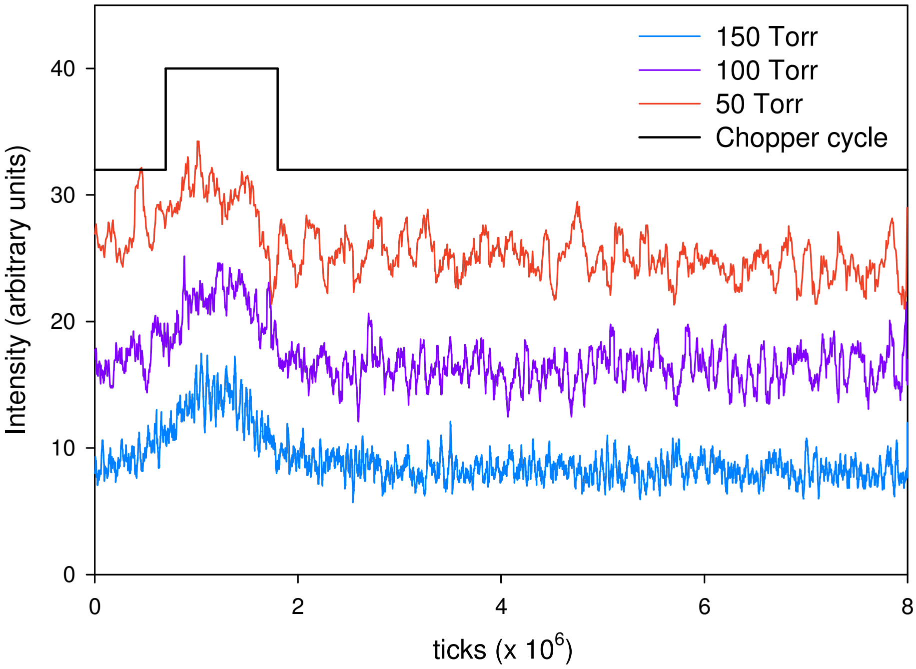

Figure 5.2: Synchronization between chopper cycle and the molecular beam measured using a leak of N_2 into 500 sccm of H_2 at 3 different pressures. The uncorrected signal is noisy due to the very short sample time and, hence, low count rate per gate used to collect this data: at 50 Torr the beam is hardly visible above the noise level. Note that the scans have been offset on the *y*-axis.

Although not directly measuring the identical chopper slit through which the beam passes, this detection system is offset in such a way that there is an exact match between the phase of the physical beam and the OPTO-IR measurement (Figure 5.2). The rising edge of this square wave provides the initiation for the time-gated detection system.

The stepper-motor control allows a frequency to be set which correlates with the beam-chopping frequency as shown in the following table:

Motor frequency Hz	*Chopper frequency* Hz
50	2.5
100	5
200	10
500	25
1000	50

Table 12: Correlation between stepper-motor frequency and beam-chopping frequency.

The chopper was operated at frequency at which the detection system was stable (see section 5.2) and this meant using values around frequencies of 10 Hz because the algorithm could not cope with faster speeds and data collection was too lengthy any slower than this. Optimization of this parameter allowed a maximum signal to be achieved in as short a time as possible and with no interference from the software failing. Testing involved running the system at both 2 Hz and 10 Hz whilst measuring the m/z = 28 N_2 signal from a cold gas mixture of 88.2% H_2, 4.5% CH_4, 7% Ar and 0.3% N_2. The aim was to ensure that at 10 Hz enough counts per gate could be measured above the noise level to allow quantitative analysis to be carried out. Interestingly, the 10 Hz analysis resulted in signal intensities only slightly weaker (~15%) than the 2 Hz values (*i.e.* with gate lengths five times longer) and the background-subtracted signal achieved a greater linearity when scaled against chamber pressure (p = 75 to 150 Torr). The increased accuracy is a result of the greater number of samples per second at 10 Hz and it was this frequency which was employed in all later analysis.

It was noticed that when running the MBMS system for periods over 2 h the stepper motor driving the chopper overheated and an interlock then cut in to allow it to cool. Occasionally this would coincide with an experiment causing an interruption in the data collection and the measurement to be aborted because the time gating de-synchronized. This is, obviously, unwanted behaviour that derives from the lack of conductive pathways within the UHV system for cooling the motor assembly. We approached the issue from two angles, firstly, by constructing a bulky copper heat sink which was bolted to the motor assembly (Figure 5.1b) and, secondly, by decreasing the electrical current supplied to the motor by the control box. Both methods resulted in a much more stable chopping system which did not overheat when running for a whole day and, thus, removing a significant, albeit intermittent, interference from the data collection process.

5.1.4 Pumping efficiency & Sampling orifice

Establishing how well these modifications had worked in improving the MBMS system was first done by testing the pumping efficiency of the system using different gases in the MW chamber with increasing pressure. Hydrogen, nitrogen and argon were added separately to the reactor at 500 sccm and the pressure (and MS response, but not shown here) was measured throughout the system as the *p*(MW) was increased from 0 to 200 Torr (Figure 5.3).

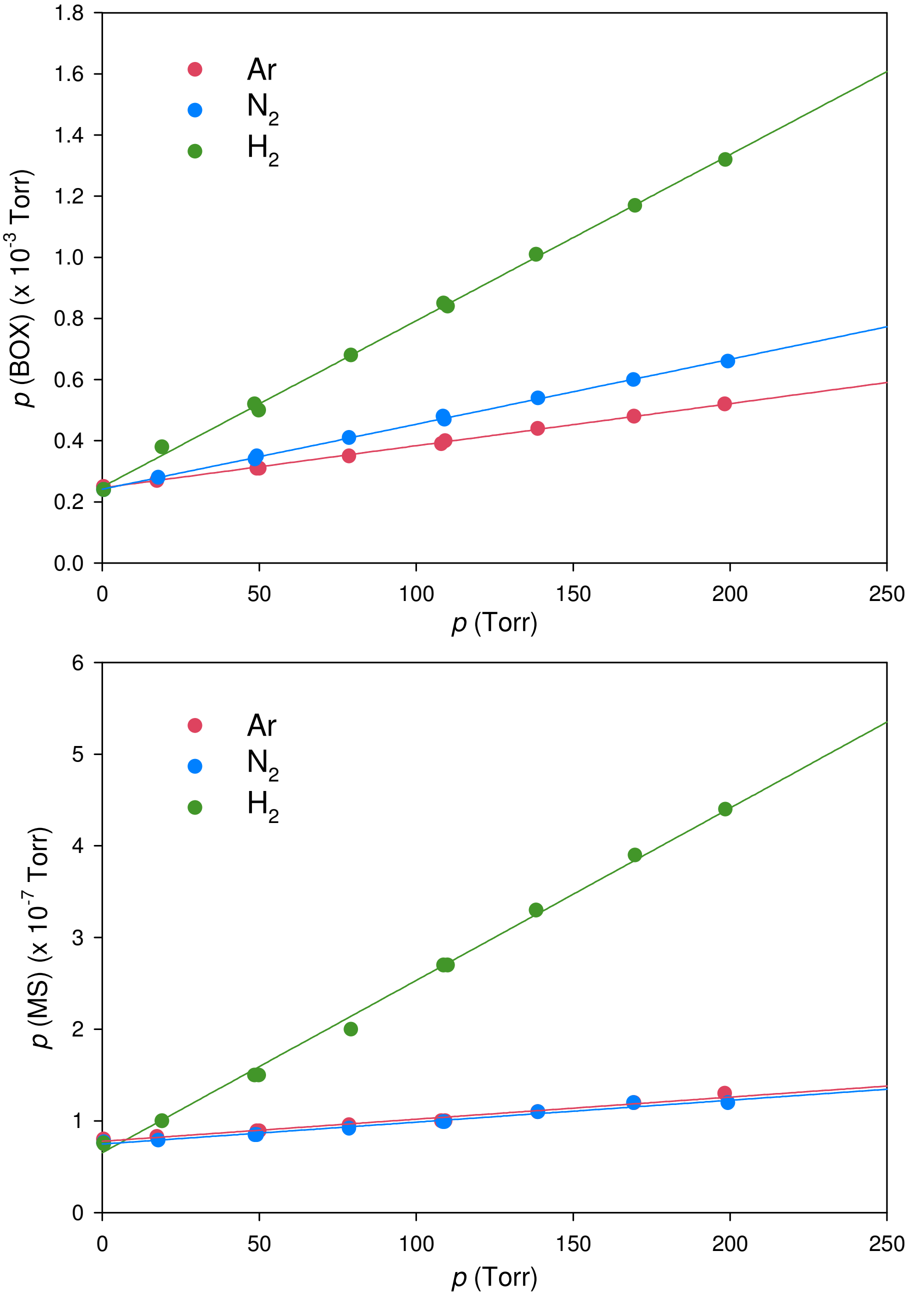

Figure 5.3: Pressure increases throughout the differentially pumped MBMS system for different gases shows poorer pumping of H_2 compared with N_2 and Ar. The experiment contains some points which were repeated to see how much variation there was. Measurements were made with the initial 100 μm aperture.

Obviously, we see the pressure increase in the other stages although the rise is more dramatic for H_2 as it is not as efficiently pumped and causes a considerable rise in p(MS), the pressure in the QMS chamber. As the pressure in this chamber is synonymous with the number density in the ion source this will obviously influence the detected intensities. Also noteworthy is the comparison between H_2 and Ar as they result in different behaviour, with Ar producing a much less dramatic change in the final pressure stage.

To address this problem we propose a calibration system to normalize these effects and this is described in section 5.3.4. However, other extreme behaviour was recorded when using high H_2 mole fractions which consisted of a spontaneous increase in p(BOX) caused by the diffusion pump flooding and failing to maintain a constant pumping speed. This led to a pressure rise higher than the 1.3 mTorr maximum observed in the pressure tests, and meant that the experiment had to wait until the pump and the pressure recovered. Generally, this occurred when stepping up the pressure when sampling gas mixtures with high $\chi_0(H_2)$ and is, obviously, unwanted behaviour. To prevent this from happening, the aim was to fabricate a sampling insert with a smaller orifice size and reduce the p(BOX) a small amount so that the pump no longer struggled. Of course, this was a balance between the pumping stability and the beam flux because any reduction in pressure would lead to lower densities of sampled species in the ion source and, hence, lower signal intensities. Conversely, a smaller orifice would achieve a greater pressure drop into the first stage and produce a beam with a longer mean-free path and, perhaps, better resolution of radical species. The initial orifice diameter was decided by producing a model of the pumping system that delivered the required beam flux to the ion source (Crichton, 2007). Factored into this was the issue of diamond deposition onto the edge of the orifice which may restrict or block the flow. However, periodic SEM monitoring of the orifice showed that after more than 6 months of analysis the aperture remained at 100 μm even though diamond material had deposited around its edge, as seen in Figure 5.4a. As diamond deposition was not a problem, a smaller orifice with diameter 75 μm was proposed as it would result in a ~1.8 decrease in the area of the aperture and should produce a lower p(BOX) preventing the pump from flooding. To mount the new orifice (Agar Scientific A0908M) a new Mo sampling insert was also fabricated using electric discharge machining (by wire erosion at Gemini Technology Ltd., www.geminitechnologyltd.com) allowing both orifice plates to be utilized if required. The new orifice before plasma exposure is shown in Figure 5.4b. The orifice was brazed into the Mo annulus by the Culham Centre for Fusion Energy (United Kingdom Atomic Energy Authority).

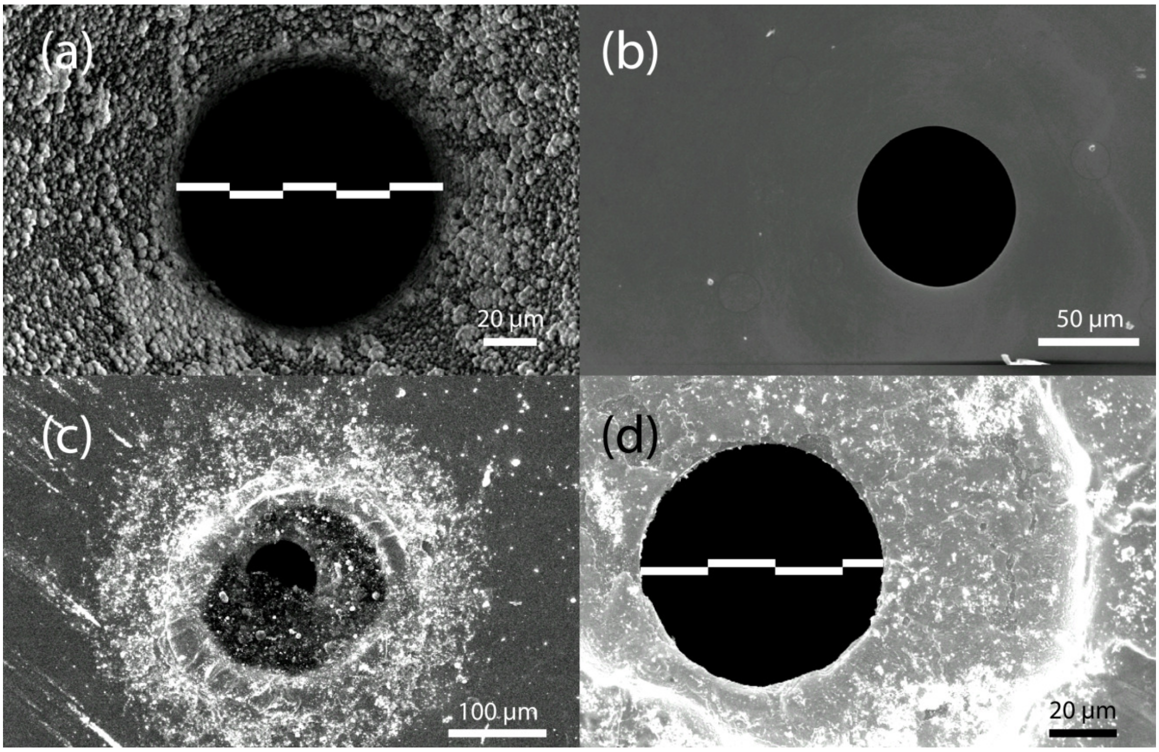

Figure 5.4: Electron microscope images of the sampling orifice at various stages throughout the project. (a) the build up of diamond material on the initial, 100 µm-diameter design after about 6 months of use. (b) the new 75 µm orifice aperture before being brazed into the sample insert and exposure to any plasma. (c) the same orifice blocked by braze material following plasma testing and (d) the orifice after cleaning with a H_2/Ar plasma.

During the testing of the new plate it was noticed that some of the brazing material used to hold the aperture into the sampling plate had melted and partially blocked the orifice (see Figure 5.4c). This is clearly detrimental to the MBMS system but, fortunately, it could be removed by using a high-pressure H_2/N_2/Ar plasma to etch away the material (Figure 5.4d). However, some material has remained near the orifice and warrants further monitoring to ensure that the problem does not recur.

Despite these problems, tests of the new orifice were very promising and the diffusion pump no longer floods when using high hydrogen fractions. The working pressures in the pumping stages have only decreased a small amount, for example by ~0.3 mTorr in *p*(BOX) and, as we shall see, the sensitivity of the instrument has, overall, improved as a result of this, and other, modifications (section 5.3.2).

5.2 Software development

5.2.1 MASsoft & Labview MS control programmes

Proprietary software for controlling the mass spectrometer is provided by the Hiden MASsoft program (version 5) and was frequently used to run fast MS measurements or multiple ion scans where the analysis did not require synchronization with the beam chopper and gating system. A greater control over the MS and synchronization with the beam chopper is achieved using a bespoke Labview 8.2 program. Quick measurements, such as determining the n_S and n_B ratio (section 5.1), were carried out using the previous MASsoft file written for a particular test which then kept the MS parameters consistent and allowed results to be compared quantitatively. The second main usage of the MASsoft program was for simultaneous detection of multiple ions because this can be useful for comparing unknown masses with references. Thirdly, the program was used exclusively for running mass scans where the raw count rates are recorded over a range of amu values (between the limits of 0.4-100 amu) and with a set incremental step in mass. This was important for monitoring of the background species within the high vacuum environment, such as H_2O, N_2, CO_2 and rotary-pump oils, over the course of the project.

Despite these important contributions to the research, the MASsoft program is limited in two respects: firstly, it is not possible to synchronize the data collection measurements with the beam-open and beam-closed phases of the chopper. This means that recording the signal and background intensities separately cannot be achieved and, therefore, none of the benefits from background subtraction can be implemented. Combined with this is the inherent averaging of the spectrometer signal which, although limiting the noise, serves to mask some of the subtler changes in the detected count rate and reduces the overall instrument sensitivity.

An alternative data collection algorithm using National Instrument's LabView system, version 8.2 (www.ni.com/labview) is currently being developed based on MS drivers written by Hiden Analytical. In its current incarnation (MWMBMS v6.4.vi) this programme measures the chopper frequency and phase so that it can synchronize signal (chopper open) and background (chopper closed) gates of specific length during which MS data is collected. The gating system is based on an 8 MHz counter card (NI6022) which specifies the gate lengths (measured in *ticks*) and their position in relation to the chopper rotation cycle. Using a specific number of *ticks* rather than a millisecond delay allows the instrument to be operated at different chopper speeds while maintaining proportionally the same gate lengths. The gating information is shown as a tab in the Labview program (Figure 5.5).

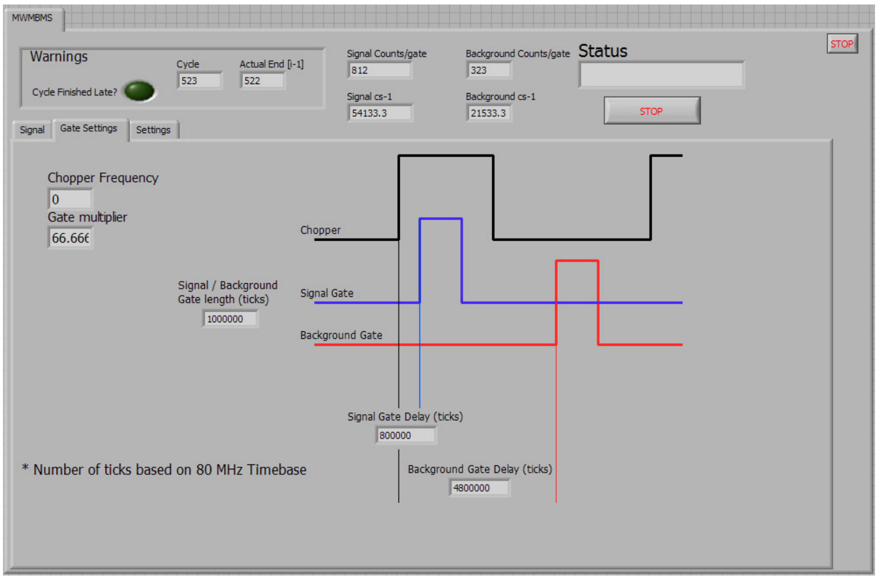

Cycle Finished Late?
Cycle: 523
Actual End [i-1]: 522
Signal Counts/gate: 812
Background Counts/gate: 323
Signal cs-1: 54133.3
Background cs-1: 21533.3
Chopper Frequency: 0
Gate multiplier: 66.666
Signal / Background Gate length (ticks): 1000000
Signal Gate Delay (ticks): 800000
Background Gate Delay (ticks): 4800000
* Number of ticks based on 80 MHz Timebase

Figure 5.5: Gate settings panel from MWMBMS v6.4.vi displays the time-gating parameters used which are based on calculations on the measured chopper frequency.

Here we see that the gate length and delay can be set by the user and measured on an 80 MHz timebase, for example a gate length of 1,000,000 ticks is 1/8 of the full cycle measured between the rising edges of the chopper optical output (shown in black). The signal/chopper-open state is measured 800,000 ticks after the chopper rising-edge (blue), and the background/chopper-closed phase measured 4,800,000 ticks after the cycle start. The proportion of beam-on and -off in the cycle is determined by the design of the chopper wheel. Subtraction of the beam-on from the beam-off state provides a corrected measurement which is displayed on the front panel.

When beginning a measurement the program first measures the chopper frequency and calculates the gate lengths and position as we have described. Then the user is offered a number of *global* parameters which set the electronic variables of the ion source and detector:

i) **Energy**: the electron energy of the ioniser (6 → 150 eV). Set according to the IP and AP of the target species.
ii) **Cage**: the voltage which extracts ions from the ion source (0 → 10 V but set to 3 V).
iii) **Emission**: sets the current of emitted electrons (20 → 1000 μA but kept at 120 μA).
iv) **Multiplier**: sets the voltage across the detector (0 → 3000 V but kept at 2100 V).
v) **Discrim**: sets the level at which low level noise is rejected (±100% but set to –10%).

The electron energy is typically set ~1 eV above the IP although care was taken not to saturate the detector when sampling H_2, H_2O, Ar and other dominant species. The cage voltage of 3 V correlates with the maximum in count rates for most species. The multiplier is set to a *plateau* region which ensures the greatest signal intensity without reducing the detector lifetime. In addition to these variables, the dwell and settle times, which determine the sampling rate were chosen to match with the time-gated cycles.

Once the MS settings have been chosen, a particular mass is targeted and the system begins to collect data by recording the count rates in each signal (chopper open) and background (chopper closed) phase. These data are displayed on the front panel (Figure 5.6) plotted against time and so changes to the intensity are quickly observed.

Cycle: 120
Actual End [i-1]: 131
Signal Counts/gate: 0
Background Counts/gate: 26
Signal cs-1: 0
Background cs-1: 1485.71
Status: Saving...

Figure 5.6: Count-rate data panel from MWMBMS v6.4.vi records raw intensity of probed peak against time and displays the signal and background count rates as well as the number of cycles undertaken.

The final tab in the program records the file details and error messages from the spectrometer or data analysis system. Three data sets are recorded against cycle number and millisecond delay, which include the signal and background count rates, an averaged signal minus background, and also the MS settings that have been input.

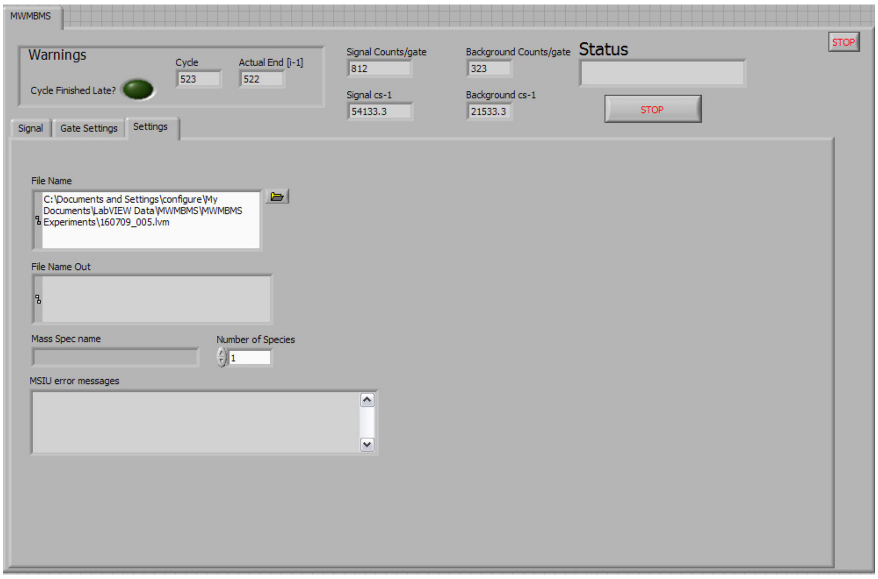

Cycle 523
Actual End [i-1] 522
Signal Counts/gate 812
Signal cs-1 54133.3
Background Counts/gate 323
Background cs-1 21533.3
File Name C:\Documents and Settings\configure\My Documents\LabVIEW Data\MWMBMS\MWMBMS Experiments\160709_005.lvm
File Name Out
Mass Spec name
Number of Species 1
MSIU error messages

Figure 5.7: Settings panel from MWMBMS v6.4.vi allows the file names to be entered and records any error messages fed back from the Hiden electronics.

5.2.2 Ongoing work

As part of the current project many updates were made to the program to make it easier to use, incorporate more functions and prevent software-induced noise. Interference with the data collection from the software itself is mainly due to the acquisition cycle not being completed when a gate is misplaced or skipped due to an error in the program, the counter card, or the computer processor. More often, however, these erroneous cycles, appearing as spikes in the data plot, are due to an odd-shaped signal from the chopper. Before the heat-sink and lower-current modifications were made to the chopper, the OPTO measurement of the chopper phase frequently contained very short or poorly formed rising edges which triggered the gate at the wrong time. While not immune to this problem these data spikes are much less of a problem in the latest version. Allied to this is an overestimation of the count rates at the beginning of the scan when there have not been enough cycles to take an average over, and so the first 10 cycles are ignored in the updated programme.

Other modifications include measurement of the chamber, box and MS pressures as the MS measurement is made, because this will allow us to monitor the pumping efficiency over time and with different gas mixtures. Many other improvements have been made to the Hiden drivers making them simpler and more user-friendly; however, the current version still lacks the ability to record the signal for two different masses due to the considerable difficulty of swapping masses in synchronicity with the beam modulation. Inherent delays when the QMS moves between two *m*/*z* values will add a large source of timing errors and missed cycles. Other improvements could be made to the data averaging and noise reduction of the signal in future versions of the program.

5.3 Testing with different gas mixtures

5.3.1 Gas testing and standards

In order to cover as much of the expansive parameter space as possible a range of standard conditions were set for this analysis in a similar manner to previous studies using absorption and emission spectroscopy. Maximum flexibility could be attained using p = 100 Torr and P = 1 kW as base plasma parameters together with four gas mixtures which cover the range of H_2/Ar values of interest and, needless to say, we limited ourselves to the least complex system of H/C/Ar chemistry for these initial experiments. For ease of use the four standard mixtures are referred to by the ratios of the hydrogen and argon flow rates (in sccm), covering a range from MCD to NCD deposition conditions: 500/0, 500/40, 300/200 and 150/350. This has been simpler than using the absolute mole fractions, as they will change with how much CH_4 or C_2H_2 is added. In the following discussion these labels are commonly used to indicate which gas mixture is referred to. When the situation required a standard amount of hydrocarbon to be included in the gas mixture either 25 sccm CH_4 or 12.5 sccm C_2H_2 was used. Addition of a small trace reference, usually Kr, would also impose on the absolute mole fractions. In most cases 5 sccm of Kr was included in the gas mixtures and was thought to have negligible influence on the plasma although it was included in any of the calculations of mole fractions. It is the presence of the trace Kr that means that in some cases the sum of the mole fractions quoted does not quite reach unity.

Through optimization of the mass spectrometer another realm of standardization is required. For most situations it is necessary to achieve the highest signal intensity possible, and so parameters for controlling the ion optics – the cage and focus voltages at the ion source and the multiplier voltage at the detector – were chosen to provide maximum count rates for a particular species.

5.3.2 MBMS sensitivity

Advances made during the various hardware modifications were monitored using a method for determining the detection limit of the MBMS system using a standardized gas mixture and pressure within the CVD chamber (Park *et al.*, 2004). This technique is based upon measurement of the count rates for a set of the most abundant krypton isotopes and comparison with their relative abundances. Extrapolation of these values back to the lowest detectable signal to noise level then provides a value for the absolute detection limit of the instrument. Realistically, this is likely to be a best possible case as the background noise level in the 80-90 amu region where the Kr isotopes are situated is lower than in, say, the 10-20 amu region where the hydrocarbon species lie. Krypton was used in this test as it is present in a range of naturally occurring isotopes with the most important listed in the following table.

isotope	*m/z*	*relative abundance*
	amu	%
^{78}Kr	77.9	0.35
^{80}Kr	79.9	2.28
^{82}Kr	81.9	11.58
^{83}Kr	82.9	11.49
^{84}Kr	83.9	57.00
^{86}Kr	85.9	17.30

Table 13: Masses and relative abundances of six commonly occurring krypton isotopes.

For the first test, allowing comparison with earlier analysis (Crichton, 2007), a leak of 3 sccm Kr was added to a 100 Torr gas mixture of $\chi_0(H_2) = 0.88$, $\chi_0(Ar) = 0.07$, $\chi_0(CH_4) = 0.04$, *i.e.* the 500/40 system. Before modifications, the detection limit, measured in this way, was a mole fraction of ~2×10^{-5} as shown in Figure 5.8.

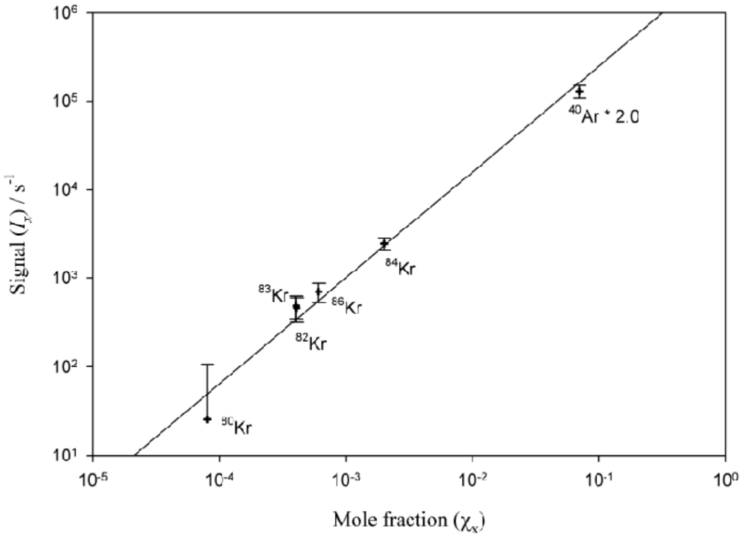

Figure 5.8: MBMS system detection limit of ~2×10^{-5} measured by extrapolating a plot of Kr isotope mole fraction against signal intensity, with the addition of the ^{40}Ar signal scaled with the appropriate ionization cross-section (Crichton, 2007).

After implementation of the various updates we have described, the detection limit measured under the same conditions had been lowered to 5×10^{-6} for the same gas conditions, *i.e.* the 100 Torr data in Figure 5.9(d). If we compare like with like, before and after modifications, the absolute count rates all show a moderate increase which then leads to a lower detection limit. Moreover, this new measure of the spectrometer sensitivity was achieved with the smaller orifice size (75 μm) which would be expected to limit the intensity of any mass peak.

As the tests were fairly straightforward to perform it was decided to investigate how the detection limit, calculated in this manner, varied with gas mixture, chamber pressure, addition of hydrocarbon and with or without a plasma running. The data for cold (*i.e.* no plasma) and hot (*i.e.* plasma ignited) are shown in Figure 5.9 & Figure 5.10, respectively, where the results are separated between gas mixtures without ((a) to (c)) and with ((d) to (f)) methane, for three different gas mixtures: 500/40, 300/200 and 150/350. In these log-log plots, two of the isotopes, ^{82}Kr and ^{83}Kr, have similar abundances and so overlap. It is important to note that the ^{78}Kr isotope (0.35% abundant giving $\chi_0(^{78}\mathrm{Kr}) \sim 2\times10^{-5}$) could only just be detected after background subtracted and is not included in these results. This means that the real detection limit is likely to be slightly higher than the value calculated by the extrapolation method although it is still a very useful and systematic way of looking at the behaviour of the instrument over time and sampling different gas mixtures.

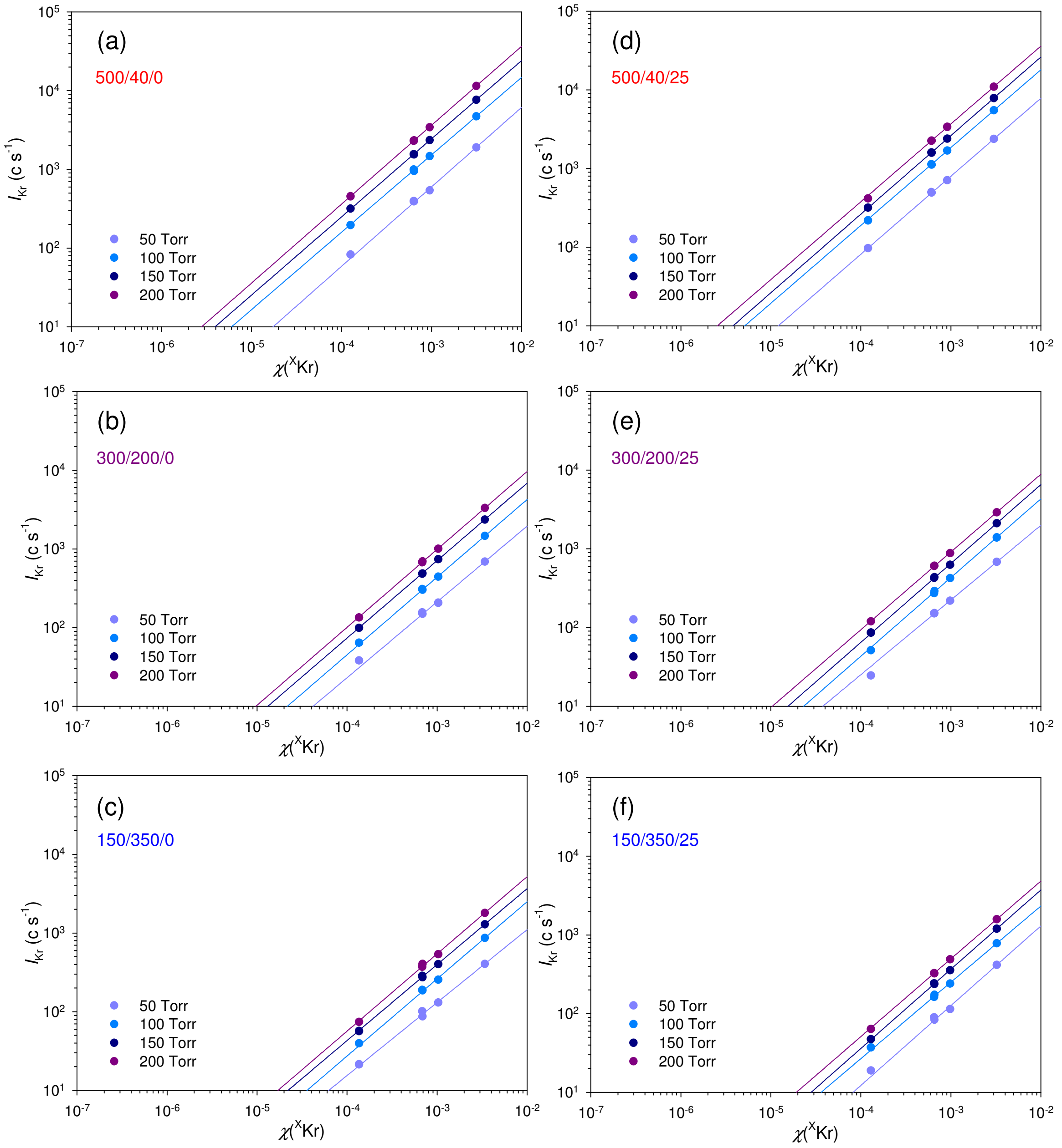

Figure 5.9: Determination of MBMS sensitivity or detection limit using mole fractions of five Kr isotopes in different gas mixtures at a range of pressures with no plasma initiated. (a) to (c) gas mixtures with different H_2/Ar ratios and (d) to (f) the same gas mixtures with the addition of methane.

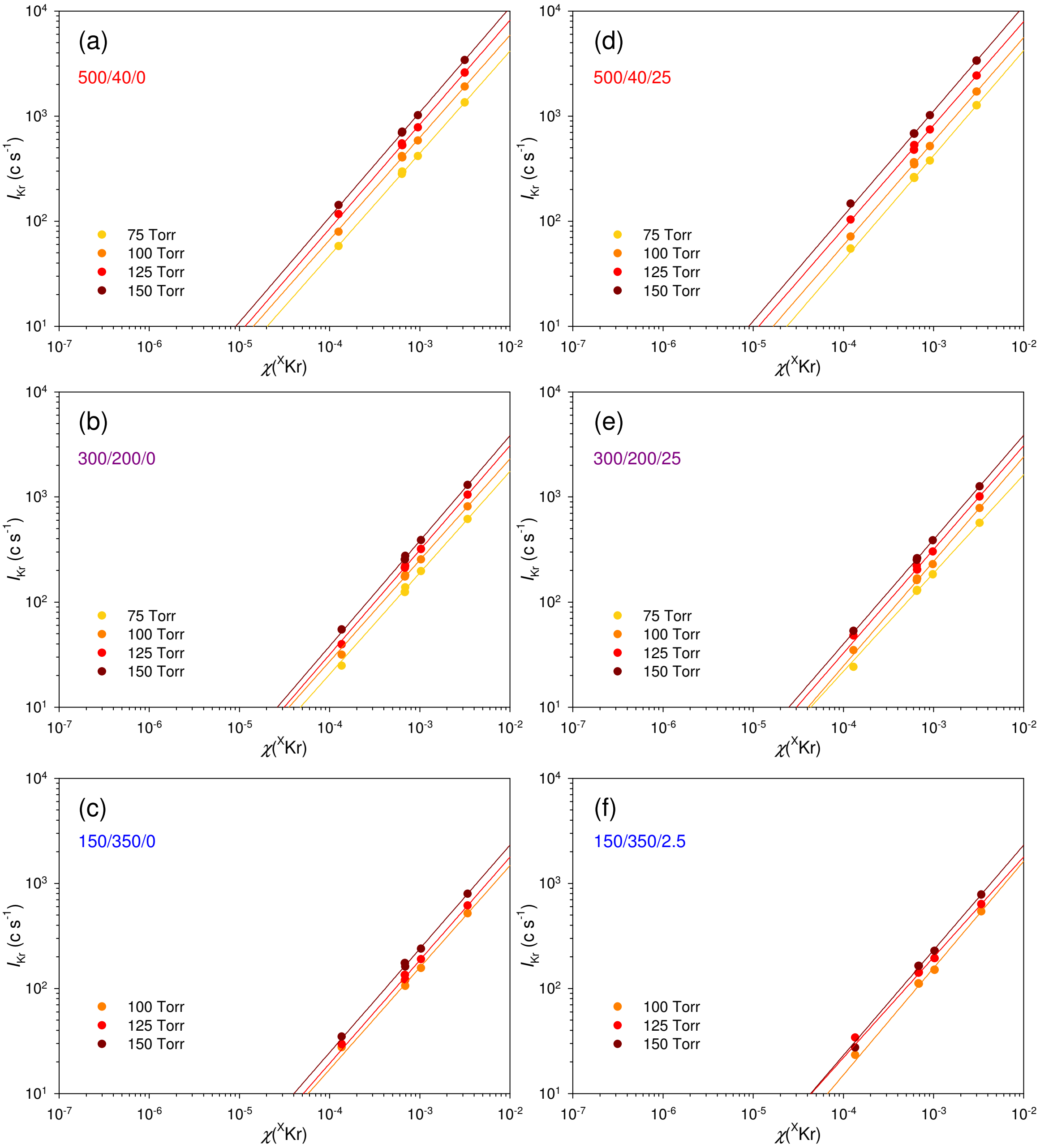

Figure 5.10: Determination of MBMS sensitivity or detection limit using mole fractions of five Kr isotopes in different gas mixtures at a range of pressures with a P = 1 kW plasma. (a) to (c) gas mixtures with different H_2/Ar ratios and (d) to (f) the same gas mixtures with the addition of methane. Due to instability in the plasma the maximum pressure of 200 Torr could not be reached and a narrower range (75 to 150 Torr) was employed. Similarly, at 75 Torr the 150/350 plasma volume is too large to be operated safely.

The trends evident in these plots are summarised in the next plot which shows the detection limits that have been calculated by extrapolating back to a 10 counts s^{-1} (c s^{-1}) baseline. In general, this limit is always higher when the plasma is running (comparing Figure 5.11(a) and (b)) although the widest discrepancy is observed for the 500/40 plasma whereas the other two gas mixtures are perturbed to a lesser extent. The count rates are all lower when running the plasma indicating a decrease in the extraction efficiency of the hotter gas mixture.

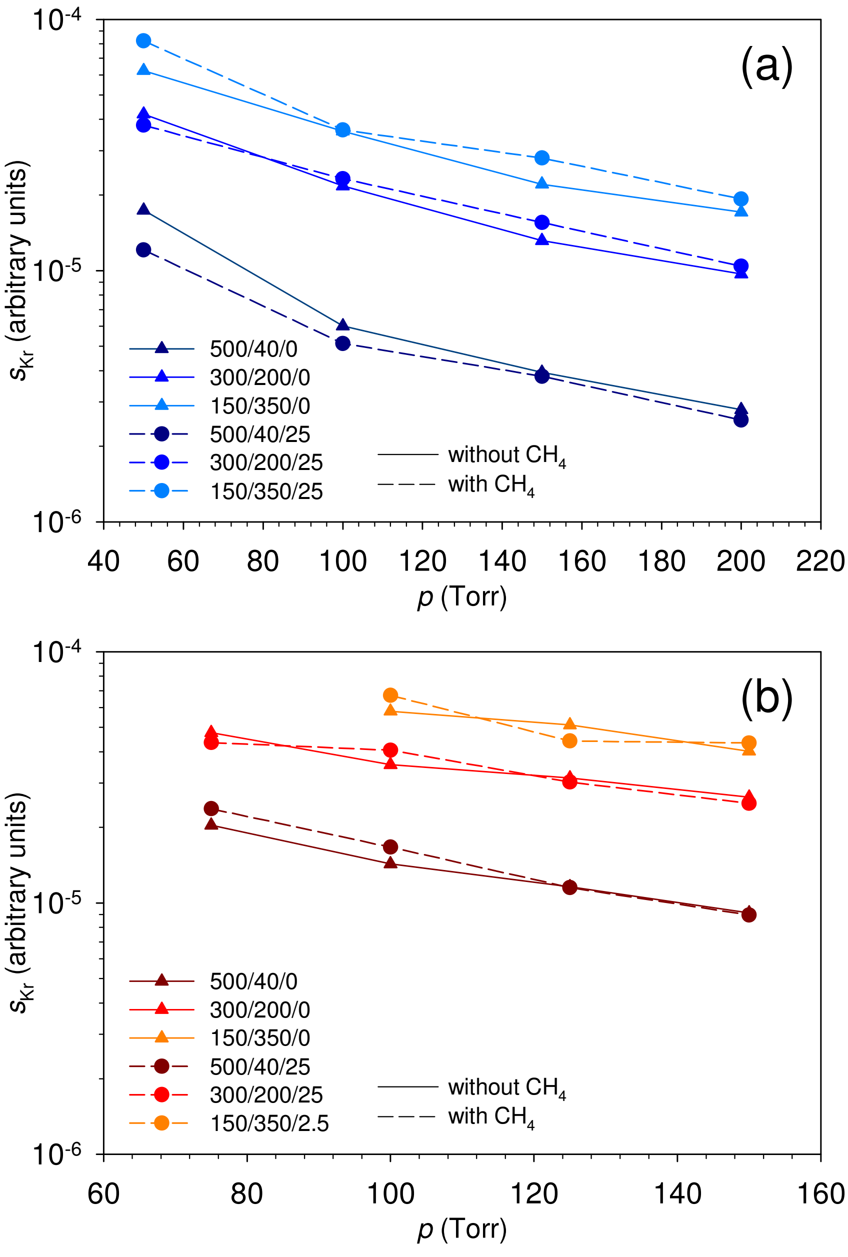

Figure 5.11: Summary of MBMS sensitivities to low mole fractions of Kr in different cold (a) and hot (b) gas mixtures. Due to the inherent stability of the plasma under certain conditions it was necessary to cover a shorter range of reactor pressures than was used for the room temperature experiments.

A marked difference in detection limit is recorded for the range of gas mixtures used with the 500/40 mixture exhibiting a lower limit than either the 300/200 or the 150/350 environments. The 150/350 system showed the highest values with calculated detection limits between 4 and 5 times higher than the corresponding 500/40 system at the same pressure. We can explain this observation by the variation in the beam flux through the system with different average masses of the sampled gas mixture and the resulting changes in pressures as the different gas mixtures are pumped with varying efficiencies (see section 5.1.4). On average, the beam in the 500/40 mixture will be considerably lighter than the 150/350 system and so will be transmitted to the detector faster with less chance for beam scattering as the beam expands into the vacuum system. As a result the detected intensities of all species in the 150/350 measurements are lower than the H_2-dominated case which then gives rise to higher detection limits. This disparity between the different gas mixtures (nominally MCD and NCD deposition conditions, respectively) will be observed throughout the MBMS analysis and methods of normalizing them addressed in section 5.3.4.

As we might expect, a reduction in the calculated limit is also noticeable when increasing the chamber pressure although this is more apparent in the cold gas mixtures (×5 decrease) than the plasma heated ones (× 1.5 decrease but over a smaller range). This is due to the increase in p not only in the MW reactor but throughout the MBMS system which will increase the number density of each Kr isotope in the ion source and, therefore, the corresponding count rate resulting in a lower detection limit. As the plasma can become unstable at extremes of pressure a narrower range of values was utilized for these results compared with the cold gas analysis.

There appears to be no measureable influence of adding CH_4 to either a cold gas mixture or the plasma as, within the uncertainty margins, the plots for systems with and without methane overlap. Overall, the sensitivity has been improved compared with previous results and our own, ongoing, system diagnostics, especially when one considers the ~ 43% reduction in the sampling area of the orifice. This outcome is made possible through accurate alignment of the beam optics although further improvement may be necessary for detection of radical species. We have seen that the temperature, the average molar mass and the pressure of the sampled gas mixture all exert an influence on the measured count rates and detection limit of our Kr reference, although addition of CH_4 does not perturb the system significantly.

5.3.3 Ionization and appearance potentials

In section 4.2.4 we discussed the use of threshold-ionization methods to enhance the MBMS technique by allowing specific radical species to be quantified without forming them in the ion source. Consequently, it is important to calibrate the energy scale of the ion source to determine if there is any offset between the value set in the software and the ion-source potential. A linear offset of a few eV is often observed in MS apparatus due to the device electronics, and this must be determined when using threshold-ionization MS. We measured the ionization potentials of

C_2H_2 and CH_4 in gas mixtures containing ~2% hydrocarbon in H_2 at 100 Torr by increasing the ion-source electron energy and recording the detected count rate at *m*/*z* = 26 and 16, respectively. At the same time the MS was used to determine the appearance potential of radical fragments (C_2H and C_2 from C_2H_2 and CH_3, CH_2, CH and C from CH_4) by looking at their specific masses. The results show curves that contain linear regions which are extrapolated back to the horizontal axis to determine the IP and AP values, and curved regions due to the thermal spread of the electrons and the parent ions in the ion source.

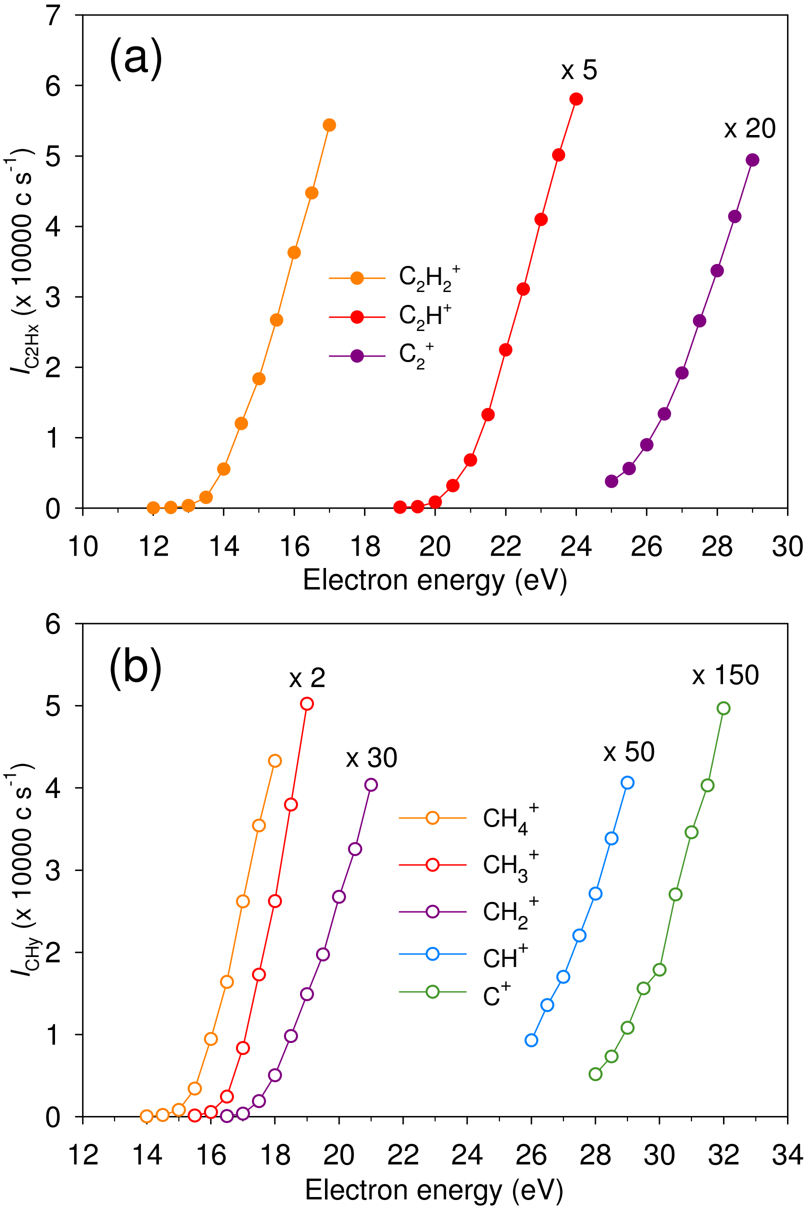

Figure 5.12: Hydrocarbon ionization and appearance potentials from gas mixtures containing (a) C_2H_2 and (b) CH_4. The intensity decreases as formation of the fragment ions becomes less likely and a suitable scaling factor has been applied. Parameters were 2% C_xH_y in H_2 at *p* = 100 Torr.

The results were then compared with literature values derived from a range of publications and using electron-impact ionization (Lias *et al.*, 2011).

$X + e \rightarrow X^+ + 2e$	E_{LIT} eV	E_{EXP} eV	ΔE eV
$\mathrm{C_2H_2 + e \rightarrow C_2H_2{}^+ + 2e}$	11.4	14.0	+2.60
$\mathrm{C_2H_2 + e \rightarrow C_2H^+ + H + 2e}$	16.7	20.7	+3.99
$\mathrm{C_2H_2 + e \rightarrow C_2{}^+ + 2H + 2e}$	22.6	25.7	+3.14
$\mathrm{C_2H_2 + e \rightarrow C_2{}^+ + H_2 + 2e}$	18.2	25.7	+7.57
$\mathrm{CH_4 + e \rightarrow CH_4{}^+ + 2e}$	12.6	15.5	+2.88
$\mathrm{CH_4 + e \rightarrow CH_3{}^+ + H + 2e}$	14.0	16.7	+2.65
$\mathrm{CH_4 + e \rightarrow CH_2{}^+ + 2H + 2e}$	15.1	17.9	+2.79
$\mathrm{CH_4 + e \rightarrow CH^+ + 3H + 2e}$	22.3	25.8	+3.48
$\mathrm{CH_4 + e \rightarrow C^+ + 4H + 2e}$	25.0	28.8	+3.80

Table 14: Experimental and literature values of ionization potentials of C_2H_2 and CH_4 and appearance potentials of C_2H, C_2 from C_2H_2 and CH_3, CH_2, CH and C from CH_4 from electron-impact ionization studies of acetylene (Plessis & Marmet, 1986, Zheng & Srivastava, 1996) and methane (Branson & Smith, 1953, Plessis *et al.*, 1983). The difference in energy between the experimental and literature values for dissociation of C_2H_2 into C_2^+ and H_2 is large enough to indicate that fragmentation *via* this route does not occur. There is a large variation in the reported values of AP for CH_2^+, CH^+ and C^+ from CH_4.

We see a range of offsets which are likely to be more accurate for the stable species than for the smaller fragments. Similar analysis was carried out for Ar and Kr, also diluted in H_2, as the offset was not a constant value and would need to be quantified for each species.

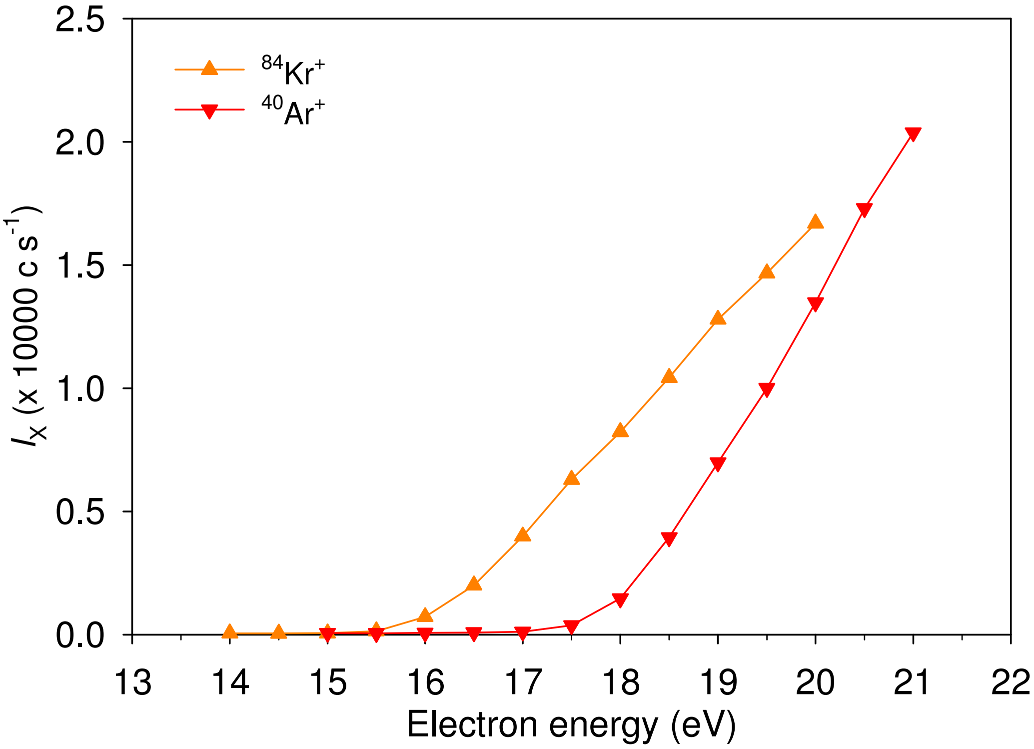

Figure 5.13: Ionization potentials of Ar and Kr measured by the MBMS system using a mixture of the inert gas diluted in H_2 at 100 Torr.

$X + e \rightarrow X^+ + 2e$	E_{LIT} eV	E_{EXP} eV	ΔE eV
$\mathrm{Ar} + \mathrm{e} \rightarrow \mathrm{Ar}^+ + 2\mathrm{e}$	15.8	17.5	+2.11
$\mathrm{Kr} + \mathrm{e} \rightarrow \mathrm{Kr}^+ + 2\mathrm{e}$	14.0	16.0	+2.04

Table 15: Experimental and literature values of ionization potentials of Ar and Kr (Rapp & Englander-Golden, 1965, Wetzel *et al.*, 1987).

The calibration process, introduced in section 4.2.5 and described in section 5.3.4, requires the ionization cross-section, the probability of ionization occurring on interaction with an electron, to be well characterized. The total ionization cross-section, σ_T, which includes all charged states, is energy dependent and so we use our working potential of 20 eV corrected by the measured offset to determine a specific value. The experimental value of E_{EXP} = 20.0 eV results in an actual E_e = 17.4 eV that lies above the IP ($\Delta E_i^{X\rightarrow X+}$) of C_2H_2 but below AP of C_2H^+ from C_2H_2. Corrected experimental potentials are extrapolated onto the following plots of ionization cross-sections against potential to provide values for two of the species, C_2H_2 (Figure 5.14) and Kr (Figure

5.15), which are used in the MBMS calibration process. Detection of other species will require similar analysis to determine the σ_X/σ_R values.

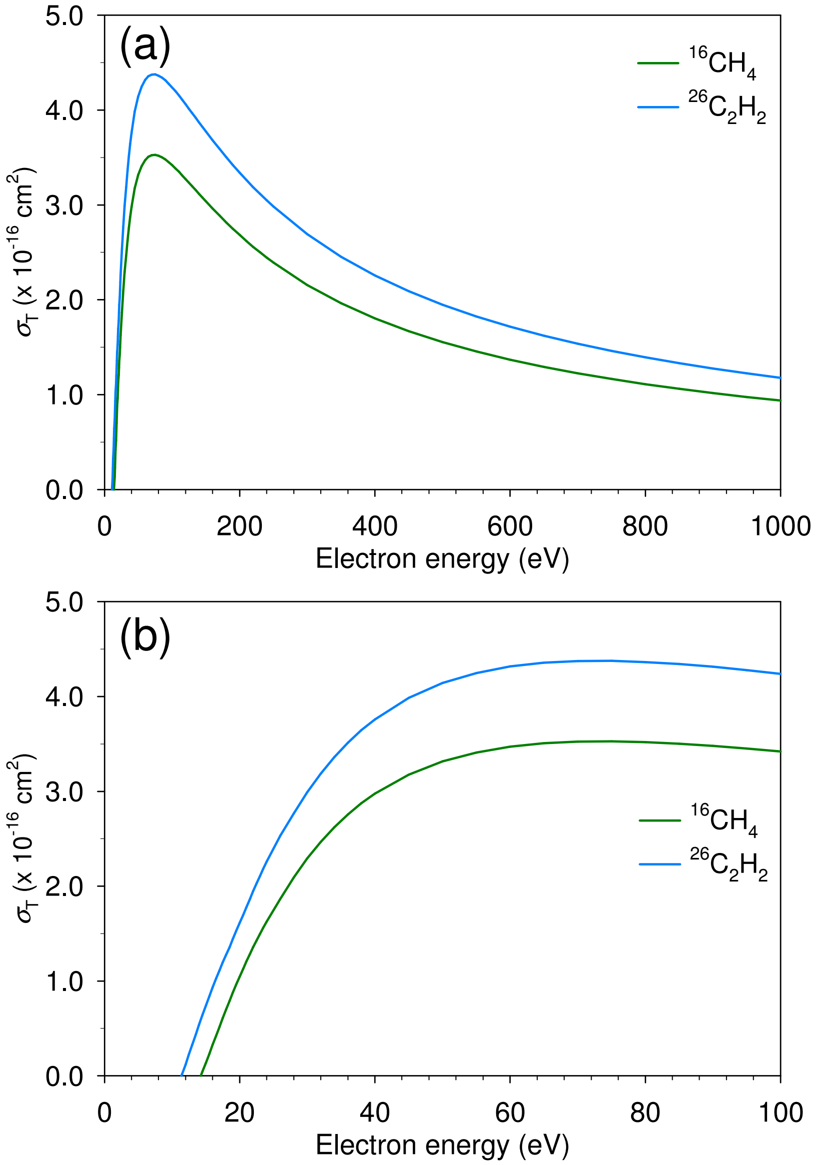

Figure 5.14: Ionization cross-sections (σ_T) for stable hydrocarbon species (Kim *et al.*, 1997a, Kim *et al.*, 1997b).

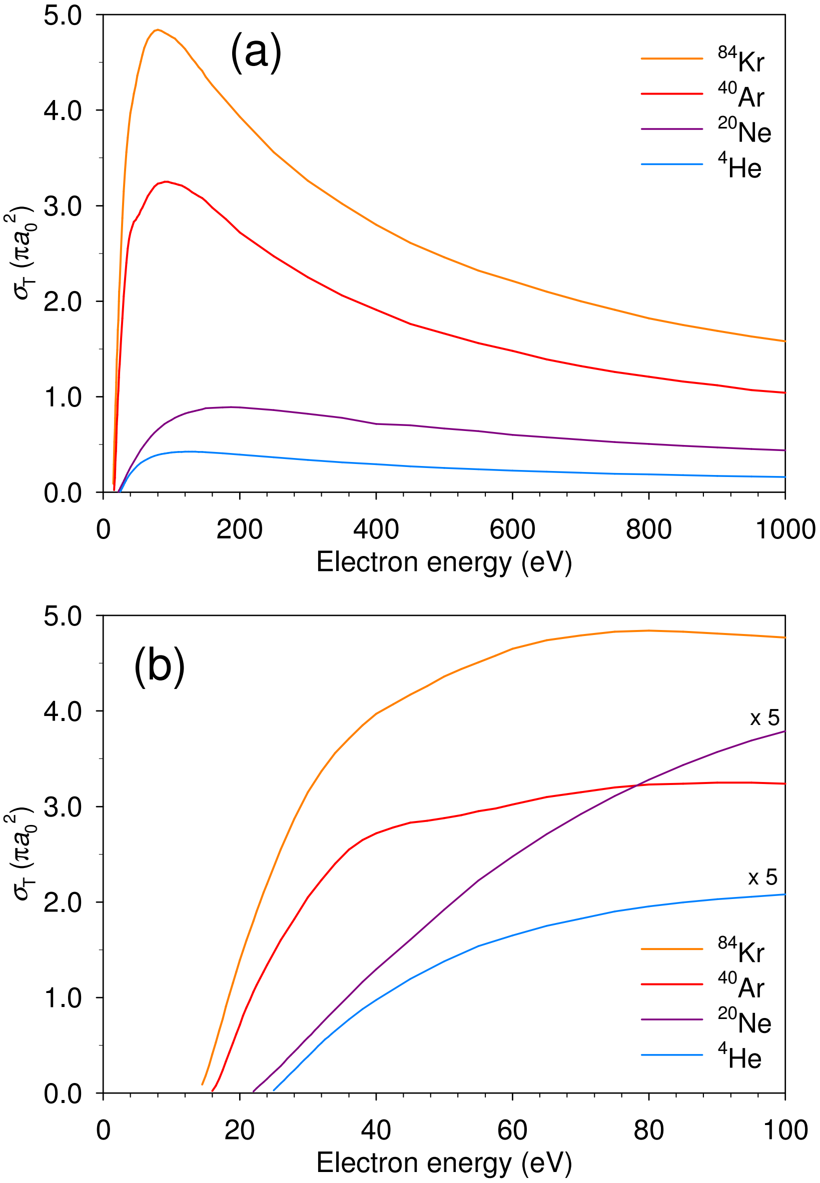

Figure 5.15: Ionization cross-sections (σ_T) for four noble gases (Rapp & Englander-Golden, 1965, Wetzel *et al.*, 1987).

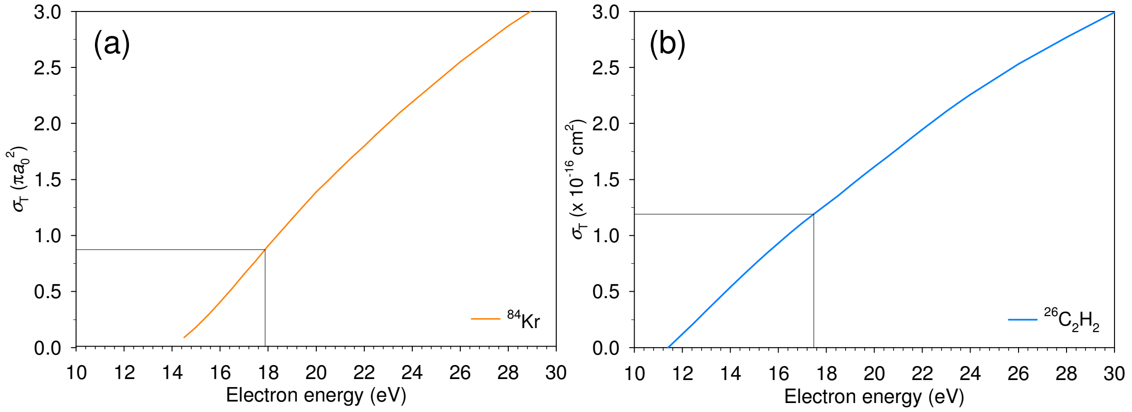

Figure 5.16: Expanded versions of ionization cross-section data showing experimental values used in the evaluation of $\chi(C_2H_2)$.

It is crucial to note that the two literature ionization cross-sections, for Kr and C_2H_2, are given in different units: πa_0^2 (where a_0 is the Bohr radius = 5.2918×10^{-11} m) and 10^{-16} cm^2, respectively. To achieve the same units the following factor is used:

$$\pi a_0^2 = 8.7973 \times 10^{-17} \text{cm}^2 \tag{5.1}$$

Therefore, the cross-sections used for Kr were multiplied by 0.87973 to give the common units (10^{-16} cm^2) which then cancel in the calculation of $\sigma_{C2H2}/\sigma_{Kr}$. It should be noted that there is only one working potential but due to the slightly different offsets it was decided that each should be treated separately when calculating the ionization cross-sections.

$X + e \rightarrow X^+ + 2e$	ΔE	E_{WORK}	E_{EXP}	σ
	eV	eV	eV	10^{-16} cm^2
$C_2H_2 + e \rightarrow C_2H_2{}^+ + 2e$	+2.596	20.0	17.404	1.18
$Kr + e \rightarrow Kr^+ + 2e$	+2.035	20.0	17.965	0.787

Table 16: Values used to calculate ionization cross-sections for C_2H_2 and Kr.

In future analysis using this MBMS apparatus, the use of the threshold methods outlined here will become more important as quantitative detection of radical species, such as CH_3, will rely on careful placement of E_{WORK} to ensure that the detected species are not being made by dissociation reactions in the ion source.

As in earlier work, measurements of the IP of H_2 and H were limited by beam losses indicative of these low-mass species and will need further attention as the project is taken forward (Crichton, 2007).

5.3.4 C_2H_2 analysis

5.3.4.1 Cold gas calibration

Rather than using an effusive source located in the lowest pressure stage of a MBMS system (Hsu & Tung, 1992) we planned to use a trace of Kr (~0.5%) in different gas mixtures to calibrate both for variation in the beam dynamics and the QMS. This had previously been segregated into two factors, a_{GD} and a_{MS} but we collected them into one correction factor, $a^{H2/Ar}$, dependent on the $\chi_0(H_2)/\chi_0(Ar)$ ratio as this seemed to have the most dramatic influence on the system pumping and beam dynamics (see section 5.1.4). Using a ^{84}Kr reference that is much heavier than the probed species would hopefully mean that it would not be involved with many collision reactions which might perturb, for example, the ^{2}H measurement. At the same time we assume that loss of lighter species from the beam is similar for both the hot and cold gases, although the additional thermal energy when the plasma is running is likely to have some influence. By calculating these factors for specific gas mixtures and sampled pressures without a plasma it was hoped that quantitative measurement would result from corrected analysis of the diamond-deposition environments.

The intensities of m/z = 26 C_2H_2 (for which the mole fraction is unknown when running the plasma) and m/z = 84 Kr (the unreactive reference added in a trace amount) are measured in a variety of cold gas (plasma off) mixtures and at a range of chamber pressures. As ^{84}Kr is only 57% abundant the measured intensities (I_{84Kr}) are corrected to give a projected intensity (I_{Kr}) for all the isotopes. These results are then used to determine a calibration factor, $a^{H2/Ar}$, using the known mole fractions and the ratio of the ionization cross-sections determined above.

$$a^{\mathrm{H2/Ar}} = \frac{\left({}^{I_{\mathrm{C2H2}}}/{}_{I_{\mathrm{Kr}}}\right)}{\left({}^{\sigma_{\mathrm{C2H2}}}/{}_{\sigma_{\mathrm{Kr}}}\right)\left({}^{\chi_{\mathrm{C2H2}}}/{}_{\chi_{\mathrm{Kr}}}\right)} \tag{5.2}$$

After measuring the intensities of $^{26}C_2H_2$ and ^{84}Kr in diamond-depositing CVD plasmas, where the exact concentrations of different reactive species was unknown, we could use the calibration factors and the known $\chi_0(Kr)$ to estimate the $\chi(C_2H_2)$ as a function of process conditions.

$$\chi_{\mathrm{C2H2}} = \frac{\left({}^{I_{\mathrm{C2H2}}}/{}_{I_{\mathrm{Kr}}}\right)}{\left({}^{\sigma_{\mathrm{C2H2}}}/{}_{\sigma_{\mathrm{Kr}}}\right)} \times \frac{1}{a^{\mathrm{H2/Ar}}} \times \chi_{\mathrm{Kr}} \tag{5.3}$$

While we show results for determining $\chi(C_2H_2)$, the method will in future be expanded to measure other stable species, CH_4 and HCN, and radicals CH_3, C_2H, if the sensitivity can be improved.

It should be noticed that the non-negligible influence of the sampled T_{gas} (observed in the Kr detection limit tests) should be incorporated into the correction factor. This will be true if the influence of T_{gas} on C_2H_2 and Kr in the beam is similar, and this may be a source of error which could be analysed in future by measuring the variation of *a* with T_{gas} and *m*/*z*. The issue is likely to be more of a problem comparing a heavy reference gas, *e.g.* Kr, with a light probed gas, for example H_2.

The raw data for I_{C2H2} and I_{Kr} is shown in Figure 5.17 & Figure 5.18, respectively.

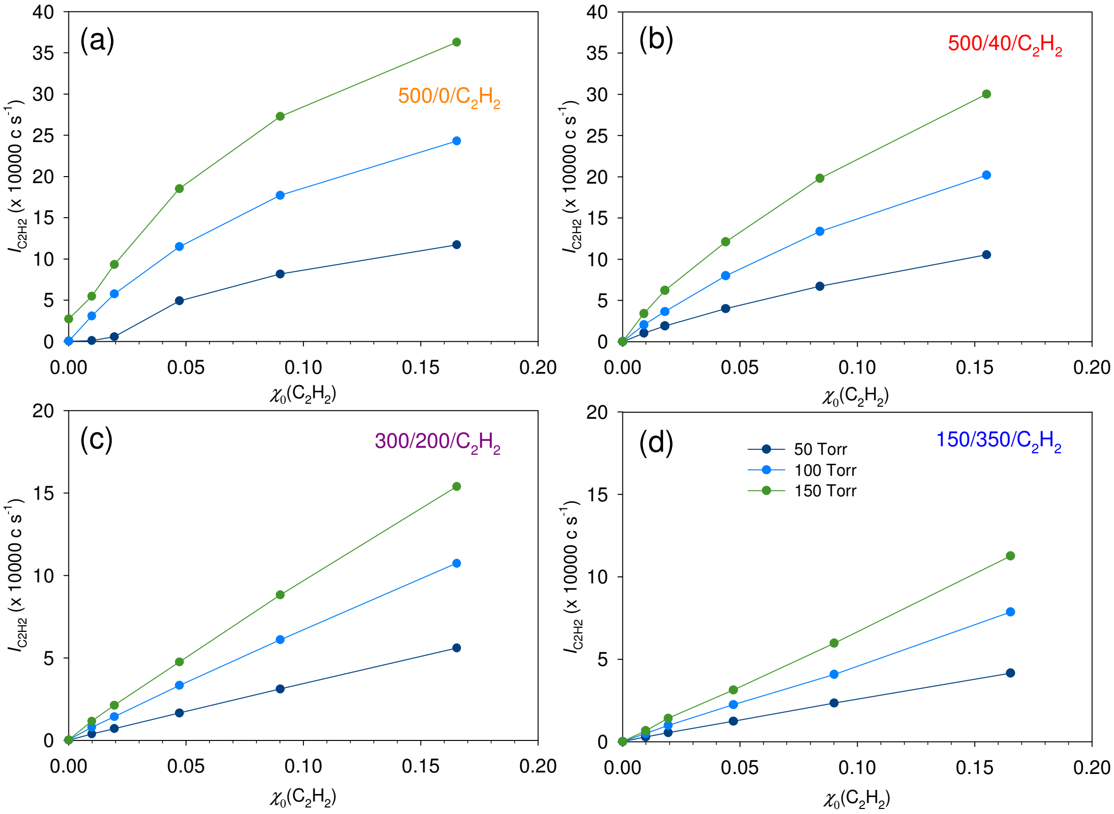

Figure 5.17: Raw count-rate data for the *m*/*z* = 26 C_2H_2 peak for calibrating the MBMS system with increasing $\chi_0(C_2H_2)$. Calibration curves were obtained for four standard gas conditions (where $F(H_2)/F(Ar)$ were (a) = 500/0, (b) = 500/40, (c) = 300/200 & (d) = 150/350) and three chamber pressures (p = 50, 100 & 150 Torr).

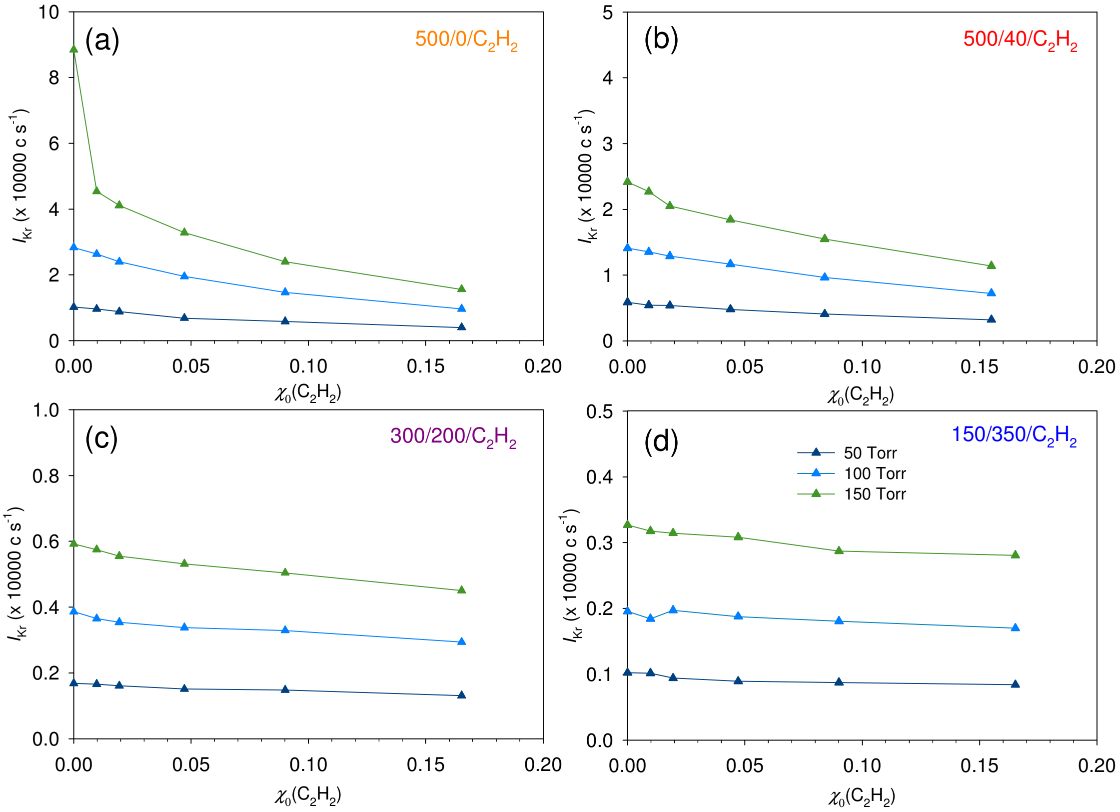

Figure 5.18: Raw count-rate data for the m/z = 84 ^{84}Kr peak for calibrating the MBMS system with increasing $\chi_0(C_2H_2)$. Calibration curves were obtained for four standard gas conditions (where $F(H_2)/F(Ar)$ were (a) = 500/0, (b) = 500/40, (c) = 300/200 & (d) = 150/350) and three chamber pressures (p = 50, 100 & 150 Torr).

The results of I_{C2H2} measurements show contrasting behaviour between the different gas mixtures but proportionality with increasing pressure. Count rates are higher in the H$_2$-rich mixtures compared with the Ar-rich ones even though the MS response is not as linear as we would expect when increasing $\chi_0(C_2H_2)$. The I_{Kr} results show slightly falling (in high $\chi_0(H_2)$) or unchanging (in low $\chi_0(H_2)$) count rates as $\chi_0(C_2H_2)$ rises.

Applying equation 5.2, we can plot the calibration factors against increasing $\chi_0(C_2H_2)$ for the experimental gas mixtures and chamber pressures (Figure 5.19). The results show negligible dependence on $\chi_0(C_2H_2)$ but higher values of $a^{H2/Ar}$ at lower pressure and for lower $\chi_0(H_2)$ where the molecular beam transmission efficiency will be reduced in both cases. We also note two inconsistent results (for the 50 Torr 500/0 mixture) which derive from the poor measurement of I_{Kr} for these conditions. Apart from these anomalies, the results fall within fairly tight ranges for each gas mixture and for further analysis we take the average of the 100 Torr mixture (as this is the standard pressure for the subsequent work) which gives $a^{500/0}$ = 0.80, $a^{500/40}$ = 0.94, $a^{300/200}$ = 1.31 and $a^{150/350}$ = 1.62.

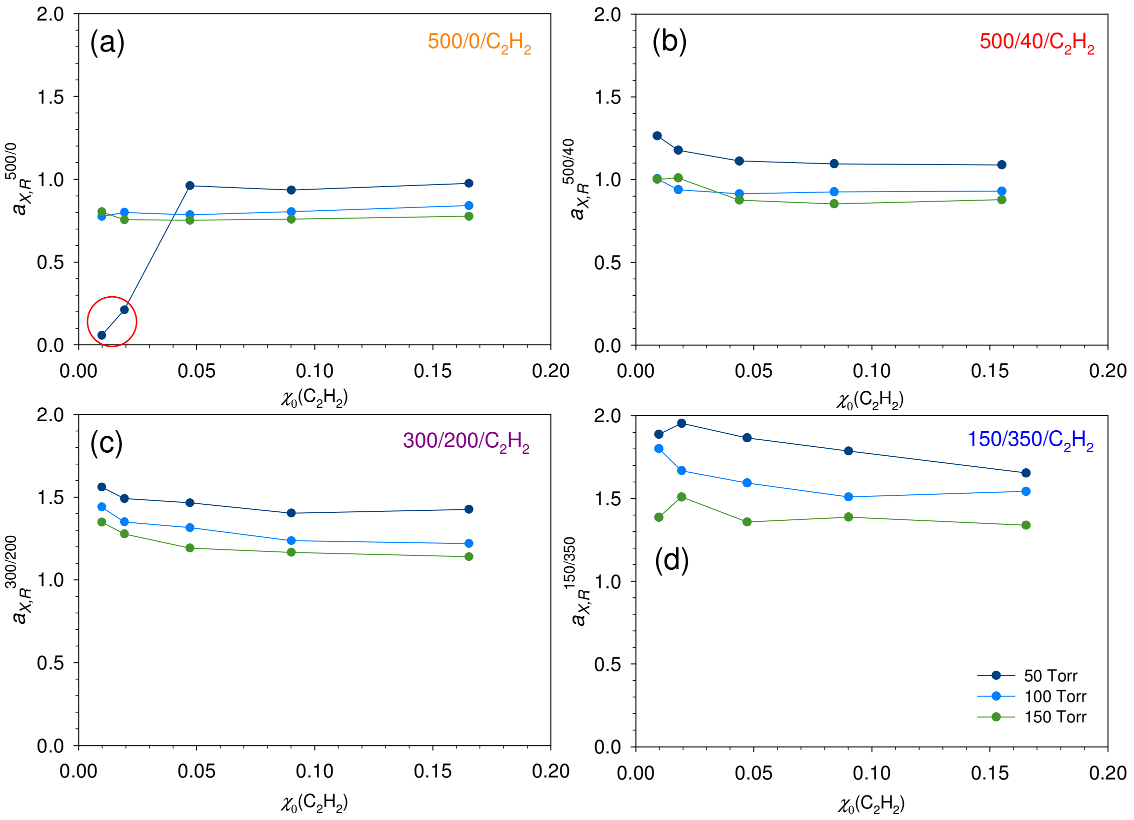

Figure 5.19: Calibration factors ($a^{\mathrm{H2/Ar}}$) calculated from correlation between known and measured $\chi_0(C_2H_2)$ using plots shown in Figure 5.17 & Figure 5.18. Calibration factors were obtained for four standard gas conditions (defined previously) where (a) = $a^{500/0}$, (b) = $a^{500/40}$, (c) = $a^{300/200}$ & (d) = $a^{150/350}$. Two, highlighted, points in (a) display values for which the validity is questionable.

5.3.4.2 Plasma diagnostics

Following completion of the cold-gas calibration, the system was tested using a set of plasma conditions. To test the analytical method the first species to be analysed was the stable and abundant hydrocarbon C_2H_2. $\chi(C_2H_2)$ was determined for the range of four gas mixtures, which had been calibrated, as a function of the process conditions including (a) input power, P, (b) chamber pressure, p, (c) hydrogen fraction, $\chi_0(H_2)$, (d) hydrocarbon fraction, $\chi_0(C_2H_2)$ or $\chi_0(CH_4)$ and (e) total flow rate (residence time), F_T. As for the cold-gas calibrations, 5 sccm (~1%) of Kr was added to the plasma as a reference.

It should be noted that one final stage in the analysis is missing here, because to give an absolute mole fraction the other components must also be measured and then summed together:

$$\chi_{H_2} + \chi_{CH_4} + \chi_{C_2H_2} + \chi_{Ar} = 1 \qquad (5.4)$$

We assume that these constituents make up the whole plasma system and that any other species contribute negligible amounts to the overall fraction. It is our measured mole fraction normalized to this summed mole fraction which is the true concentration of the sampled species. However, measurements of $\chi(H_2)$ is still not reliable in the current MBMS system although recent modifications have improved the design. It is not thought that this final manipulation will influence the result very much and so we present the results remembering this small proviso.

(a) Input MW power, *P*

These results are conducted for constant p = 100 Torr and for either $\chi_0(C_2H_2) = 0.025$ ($F(C_2H_2)$ = 12.5 sccm) or $\chi_0(CH_4) = 0.05$ ($F(CH_4)$ = 25 sccm). It is also noticeable that high P results are lacking for the 150/350 system as the plasma becomes too large allowing only a measurement up to P = 1.1 kW. Both the raw count rates for C_2H_2 and Kr show no influence (Figure 5.20) of the MW power between 0.7 and 1.5 kW although there is a spread in measurements depending on the gas mixture used with higher intensities recorded for the high $\chi_0(H_2)$. After manipulation this variation is almost completely removed although the 500/0 mixture remains slightly higher than the others. We see that all the added acetylene remains as C_2H_2 because $\chi(C_2H_2) \sim \chi_0(C_2H_2)$, *i.e.* only a small fraction of the total hydrocarbon content is involved with the CVD process. Comparison between the different source gases shows that the CH_4 addition results in slightly higher $\chi(C_2H_2)$ which is surprising and probably means that the results need correcting against the total mole fraction. In general, the invariance with P is to be expected as, within this range, there are only small changes in T_{gas} and any variation will influence the fractions of radical species rather than the stable C_2H_2. The results agree with previous MBMS analysis (Leeds *et al.*, 1999a) and laser absorption studies (Ma, 2008) which show no variation of the $\chi(C_2H_2)$ with P.

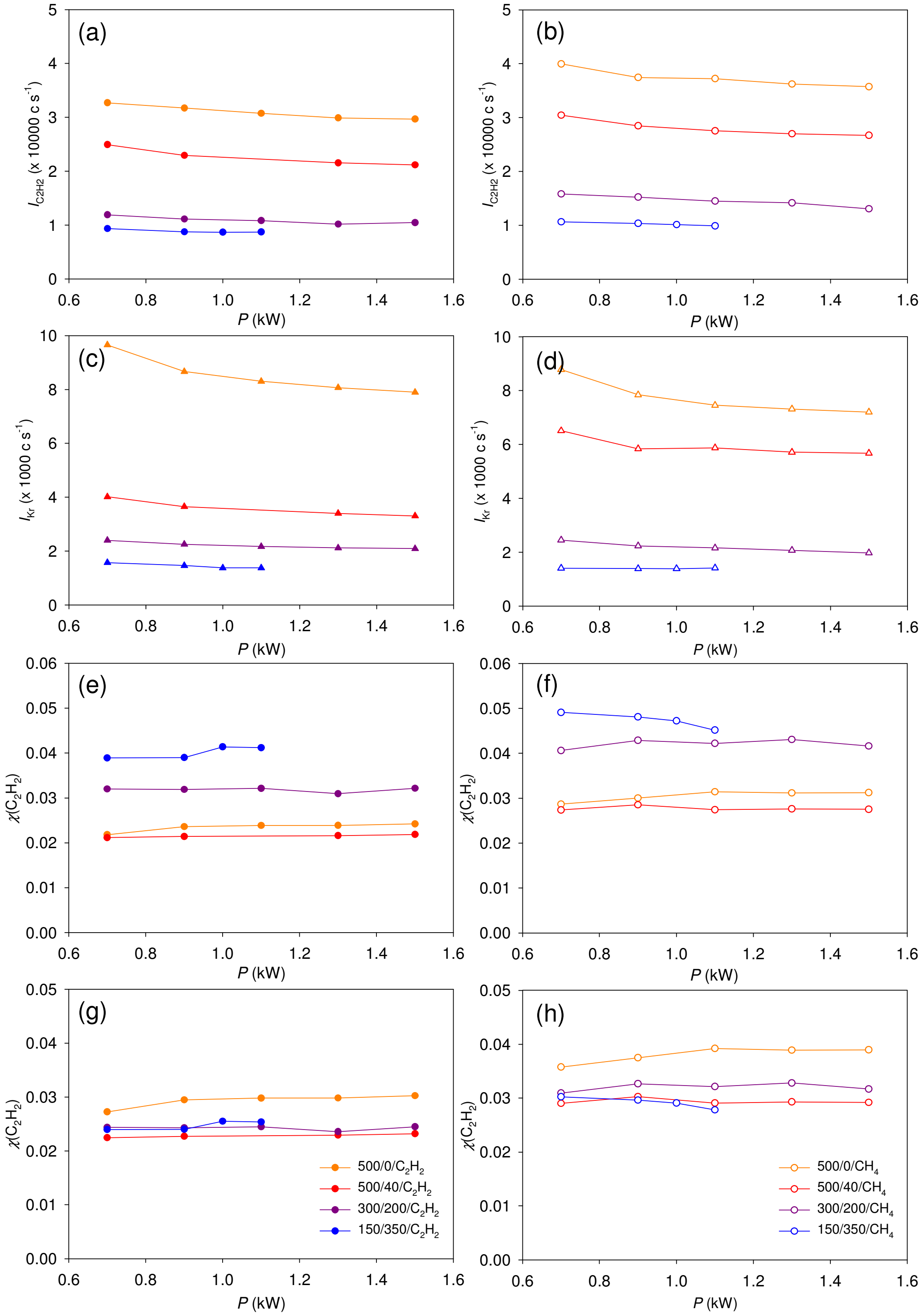

Figure 5.20: Variation of $\chi(C_2H_2)$ with input power (P) for H_2/Ar plasmas at p = 100 Torr with either C_2H_2 (●) or CH_4 (○) added at $F(C_2H_2)$ = 12.5 sccm and $F(CH_4)$ = 25 sccm, respectively. (a) and (b) raw count rates (I_{C2H2}) for the m/z = 26 C_2H_2 peak. (c) and (d) raw count rates (I_{Kr}) for the m/z = 84 ^{84}Kr reference peak. (e) to (h) the calculated $\chi(C_2H_2)$ before ((e) & (f)) and after ((g) & (h)) the appropriate $a^{H2/Ar}$ correction factor has been applied. Measurements were made at the four standard gas mixtures defined previously.

(b) MW reactor pressure, *p*

A greater variation in sampled intensities is expected for changes in the CVD reactor pressure (between 75 and 175 Torr) as the pressure varies throughout the MBMS instrument. These measurements were made at constant P = 1 kW and hydrocarbon fractions as previously defined. During the calibration we noted that the correction factors, $a^{\mathrm{H2/Ar}}$, change with pressure and so the factors were determined for each pressure value using linear regression of the calibration points shown in Figure 5.21.

The raw count rates for both C_2H_2 and Kr, indeed, show an increase in intensity with p (Figure 5.22) and over a wide range due to the contrasting behaviour of each gas mixtures. But, as the analysis is gradually applied, first by referencing to the Kr signal and then division by the pressure-specific correction factor, the variation of $\chi(C_2H_2)$ with pressure is no longer apparent for both C_2H_2 and CH_4 starting hydrocarbons.

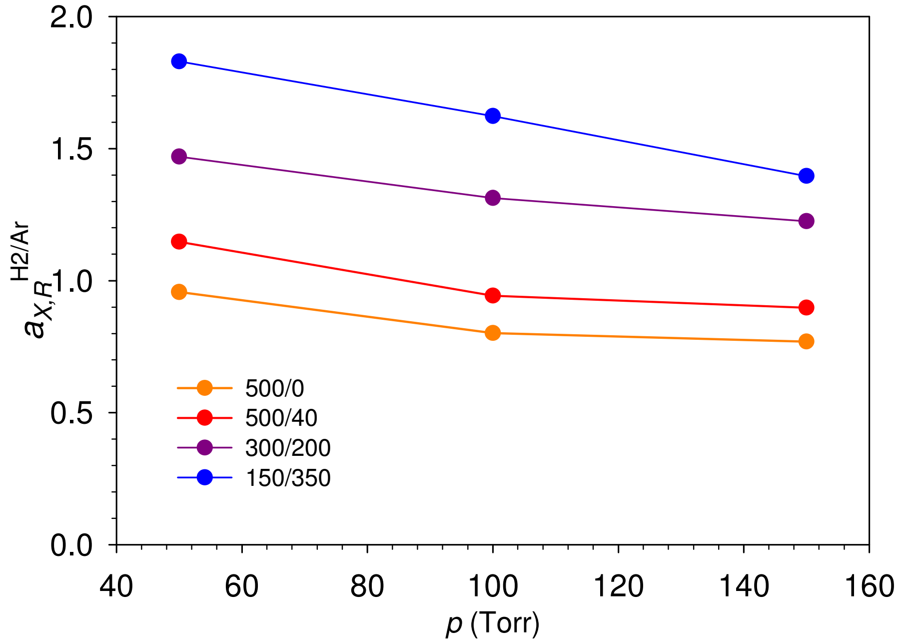

Figure 5.21: Data taken from Figure 5.19 plotting the mean value $a^{\mathrm{H2/Ar}}$ of the correction factor against MW reactor pressure, showing decreasing values for increasing p.

These conclusions agree with previous analysis by MBMS (Crichton, 2007) and laser absorption (Ma, 2008) which look at similar systems. Again, there appears to be some problem forcing the $\chi(C_2H_2)$ for the $H_2/Ar/CH_4$ system to be too high and above the level of the carbon at the input.

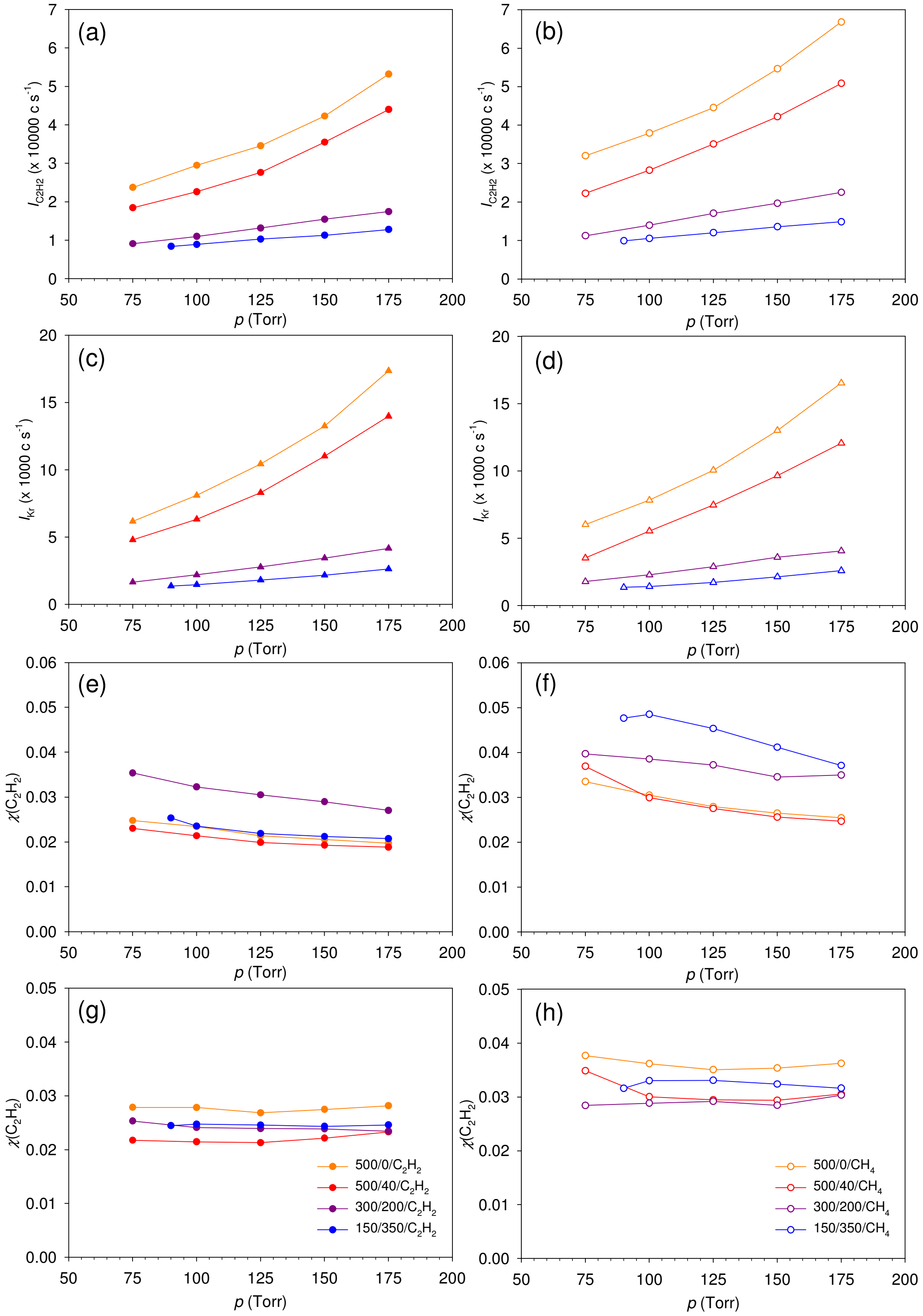

Figure 5.22: Variation of $\chi(C_2H_2)$ with reactor pressure (p) for H_2/Ar plasmas at P = 1 kW with either C_2H_2 (●) or CH_4 (○) added at $F(C_2H_2)$ = 12.5 sccm and $F(CH_4)$ = 25 sccm, respectively. (a) and (b) raw count rates (I_{C2H2}) for the m/z = 26 C_2H_2 peak. (c) and (d) raw count rates (I_{Kr}) for the m/z = 84 ^{84}Kr reference peak. (e) to (h) the calculated $\chi(C_2H_2)$ before ((e) & (f)) and after ((g) & (h)) the appropriate $a^{H2/Ar}$ correction factor has been applied. Measurements were made at the four standard gas mixtures defined previously.

(c) Hydrocarbon mole fraction, $\chi_0(C_2H_2)$ or $\chi_0(CH_4)$

Trends in $\chi(C_2H_2)$ with increasing hydrocarbon mole fraction, methane or acetylene, were obtained for the four gas mixtures in plasmas working at P = 1 kW and p = 100 Torr by measuring I_{C2H2} and the reference I_{Kr} whilst increasing $\chi_0(C_2H_2)$ ~ 0-0.045 or $\chi_0(CH_4)$ ~ 0-0.08 (the exact values being different for each gas mixture). $\chi_0(CH_4)$ was roughly twice $\chi_0(C_2H_2)$ to maintain similar overall carbon input fractions. The raw count-rate data and calculated $\chi(C_2H_2)$ values before and after correction are shown in Figure 5.23.

Linear increases in $\chi(C_2H_2)$ with carbon input would be predicted and are, indeed, observed agreeing with previous MBMS and absorption studies (Aubry *et al.*, 2002, Crichton, 2007, Hsu & Tung, 1992, Ma, 2008). Increasing the hydrocarbon fraction to just 8% of the total plasma is unlikely to have any profound influence on the plasma chemistry apart from slight fluctuations in the T_e. Addition of more methane or acetylene only increases the amount of radical species in the plasma (*e.g.* CH_x) which go on to recombine into neutral products (such as C_2H_2). Over this range of values, and even in the Ar-rich 150/350 mixture, there is an abundance of H atoms compared with $\chi(C_xH_y)$ to drive the interchange reactions between hydrocarbon species.

Theoretically, of course, this should be a 1:1 relationship (ignoring the negligible contribution from other hydrocarbons) but this is not quite observed hinting at the requirement for some adjustment to the final values. Especially in the case of the CH_4-containing plasma the calculations of $\chi(C_2H_2)$ are being overestimated by a small amount. This issue will be addressed once quantitative data is collected for the other stable plasma species: CH_4, H_2, Ar.

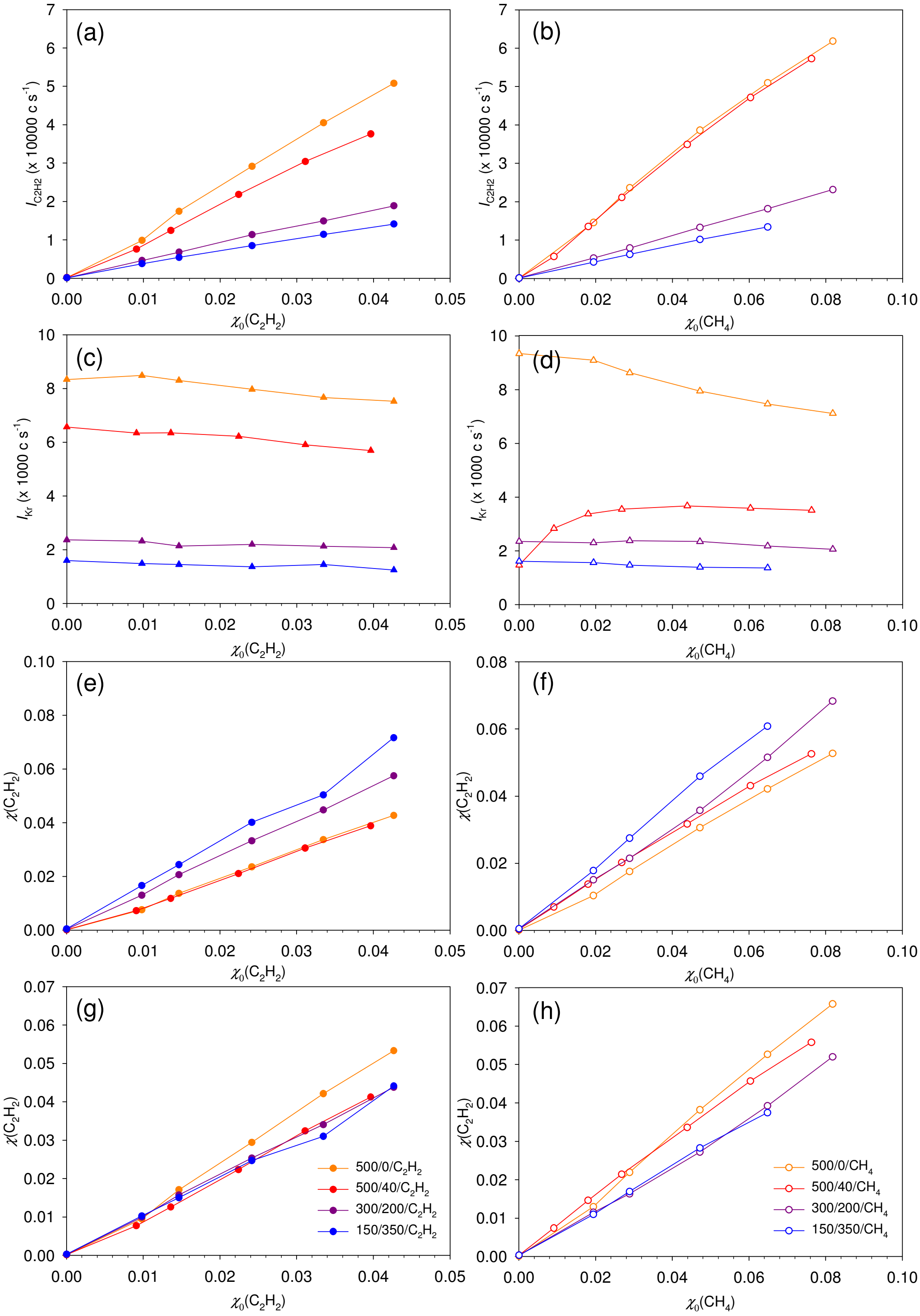

Figure 5.23: Variation of $\chi(C_2H_2)$ with input hydrocarbon mole fraction ($\chi_0(C_2H_2)$ (●) or $\chi_0(CH_4)$ (○)) for H_2/Ar plasmas at P = 1 kW and p = 100 Torr. (a) and (b) raw count rates (I_{C2H2}) for the m/z = 26 C_2H_2 peak. (c) and (d) raw count rates (I_{Kr}) for the m/z = 84 ^{84}Kr reference peak. (e) to (h) display the calculated $\chi(C_2H_2)$ before ((e) & (f)) and after ((g) & (h)) the appropriate $a^{H2/Ar}$ correction factor has been applied. Measurements were made at the four standard gas mixtures defined previously.

(d) Hydrogen mole fraction, $\chi_0(H_2)$

From the analysis of varying *p* (75-175 Torr), *P* (0.7-1.5 kW) and $\chi_0(C_xH_y)$ (0-0.08) we can conclude that the hydrogen fraction (and, therefore, the argon fraction because $\chi_0(Ar) \sim 1 - \chi_0(H_2)$) does not have any discernable influence on the MBMS-measured $\chi(C_2H_2)$. However, it should be remembered that we are using a correction factor dependent on the H_2/Ar ratio and so some effects could be masked by this manipulation. But as the factors derive from the cold-gas calibration any variation with $\chi_0(H_2)$ should still be apparent in the results. Even though this is not the case, and, within the stated ranges, the trends in *p*, *P* and $\chi_0(C_xH_y)$ overlap with each other, this fact should be borne in mind. In our reaction scheme (Figure 1.5) we see that C_2H_2 is formed through a series of H-atom abstraction reactions of C_2H_5 and C_2H_6 species, and in all these systems the H-atom density is sufficiently high to allow these reactions to occur and form C_2H_2, irrespective of the overall H_2/Ar ratio.

(e) Total flow rate, F_T

Theoretically, the total flow rate of gas through the reactor, or, to put it another way, the residence time of gas within the reactor, should not influence the plasma chemistry. This is likely to hold at least at the flow rates we employ, however, there is, obviously a lower limit below which either new gas is required for reactions or the pressure cannot be maintained. The influence of total flow rate (F_T) on $\chi(C_2H_2)$ was measured for two different gas mixtures as shown in Figure 5.24.

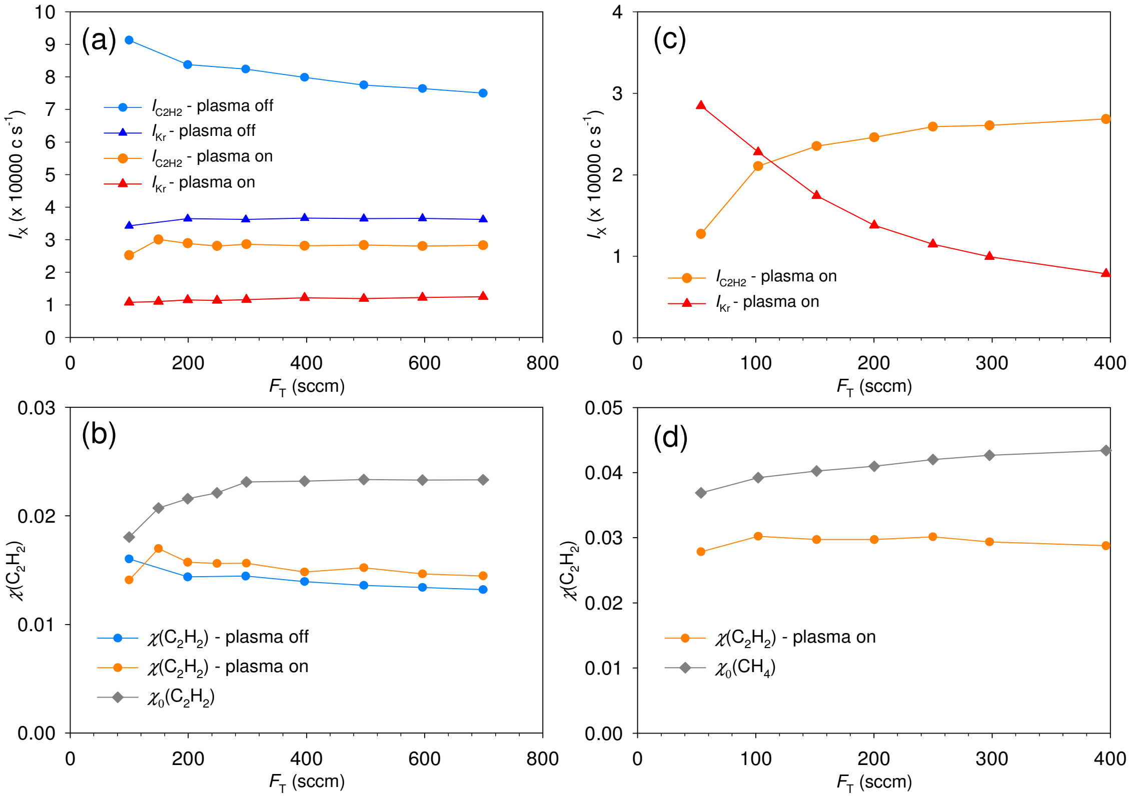

Figure 5.24: Variation of $\chi(C_2H_2)$ with total flow rate (F_T) for a selection of different plasma conditions. (a) & (b) results for the $\chi_0(H_2) = 0.98$, $\chi_0(Ar) = 0$ and $\chi_0(C_2H_2) = 0.02$ gas mixture (*cf.* 500/0) at room temperature and with a $P = 1$ kW/$p = 100$ Torr plasma. (a) the raw count rate data for I_{C2H2} (●) and I_{Kr} (▲). (b) the calculated $\chi(C_2H_2)$ (●) and the input mole fraction $\chi_0(C_2H_2)$ (◆). (c) & (d) the $\chi_0(H_2) = 0.88$, $\chi_0(Ar) = 0.07$ and $\chi_0(CH_4) = 0.04$ mixture (*cf.* 500/40; here only with the plasma on at $P = 1$ kW/$p = 100$ Torr) but where the added hydrocarbon is CH_4 rather than C_2H_2 used in (a) & (b). (c) the count rates for I_{C2H2} (●) and I_{Kr} (▲) and (d) the calculated $\chi(C_2H_2)$ (●) and the input mole fraction $\chi_0(CH_4)$ (◆).

The plots, indeed, show constant $\chi(C_2H_2)$ as F_T increases from ~50 to either 700 sccm (in the first case with flows proportional to 500/0) and from ~50 to 400 (in the second test plasma where flows are proportional to 500/40). Nevertheless, there appears to be some variability in the raw count rates when $F_T < 150$ sccm with a more significant variation observed in the 500/40 case. What is equally remarkable is that this variation in I_{C2H2} ($m/z = 26$) at low flow rates is corrected perfectly by an opposite trend in I_{Kr} ($m/z = 84$) which cancels out in the calculation of $\chi(C_2H_2)$. While the reasons for these observations are not fully understood it does appear to be a real trend and the rising I_{C2H2} has been recorded in previous experiments not shown here. If it is an artefact of sampling gas mixtures with lower flow rates, or longer residence times, then further investigation is necessary to determine why it is so obvious when sampling the 500/40 plasma and not so in the 500/0 system. What is clear is that there is no measured perturbation of the plasma at F_T down to 100 sccm and any variation is due to the MBMS sampling.

Although this analysis has not enlightened us about the diamond-deposition mechanism it has shown that the experimental method can provide credible results and allow comparisons to be made between gas conditions and other parameters. Crucially, any variation arising from the sampling system can be identified and removed from the analysis allowing a complete explanation of the results in terms of the plasma processes and chemistry.

We can compare these results with CRDS and OES analysis of radical species (C_2, CH and H) which show a different behaviour (section 3.3.9) increasing with p, P and $\chi(CH_4)$ as T_{gas} at the plasma centre increases. The challenge is to improve the sensitivity and detection limit of the MBMS instrument so that it can measure some of these reactive radical species.

5.3.5 Radical species

After achieving a better beam alignment, as indicated by the improvement in the signal-to-background ratio, attempts were made to detect the, supposedly most abundant, radical CH_3. Computational predictions of the gas mixtures show that at z = 0.5 mm, *i.e.* where the MBMS is sampling, the concentration of CH_3 is ~100 times less than that of C_2H_2 in MCD conditions like the 500/40 mixture and ~1000 times less in NCD-type conditions, analogous to the 150/350 gas composition . If we expect similar transmission for these hydrocarbon species, which is, however, unlikely, then count rates of ~300-500 s^{-1} would be achieved in the H_2-dominated system. This should be visible over the noise level after background subtraction. As CH_3 is predicted to be less abundant at lower $\chi_0(H_2)$, at the expense of larger hydrocarbons > C_2H_y which are prevalent in these systems, it is unlikely that the MBMS instrument, in the current configuration, will be able to measure this radical based on the measured I_{C2H2}. This is a major problem as the present C_2H_2 diagnostics were made at ~17.5 eV which lies above the AP of CH_3 from CH_4. Any accurate measurement of CH_3 would have to work at lower ionization potentials to prevent ionization *via* this dissociative route and this will also result in a reduction in the intensity of any signal measured.

Some initial testing at m/z = 15 was carried out using the high-$\chi_0(H_2)$ mixture and a lower potential of ~15 eV which did produce some recognizable signal just above the noise level, but this was not good enough for any accurate measurement. Further improvement to the alignment or experimentation with alternative beam apertures will, hopefully, allow measurement of this and other radical species with the MBMS apparatus.

5.4 Current position of project

A number of engineering, software and procedural issues have been addressed and modifications made to the MBMS system concerning the vacuum system, the beam optics and alignment, and the time-gated, detection algorithm. All have combined to produce a more advanced, reliable and sensitive instrument for analysis of the diamond-deposition environment. Testing with C_2H_2 has shown that the MBMS is capable of quantitative measurement over a wide range of process conditions and it is hoped that this work can be continued, first looking at the other abundant species, H_2, Ar and then at CH_4. Improvements to the vacuum and the beam alignment has allowed the system to achieve a signal-to-background ratio of ~58% compared with the previous values ~23% and this has corresponded to a decrease in the Kr-measured detection limit. This is despite using a smaller orifice which has prevented the pumping becoming unstable allowing high-$\chi_0(H_2)$ systems to be measured reliably. The LabView software and drivers have been rewritten to make them more efficient to cope with faster beam modulating frequencies and produce accurate, noise-free data in the required format. Using Kr as a reference has allowed a quick method to be formulated which can provide quantitative results by correcting any variation observed due to the changing gas mixture. Even though it has been relatively straightforward to measure these results they have proven that the system can work and produce data which is in agreement with previous MS and absorption diagnostics. In future, validation of this correction factor method may be compared with data which uses the H_2 signal as a reference (Leeds, 1999).

However, there are many improvements still waiting to be implemented which will allow a heightened sensitivity and lower detection limit which will facilitate measurement of radical and other low concentration species. In the short term, more precise beam alignment could be accomplished with careful positioning of the beam optics. Use of different skimmer apertures may also allow a greater beam flux into the ion source without resulting in a higher background.

The system will also benefit from updates to the data collection which could allow more than one mass to be measured during a single run, although synchronizing this with the chopper and the data averaging is not trivial.

6.0 Diamond X-ray lens project

6.1 Introduction

The fabrication of diamond lenses for focusing of high-energy X-ray synchrotron radiation, at the Diamond Light Source facility (www.diamond.ac.uk) at Harwell, Oxfordshire, was proposed as a joint venture between the Science and Technology Facilities Council (STFC) Micro-Nano Technology Centre (Rutherford Appleton Laboratory), the Diamond Light Source and the diamond group at the School of Chemistry, University of Bristol.

High-brilliance third-generation synchrotron X-ray sources have proven to be outstanding tools for the study of condensed matter (Laclare, 2001). The Diamond facility produces high-energy synchrotron radiation, with wavelengths from X-ray to far infra-red, emitted from electrons travelling close to the speed of light. The 13 beamlines have become essential tools for many diverse fields of scientific research, including particle physics, medicine, environmental studies and crystallography, since user operations began in January 2007. At present high-quality bent and bimorph silicon mirrors, up to 1 m in length, are used to focus the X-ray radiation using a grazing angle of incidence. However, there would be many advantages – including smaller optics, less precise apertures and no requirement for vacuum or bending apparatus – in using refractive (Snigirev *et al.*, 1996) or refractive-diffractive (Evans-Lutterodt *et al.*, 2003) optics for certain focusing operations at the Diamond Light Source and other synchrotron facilities. Nanofocusing has become particularly pertinent as the various analytical applications demand increasingly smaller focal-spot sizes for imaging with high spatial resolution on the atomic scale.

6.2 Hard X-ray focusing

6.2.1 X-ray optics

The focusing of X-ray radiation has occupied physicists for over a century and many techniques have been developed including diffractive optics, such as multilayer Laue lenses (Kang *et al.*, 2006) and Fresnel/Bragg-Fresnel zone plates (Chao *et al.*, 2005), or reflective optics, such as solid-metal X-ray mirrors (Yumoto *et al.*, 2006) or ellipsoidal capillaries (Snigirev *et al.*, 2007). These methods are generally based on either diffractive or reflective optics rather than on the refraction of the radiation (Suehiro *et al.*, 1991) as it is often assumed that the refraction of X-rays by a single lens is too small – the refractive index is close to unity – and the absorption of an array of lenses too high (Michette, 1991). However, there are two main types of lens structure which do employ refractive properties for focusing high-energy/hard X-ray radiation ($E > 4$ keV), both receiving considerable attention in recent literature. Kinoform lenses consist of computer-generated phase optics where the path length and focal-spot size can be calculated into the lens design with the advantage that they can yield 100% efficiencies in the resultant image (Jordan *et al.*, 1970). Using Fresnel-type kinoform lenses, with passive sections of the lens removed, significantly reduces the amount of material through which the beam passes thereby lowering the absorption (Ceglio *et al.*, 1983, Yang, 1993). Kinoform-lens designs fall into either *long* or *short* forms: in the latter the lens elements are folded back onto the same plane to save space.

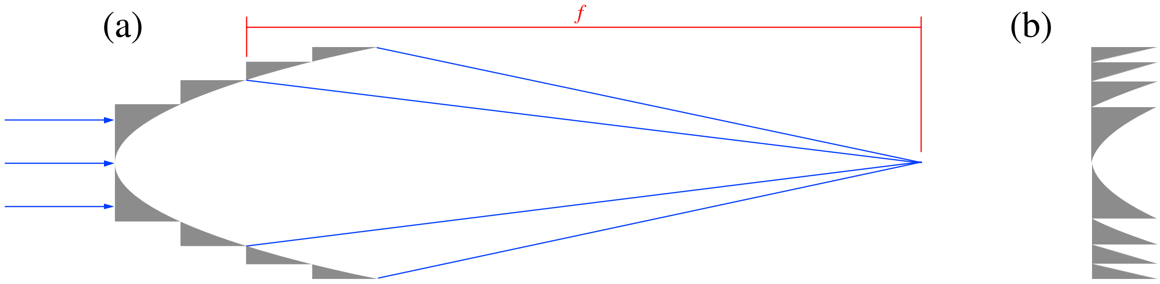

Figure 6.1: Diagram of (a) long Fresnel-type kinoform lens with focal length, *f*, shown and (b) contracted short form with lens elements on the same plane.

Arrays of kinoform lenses have been used to focus hard X-rays exceeding the critical angle limit of the single lens, *i.e.* the incident angle at which the beam is refracted along the normal (Evans-Lutterodt *et al.*, 2007).

6.2.2 Compound Refractive Lenses

The second major type of refractive X-ray optic is the compound refractive lens (CRL) which consists of an array of parabolic surfaces. Each lens contributes only a small amount of focusing but when combined together in a linear array reduces the focal length, overcoming the weak refraction associated with X-rays. CRLs are often less complicated structures compared with kinoform lenses but are slightly limited by effective aperture and absorption.

Refraction of X-ray radiation occurs when the waves pass between regions of different optical density and is described by:

$$n^* = n - i\beta \tag{6.1}$$

where n is the real part and β is the extinction coefficient and imaginary part of the complex index of refraction. This can be written as:

$$n^* = 1 - \delta - i\beta \tag{6.2}$$

We see that the real part, n, is determined by the refractive index decrement, δ, and, for X-rays, makes it smaller than unity by a term of order 10^{-4} to 10^{-6}, depending on the photon energy. This originates from the relationship between δ and the properties of the optical material:

$$2\pi(\delta + i\beta) = N_a r_e \lambda^2 (f_1 + if_2) \tag{6.3}$$

where N_a = atomic density of the material, r_e = classical electron radius (2.818×10^{-15} m), λ = the wavelength of the radiation and f_1 and f_2 = the real and imaginary components of the atomic scattering factor. The scattering factor f_2 is a function of the photoabsorption cross section, σ_a:

$$f_2 = \frac{\sigma_a}{2r_e\lambda} \tag{6.4}$$

The factor, f_1, is the number of electrons which interact with the electromagnetic wave and can be related to the atomic number, Z, using a Kramers-Kronig dispersion relation:

$$f_1 = Z^* + \frac{1}{\pi r_e hc}\int_0^\infty \frac{\varepsilon^2 \sigma_a(\varepsilon)}{E^2 - \varepsilon^2} d\varepsilon \tag{6.5}$$

At high photon energy, E, this approaches Z^* and can be related to the atomic number Z using a slight relativistic correction:

$$Z^* \approx Z - \left(\frac{Z}{82.5}\right)^{2.37} \tag{6.6}$$

Consequently, δ is larger for heavier atoms and means that materials for X-ray optics must have low Z in order to keep the decrement as small as possible (Kronig, 1926). Absorption of radiation by the lens material occurs mainly through the photoelectric effect and Compton scattering at $E <$

1 MeV, with an additional contribution from electron-positron pair formation for $E > 1$ MeV. Both photoelectric and inelastic Compton scattering of X-ray photons by electrons in the lens material results in a reduction in the beam transmission. To minimize the absorption losses, materials of low Z (*e.g.* Be, B, C, Al, Si) with a lower electron density and photon energies above ~10 keV have to be used for both kinoform lenses and CRLs. Lower-Z materials have a reduced electron density with which the X-rays can interact and, thereby, minimize the amount of energy lost to the lens material (Henke *et al.*, 1993). Conversely, Compton scattering becomes more important when $Z < 10$ and needs to considered when calculating transmission and absorption values (Hubbell *et al.*, 1975). While photoelectric cross-sections decrease as $\sim E^{-3}$, the Compton-scattering cross-sections rise with beam energy leading to a turning point in the transmission with increasing beam energy: in effect there is a theoretical maximum in the transmission for a certain material. This has been calculated to be 99.6% transmission at 18.8 keV for diamond kinoform lenses and slightly lower for silicon lenses (Isakovic *et al.*, 2009). Similar behaviour is expected in the CRLs where there is an optimum number of lens elements, N, and photon energies, E, for which the transmission peaks.

The small, positive value of δ means that X-ray radiation entering a solid material from vacuum ($n = 1$) is bent *away* from the normal, in contrast to visible light which is bent *towards* the normal of the refracting surface. As a result, refractive X-ray optics are designed with a biconcave shape, where the centre is thinner than the edges, as seen in both kinoform and CRL forms.

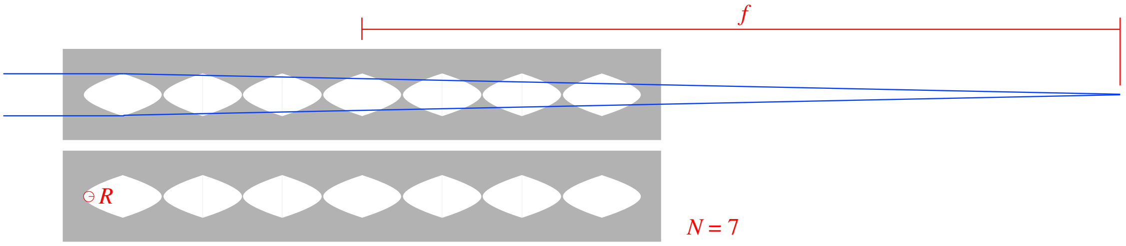

Figure 6.2: Fundamental CRL concept and parameters used for calculating focal length.

The focal length, f, of a refractive lens (Figure 6.2) can be calculated from the radius of curvature, R, and the index decrement, δ:

$$f = \frac{R}{2\delta} \tag{6.7}$$

For a linear array of lenses the focal length is shortened by a factor N, the number of refractive elements in the CRL:

$$f = \frac{R}{2\delta N} \tag{6.8}$$

From this we note that radius of curvature of the lens should be as small as possible in order to minimize the focal distance. Modern fabrication techniques are able to produce features with $R <$ 1 μm making focusing where $f <$ 1 m feasible.

The gain, G, of the lens is defined as the ratio of the flux density in the focal spot to the flux density in the same area without the lens and can be estimated from:

$$G = T \times \frac{A}{\sigma} \tag{6.9}$$

where A is the aperture, T the transmission and σ the focused beam size.

The first CRL lenses for focusing X-rays were proposed in the early 1990s (Tomie, 2010) and were produced mechanically, either by drilling a linear array of holes in plates of Al (Snigirev *et al.*, 1996) or by pressing parabolic forms into Be (Lengeler *et al.*, 2004), achieving point focal spots of a few micrometres. They were limited by approximating the ideal parabolic shape with circular forms and distortion of the lens walls as the adjacent voids were drilled. Arrays of cylindrical holes in two perpendicular planes produce a point-focus but suffer from spherical aberration. Greatly improved resolution and image quality could be attained by using parabolic CRLs pressed into Al but these were still hindered by absorption compared to materials with lower atomic masses (Lengeler *et al.*, 1999). The rotationally symmetric geometry of these lenses produced a good point-focus but the achievable minimum radius of curvature limited the focal length. More recently, microfabrication technologies, such as electron-beam or photolithography and reactive ion etching, have been used to produce increasingly intricate designs with the emphasis on increasing high spatial resolution and nano-scale focusing (Schroer *et al.*, 2003).

Fabrication of either kinoform lenses or CRLs from diamond offers distinct advantages as an optic material for hard X-rays with its relatively large decrement in refractive index, low absorption coefficient and high thermal conductivity. As such, single-crystal diamond has already found many uses in synchrotron X-ray optics including monochromators, polarizers and beam splitters. The ability to withstand high heat loading is becoming more apparent in the latest generation of synchrotron sources, some of which use of self-amplifying spontaneous emission in a free-electron laser (xfel.desy.de). Bonding of the planar CRL chip onto a larger diamond plate offers an efficient solution to the problem of heat dissipation. The main shortcoming in using diamond is the difficulty in moulding it into the precision forms with minimal phase errors required for synchrotron optics. Consequently, silicon optics are, although not ideal, still often preferable in current synchrotron sources due to the sufficiently low absorption and ease in machining.

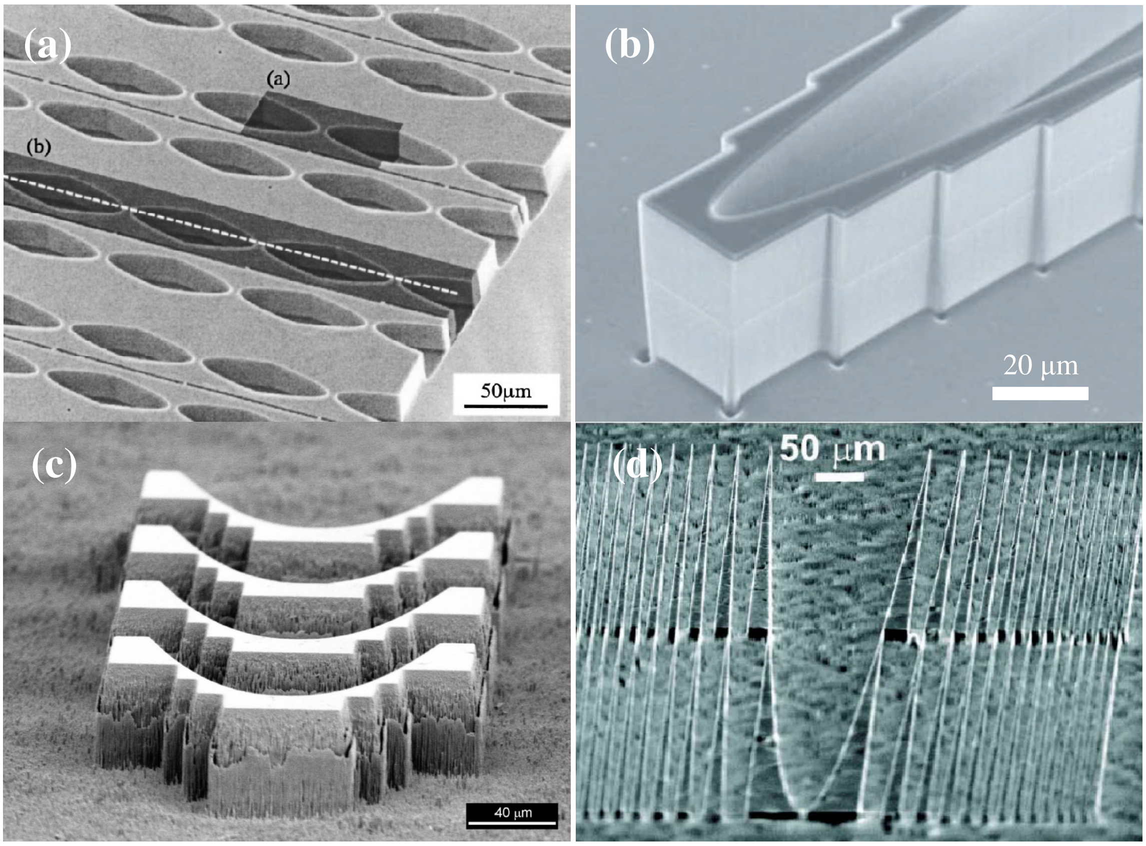

Figure 6.3: Earlier X-ray optics formed using etch processes. (a) an image of CRLs etched into Si (Schroer *et al.*, 2003), (b) a kinoform design accurately etched in Ge (Alianelli *et al.*, 2009), (c) an SEM image of a different kinoform design etched into diamond but with some material still remaining close to the lens base (Nöhammer *et al.*, 2003) and (d) another kinoform design etched into diamond (Isakovic *et al.*, 2009).

The earliest refractive synchrotron optics to use diamond (Nöhammer *et al.*, 2003) were kinoform-type lenses created on 200 µm thick CVD polycrystalline diamond substrates by e-beam lithography and deep reactive ion etching methods developed for fabricating Si lenses (Aristov *et al.*, 2000, Schroer *et al.*, 2005). Erosion of the chromium mask during the etch process led to problems with non-vertical lens walls and limited the lens performance somewhat by causing spherical aberrations. Observed efficiencies were fairly high – 78% at 17.5 keV – but lower than expected from calculations, primarily due to scattering of the radiation from the polycrystalline diamond grains and the rough surfaces typical of the etch process. Absorption losses were less than 5% for the diamond lenses but larger for silicon ones. Kinoform lenses have also been produced by plasma etching of diamond substrates into the required pattern (Isakovic *et al.*, 2009) and in germanium at the Diamond Light Source (Alianelli *et al.*, 2009). The former study aimed to illustrate the advantages of using diamond over silicon optics by looking at the transmission through a range of kinoform lenses with different numbers of elements, N, and X-ray wavelengths. The results produced focal-spot sizes of ~1 µm (at E = 11.3 keV and f = 0.2 m) for the diamond lenses and 1.3 μm (at 20 keV and *f* ~ 1 m) for the germanium lenses. CRLs and kinoform lenses produced by etching processes tend only to focus the beam in one plane and so two perpendicular arrays are required to produce a point-focus.

6.3 CRL diamond specification

At the outset, it was not immediately obvious what sort of diamond crystallite size would be most suitable for application as X-ray optics. Theoretically, the ideal lens would be fabricated from a single crystal but this is fundamentally limited by the current size of SCD samples with surface areas of only a few mm^2: lenses ~2 cm^2 would therefore have to be fabricated from either NCD or MCD. Lowering of the crystallite grain size would result in a greater fraction of non-diamond carbon – as graphite or amorphous carbon – being present at the grain boundaries which could prove detrimental by increasing the X-ray absorption or the amount of scattering. It was supposed that scattering from large, planar grain boundaries in a MCD film would distort the beam to a greater extent than from grains of 10-100 nm and that the films should, therefore, be nanocrystalline in texture with a minimal spread of grain sizes. Any remaining forward scattering would form a background to the focal spot and have a negative influence on the signal-to-noise ratio.

As we have seen, NCD can be fabricated using at least three different gas mixtures in our MWCVD apparatus: i) increasing the $\chi_0(CH_4)$ above a threshold of ~ 0.1 (*c.f.* section 3.2.2.1), ii) using an Ar-rich plasma ($\chi_0(Ar) > 0.8$, *c.f.* section 3.3) or iii) adding a trace amount of N_2 to MCD-depositing plasmas (*c.f.* section 3.4). The determining factor in deciding which of these to use was the required growth rate for the deposition. For use on the synchrotron beamline the lenses must be thick enough to transmit the beam – albeit after it has been trimmed through a slit – and, therefore, over 50 μm of diamond would need to be deposited on the Si mould. This precludes the use of high $\chi_0(Ar)$ chemistry as the growth rate of < 0.5 μm h^{-1} would be too slow to produce a thick enough film in our setup on a feasible time scale. The addition of N_2 to induce a nanocrystalline morphology *and* increase the growth rate seems an ideal solution to our problem and work that was carried out investigating and optimizing the addition of N_2 (section 3.4) found an almost immediate practical use here.

Fabrication of CRLs and kinoform lenses from diamond using etching and milling processes has, in the past, been hampered by a lack of smooth surfaces at the bottom of the recessed areas. In using a mould, the lens surface roughness, and, hence, the scattering, can be reduced, as long as the diamond nucleation and early growth stages were completed precisely enough. Subsequent removal of the Si mould would leave a freestanding NCD lens structure.

Usage of the beamline at the Diamond Light Source means testing of any optics can only be carried out at pre-booked times and, therefore, the diamond deposition runs were completed in batches. Intermediate testing of the lenses on the beam allowed improvements to the design, etching process and diamond deposition to be made before the next batch was fabricated. As such, we describe each group of samples in turn with the first batch also describing in detail the various stages in the fabrication and the beam testing processes. Modifications to the designs and methods will then be discussed as they arose when working on the second batch of samples.

6.4 Batch 1 of lens samples

6.4.1 Preliminary deposition experiments

Before subjecting a patterned Si substrate to the plasma, the growth conditions were tested on 1.4 cm^2 Si substrates of 0.3 mm thickness. This allowed the required N_2 fraction to be determined by analysing the resultant growth rate and crystallinity. To reduce the number of experiments needed, a temperature gradient was established across the substrate by tilting it into the plasma. using a small piece of Mo wire (250 μm thickness) to raise one end higher, and measured at 5 periodic points using the pyrometer. Plasma conditions of $\chi_0(H_2) \sim 0.94$, $\chi_0(CH_4) \sim 0.06$ (F_T = 535 sccm, P = 1.0 kW, p = 130 Torr and t = 2 h) initially without and then with 1400 ppm N_2 (0.75 sccm) formed the growth parameters for this test. The same five points across the substrate were then subjected to analysis by UV-Raman spectrometry (section 2.7.4) showing that higher T_{sub} leads to a more nanocrystalline texture with an increased amount of sp^2 carbon. Higher substrate temperatures were observed with the trace nitrogen added although a lower value is expected when using the larger, thicker patterned Si substrates. For both gas mixtures a threshold of $T_{sub} \sim 850$ °C marks the crossover to nanocrystalline morphology. To maintain the necessary substrate temperature with larger and thicker substrates required operation at higher power densities than these test runs.

6.4.2 Substrate manufacture

The replication method requires a high-quality Si mould to form a patterned substrate on which the NCD lens layer is deposited, and has been used for other microfabrication techniques (Jubber *et al.*, 1998, Ribbing *et al.*, 2003).

Rather than producing each CRL separately, a 2 cm^2 chip was designed which contained 16 lens arrays with differing numbers of elements allowing a range of photon energies to be tested. The individual CRL arrays are designed with a specific R = 50-60 μm and N to suit a specific photon energy increasing in 1 keV steps between 5 and 20 keV and a constant focal length of f = 0.55 m.

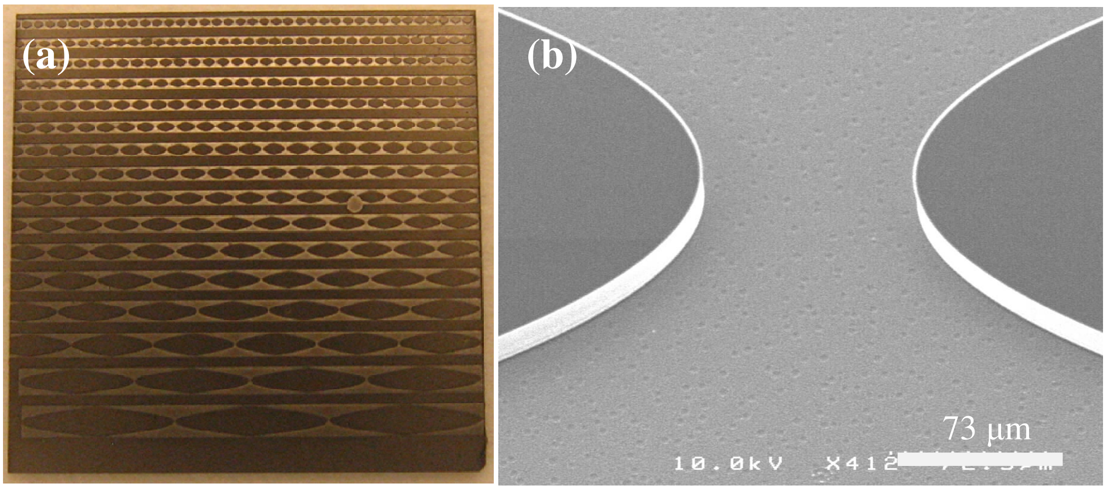

Figure 6.4: (a) example of a 20×20 mm lens chip with different numbers of elements N to focus different photon energies from 20 keV at the top of the image to 5 keV at the bottom and (b) SEM image of a Si mould showing the clearance between two lens parabolas.

The lens design was then etched as a negative into a Si substrate using a standard lithographic process carried out at the STFC Micro & Nanotechnology Centre which consisted of:

[redacted]

Previous etching studies using this process highlighted the problem of scalloping of the lens sidewalls due to anisotropic etching and can be seen in Figure 6.5.

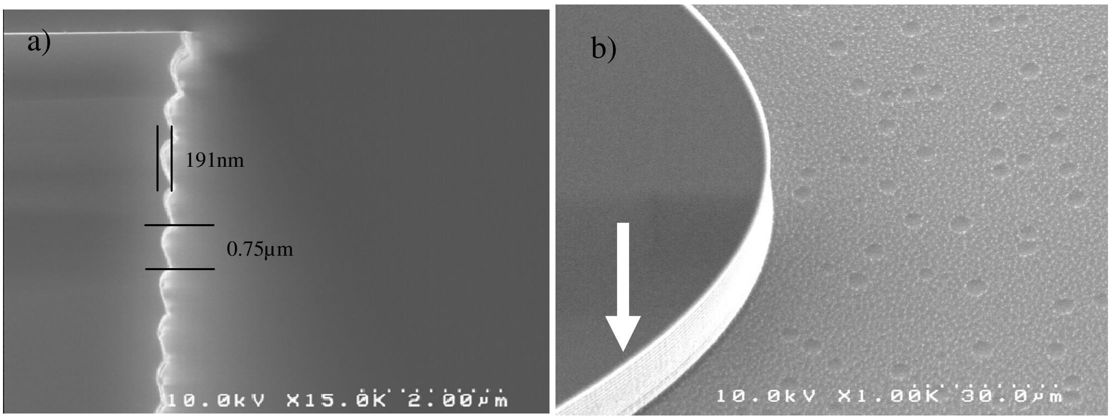

Figure 6.5: a) Si wall scalloping due to anisotropic lens etch, with the vertical and horizontal components quantified, can even be seen at lower magnification b). SEM images courtesy of A. Malik, STFC Micro & Nanotechnology Centre.

As well as minimizing the scalloping, the etching process must be optimized to achieve as near to vertical sidewalls as possible without any undercutting of the resist layer. The equipment used specifies a variation in the verticality of 90 ± 3° and in the first etch runs using a process outlined in Table 17 a slightly undercut profile was obtained with an angle of 88°.

	[redacted]	[redacted]
[redacted]	[redacted]	[redacted]
[redacted]	[redacted]	[redacted]
[redacted]	[redacted]	[redacted]
[redacted]	[redacted]	[redacted]
[redacted]	[redacted]	[redacted]
[redacted]	[redacted]	
[redacted]	[redacted]	

Table 17: Parameters for standard etch recipe developed at STFC Micro & Nanotechnology Centre.

The control over the verticality was achieved by adjusting the etch-to-passivation ratio, $R_{e/p}$, where lower values produce undercut profiles and higher values give the opposite profile where not enough etching occurs at the base of the mould. A series of tests allowed an optimum $R_{e/p}$ of [redacted]. Further improvement is possible and will be addressed in later batches.

A number of samples were prepared with identical CRL-mould patterns but different etch depths of 20, 40 and 100 μm for testing in the MWCVD reactor.

6.4.3 NCD deposition

Although the use of N_2 to induce a NCD morphology and fast growth rate had been established it took a number of trials to achieve the required diamond layer on top of the patterned substrates. Specifically, this meant achieving a good enough seed layer at the bottom of the recesses in the Si mould, running the CVD reactor for long enough times to properly fill the mould with diamond, and ensuring the MW power density and the H_2/Ar/CH_4 ratio were chosen to support the high growth rate and nanocrystalline morphology.

The initial run was conducted on a 20-μm-deep/30-mm-diameter substrate seeded with 5 nm ND (suspended in methanol) in the electrospray apparatus (section 2.5.5) and located on a 30-mm-diameter Mo plate within the reactor. To test the nucleation, a plasma was run initially without N_2 in the mixture of $\chi_0(H_2) = 0.847$, $\chi_0(Ar) = 0.068$, $\chi_0(CH_4) = 0.085$ ($F_T = 590$ sccm, $P = 1.2$ kW, $p = 120$ Torr and $t = 30$ h). The additional height of the substrate above the plate caused excessive heating at its edge resulting in an increase in the deposition of non-diamond carbon. Once started this problem escalates as the amorphous material attracts the plasma towards it and heats up. The result is a ring of non-diamond carbon around the rim of the substrate disk and a non-uniform coating inside it where the plasma has been pulled off axis. Despite the poor uniformity, adequate filling of the trenches had been achieved although they were still visible on the upper side of the film as the form had been 'translated' through the growth run (**RAL1**). The next deposition incorporated the trace N_2 (and not the Ar) in the proportions $\chi_0(H_2) = 0.924$, $\chi_0(N_2) = 0.002$, $\chi_0(CH_4) = 0.074$ ($F_T = 541$ sccm, $P = 1.4$ kW, $p = 110$ Torr and $t = 12$ h) with the pressure slightly lower than the first run to prevent the plasma concentrating on the substrate edge (**RAL2**). Again excessive heating was observed at the edge of the mould, and on cooling the diamond film cracked away from the substrate. However, the NCD morphology looked promising so the run was repeated for $t = 22$ h taking care to cool the substrate more slowly. This sample was good enough to allow post-processing and trial the Si-mould-removal step (**RAL3**).

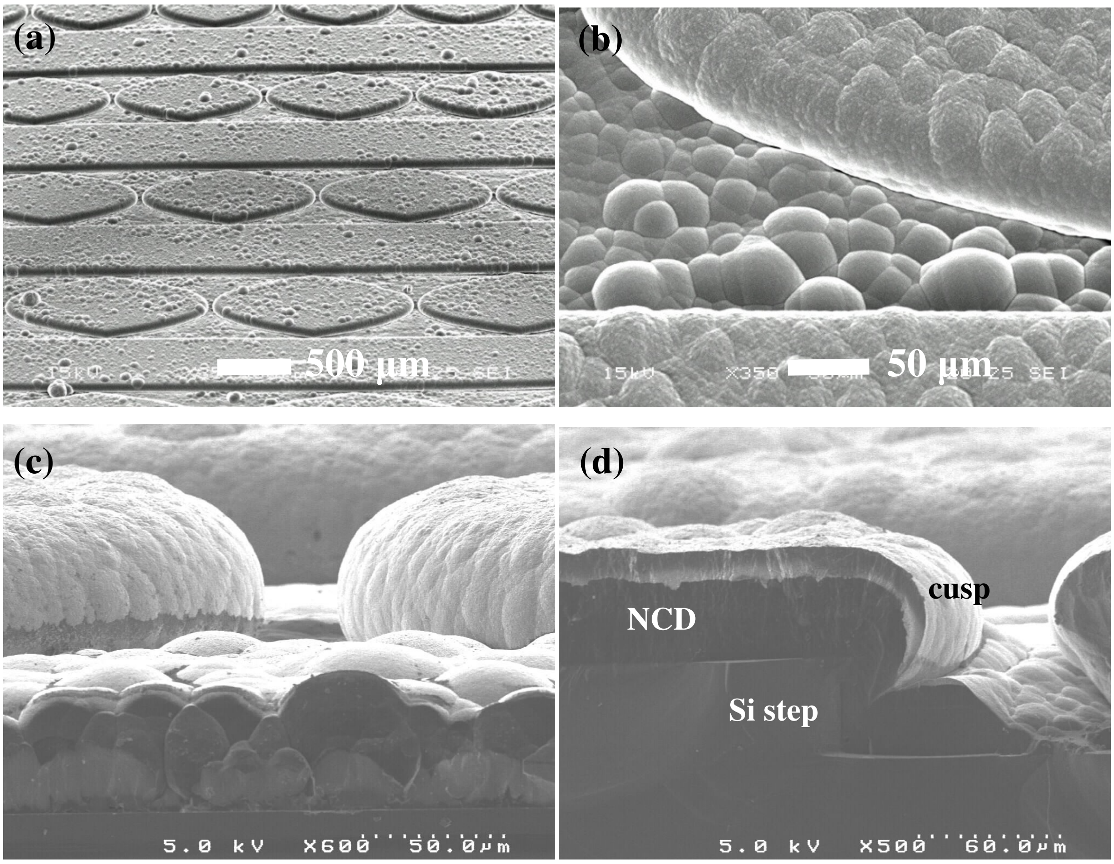

Figure 6.6: (a) & (b): Upper surface images of diamond-CRL deposition **RAL3** at two different magnifications showing NCD morphology across a large area and (c) & (d): Two cross-sections through the same sample showing adequate diamond deposition but too much overlap (a) away from and (b) on a Si step. Cross-sectional SEM images are from A. Malik, STFC Micro & Nanotechnology Centre.

While the recesses are not adequately filled there is a large amount of diamond in the mould which would be acceptable if deposition was allowed to run for a longer period. A cusp is noticeable above the Si step-edge where the faster growth rate closer to the plasma has overgrown material depositing in the recess. An unexpected change in diamond morphology is also visible in the sections and may correspond with exposing the sample to air between deposition runs because this sample was grown in a number of stages. Both these issues were addressed in subsequent work while the overall film thickness of this deposition was satisfactory.

The uniformity was still a problem, with regions of MCD amongst the NCD film, which could only be solved by recessing the substrate into a Mo holder. This was specially designed to hold 20×20 mm substrates with a depth of 1 mm (Figure 6.7) and required the circular Si moulds to be cut into squares using a laser milling machine (Oxford Laser micromachining system).

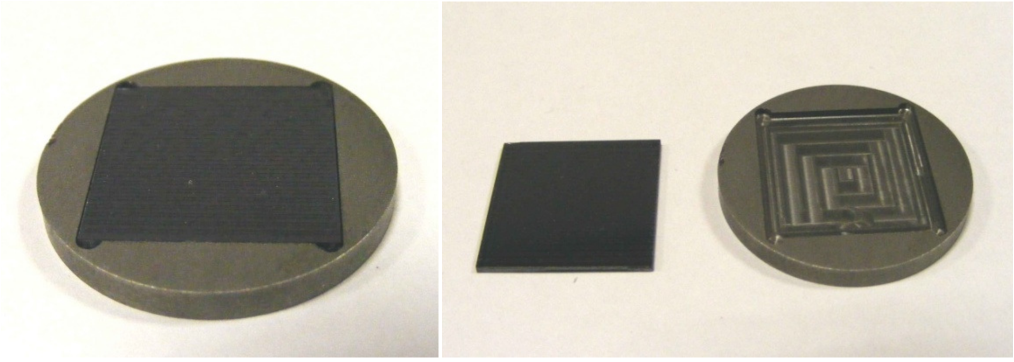

Figure 6.7: Newly milled molybdenum substrate holder with 20×20×1 mm recess. Shown with (left) and without (right) Si substrate in place.

The new substrate design was tested using roughly the same parameters as the first test **RAL1** but with the possibility of using higher p =150 Torr but lower P = 1 kW (**RAL4**). Not having N_2 to influence the growth chemistry led to deposition of partially MCD films.

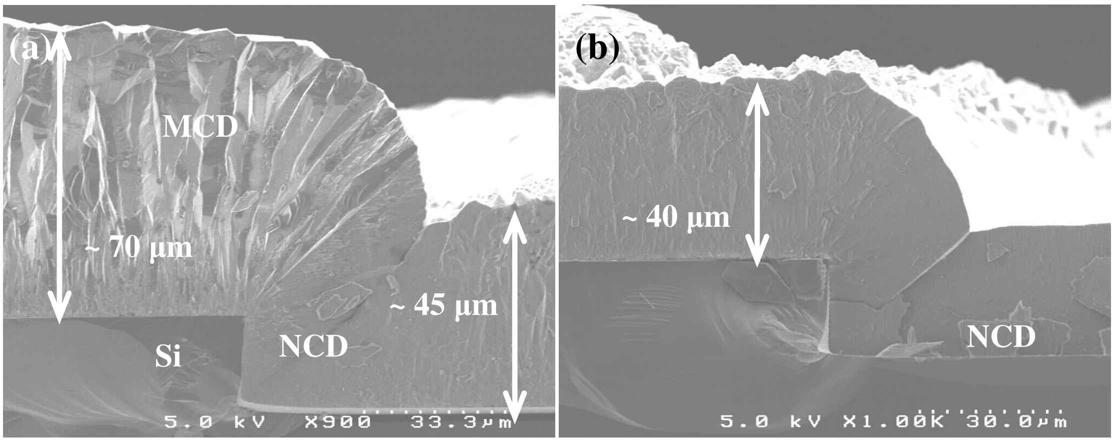

Figure 6.8: Cross-sectional SEM images of sample **RAL4** showing (a) faster growth rate but unwanted MCD texture unsuitable to synchrotron optics and (b) thinner film but requisite NCD morphology. SEM images are from A. Malik, STFC Micro & Nanotechnology Centre.

SEM imaging of the cross-sections through the diamond film (**RAL4**) allows the internal texture of the diamond to be analysed and show a marked improvement in the diamond morphology from undesirable MCD crystals to thinner NCD more suitable for synchrotron optics (Figure 6.8). In the section through the MCD area we see a fundamental problem of long growth runs where individual crystals grow in size with time: starting as nanocrystalline nuclei at the substrate and becoming large-faceted MCD on the exposed, upper surface. It is, therefore, pleasing to see that this problem manifests itself only in certain areas within the film. Other NCD regions show good filling of the mould and consistent crystal texture.

Maintaining a high growth rate was also important throughout this work, so the $\chi_0(CH_4)$ added was higher than normally used for MCD or NCD deposition. Similarly, the maximum possible power density was used without causing the plasma to become unstable and arc onto the substrate. With the longer growth runs there was still some build up of material at the periphery of the substrate which then reduced the uniformity (**RAL5**).

Subsequent depositions found an optimum power density resulting from P ~ 1.1 kW and $p = 125$ Torr and produced three more samples which were suitable for further development as shown in the following table (**RAL6-8**). It is obvious that optimization of the parameters resulted in a higher growth rate because shorter deposition times were required in the later depositions to achieve similar coverage.

sample	*depth* µm	$\chi_0(H_2)$	$\chi_0(N_2)$ ppm	$\chi_0(CH_4)$	$\chi_0(Ar)$	P kW	p Torr	T_{sub} °C	t h	*Good?*
RAL1	20	0.847	0.0	0.085	0.068	1.2	120	600-770	30	
RAL2	20	0.924	1800	0.074	0.0	1.4	110	650-700	12	
RAL3	40	0.924	1800	0.074	0.0	1.4	110	670-700	22	✓
RAL4	20	0.847	0.0	0.085	0.068	1.0	150	730-740	13	✓
RAL5	40	0.924	1800	0.074	0.0	1.0	125	720-755	6	
RAL6	40	0.916	1800	0.074	0.0	1.2	125	740-760	8	✓
RAL7	100	0.916	1800	0.082	0.0	1.1	125	750-760	10	✓
RAL8	100	0.916	1800	0.082	0.0	1.1	125	740-750	6	✓

Table 18: Deposition conditions for eight lens trials carried out in the Bristol MWCVD reactor. T_{sub} varied during the deposition and across the substrate area and is given as a range. Those films that were uniform and had suitable morphology for further testing are indicated by a tick.

Another important conclusion drawn from the cross-sections is the difference in film thickness between the higher and the recessed regions of the Si template. The different growth rates are to be expected due to the variation in substrate temperature and the proximity to the plasma. There could feasibly be a difference in the seeding density from the electrospray deposition but this is unlikely to be dominant over the T_{sub} variation.

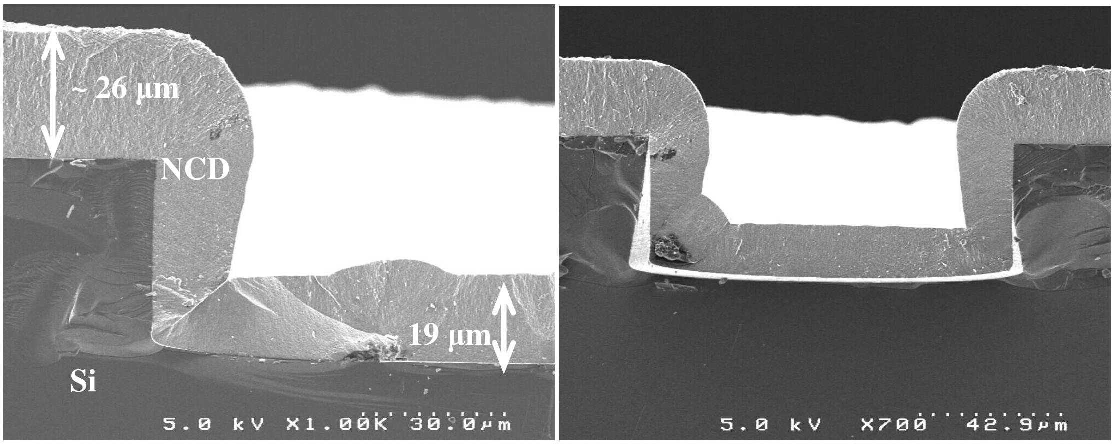

Figure 6.9: Cross-sectional SEM images of sample **RAL6** exhibiting excellent grain texture and uniformity but overall thinness due to the shorter deposition time. SEM images are from A. Malik, STFC Micro & Nanotechnology Centre.

By **RAL6** the uniformity had been substantially improved by addition of N_2 to the gas mixture although with a shorter deposition time the recesses are not filled as much as previous runs, as seen in the cross-sections in Figure 6.9. There was, however, still a disparity between the growth rates at the top and bottom of the recesses.

Future depositions concentrated on improving the uniformity, eliminating the small overhang observed at the corners of the mould and attempting to fill the recesses completely.

6.4.4 Substrate removal and characterization

Although not yet reaching the ideal lens structure and morphology, the two most suitable substrates were prepared for beam testing by removing the silicon mould to leave the free-standing diamond lens. This was a test of the robustness of the diamond film as much as a test of the lens properties.

Removal of the Si mould was achieved in a high-etch-rate plasma process at MNTC RAL. The two lens structures (**RAL6** and **RAL7**) were then each bonded on the diamond side to a 10×10×0.5 mm single-crystal diamond handling chip (purchased from Element Six, Ltd.) using epoxy resin and cured at 120 °C for 2 h. Removal of the Si mould was achieved in a high etch rate plasma process. SEM images of the diamond lens chip and SCD handling chip are shown in Figure 6.10. The chips responded well to this processing and seemed robust enough, remaining free from cracks or structural damage. There was some slight non-verticality in the sidewalls visible in the higher magnification image which may result from some release of stress as the Si was etched away. It is noticeable from Figure 6.10 that the handling chip is smaller than the CRL film which is not ideal and larger SCD chips were used in more recent work.

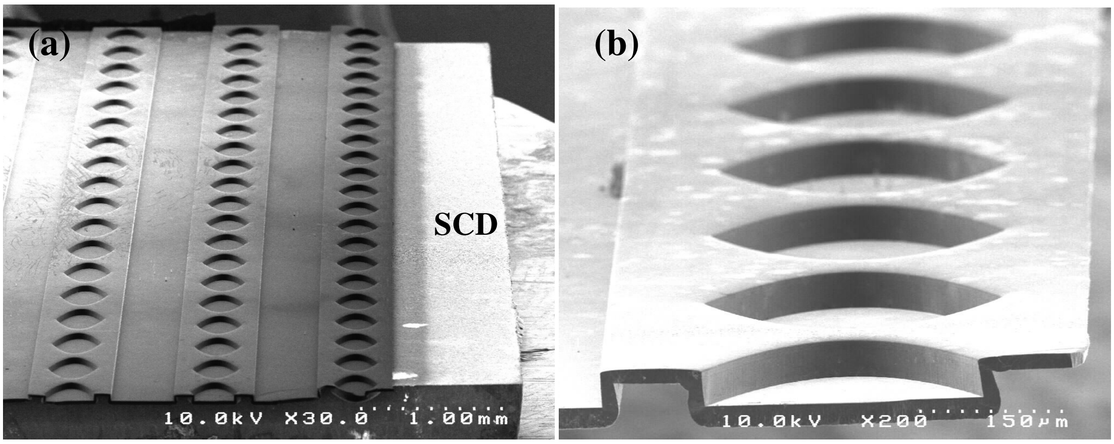

Figure 6.10: Diamond CRL made from deposition **RAL6** after removal of the Si mould showing (a) whole array and handling chip and (b) high quality, form fidelity and diamond surface homogeneity. SEM images are from A. Malik, STFC Micro & Nanotechnology Centre.

For the 100-µm-deep samples (**RAL7** and **RAL8**) the deposition time was about the same as for **RAL6** and, as such, the mould is less well filled, as seen in Figure 6.11. The higher aspect ratio of these films means they are less robust and could not be tested on the beam. In any case, it is unlikely that enough diamond had been deposited (~15 µm) on the sidewalls to allow sufficient focusing of the X-ray beam.

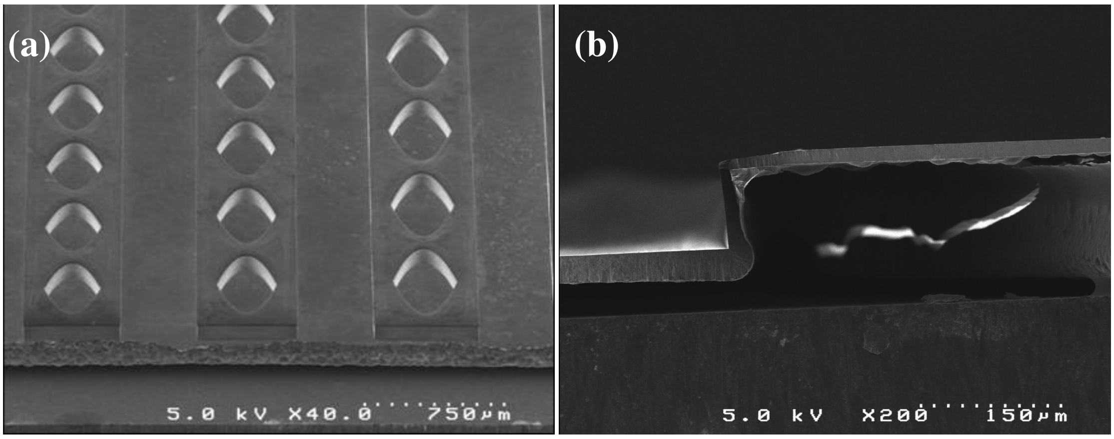

Figure 6.11: Diamond CRL from deposition **RAL7** after removal of the Si mould leaving relatively thin free-standing film because the mould depth was 100 µm. SEM images are from A. Malik, STFC Micro & Nanotechnology Centre.

6.4.5 Beam testing of Batch-1 lenses

The lenses on chip **RAL6** were tested on the B16 beamline at the Diamond Light Source, which is used for a wide range of experiments in optics and instrumentation development, and the results have recently been reported (Alianelli *et al.*, 2010). The bending-magnet X-ray source is coupled with a double-crystal silicon monochromator and slits to shape the incident beam so that it illuminates only one refractive lens array on the CRL chip.

After the diamond CRL, the focused beam is detected using a high-resolution system consisting of a 5 µm europium-doped lanthanum aluminium garnet, $La_3Al_5O_{12}$ (LAG), scintillator, a microscope objective and a PCO4000 CCD camera. Precise knife-edge measurements of the focal spot-size can be obtained using a piezo-mounted thin gold wire.

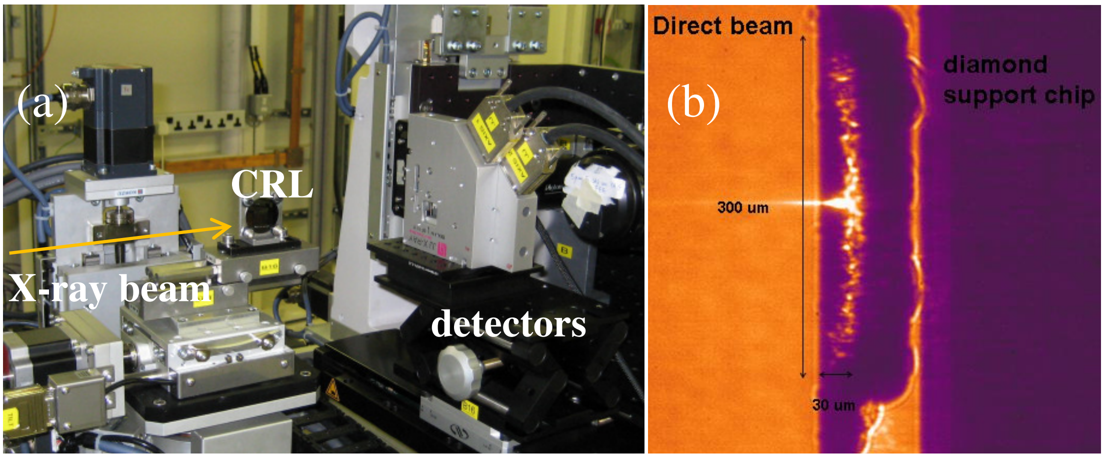

Figure 6.12: (a) experimental setup at beamline B16 and (b) batch-1 lens illuminated by the synchrotron X-ray beam showing the microfocused beam as the bright central spot, the unfocused beam (orange area) and scattering in a vertical line along the 'bottom' of the lens chip. Images courtesy of L. Alianelli, Diamond Light Source.

The degree of scattering can be determined by illuminating the vertically mounted lens with a wide X-ray beam and measuring the extra light transmitted in addition to the intense linear focus expected from the CRL. The low absorption of diamond enables low-level scattering to be observed and allows improvements to the fabrication process to be evaluated accurately.

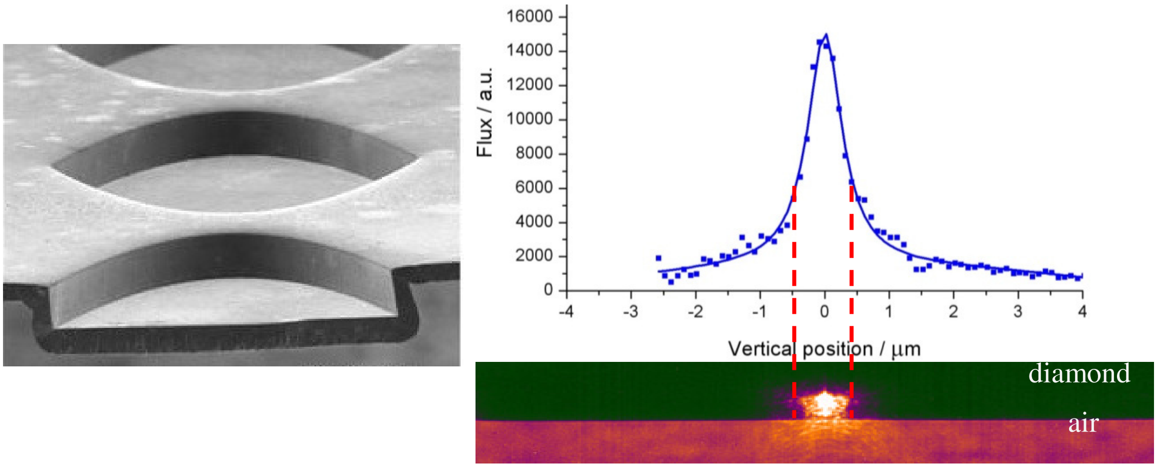

Figure 6.13: Performance of diamond CRL (left) displayed both as an image (bottom-right image, rotated anticlockwise by 90°) and a plot of flux against vertical position (top-right). The FWHM of this curve is used to determine the focal spot-size. Data courtesy of the Diamond Light Source.

For the initial tests, just the lenses designed for photon energy values E = 18 keV (lens A) and 12 keV (lens B) were analysed due to the amount of time required to set up the lens and move it into the correct position. The detector was placed at distances f = 1.06 m and f = 0.56 m from lenses A and B, respectively, and focal spot-sizes were quantified by using the FWHM of the flux of radiation through the lens as a function of vertical position. The results are shown in the following table, from which we see that the shorter focal lengths/lower photon energy achieves smaller FWHM values.

lens	*E* keV	*f* m	*demagnification*	*theoretical focus FWHM* µm	*observed focus FWHM* µm
A	18	1.06	44	1.8-2.25	2.2
B	12	0.56	84	0.95-1.2	1.6

Table 19: Summary of beamline testing of Batch-1 diamond CRLs (Alianelli *et al.*, 2010).

The sides of the focused-beam profile are mainly due to the scattering of radiation by the diamond grain boundaries and the side-wall scalloping from the etch process and may result in the purely Lorentzian fitting required, whereas the incident beam should have a Gaussian profile (see Figure 6.14). As we have mentioned, improvements to the etch cycle should improve this problem. Another detrimental effect is the bending and distortion of the lens and will require further attention to produce a more robust structure by growing a thicker diamond layer and using a more effective bond to the handling substrate.

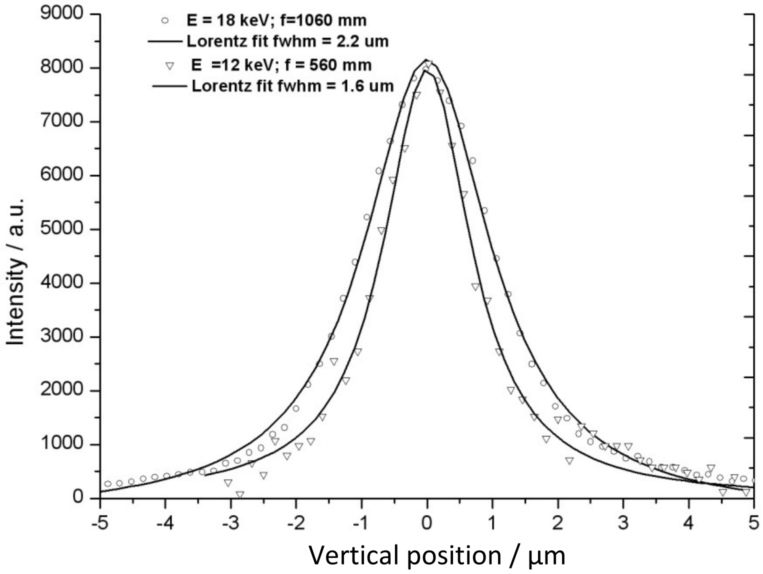

Figure 6.14: Fit of Lorentzian curves to the vertically focused profiles showing the E = 18 keV (○) and E = 12 keV (▽) CRLs with corresponding FWHM of 2.2 and 1.6 µm, respectively.

Absorption in the lens limits the efficiency and the 'effective aperture', which is defined as the aperture which transmits 75% of the full flux from the lens. The beam testing showed that for these diamond lenses the efficiency is proportional to the illuminated aperture: that is, the transmission is constant within this range. This has been made possible by utilizing a low-*Z* material and means larger apertures can be used whereas Si lenses, for example, will be more absorbing and have much smaller effective apertures.

Issues concerning the robustness of the diamond CRLs came to the fore when the same lens chip was tested at the European Synchrotron Radiation Facility in Grenoble (www.esrf.eu) and no real focusing could be detected. This indicated a likely failure in the diamond lens structure as an identical experimental setup was used. Bending of the lens array, fracturing of the material or release from the handling chip are all possible reasons for the failure which would all, to a greater or lesser extent, benefit from thicker, stronger lenses being fabricated.

6.5 Batch-2 lens samples

6.5.1 Improvements to the Si mould

As we have seen, the first batch of diamond CRLs performed well in the beam testing and a number of improvements to the design were proposed for the second trials. Firstly, to remove the need for the crude laser cutting into 20×20 mm chips the Si moulds would be initially fabricated to the correct dimensions from the outset. [redacted].

6.5.2 Diamond deposition and modifications

Aside from the changes to the mould, the diamond deposition step was continued in much the same way as the previous work and the MWCVD parameters are outlined in the following table.

Again, the first run (**RAL10**) is a test of the seed layer on these new substrates using standard MCD growth conditions. Having shown acceptable coverage we moved back to using the optimized conditions with added N_2.

sample	***depth***	$\chi_0(H_2)$	$\chi_0(N_2)$	$\chi_0(CH_4)$	$\chi_0(Ar)$	P	p	T_{sub}	t	*Good?*
	µm		ppm			kW	Torr	°C	h	
RAL10	**50**	0.862	0.0	0.069	0.069	1	150	830	5	
RAL11	**50**	0.915	2500	0.083	0.0	1.1	125	685-690	8	✓
RAL12	**50**	0.915	3000	0.082	0.0	1.1	125	833-850	7	✓
RAL13	**50**	0.915	3000	0.082	0.0	1.2	125	820-840	7	
RAL14	**50**	0.915	3000	0.082	0.0	1.2	125	840-850	13	
RAL15	**50**	0.933	1800	0.065	0.0	1.2	125	840	12	
RAL16	**50**	0.933	1800	0.065	0.0	1.2	125	740	6	✓
RAL17	**50**	0.933	1800	0.065	0.0	1.2	125	775	17	✓

Table 20: Deposition conditions for batch-2 lenses in the Bristol MWCVD reactor. Substrate temperatures varied during the deposition and across the substrate area and are sometimes given as ranges. Those films uniform enough and with suitable morphology for further testing are indicated with ticks. **RAL9** is missing from this table because it was a spare substrate from batch-1 and not grown on.

Some samples failed to be as uniform as hoped as a result of anisotropy of the plasma and build up of amorphous or graphitic carbon around the edge of the Mo holder (Figure 6.16). This was partially alleviated through lowering of $\chi_0(CH_4)$ which, in turn, allowed a higher MW power to be used (P = 1.2 kW) and an improvement can be seen in Figure 6.17.

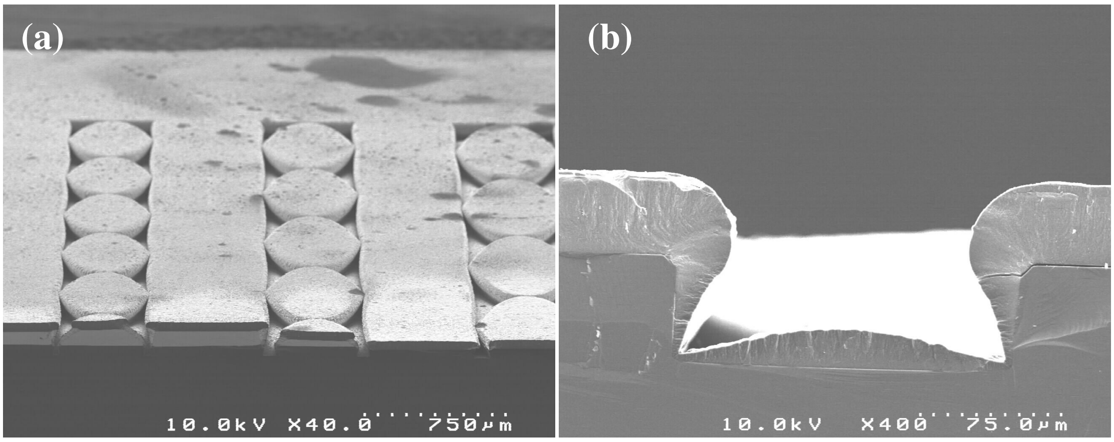

Figure 6.15: Diamond CRL from deposition **RAL15** where growth rates at the bottom of the recesses were lower than expected possibly due to insufficient seeding. The fragility of this film is indicated by the crack on the right in (b) where the different thicknesses of diamond have broken apart. SEM images are from A. Malik, STFC Micro & Nanotechnology Centre.

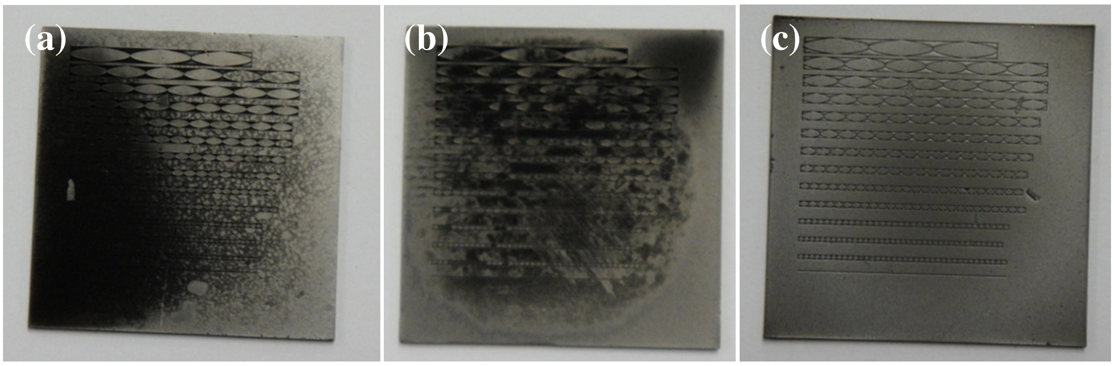

Figure 6.16: Photographs of two failed films (a) = **RAL13** & (b) = **RAL14**) where plasma conditions produced too much non-diamond carbon and resulted in very poor quality samples. In both there are regions of amorphous carbon (black) and NCD (grey). (c) the highest quality NCD-covered CRL chip (**RAL17**) which was subsequently tested at the synchrotron. There are some fragments of diamond which lie on the growing surface and originate from the Mo holder. The occurrence of these should be minimized but they do not appear to have any influence of the CRL as they are not present on the other side of the film.

Experiments were not as repeatable as hoped (Figure 6.16) and finding a more robust method which can reliably produce uniform lens substrates that are free from non-diamond growth at the periphery of the substrate and holder became a priority for the next stage of the project. In general, the modifications made in the second batch of samples significantly improved the lens morphology, form fidelity and robustness, as will be seen from the beamline test results.

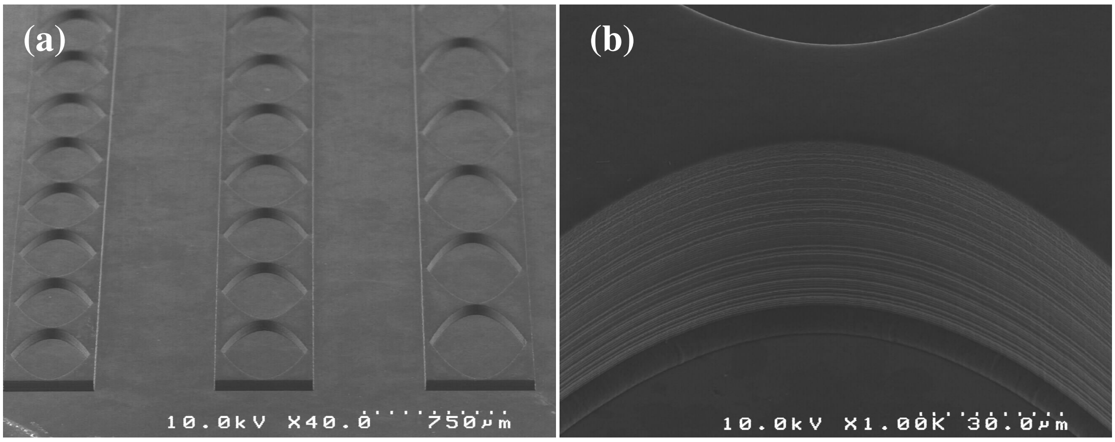

Figure 6.17: SEM images of lenses on chips **RAL16** (a) and **RAL17** (b) showing improvements in diamond quality and substrate coverage after removal of the Si mould. SEM images are courtesy of A. Malik, STFC Micro & Nanotechnology Centre.

The coverage of the mould in the most recent deposition attempts has been much better as a result of more careful electrospray seeding, cooling and heating of the substrate and Mo holder and removal of diamond deposits on the holder between depositions. The problem of horizontal etch scalloping remains an issue to be addressed by the MNTC in future work.

6.5.3 Beam testing of Batch-2 CRLs

The second batch of lenses were tested at the Diamond Light Source B16 beamline using identical methods to those described in section 6.4.5 and the improvements made to both the diamond morphology and the bonding to the handling chip are evident in Figure 6.18.

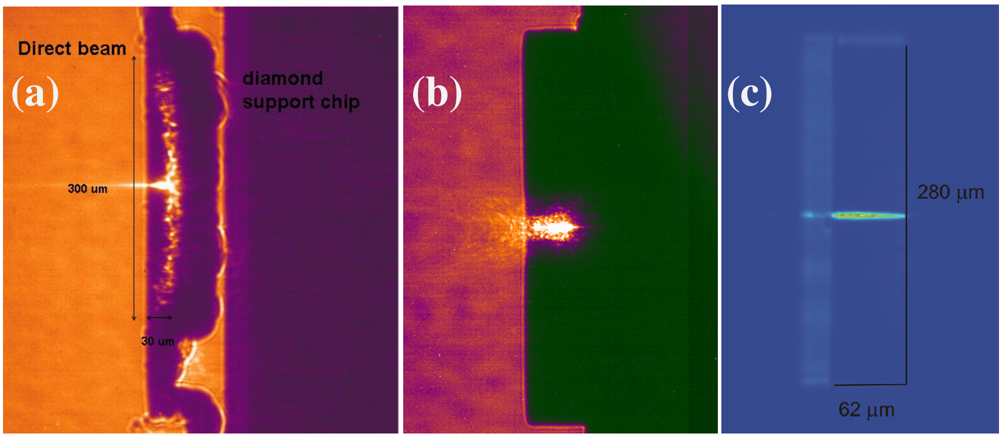

Figure 6.18: High resolution X-ray images illustrating the performance of a diamond CRL from (a) batch 1 and (b) batch 2 and (c) the performance of analogous silicon optics. Images courtesy of L. Alianelli, Diamond Light Source.

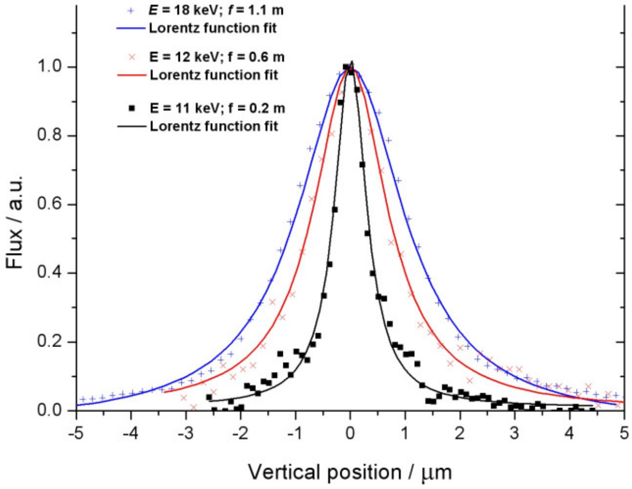

Figure 6.19: Improvements to the focusing comparing batch-1 lenses (— at 18 keV and — at 12 keV) and the new lenses on RAL17 (— at 11 keV). Data courtesy of L. Alianelli, Diamond Light Source.

While the differences (Figure 6.19) between the first and second batches of diamond CRLs are considerable, the latest tests show that the performance can still be improved to meet the performance of current Si CRL optics, but with the advantage of unprecedented flux over wider apertures. The silicon-based optics project, running alongside the diamond research and involving high accuracy etching of silicon into the kinoform lens structures, has achieved focusing down to 200 nm FWHM.

Both the images and the vertical profiles indicate a smaller focal width with FWHM of 650 nm in the latest lens chip. This is a very satisfactory result but has been surpassed by the most recent testing of this lens which achieved a focal FWHM of 400 nm, *i.e.* comparable with etched diamond optics. The focal spot can, hopefully, be reduced even further by using higher quality films and shorter focal lengths.

	lens chip	*E*	*f*	*focus FWHM*
		keV	m	µm
Batch 1 (2010)	RAL6	12	0.56	1.6
Batch 2 (2011)	RAL17	11	0.192	0.65

Table 21: Comparison of first and second diamond CRL tests at the Diamond Light Source.The higher degree of small angle scattering, identified by the non-Lorentzian data at the bottom of the vertical profiles, will need to be addressed in future deposition runs. This is especially apparent when using anti-scatter slits before the detector which produce much better fitting and a slightly smaller FWHM result. Complete removal of this effect might not be possible due to the nature of the NCD material but the grain size can be adjusted by using different concentrations of N_2 in the CVD process.

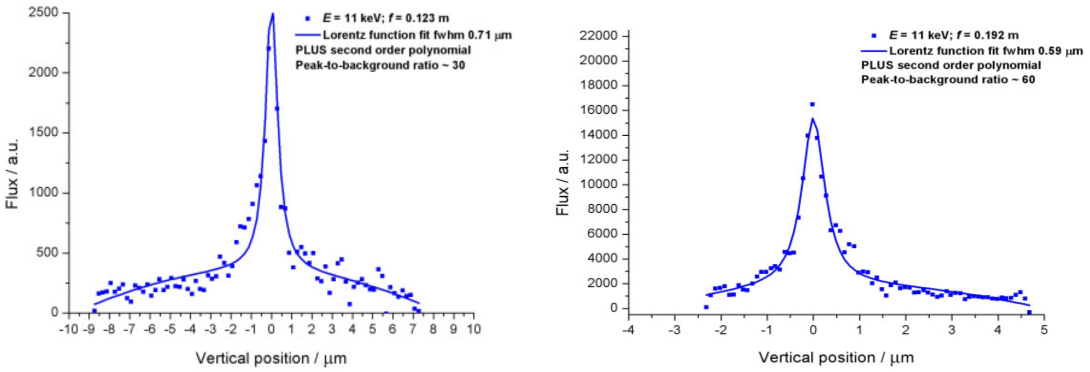

Figure 6.20: Use of anti-scatter slits removes unwanted dispersion of the beam at the base of the vertical profile. Data from L. Alianelli, Diamond Light Source.

As well as the focusing experiments we have discussed, the crystalline phases in the CRL samples were established by powder diffraction, which indicated that only diamond and no crystalline graphite phases were present. It should be pointed out that only crystalline phases can be detected and other spectroscopic studies will be necessary to discover what other impurities are present within the CVD diamond structure. Importantly, no change in the XRD pattern was detectable after irradiation which would indicate that the diamond phase had not been altered by the X-ray beam or any heating effects. The diffraction studies also showed that the diamond domains were in the range of 20-30 nm correlating with the theoretical grain size and previous work on NCD deposition.

Other research has recently demonstrated focusing with a FWHM of 360 nm using diamond CRLs produced by reactive ion etching in the collaboration between TU Dresden, Fraunhofer IAF and Diamond Materials (Schroer, unpublished work). The aim for the present project is to emulate the smaller R and f to achieve comparable if not superior focusing with as little scattering as possible.

6.6 Further work

6.6.1 Lens characterization at Diamond

Comprehensive diagnostics can be performed using the diamond lenses already fabricated to determine properties of the CRL, including the percentage transmission, the relative influences of scattering and absorption and heating of the diamond, at different photon energies. Additional information on the diamond crystal structure, crystallite size, impurity level, density and grain-boundary composition will also be analysed. In particular, the density of the NCD material is an important parameter to be determined, with initial results from refractive index measurements of 3.05 g cm^{-3}. This falls slightly lower than theoretical single-crystal diamond value of 3.5 g cm^{-3} as would be expected for a film with a higher sp^2 content. Accurate quantification of the density is crucial as this will be used to design kinoform lenses where the structure and path lengths have a finer margin of error.

6.6.2 Future lens depositions

The success of the most recent diamond CRLs tested on the beam merits further investigation with new designs incorporating narrower clearances between lens elements and smaller R (~20 μm, *i.e.* twice as small as the present lenses) leading to smaller focal-spot sizes (Schroer & Lengeler, 2005). There are still many ways in which the deposition can be modified to achieve more robust substrates (free from any bowing when the Si substrate is removed) with the desired diamond morphology and thickness. Attempts will be made to prevent deposition of diamond on the side, or even back, of the mould as this can hinder the Si-removal step.

Si moulds will also be developed to allow deposition of diamond kinoform lenses, reducing the amount of diamond through which the X-rays must pass and its associated absorption. With both projects the aim will be to successfully nucleate and grow diamond in increasingly narrower recesses. In particular the kinoform lenses have steps with dimensions of only ~5×30 μm and *R* ~ 1 μm and it is not apparent at the moment whether diamond growth on features of this size would be possible using the current nucleation and deposition method. Overall, both modifications will allow shorter focal lengths and nanofocusing to be achieved with a reduction in the scattering and beam absorption. For acceptable nanofocusing, the amount of scattering observed will have to be reduced by tuning the diamond deposition and the Si-etch process. To enable point focusing the next batch of lenses will consist of two designs with different focal lengths which can be used in a perpendicular arrangement in series.

Another way of fabricating both CRLs and kinoform lenses will also be investigated, whereby thick microcrystalline and nanocrystalline diamond films will be milled out to different designs using focused ion beam (FIB) techniques. At present, the main problem is the amount of material which needs to be removed from the sample by the FIB machine and the success of this proposal may rely on crudely removing the majority of the material with some other etching or milling method before the fine structure is sculpted with the FIB.

6.7 Conclusions

Diamond CRLs have been successfully fabricated using state-of-the-art silicon microtechnology and nanocrystalline diamond CVD methods showing excellent morphology in terms of vertical sidewalls, minimized etch-induced scalloping and high form fidelity. Subsequent testing on the synchrotron beamline has shown improvements made to the fabrication techniques have resulted in less scattering or aberrations and a smaller focal-spot line width. For the three focal lengths tested, 1.1 m, 0.6 m and 0.2 m (at 18, 12 & 11 keV), we have achieved focal widths of 2.2 μm, 1.6 μm and 0.7 μm, respectively.

As the diffractive limit has yet to be reached for the current lenses, modifications to the design and manufacturing processes will hopefully achieve smaller focal spot sizes and provide a route to greater use of diamond optics in worldwide synchrotron and other X-ray sources requiring nanofocusing.

7.0 Applied and other work

7.1 Hydrogenation experiments

Conditions in a pure H_2 plasma are such that exposure of a diamond surface for even a short amount of time will result in termination of a vast majority of the surface bonds with atomic H. For many electrical and biological applications utilizing doped-diamond the complete H termination of a surface is important, and H_2-plasma exposure necessary, to obtain the required property of the diamond surface, film or powder. The MWCVD reactor has been used for this treatment procedure for a number of different studies at various different research establishments covering a wide range of diamond applications. The hydrogenation experiments carried out are described here in turn as they often differ in many details. The diversity of collaborations we have been lucky enough to be involved with should also become apparent from this section and those which follow it.

7.1.1 Single-crystal diamond hydrogen termination

As part of a study into the electrochemical properties of B-doped single-crystal diamond (Barbu, 2009) ongoing in the group of Dr. Mark Newton, Department of Physics, University of Warwick, some samples were hydrogen terminated using a pure H_2 plasma at ~60 Torr with exposure times up to 2 min (reaching T_{sub} ~ 1000 K). Samples were allowed to cool in a H_2 flow for 5 min after the plasma had been extinguished. The success of the hydrogenation termination was established using hydrophobicity tests which showed contact angles of 90°. Similar substrate treatments were carried out for Diamond Detectors, Ltd., with short hydrogenation runs on both intrinsic and B-doped SCD samples in a 1 kW/50 Torr plasma.

7.1.2 H-terminated SCD for electronic devices

Field-effect transistors (FETs) are commonly used as signal amplifiers as they function by controlling the current flowing through a piece of semiconducting material – along a *channel* connecting the *source* and *drain* electrodes – by varying the voltage on a control or *gate* electrode. Fabrication of field-effect transistors (FET) from diamond has been a recent goal of many different research groups working with slightly different parameters and diamond-based materials. Apart from the plasma treatment, the work described here has been carried out by Dr. David Moran at the School of Engineering, University of Glasgow and recently reported in IEEE Electron Device Letters (Moran *et al.*, 2011). The aim of this work was to produce sub-100 nm gate lengths as this had not yet been reported and investigate the scaling of the device as these smaller dimensions were approached.

For conduction to occur on the diamond surface it must be hydrogen terminated (section 1.5.2) and this has been achieved by exposing single-crystal and polycrystalline diamond substrates to a hydrogen plasma in the MWCVD reactor. A number of different substrates were treated in the plasma and those exhibiting suitable electronic properties were processed further to produce the working FET device. Single-crystal diamond samples (4.7 × 4.7 mm) and one larger (10 × 10 mm) PCD substrate were supplied by Element Six, Ltd., and cleaned using nitric acid to remove any contamination from the polishing process.

Hydrogenation treatments consisted of both short exposures to the plasma, similar to treatments carried out in section 7.1.1, and longer, 15 min exposures. Although exposure for 1 min and 15 min should, theoretically, both result in complete H termination of the surface it was interesting to see if any differences in surface morphology and electronic transport could be determined. In both situations plasma parameters consisted of $P = 1$ kW, $p = 60$ Torr and $T_{\text{sub}} \sim 450$ °C, although the temperature depended heavily on the shape and thickness of the substrate being treated. H_2 was flowed through the reactor as the sample cooled to prevent any reversal in the hydrogenation. Samples were, generally, small (< 5 mm width) allowing a number of them to be hydrogenated in the CVD reactor at the same time and, hopefully, remove any variance between plasma treatments.

AFM profiling indicated no measureable increase in surface roughness following plasma treatment. Simple 2-point probe testing showed, somewhat surprisingly, that substrates exposed for 15 min were more conductive than those treated for 2 min and may point towards incomplete hydrogenation on the shorter timescale if experimental variation, such as the amount of adsorbed water on the surface (relative humidity), can be ruled out. It could also indicate that something different was occurring on the longer timescale influencing the electrical properties. In general, the Element Six SCD substrates performed better in the initial testing than the PCD ones, and were processed further to produce the FET devices by attaching gold ohmic contacts and lithographically patterning the surface using various steps. A second batch of substrates was treated similarly but showed 3× higher resistances and were re-treated, at higher T_{sub} = 625 °C using higher P = 1.4 kW and p = 130 Torr, without improvement in the conductivity. There appeared to be substantial variation in the results from hydrogenating different SCD substrates and may be due to impurities on the diamond surface not removed in the polishing or cleaning processes.

Characterization of the devices on the most conductive substrate, with gate lengths ranging between 1 μm and 50 nm, was successful (Moran *et al.*, 2011) and results were encouraging enough for further exploration of hydrogen-terminated diamond in high-frequency FET systems.

7.1.3 H-termination of ND powders I

Although hydrogenation of single-crystal or polished polycrystalline diamond substrates has proven to be a very effective and fast technique to hydrogen-terminate surfaces, the treatment of diamond powders is more problematic. Depending on the origin of the nanodiamond (ND) material, there are often varying quantities of sp^2 carbon on the surfaces of the powder due to their origin from either detonation soot (Danilenko, 2004) or HPHT diamond. The sp^2 carbon in ND powders can have a detrimental effect on the electrochemical properties so various methods for de-agglomerating and removing non-diamond material have been investigated. Bead-milling and high power ultrasonication has produced ND with a narrow size distribution down to 5 nm, and this material can then be enhanced by various surface functionalization methods (Krüger *et al.*, 2005, Krüger *et al.*, 2006, Krüger *et al.*, 2007). Other methods have involved annealing the material at 750 K under a hydrogen atmosphere at 10 mbar for 5 h followed by dispersion in water and separation of different particle sizes by high speed centrifugation (Williams *et al.*, 2010).

Working with Wiphada Hongthani and Dr. David Fermín, School of Chemistry Electrochemistry group, University of Bristol, hydrogenation of diamond nanoparticles was attempted by exposing them to a MW-activated hydrogen plasma. This was part of a concerted effort to produce novel and efficient photoelectrochemical devices that employ Au and diamond nanoparticles in various configurations.

The diamond nanoparticles used here were produced from HPHT diamond with sizes varying between 5 and 500 nm. The samples were acid washed – resulting in predominant oxygen termination – and then exposed to a H_2 plasma at 50 Torr for 3 min (1.0 kW MW power) to achieve appropriate surface hydrogen termination. The relative success of the treatment was measured using IR spectroscopy of the powder before and after exposure which would indicate the removal of oxygen- and nitrogen-terminated carbon atoms on the surface after a successful exposure. One major drawback of this plasma treatment is that complete hydrogenation of every nanoparticle is not possible with many surfaces in contact with each other or facing away from the plasma. This causes the retention of OH and CO bands in the post-treatment IR spectrum. Agitation and mixing of the ND sample between discrete plasma runs allowed us to maximise the surface exposure and resulted in a reduction, if not complete suppression, of the non-H-terminated carbon IR bands.

After three exposures to the hydrogen plasma the nanodiamond material is dispersed in a positively- or negatively-charged buffer solution and evaporated onto indium-tin-oxide-coated glass plates. A small, controlled area of this conductive surface is left exposed as the plates are wrapped in insulating tape, and cyclic voltammetry is then performed to determine the electrochemical properties of the diamond layer. Measurement of the redox properties of these films allowed comparison between other non-H-terminated layers and different particle sizes. The analysis described here was performed by the Electrochemistry group with feedback on the hydrogenation allowing adjustments to the process to be made. Sufficient H-termination was achieved to allow direct electron transfer from the valence band and the desired electrochemical properties.

7.1.4 H-termination of ND powders II

As well as modifying the electrochemical properties by shifting the band gap, H-termination can be important for functionalization of the diamond surface and subsequent biochemistry and cell growth. Similar advances in biological functionalization have already been demonstrated for DLC and current research aims to investigate the use of H-ND as a substrate for attachment of various organic fragments and even neuronal cells (Kelly *et al.*, 2008).

Two different processes were investigated for this material (again HPHT derived), firstly continuing the repeated, short exposures to the H_2 plasma discussed above and, secondly, a longer exposure at lower MW power. Exposure of ND to an 800 W H_2 plasma for 1 h has been demonstrated as a suitable treatment for preparing diamond substrates for attaching various molecules using Suzuki coupling reactions (Yeap *et al.*, 2009).

Further treatment of the material by Dr. Frederik Claeyssens, at the University of Sheffield, involved forming a range of different, amine, aldehyde, hydroxyl and carboxyl, functionalities on the surfaces and subsequent cellular growth and biocompatibility testing. Results showed that the samples were easily functionalized after plasma treatment and meant that preferential growth of neural cells was observed on functionalized ND samples (Claeyssens, unpublished work). Future advances will include quantification of the H-termination using XPS.

These varied hydrogenation projects serve to show how sought-after our expertise in hydrogen terminating single-crystal diamond, polycrystalline substrates and ND powders has become.

7.2 Diamond deposition for other research

7.2.1 NCD deposition for friction studies

Studies of nanotextured surfaces and interfaces are becoming increasingly important in modern science with an improved understanding of frictional properties across different surfaces required. The research group of Dr. Wuge Briscoe, at the School of Chemistry, University of Bristol, together with Prof. Per Claesson, Department of Chemistry, Royal Institute of Technology (KTH), Sweden, has recently undertaken a project to make friction measurements on several nanostructured surfaces using atomic force microscopy (AFM) in the hope to test Amontons' laws of friction (Pilkington *et al.*, 2011). A range of different surface geometries and compositions were fabricated using ZnO nanorods, ZnO nanograins, Al_2O_3 nanodomes and nanocrystalline diamond films. The latter were formed by MWCVD using methods outlined in section 3.0. To get a selection of different crystal sizes and to broaden the range of results for the friction measurements, films were deposited in the four inert gases analysed previously: He, Ne, Ar and Kr. The results (Pilkington *et al.*, 2011) showed, with some deviation due to difficulty of getting contact between the cantilever tip and the rough surface, that the frictional forces vary linearly with applied load and, therefore, obey Amontons' first law. From the analysis it was proposed that the frictional coefficient, μ, is the sum of an intrinsic friction coefficient, μ_0, (determined by the material properties) and a geometric friction coefficient, μ_g, (determined by the topography of the sample), *i.e.* $\mu = \mu_0 + \mu_g$. Although this work, carried out by colleagues at

KTH University in Stockholm, is somewhat removed from the present project it has provided an interesting and detailed analysis of the NCD films. In particular, the AFM imaging of the films has given a different perspective on the NCD deposition in the range of inert gas plasmas and allowed more precise measurements of the average surface roughness to be made.

We define the domain size as the dimensions of larger scale features – the dome-shaped regions in the He-grown films and the elongated, ellipsoidal areas in the Ar and Kr systems (see Figure 3.21) – and these decrease in size from He to Kr with the exception of the Ne-deposited film which appears to be distinct from the rest across the range of parameters measured. The crystallite size is determined by the average diameter of the individual diamond crystals and, apart from the Kr-grown film, agrees with observations made in the fuller study of NCD deposition in inert-gas-rich plasmas with a reduction in crystal size down the group.

plasma	*Domain size* nm	*Crystallite size* nm	*RMS* nm	*Mean height* nm
He	216	55	49.1	97.2
Ne	220	44	45.2	245.0
Ar	119	25	25.9	79.7
Kr	70	72	44.7	75.2

Table 22: Measured geometric dimensions and roughness parameters of nanodiamond films (Pilkington *et al.*, 2011).

It is apparent from the data in Table 22 that the roughness of the Kr-grown film was greater than expected although this may be due to the region sampled as this film was not completely homogenous across the entire substrate. The large height measured for the Ne-deposited film is also unexpected and may be an artefact of the AFM analysis at the point the measurement was taken.

Imaging of diamond surfaces with AFM is not straightforward because the combination of intrinsic hardness and topographical roughness means that cantilever probes are rapidly degraded leading to significantly restricted resolution. For the images shown below it was not unusual for a new tip to be used for each sample as the quality had reduced so much during each measurement.

The dimensions listed in Table 22 correlate with the images shown below where the overall decrease in grain size is obvious, as well as the change in the domain topography from spherical regions (He) to elongated ones (Kr). On these scales the smallest resolvable areas are, in fact, clusters of adjacent grains or crystal twins on larger diamond regions. This is most noticeable in the, slightly anomalous, film grown in the Ne mixture.

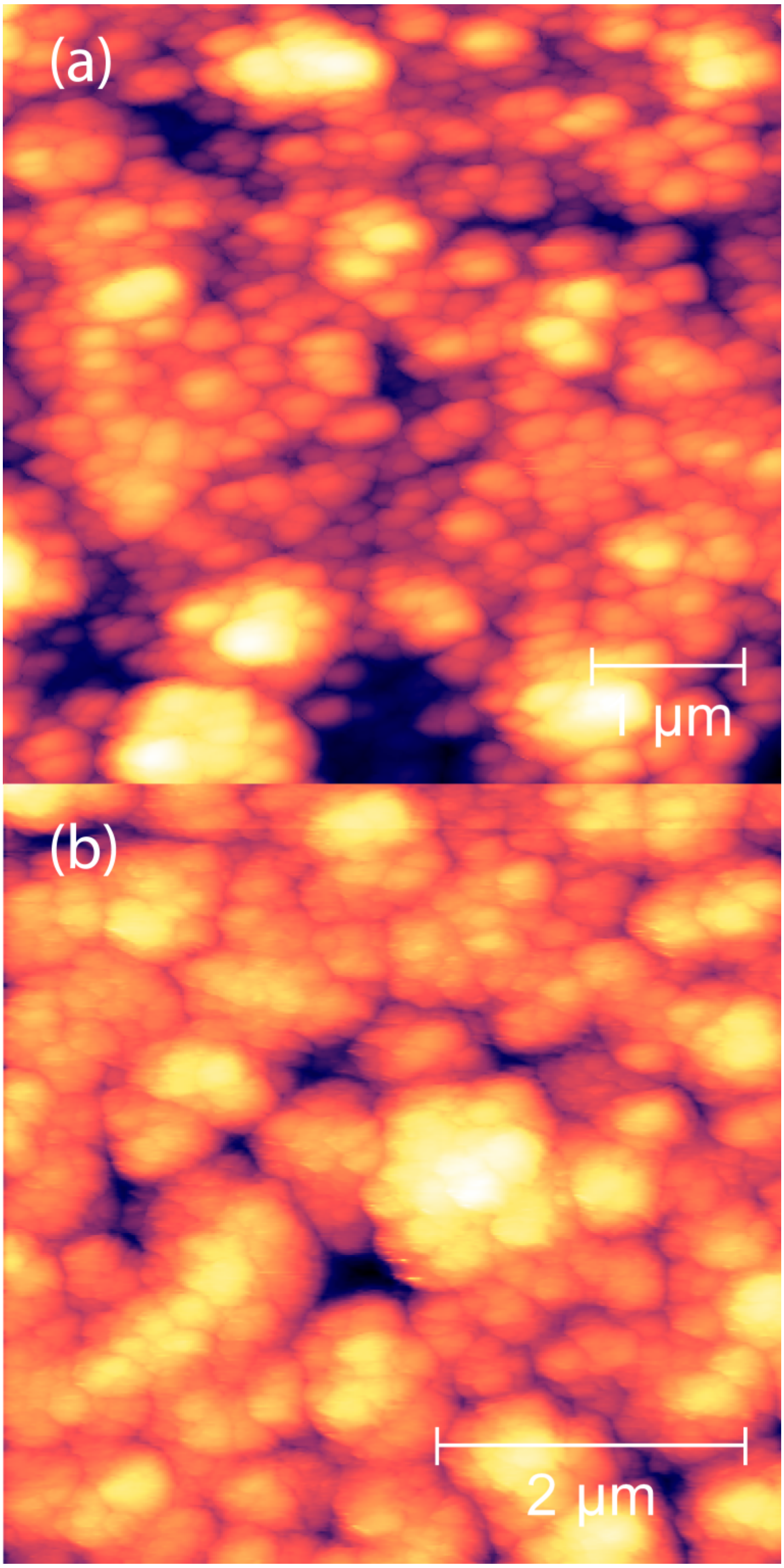

Figure 7.1: Contact-mode AFM images of NCD samples grown in (a) a $He/H_2/CH_4$ plasma and (b) a $Ne/H_2/CH_4$ plasma.

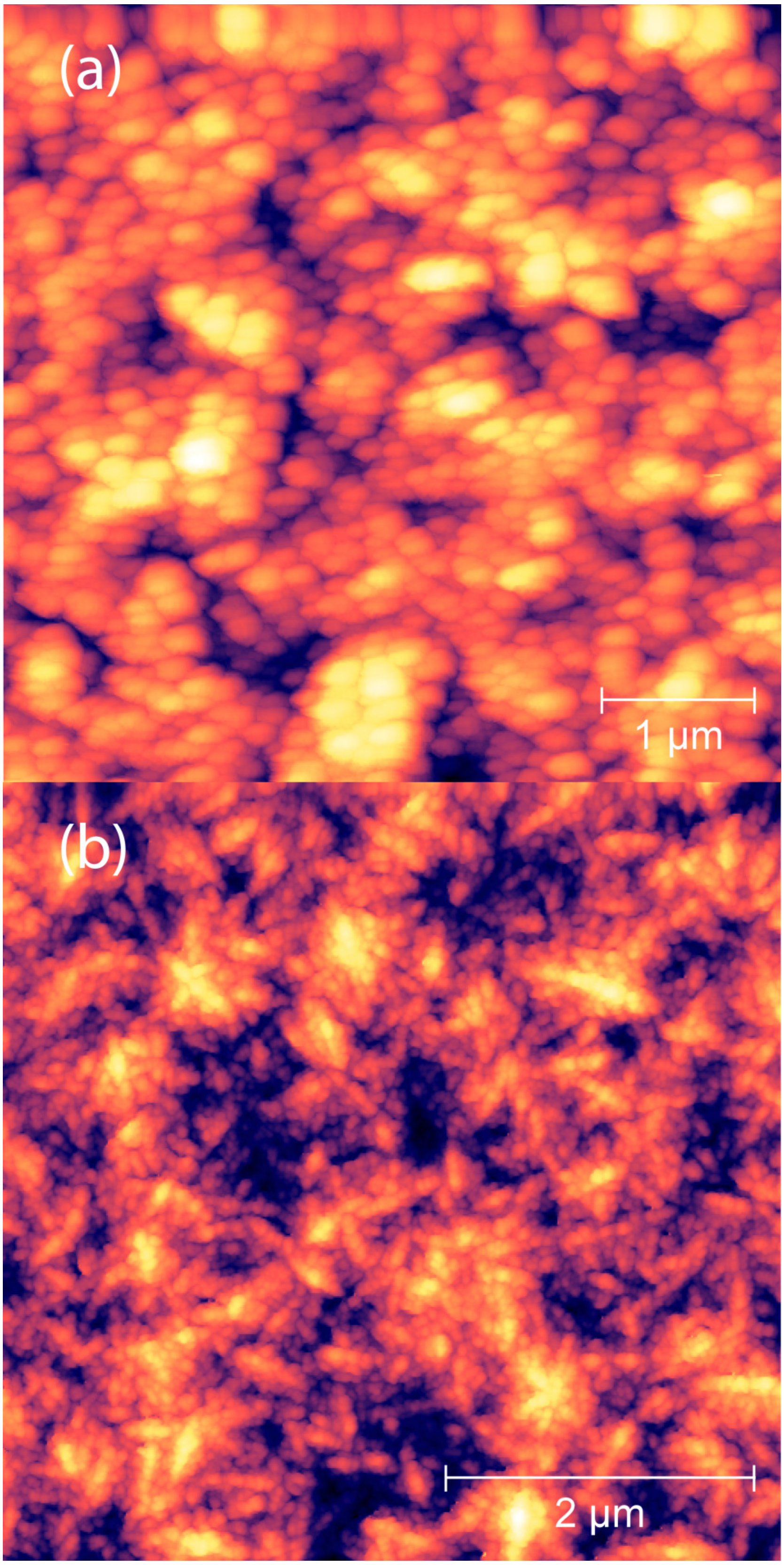

Figure 7.2: Contact-mode AFM images of NCD samples grown in (a) an Ar/H_2/CH_4 plasma and (b) a Kr/H_2/CH_4 plasma.

7.2.2 NCD for radiation testing

As part of a long-running partnership between the University of Bristol and Dr. Marcelino Barboza-Flores, Universidad de Sonora, Mexico, thick NCD diamond films were deposited by two different techniques onto silicon substrates. The project is concerned with thermoluminescence (TL) of diamond samples irradiated with β-radiation, UV and visible light and allows insights into the possible use of different diamond materials as radiation dosimeters (Chernov *et al.*, 2009, Melendrez *et al.*, 2009). In the analysis, the TL glow curves are produced by increasing the temperature of the irradiated diamond sample and measuring the count rate emitted.

	$\chi_0(H_2)$	$\chi_0(Ar)$	$\chi_0(N_2)$	$\chi_0(CH_4)$	F_T sccm	P kW	p Torr	T_{sub} K	t h
Sample 1	0.91	0.0	0.01	0.08	550	1.0	125	996	10
Sample 2	0.81	0.07	0.0	0.12	615	1.2	150	1108	10

Table 23: Deposition conditions for growth of NCD films by two contrasting methods.

The aim was to produce diamond morphologies different from the HFCVD MCD which had already been grown and tested (Chernov *et al.*, 2010) and this was done by running NCD deposition in the two different environments. While both are nominally NCD films, the surface topography and roughness, the crystallite size and the proportions of sp^2 and sp^3 carbon in the two films vary significantly. The differences in surface structure are obvious in the SEM images which show NCD grains ~40-100 nm for the film grown with N_2 within a fairly smooth surface. The high $\chi_0(CH_4)$ film (sample 2) shows a more characteristic ballas-diamond morphology where grains are arranged into much larger spherical domains up to 20 μm in diameter .

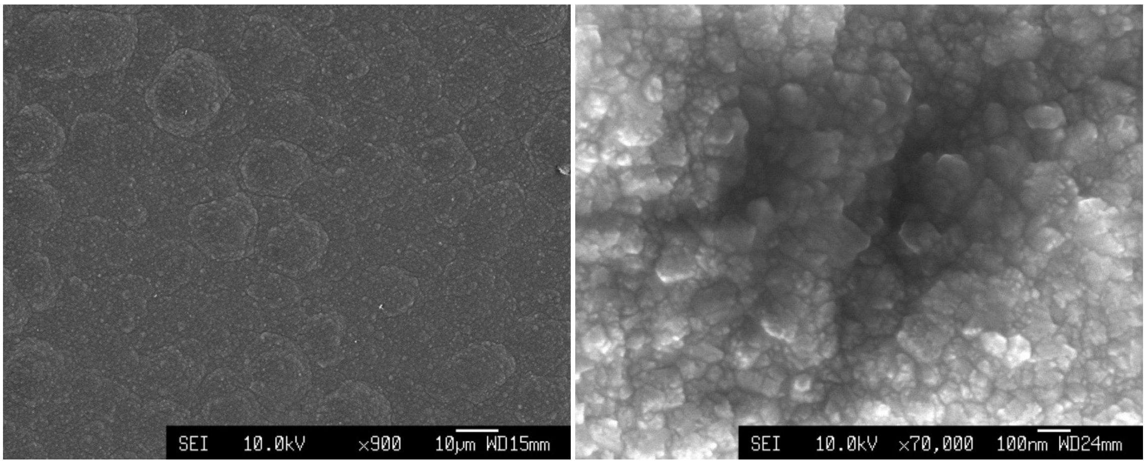

Figure 7.3: SEM images of sample 1 grown in a $H_2/N_2/CH_4$ plasma showing a smooth NCD surface and an average crystal size between 30 – 100 nm.

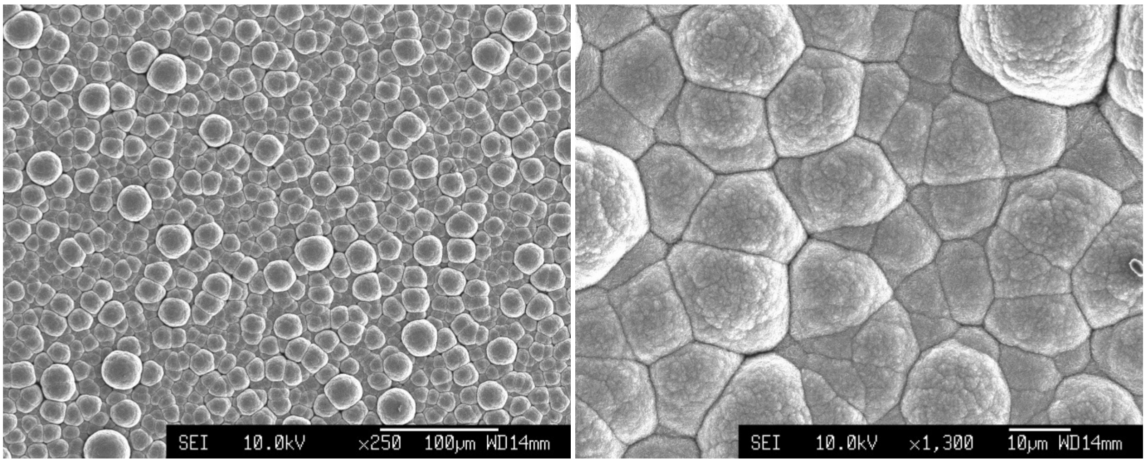

Figure 7.4: SEM images of sample 2 grown in a $H_2/Ar/CH_4$ showing a ballas NCD surface.

Differences between the two samples are also apparent in the UV-Raman spectra (Figure 7.5) which show a stronger $I(sp^3)$ resonance for the film grown with N_2 which points towards a larger crystal size and less grain boundary, non-diamond material. Interestingly, there is a shift observed in the I(D) peak from ~1380 cm^{-1} for the N_2 sample to ~1415 cm^{-1} for the high-$\chi_0(CH_4)$ film that could be induced by stress in the film with the higher proportion of sp^2 material.

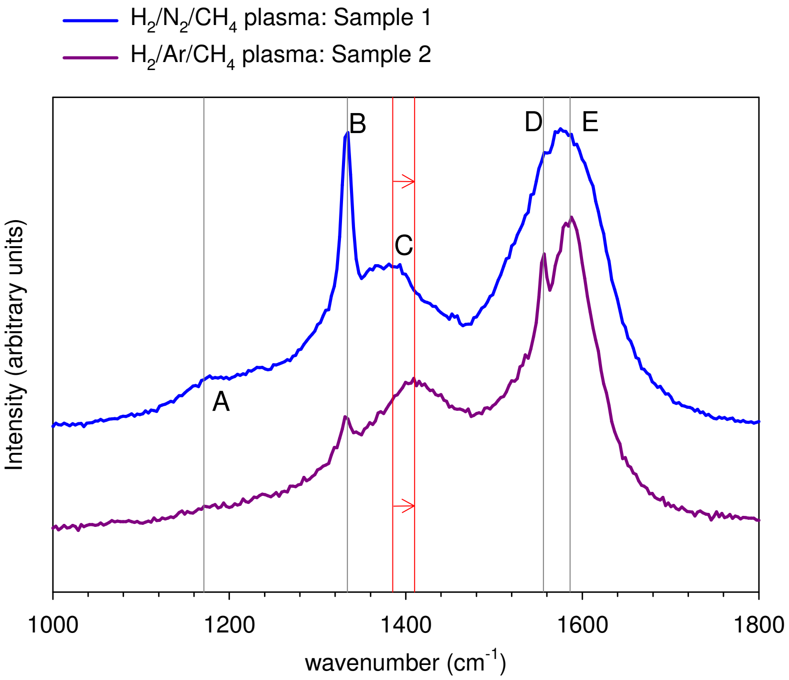

Figure 7.5: UV-Raman spectra at room temperature and excitation wavelength of 325 nm (HeCd) of two NCD films showing different characteristics. A = NCD, B = sp^3 carbon (diamond), C = sp^2 D peak (with shift shown), D = silicon substrate, E = sp^2 carbon G peak (graphite).

7.2.3 MCD for microplasma research

From the MWCVD experiments we know that moderate pressure plasmas can easily become unstable, forming filaments or arcs and so must be run at lower than atmospheric pressure. Similarly, plasma discharges formed between two electrodes become more stable as the distance between them decreases, and devices known as microplasmas can be fabricated. In many applications it would be desirable to form these plasmas at atmospheric pressure and so electrode separation distances ≤ 1 mm are necessary for readily achievable breakdown voltages (Eden & Park, 2005). Microplasma arrays typically consist of two electrodes separated by an insulting dielectric and a discharge is usually initiated using a dc current, although ac, RF and MW ignition have also been employed. Such devices would be important for analytical diagnostics and chromatography where different samples of gases or vaporized liquids could be detected quickly in a so-called *lab-on-a-chip* tool. Alternatively, similar constructions could be applied as radiation sources (for example, using the ArF excimer (Simeonsson & Miziolek, 1993)) or for surface treatment, such as cleaning or etching (Yoshiki *et al.*, 2003).

These systems are also interesting scientifically due to their high T_e ~ 6 eV and electron density, n_e ~ 10^{15} cm^{-3} (Moselhy *et al.*, 2003) but this harsh environment necessitates forming the cavities from robust material such as diamond, although arrays have been formed from silicon, aluminium and ceramics. CVD-grown diamond offers a multitude of advantages as well as being a robust, inert material for use in these arrays. Foremost among them is the fact that individual layers can be deposited which can either be conducting if boron is incorporated (the electrodes) or insulating (the dielectric), allowing a monolithic microplasma device structure to be formed. Additionally, the low coefficient of thermal expansion, high thermal conductivity and resistance to extreme conditions all lend themselves to this application.

As part of an ongoing project, between the University of Bristol, STFC and the Open University, initial designs have been fabricated by layering undoped MCD deposited by MWCVD onto pre-existing B-doped MCD substrates. A few deposition experiments were used to determine if the deposition times were long enough to produce a film thickness which would be suitably insulating.

7.2.4 Li-doped NCD

One of the recent areas of interest in doping diamond for use in solar-converter devices is the incorporation of lithium to induce a negative electron affinity (NEA) surface, and thereby significantly lower the workfunction, opening up routes to forming more efficient field and thermionic emitters. In particular, alkali- or alkali-halide-doped (Wong *et al.*, 1999) diamond materials would allow thermionic emission at temperatures at which other dopants, such as Cs (as a monolayer combined with an oxygenated surface: Cs–O) or H, become unstable and deteriorate (O'Donnell *et al.*, 2010). Achieving a stable doping level of Li in diamond is not trivial and requires careful methods because the dopant atoms easily diffuse through the film and can combine into clusters which are electronically inert. There are various methods by which diamond can be doped with Li including mixing and annealing of diamond ND and lithium carbide, which leads to diffusion of Li into the diamond, or deposition of a diamond film by CVD onto a substrate seeded with lithiated diamond nanoparticles. As part of a project led by Dr. Neil Fox, Department of Physics, University of Bristol, and funded by an *E-ON International Research Award* the latter method was attempted. Both MCD and NCD films were deposited using standard conditions with H_2-rich plasmas and high or low $\chi_0(CH_4)$ by HFCVD and MWCVD on Li-C-seeded Si substrates. The films were analysed (by Tomas Martin) using SIMS to measure the depth profile of Li remaining in the sample. The aim was to incorporate Li-based defects into the diamond lattice as it grew but in most cases the harsh conditions of activated-H_2 mixtures or plasmas proved too extreme for any Li to remain in the film. Instead, the Li either disappeared completely or was found to build up at the diamond-Si interface at the base of the film. Other doping routes have also been extensively studied and modelled looking at emission from H- and O-terminated surfaces but this does not directly involve any CVD methods and are not discussed here (Martin, 2011).

8.0 Summary of projects

Covering broad areas of modern diamond research, the experiments discussed here bring some new insights into the gas-phase deposition chemistry in environments designed to produce diverse material morphologies. Nucleation of diamond films on heteroepitaxial substrates has been studied by using different seeding methods, ND dispersions and deposition environments. We have pioneered a novel technique for nucleating substrates with a dense layer of nanoparticles which has proven essential for deposition of NCD films onto complex, patterned substrates as well as large, 6” planar wafers. This electrospray method compares favourably with other seeding methods, such as ultrasonic abrasion, that are currently used in diamond research.

8.1 Diamond deposition

Diamond deposition experiments have shown the influence of hydrocarbon mole fraction, pressure, input power and amount of argon on growth rates, crystalline morphology and gas-phase chemistry of microcrystalline diamond deposition. The formation of nanocrystalline diamond has been investigated *via* a number of different routes including high methane fractions, predominantly inert-gas plasmas and trace addition of nitrogen. Extensive studies of the inert gases, He, Ne, Ar and Kr, as major components in the deposition system began with deposition of diamond films, which showed similar morphologies arising from each gas mixture, although trends in crystal size, emission intensities of various species and column densities of atomic hydrogen were explained using knowledge of the plasma system and the variation in the gas properties. Detailed investigation of the Ar-rich plasma using emission and absorption spectroscopy has been combined with a complex self-consistent, 2D model of the plasma to explain the empirical observations, and to make predictions about the concentrations of proposed growth precursors just above the substrate. While these plasmas involve fairly low NCD growth rates, addition of nitrogen has allowed very rapid deposition together with changes in morphology and even deposition of crystals other than diamond.

8.2 MBMS

A range of engineering and software modifications have been applied to the MBMS system to improve the reliability, noise level, pumping efficiency, detection limit and sensitivity of the instrument. This has resulted in a more robust and user-friendly piece of analytical apparatus which has been shown to measure C_2H_2 quantitatively, albeit with a few small sources of error still needing attention. Accurate calibration across a wide range of process parameters has provided a way of correcting for variation in the beam composition as the sampled gases change identity. There are, however, many other issues which need addressing before the instrument will accurately measure radical species and light gases such as H_2. Precise alignment of the beam optics has been the largest contributor to the increase in sensitivity and this might still warrant further adjustment to reach the optimum arrangement. Other than this, the modelling and testing of different sized-apertures may be required to achieve greater resolution of these elusive radical species.

8.3 Diamond CRL fabrication

Knowledge gained from NCD deposition studies with nitrogen has been applied to a project to fabricate planar refractive lenses used to focus X-ray synchrotron radiation. The diamond lenses are grown by CVD using patterned silicon templates which are subsequently removed to leave thick, free-standing diamond which fills the mould remarkably well. Testing on a Diamond Light Source beamline has shown improvements in the focal-spot sizes from 2.2 μm in the first batch to 400 nm in the second, an achievement which is coupled with an increase in the lens robustness and a reduction in the beam scattering. New designs for even sharper focusing and reduced scattering are currently in preparation.

Published & Presented Work

Lead author on published papers:

Fox, O. J. L., Ma, J., May, P. W., Ashfold, M. N. R., & Mankelevich, Yu. A. (2009), The role of inert gas in MW-enhanced plasmas for the deposition of nanocrystalline diamond thin films, *Diamond and Related Materials* **18**(5-8), 750 (Fox *et al.*, 2009).

Fox, O. J. L., Holloway, J. O. P., Fuge, G. M., May, P. W., & Ashfold, M. N. R. (2010), Electrospray deposition of diamond nanoparticle nucleation layers for subsequent CVD diamond growth, *MRS proceedings: Diamond Electronics - Fundamentals to Applications* **1203**, J17 (Fox *et al.*, 2010).

Joint author on published papers:

Alianelli, L., Sawhney, K. J. S., Malik, A., Fox, O. J. L., May, P. W., Stevens, R., Loader, I. M., & Wilson, M. C. (2010), A planar refractive x-ray lens made of nanocrystalline diamond, *Journal of Applied Physics* **108**(12), 123107 (Alianelli *et al.*, 2010).

Richley, J. C., Fox, O. J. L., Ashfold, M. N. R., & Mankelevich, Yu. A. (2011), Combined experimental and modeling studies of microwave activated $CH_4/H_2/Ar$ plasmas for microcrystalline, nanocrystalline, and ultrananocrystalline diamond deposition, *Journal of Applied Physics* **109**(6), 063307 (Richley *et al.*, 2011).

Pilkington, G. A., Thormann, E., Claesson, P. M., Fuge, G. M., Fox, O. J. L., Ashfold, M. N. R., Leese, H., Mattia, D., & Briscoe, W. H. (2011), Amontonian frictional behaviour of nanostructured surfaces, *Physical Chemistry Chemical Physics* **13**(20), 9318 (Pilkington *et al.*, 2011).

Moran, D. A. J., Fox, O. J. L., McLelland, H., Russell, S., & May, P. W. (2011), Intrinsic scaling of hydrogen-terminated diamond FETS to sub-100 nm gate dimensions, *IEEE Electron Device Letters* **32**(5), 599 (Moran *et al.*, 2011).

Alianelli, L., Fox, O. J. L., & Malik, A. (2011), A planar refractive x-ray lens made of nano-crystalline diamond, *Diamond Annual Review* **2010/2011**, 78 (Alianelli *et al.*, 2011).

Oral Presentations & Seminars:

Fox, O. J. L., May, P. W., Ashfold, M. N. R., Molecular beam mass spectrometry studies of chemical species at the diamond growth surface in a MWCVD reactor, *8th Technological Plasma Workshop*, University of Bristol, United Kingdom (January 2011).

Poster Presentations:

Fox, O. J. L., May, P. W., Ashfold, M. N. R., Substrate seeding methods for the nucleation of nanocrystalline diamond thin films grown by MW-CVD, *Hasselt Diamond Workshop 2008 - SBDD XIII,* Cultuurcentrum Hasselt, Hasselt, Belgium (February 2008).

Fox, O. J. L., May, P. W., Ashfold, M. N. R., Comparison of different inert gas plasma mixtures used in the CVD growth of nanocrystalline diamond, *The 59th De Beers Diamond Conference*, University of Oxford, Oxford, United Kingdom (July 2008).

Fox, O. J. L., May, P. W., Ashfold, M. N. R, Fuge, G. M., Fox, N. A., Smith J. A., Comparison of different substrate pre-treatment procedures for NCD films, *19th European Conference on Diamond, Diamond-Like Materials, Carbon Nanotubes & Nitrides*, Sitges, Spain (September 2008).

Fox, O. J. L., May, P. W., Ashfold, M. N. R., Controlling diamond thin film morphology by addition of nitrogen to standard MW-CVD gas mixtures, *Hasselt Diamond Workshop 2009 - SBDD XIV,* Cultuurcentrum Hasselt, Hasselt, Belgium (March 2009).

Fox, O. J. L., May, P. W., Ashfold, M. N. R., Comparison of different inert gas plasma mixtures used in the CVD growth of nanocrystalline diamond, *MRS Fall Meeting - Symposium J: Diamond Electronics and Bioelectronics-Fundamentals to Applications III*, Boston (November 2009).

Fox, O. J. L., Holloway, J. O. P., May, P. W., Fuge, G. M., Ashfold, M. N. R., Electrospray deposition of diamond nanoparticle nucleation layers for subsequent CVD diamond growth, *MRS Fall Meeting - Symposium J: Diamond Electronics and Bioelectronics-Fundamentals to Applications III*, Boston (November 2009).

Bibliography

Achatz, P., Garrido, J. A., Williams, O. A., Brun, P., Gruen, D. M., Kromka, A., Steinmüller, D., & Stutzmann, M. (2007), Structural, optical, and electronic properties of nanocrystalline and ultrananocrystalline diamond thin films, *Physica Status Solidi A* **204**(9), 2874.

Agarwal, S., Quax, G. W. W., van de Sanden, M. C. M., Maroudas, D., & Aydil, E. S. (2004), Measurement of absolute radical densities in a plasma using modulated-beam line-of-sight threshold ionization mass spectrometry, *Journal of Vacuum Science & Technology A* **22**(1), 71.

Alianelli, L., Sawhney, K. J. S., Tiwari, M. K., Dolbnya, I. P., Stevens, R., Jenkins, D. W. K., Loader, I. M., Wilson, M. C., & Malik, A. (2009), Characterization of germanium linear kinoform lenses at Diamond Light Source, *Journal of Synchrotron Radiation* **16**, 325.

Alianelli, L., Sawhney, K. J. S., Malik, A., Fox, O. J. L., May, P. W., Stevens, R., Loader, I. M., & Wilson, M. C. (2010), A planar refractive X-ray lens made of nanocrystalline diamond, *Journal of Applied Physics* **108**(12), 123107.

Alianelli, L., Fox, O. J. L., & Malik, A. (2011), A planar refractive X-ray lens made of nanocrystalline diamond, *Diamond Annual Review* **2010/2011**, 78.

Anderson, J. D. (1990), *Modern Compressible Flow*, McGraw-Hill, Singapore.

Angus, J. C., Will, H. A., & Stanko, W. S. (1968), Growth of diamond seed crystals by vapor deposition, *Journal of Applied Physics* **39**(6), 2915.

Aristov, V., Grigoriev, M., Kuznetsov, S., Shabelnikov, L., Yunkin, V., Weitkamp, T., Rau, C., Snigireva, I., Snigirev, A., Hoffmann, M., & Voges, E. (2000), X-ray refractive planar lens with minimized absorption, *Applied Physics Letters* **77**(24), 4058.

Arnault, J. C. (2003), Highly oriented diamond films on heterosubstrates: Current state of the art and remaining challenges, *Surface Review and Letters* **10**(1), 127.

Arnault, J. C., Saada, S., Michaelson, S., Hangaly, N. K., Akhvlediani, R., & Hoffman, A. (2008), Bias enhanced diamond nucleation onto 3C-SiC(100) surfaces studied by high resolution X-ray photoelectron and high resolution electron energy loss spectroscopies, *Diamond and Related Materials* **17**(3), 377.

Ashcroft, N. W. & Mermin, N. D. (1976), *Solid State Physics*, Holt, Rinehart & Winston.

Aubry, O., Delfau, J. L., Met, C., De Barros, M. I., Vandenbulcke, L., & Vovelle, C. (2002), Molecular beam mass spectrometry analysis of gaseous species responsible for diamond deposition in microwave plasmas, *Journal de Physique IV* **12**(PR4), 75.

Aubry, O., Delfau, J. L., Met, C., Vandenbulcke, L., & Vovelle, C. (2004), Precursors of diamond films analysed by molecular beam mass spectrometry of microwave plasmas, *Diamond and Related Materials* **13**(1), 116.

Auciello, O., Birrell, J., Carlisle, J. A., Gerbi, J. E., Xiao, X. C., Peng, B., & Espinosa, H. D. (2004), Materials science and fabrication processes for a new MEMS technology based on ultrananocrystalline diamond thin films, *Journal of Physics - Condensed Matter* **16**(16), R539.

Awakowicz, P., Schwefel, R., Werder, M., & Kasper, W. (1997), Diamond deposition and plasma diagnostics in a 27 MHz inductive coupled reactor (ICP), *Diamond and Related Materials* **6**(12), 1816.

Bachmann, P. K., Leers, D., & Lydtin, H. (1991), Towards a general concept of diamond chemical vapor-deposition, *Diamond and Related Materials* **1**(1), 1.

Badzian, A., Badzian, T., Roy, R., & Drawl, W. (1999), Silicon carbonitride, a new hard material and its relation to the confusion about 'harder than diamond' C_3N_4, *Thin Solid Films* **354**(1-2), 148.

Barber, G. D. & Yarbrough, W. A. (1997), Growth rate of diamond on polycrystalline (110) diamond substrates from carbon disulfide in hydrogen by hot-filament-assisted chemical vapor deposition, *Journal of the American Ceramic Society* **80**(6), 1560.

Barbu, B. (2009), Electrical and Electrochemical Characterisation of Single Crystal Diamond, PhD thesis, Department of Physics, University of Warwick.

Battaile, C. C., Srolovitz, D. J., & Butler, J. E. (1997), Morphologies of diamond films from atomic-scale simulations of chemical vapor deposition, *Diamond and Related Materials* **6**(9), 1198.

Battaile, C. C., Srolovitz, D. J., Oleinik, I. I., Pettifor, D. G., Sutton, A. P., Harris, S. J., & Butler, J. E. (1999), Etching effects during the chemical vapor deposition of (100) diamond, *Journal of Chemical Physics* **111**(9), 4291.

Battaile, C. C. & Srolovitz, D. J. (2002), Kinetic Monte Carlo simulation of chemical vapor deposition, *Annual Review of Materials Research* **32**, 297.

Beloborodov, I. S., Zapol, P., Gruen, D. M., & Curtiss, L. A. (2006), Transport properties of *n*-type ultrananocrystalline diamond films, *Physical Review B* **74**(23), 235434.

Bergonzo, P., Tromson, D., Mer, C., Guizard, B., Foulon, F., & Brambilla, A. (2001), Particle and radiation detectors based on diamond, *Physica Status Solidi A* **185**(1), 167.

Bergonzo, P., Barrett, R., Hainaut, O., Tromson, D., Mer, C., & Guizard, B. (2002), Imaging of the sensitivity in detector grade polycrystalline diamonds using micro-focused X-ray beams, *Diamond and Related Materials* **11**(3-6), 418.

Bhattacharyya, S., Auciello, O., Birrell, J., Carlisle, J. A., Curtiss, L. A., Goyette, A. N., Gruen, D. M., Krauss, A. R., Schlueter, J., Sumant, A., & Zapol, P. (2001), Synthesis and characterization of highly-conducting nitrogen-doped ultrananocrystalline diamond films, *Applied Physics Letters* **79**(10), 1441.

Bingham, R. C., Dewar, M. J. S., & Lo, D. H. (1975), Ground-states of molecules .25. Mindo-3 - improved version of Mindo semiempirical SCF-MO method, *Journal of the American Chemical Society* **97**(6), 1285.

Biordi, J. C. (1977), Molecular-beam mass-spectrometry for studying fundamental chemistry of flames, *Progress in Energy and Combustion Science* **3**(3), 151.

Birrell, J., Gerbi, J. E., Auciello, O., Gibson, J. M., Gruen, D. M., & Carlisle, J. A. (2003), Bonding structure in nitrogen-doped ultrananocrystalline diamond, *Journal of Applied Physics* **93**(9), 5606.

Birrell, J., Gerbi, J. E., Auciello, O. A., & Carlisle, J. A. (2006), Investigating the role of hydrogen in ultrananocrystalline diamond thin film growth, *Journal of Physics - Condensed Matter* **18**(32), S1771.

Bohr, S., Haubner, R., & Lux, B. (1995), Influence of phosphorus addition on diamond CVD, *Diamond and Related Materials* **4**(2), 133.

Branson, H. & Smith, C. (1953), Electron impact studies in CH_4, CH_3Cl, CH_3Br and CH_3I, *Journal of the American Chemical Society* **75**(17), 4133.

Brubaker, W. H. (1968), An improved quadrupole mass analyser, *Advances in Mass Spectrometry* **4**, 293.

Bundy, F. P., Hall, H. T., Strong, H. M., & Wentorf, R. H. (1955), Man-made diamonds, *Nature* **176**(4471), 51.

Butler, J. E. & Woodin, R. L. (1993), Thin-film diamond growth mechanisms, *Philosophical Transactions of the Royal Society of London A* **342**(1664), 209.

Butler, J. E. & Oleynik, I. (2008), A mechanism for crystal twinning in the growth of diamond by chemical vapour deposition, *Philosophical Transactions of the Royal Society of London A* **366**(1863), 295.

Butler, J. E., Mankelevich, Yu. A., Cheesman, A., Ma, J., & Ashfold, M. N. R. (2009), Understanding the chemical vapour deposition of diamond: recent progress, *Journal of Physics - Condensed Matter* **21**(36), 364201.

Cao, G. Z., van Enckevort, W. J. P., Giling, L. J., & de Kruif, R. C. M. (1995a), Enhancement of phosphorus incorporation and growth-rate of epitaxial diamond films by the addition of nitrogen, *Applied Physics Letters* **66**(6), 688.

Cao, G. Z., Giling, L. J., & Alkemade, P. F. A. (1995b), Growth of phosphorus and nitrogen co-doped diamond films, *Diamond and Related Materials* **4**(5-6), 775.

Cao, G. Z., Schermer, J. J., van Enckevort, W. J. P., Elst, W. A. L. M., & Giling, L. J. (1996), Growth of 100 textured diamond films by the addition of nitrogen, *Journal of Applied Physics* **79**(3), 1357.

Ceglio, N. M., Hawryluk, A. M., & Schattenburg, M. (1983), X-ray phase lens design and fabrication, *Journal of Vacuum Science & Technology B* **1**(4), 1285.

Celii, F. G., Pehrsson, P. E., Wang, H. T., & Butler, J. E. (1988), Infrared detection of gaseous species during the filament-assisted growth of diamond, *Applied Physics Letters* **52**(24), 2043.

Celii, F. G. & Butler, J. E. (1989), Hydrogen-atom detection in the filament-assisted diamond deposition environment, *Applied Physics Letters* **54**(11), 1031.

Cen, Z. H., Chen, T. P., Ding, L., Ye, J. D., Liu, Y., Yang, M., Wong, J. I., Liu, Z., & Fung, S. (2009), Optical transmission and photoluminescence of silicon nitride thin films implanted with Si ions, *Electrochemical and Solid State Letters* **12**(2), H38.

Chao, W. L., Harteneck, B. D., Liddle, J. A., Anderson, E. H., & Attwood, D. T. (2005), Soft X-ray microscopy at a spatial resolution better than 15 nm, *Nature* **435**(7046), 1210.

Chauhan, S. P., Angus, J. C. & Gardner, N. C. (1974), Kinetic study of process of diamond growth from vapor at subatmospheric pressures using an automatic recording microbalance, *Journal of Vacuum Science & Technology* **11**(1), 423.

Chauhan, S. P., Angus, J. C., & Gardner, N. C. (1976), Kinetics of carbon deposition on diamond powder, *Journal of Applied Physics* **47**(11), 4746.

Cheesman, A. (2006), Investigations into the fundamentals of gas-phase and gas-surface chemistry prevalent in growth of Chemical Vapour Deposited diamond films, PhD thesis, School of Chemistry, University of Bristol.

Cheesman, A., Smith, J. A., Ashfold, M. N. R., Langford, N., Wright, S., & Duxbury, G. (2006), Application of a quantum cascade laser for time-resolved, *in situ* probing of CH_4/H_2 and C_2H_2/H_2 gas mixtures during microwave plasma enhanced chemical vapor deposition of diamond, *Journal of Physical Chemistry A* **110**(8), 2821.

Cheesman, A., Harvey, J. N., & Ashfold, M. N. R. (2008), Studies of carbon incorporation on the diamond (100) surface during chemical vapor deposition using density functional theory, *Journal of Physical Chemistry A* **112**(45), 11436.

Chen, I. (1988), Modeling of diamond film growth, *Journal of Applied Physics* **64**(7), 3742.

Chen, L. C., Yang, C. Y., Bhusari, D. M., Chen, K. H., Lin, M. C., Lin, J. C., & Chuang, T. J. (1996), Formation of crystalline silicon carbon nitride films by microwave plasma-enhanced chemical vapor deposition, *Diamond and Related Materials* **5**(3-5), 514.

Chernov, V., Piters, T. M., Melendrez, R., Preciado-Flores, S., May, P. W., & Barboza-Flores, M. (2009), Correlation between thermally and optically stimulated luminescence in beta-irradiated undoped CVD diamond, *Physica Status Solidi A* **206**(9), 2098.

Chernov, V., Piters, T. M., May, P. W., Melendrez, R., Pedroza-Montero, M., & Barboza-Flores, M. (2010), Comparative study of TL created in undoped CVD diamond by beta rays, UV and visible light, *Physica Status Solidi A* **207**(9), 2119.

Chiang, M. J. & Hon, M. H. (2001), Positive DC bias-enhanced diamond nucleation with high CH_4 concentration, *Diamond and Related Materials* **10**(8), 1470.

Chu, C. H. & Hon, M. H. (1993), The growth of diamond using halogenated methane, *Diamond and Related Materials* **2**(2-4), 311.

Cola, B. A., Karru, R., Cheng, C. R., Xu, X. F., & Fisher, T. S. (2008), Influence of bias-enhanced nucleation on thermal conductance through chemical vapor deposited diamond films, *IEEE Transactions on Components and Packaging Technologies* **31**(1), 46.

Comerford, D. W., Cheesman, A., Carpenter, T. P. F., Davies, D. M. E., Fox, N. A., Sage, R. S., Smith, J. A., Ashfold, M. N. R., & Mankelevich, Yu. A. (2006), Experimental and modeling studies of B atom number density distributions in hot filament activated B_2H_6/H_2 and $B_2H_6/CH_4/H_2$ gas mixtures, *Journal of Physical Chemistry A* **110**(9), 2868.

Crichton, E. (2007), Construction of a Molecular Beam Mass Spectrometer for *in-situ* probing of a Diamond Chemical Vapour Deposition Environment, PhD thesis, School of Chemistry, University of Bristol.

Csíkvari, P., Somogyi, A., Veres, M., Hárs, G., & Toth, A. (2009), Investigation of the combined effect of argon addition and substrate bias on the growth of ultrananocrystalline diamond layers, *Diamond and Related Materials* **18**(12), 1459.

Dandy, D. S. & Coltrin, M. E. (1995), A simplified analytical model of diamond growth in direct-current arcjet reactors, *Journal of Materials Research* **10**(8), 1993.

Danilenko, V. V. (2004), On the history of the discovery of nanodiamond synthesis, *Physics of the Solid State* **46**(4), 595.

Das, D. & Singh, R. N. (2007), A review of nucleation, growth and low temperature synthesis of diamond thin films, *International Materials Reviews* **52**(1), 29.

Deák, P., Kováts, A., Csíkváry, P., Maros, I., & Hárs, G. (2007), Ethynyl (C_2H): A major player in the chemical vapor deposition of diamond, *Applied Physics Letters* **90**(5), 051503.

Demuynck, L., Arnault, J. C., Speisser, C., Polini, R., & LeNormand, F. (1997), Mechanisms of CVD diamond nucleation and growth on mechanically scratched and virgin Si(100) surfaces, *Diamond and Related Materials* **6**(2-4), 235.

Donnet, J. B., Lemoigne, C., Wang, T. K., Peng, C. M., Samirant, M., & Eckhardt, A. (1997), Detonation and shock synthesis of nanodiamonds., *Bulletin de la Societe Chimique de France* **134**(10-11), 875.

Eckert, M., Neyts, E., & Bogaerts, A. (2010a), Insights into the growth of (ultra)nanocrystalline diamond by combined molecular dynamics and Monte Carlo simulations, *Crystal Growth & Design* **10**(7), 3005.

Eckert, M., Neyts, E., & Bogaerts, A. (2010b), Differences between ultrananocrystalline and nanocrystalline diamond growth: Theoretical investigation of C_xH_y species at diamond step edges, *Crystal Growth & Design* **10**(9), 4123.

Eden, J. G. & Park, S. J. (2005), Microcavity plasma devices and arrays: a new realm of plasma physics and photonic applications, *Plasma Physics and Controlled Fusion* **47**, B83.

Elliott, M. A., May, P. W., Petherbridge, J., Leeds, S. M., Ashfold, M. N. R., & Wang, W. N. (2000), Optical emission spectroscopic studies of microwave enhanced diamond CVD using CH_4/CO_2 plasmas, *Diamond and Related Materials* **9**(3-6), 311.

Eltenton, G. C. (1947), The study of reaction intermediates by means of a mass spectrometer, *Journal of Chemical Physics* **15**(7), 455.

Erdemir, A., Bindal, C., Fenske, G. R., Zuiker, C., Krauss, A. R., & Gruen, D. M. (1996), Friction and wear properties of smooth diamond films grown in fullerene plus argon plasmas, *Diamond and Related Materials* **5**(9), 923.

Evans-Lutterodt, K., Ablett, J. M., Stein, A., Kao, C. C., Tennant, D. M., Klemens, F., Taylor, A., Jacobsen, C., Gammel, P. L., Huggins, H., Ustin, S., Bogart, G., & Ocola, L. (2003), Single-element elliptical hard X-ray micro-optics, *Optics Express* **11**(8), 919.

Evans-Lutterodt, K., Stein, A., Ablett, J. M., Bozovic, N., Taylor, A., & Tennant, D. M. (2007), Using compound kinoform hard-X-ray lenses to exceed the critical angle limit, *Physical Review Letters* **99**(13), 134801.

Fedoseev, D. V. & Varnin, V. P. (1983), Mechanism of diamond formation at low-pressures, *Zhurnal Fizicheskoi Khimii* **57**(11), 2726.

Ferrari, A. C. & Robertson, J. (2001), Origin of the 1150 cm^{-1} Raman mode in nanocrystalline diamond, *Physical Review B* **63**(12), 121405.

Ferrari, A. C. & Robertson, J. (2004), Raman spectroscopy of amorphous, nanostructured, diamond-like carbon, and nanodiamond, *Philosophical Transactions of the Royal Society of London A* **362**(1824), 2477.

Field, J. (1992), *The properties of natural and synthetic diamond*, Academic Press, London.

Fink, R. L., Tolt, Z. L., & Yaniv, Z. (1998), The status and future of diamond thin film FED, *Surface & Coatings Technology* **108**(1-3), 570.

Fox, O. J. L., Ma, J., May, P. W., Ashfold, M. N. R., & Mankelevich, Yu. A. (2009), The role of inert gas in MW-enhanced plasmas for the deposition of nanocrystalline diamond thin films, *Diamond and Related Materials* **18**(5-8), 750.

Fox, O. J. L., Holloway, J. O. P., Fuge, G. M., May, P. W., & Ashfold, M. N. R. (2010), Electrospray deposition of diamond nanoparticle nucleation layers for subsequent CVD diamond growth, *MRS proceedings: Diamond Electronics - Fundamentals to Applications* **2103**, J17.

Frenklach, M. & Wang, H. (1991), Detailed surface and gas-phase chemical-kinetics of diamond deposition, *Physical Review B* **43**(2), 1520.

Fu, Y. Q., Sun, C. Q., Du, H. J., & Yan, B. B. (2002), From diamond to crystalline silicon carbonitride: effect of introduction of nitrogen in CH_4/H_2 gas mixture using MW-PECVD, *Surface & Coatings Technology* **160**(2-3), 165.

Garrido, J. A., Nebel, C. E., Stutzmann, M., Gheeraert, E., Casanova, N., & Bustarret, E. (2002), Electrical and optical measurements of CVD diamond doped with sulfur, *Physical Review B* **65**(16), 165409.

Gerber, J., Weiler, M., Sohr, O., Jung, K., & Ehrhardt, H. (1994), Investigations of diamond nucleation on a-C films generated by DC bias and microwave plasma, *Diamond and Related Materials* **3**(4-6), 506.

Gerber, J., Sattel, S., Jung, K., Ehrhardt, H., & Robertson, J. (1995), Experimental characterization of bias-enhanced nucleation of diamond on Si, *Diamond and Related Materials* **4**(5-6), 559.

Gicquel, A., Hassouni, K., Farhat, S., Breton, Y., Scott, C. D., Lefebvre, M., & Pealat, M. (1994), Spectroscopic analysis and chemical-kinetics modeling of a diamond deposition plasma reactor, *Diamond and Related Materials* **3**(4-6), 581.

Gicquel, A., Chenevier, M., Breton, Y., Petiau, M., Booth, J. P., & Hassouni, K. (1996), Ground state and excited state H-atom temperatures in a microwave plasma diamond deposition reactor, *Journal de Physique III* **6**(9), 1167.

Gicquel, A., Chenevier, M., Hassouni, K., Tserepi, A., & Dubus, M. (1998), Validation of actinometry for estimating relative hydrogen atom densities and electron energy evolution in plasma assisted diamond deposition reactors, *Journal of Applied Physics* **83**(12), 7504.

Gicquel, A., Hassouni, K., Silva, F., & Achard, J. (2001), CVD diamond films: from growth to applications, *Current Applied Physics* **1**, 479.

Goodwin, D. G. (1991), Simulations of high-rate diamond synthesis - methyl as growth species, *Applied Physics Letters* **59**(3), 277.

Goodwin, D. G. & Butler, J. E. (1998), *Theory of diamond chemical vapor deposition* in *Handbook of Industrial Diamonds and Diamond Films*, Dekker.

Graff, I. B., Pugliese, R. A., & Westmoreland, P. R. (1994), Using molecular-beam mass-spectrometry to study the PECVD of diamond-like carbon-films, *Gas-phase and Surface Chemistry in Electronic Materials Processing* **334**, 129.

Greenwood, N. N. & Earnshaw, A. (2001), *Chemistry of the Elements*, 2nd edn, Butterworth-Heinemann.

Greuel, P. G., Roberts, J. T., & Ernie, D. W. (1995), Mass spectrometric analysis of a thermal plasma used for CVD of diamond films, *Proceedings of 12th International Symposium on Plasma Chemistry* **3**, 2209.

Griffin, J. & Ray, P. C. (2006), Role of inert gas in the low-temperature nano-diamond chemical vapour deposition process, *Nanotechnology* **17**(5), 1225.

Gruen, D. M., Liu, S. Z., Krauss, A. R., Luo, J. S., & Pan, X. Z. (1994a), Fullerenes as precursors for diamond film growth without hydrogen or oxygen additions, *Applied Physics Letters* **64**(12), 1502.

Gruen, D. M., Liu, S. Z., Krauss, A. R., & Pan, X. Z. (1994b), Buckyball microwave plasmas - fragmentation and diamond-film growth, *Journal of Applied Physics* **75**(3), 1758.

Gruen, D. M., Krauss, A. R., Zuiker, C. D., Csencsits, R., Terminello, L. J., Carlisle, J. A., Jimenez, I., Sutherland, D. G. J., Shuh, D. K., Tong, W., & Himpsel, F. J. (1996), Characterization of nanocrystalline diamond films by core-level photoabsorption, *Applied Physics Letters* **68**(12), 1640.

Gruen, D. M. (1999), Nanocrystalline diamond films, *Annual Review of Materials Science* **29**, 211.

Gruen, D. M., Redfern, P. C., Horner, D. A., Zapol, P., & Curtiss, L. A. (1999), Theoretical studies on nanocrystalline diamond: Nucleation by dicarbon and electronic structure of planar defects, *Journal of Physical Chemistry B* **103**(26), 5459.

Hagelaar, G. J. M., Hassouni, K., & Gicquel, A. (2004), Interaction between the electromagnetic fields and the plasma in a microwave plasma reactor, *Journal of Applied Physics* **96**(4), 1819.

Han, Y. S., Kim, Y. K., & Lee, J. Y. (1997), Effects of argon and oxygen addition to the CH_4-H_2 feed gas on diamond synthesis by microwave plasma enhanced chemical vapor deposition, *Thin Solid Films* **310**(1-2), 39.

Harris, S. J., Weiner, A. M., & Perry, T. A. (1988), Measurement of stable species present during filament-assisted diamond growth, *Applied Physics Letters* **53**(17), 1605.

Harris, S. J. (1989), Gas-phase kinetics during diamond growth - CH_4 as growth species, *Journal of Applied Physics* **65**(8), 3044.

Harris, S. J. & Weiner, A. M. (1989), Effects of oxygen on diamond growth, *Applied Physics Letters* **55**(21), 2179.

Harris, S. J. (1990), Mechanism for diamond growth from methyl radicals, *Applied Physics Letters* **56**(23), 2298.

Harris, S. J. & Weiner, A. M. (1990), Methyl radical and h-atom concentrations during diamond growth, *Journal of Applied Physics* **67**(10), 6520.

Harris, S. J., Weiner, A. M., & Perry, T. A. (1991), Filament-assisted diamond growth-kinetics, *Journal of Applied Physics* **70**(3), 1385.

Harris, S. J. & Weiner, A. M. (1992), Diamond growth-rates *vs* acetylene concentrations, *Thin Solid Films* **212**(1-2), 201.

Harris, S. J. & Goodwin, D. G. (1993), Growth on the reconstructed diamond (100) surface, *Journal of Physical Chemistry* **97**(1), 23.

Hassouni, K., Leroy, O., Farhat, S., & Gicquel, A. (1998), Modeling of H_2 and H_2/CH_4 moderate-pressure microwave plasma used for diamond deposition, *Plasma Chemistry and Plasma Processing* **18**(3), 325.

Hassouni, K., Grotjohn, T. A., & Gicquel, A. (1999), Self-consistent microwave field and plasma discharge simulations for a moderate pressure hydrogen discharge reactor, *Journal of Applied Physics* **86**(1), 134.

Hassouni, K., Mohasseb, F., Benedic, F., Lombardi, G., & Gicquel, A. (2006), Formation of soot particles in $Ar/H_2/CH_4$ microwave discharges during nanocrystalline diamond deposition: A modeling approach, *Pure and Applied Chemistry* **78**(6), 1127.

Hassouni, K., Silva, F., & Gicquel, A. (2010), Modelling of diamond deposition microwave cavity generated plasmas, *Journal of Physics D-Applied Physics* **43**(15), 153001.

Hazen, R. M. (1999), *The Diamond Makers*, Cambridge University Press.

Henke, B. L., Gullikson, E. M., & Davis, J. C. (1993), X-ray interactions - photoabsorption, scattering, transmission, and reflection at E = 50-30,000 eV, Z = 1-92, *Atomic Data and Nuclear Data Tables* **54**(2), 181.

Hiden (1993), *HAL II Ion Counting RGA systems*, 1.1 edn, Hiden Analytical Ltd., Warrington.

Hirmke, J., Glaser, A., Hempel, F., Stancu, G. D., Ropcke, J., Rosiwal, S. M., & Singer, R. F. (2007), Improved flow conditions in diamond hot filament CVD - promising deposition results and gas phase characterization by laser absorption spectroscopy, *Vacuum* **81**(5), 619.

de Hoffman, E. & Stroobant, V. (2007), *Mass Spectometry: Principles and Applications*, 3rd edn, Wiley.

Hong, F. C. N., Liang, G. T., Wu, J. J., Chang, D., & Hsieh, J. C. (1993), Diamond deposition from halogenated methane reactants in a hot-filament chemical-vapor-deposition reactor, *Applied Physics Letters* **63**(23), 3149.

Hsu, W. L. (1991), Mole fractions of H, CH_3, and other species during filament-assisted diamond growth, *Applied Physics Letters* **59**(12), 1427.

Hsu, W. L. (1992), Gas-phase kinetics during microwave plasma-assisted diamond deposition - is the hydrocarbon product distribution dictated by neutral-neutral interactions, *Journal of Applied Physics* **72**(7), 3102.

Hsu, W. L. & Tung, D. M. (1992), Application of molecular-beam mass-spectrometry to chemical vapor-deposition studies, *Review of Scientific Instruments* **63**(9), 4138.

Hsu, W. L., McMaster, M. C., Coltrin, M. E., & Dandy, D. S. (1994), Molecular-beam mass-spectrometry studies of chemical-vapor-deposition of diamond, *Japanese Journal of Applied Physics* **33**(4B), 2231.

Hubbell, J. H., Veigele, W. J., Briggs, E. A., Brown, R. T., Cromer, D. T., & Howerton, R. J. (1975), Atomic form factors, incoherent scattering functions, and photon scattering cross sections, *Journal of Physical and Chemical Reference Data* **4**, 471.

Huff, M. A., Aidala, D. A., & Butler, J. E. (2006), MEMS applications using diamond thin films, *Solid State Technology* **49**(4), 45.

Hwang, S. C., Lein, R. D., & Morgan, D. A. (2005), *Kirk-Othmer Encyclopedia of Chemical Technology*, Wiley.

Iijima, S., Aikawa, Y., & Baba, K. (1990), Early formation of chemical vapor-deposition diamond films, *Applied Physics Letters* **57**(25), 2646.

Isakovic, A. F., Stein, A., Warren, J. B., Narayanan, S., Sprung, M., Sandy, A. R., & Evans-Lutterodt, K. (2009), Diamond kinoform hard X-ray refractive lenses: design, nanofabrication and testing, *Journal of Synchrotron Radiation* **16**, 8.

Jain, S. C., Agarwal, S. K., Borle, W. N., & Tata, S. (1971), Total emissivity of silicon at high temperatures, *Journal of Physics D-Applied Physics* **4**(8), 1207.

Jiang, X., Six, R., & Klages, C. P. (1993), The effect of substrate bias voltage on the nucleation of diamond crystals in a microwave plasma assisted chemical vapor deposition process, *Diamond and Related Materials* **2**, 407.

Jiang, X., Schiffmann, K., & Klages, C. P. (1994), Nucleation and initial growth-phase of diamond thin-films on (100)-silicon, *Physical Review B* **50**(12), 8402.

Jiang, X. & Klages, C. P. (1996), Recent developments in heteroepitaxial nucleation and growth of diamond on silicon, *Physica Status Solidi A* **154**(1), 175.

John, P., Rabeau, J. R., & Wilson, J. I. B. (2002), The cavity ring-down spectroscopy of C_2 in a microwave plasma, *Diamond and Related Materials* **11**(3-6), 608.

Johnson, C. E., Weimer, W. A., & Cerio, F. M. (1992), Efficiency of methane and acetylene in forming diamond by microwave plasma assisted chemical vapor-deposition, *Journal of Materials Research* **7**(6), 1427.

Jordan, J. A., Hirsch, P. M., Lesem, L. B., & Van Rooy, D. L. (1970), Kinoform lenses, *Applied Optics* **9**(8), 1883.

Jubber, M. G., McLaughlin, A. J., Marsh, J. H., Aitchison, J. S., John, P., Troupe, C. E., & Wilson, J. I. B. (1998), Micromachined pattern transfer into CVD diamond, *Diamond and Related Materials* **7**(8), 1148.

Kajihara, S. A., Antonelli, A., Bernholc, J., & Car, R. (1991), Nitrogen and potential normal-type dopants in diamond, *Physical Review Letters* **66**(15), 2010.

Kalish, R., Reznik, A., Uzan-Saguy, C., & Cytermann, C. (2000), Is sulfur a donor in diamond?, *Applied Physics Letters* **76**(6), 757.

Kaminsky, C. F. & Ewart, P. (1997), Multiplex C_2 CARS thermometry in a microwave assisted diamond CVD plasma, *Applied Physics B - Lasers and Optics* **64**(1), 103.

Kamo, M., Sato, Y., Matsumoto, S., & Setaka, N. (1983), Diamond synthesis from gas-phase in microwave plasma, *Journal of Crystal Growth* **62**(3), 642.

Kang, H. C., Maser, J., Stephenson, G. B., Liu, C., Conley, R., Macrander, A. T., & Vogt, S. (2006), Nanometer linear focusing of hard X-rays by a multilayer Laue lens, *Physical Review Letters* **96**(12), 127401.

Kang, H. D., Preuss, R., Schwarz-Selinger, T., & Dose, V. (2002), Decomposition of multicomponent mass spectra using Bayesian probability theory, *Journal of Mass Spectrometry* **37**(7), 748.

Karve, P., Pal, J. P., Patil, S. C., Kulkarni, A. A., Kanetkar, S. M., Parikh, N., Patnaik, B., & Kshirsagar, S. T. (1996), Use of carbonitride film as buffer layer for CVD diamond nucleation, *Diamond and Related Materials* **5**(12), 1527.

Kátai, S., Tass, Z., Bori, L., Hárs, G., Deák, P., & Geelhaar, L. (1999a), Ion beam mass spectrometer for compositional analysis of plasma assisted surface processes in the pressure range of 1-50 mbar, *Review of Scientific Instruments* **70**(8), 3324.

Kátai, S., Tass, Z., Hárs, G., & Deák, P. (1999b), Measurement of ion energy distributions in the bias enhanced nucleation of chemical vapor deposited diamond, *Journal of Applied Physics* **86**(10), 5549.

Kátai, S., Tass, Z., Bori, L., Hárs, G., & Deák, P. (2000a), Plasma analyser for plasma-assisted surface process diagnostics up to 100 mbar, *Vacuum* **56**(1), 39.

Kátai, S., Kováts, A., Maros, I., & Deák, P. (2000b), Ion energy distributions and their evolution during bias-enhanced nucleation of chemical vapor deposition of diamond, *Diamond and Related Materials* **9**(3-6), 317.

Kawato, T. & Kondo, K. (1987), Effects of oxygen on CVD diamond synthesis, *Japanese Journal of Applied Physics* **26**(9), 1429.

Kee, R. J., Grcar, J. F., Smooke, M. D., & Miller, J. A. (1985), A FORTRAN program for modeling steady laminar one-dimensional premixed flames, *Sandia Report, SAND85-8240 UC-401* .

Kelly, S., Regan, E. M., Uney, J. B., Dick, A. D., McGeehan, J. P., Mayer, E. J., & Claeyssens, F. (2008), Patterned growth of neuronal cells on modified diamond-like carbon substrates, *Biomaterials* **29**(17), 2573.

Kim, Y. K., Ali, M. A., & Rudd, M. E. (1997a), Electron-impact total ionization cross sections of CH and C_2H_2, *Journal of Research of the National Institute of Standards and Technology* **102**(6), 693.

Kim, Y. K., Hwang, W., Weinberger, N. M., Ali, M. A., & Rudd, M. E. (1997b), Electron-impact ionization cross sections of atmospheric molecules, *Journal of Chemical Physics* **106**(3), 1026.

Klauser, F., Steinmuller-Nethl, D., Kaindl, R., Bertel, E., & Memmel, N. (2010), Raman studies of nano- and ultra-nanocrystalline diamond films grown by hot-filament CVD, *Chemical Vapor Deposition* **16**(4-6), 127.

Knight, D. S. & White, W. B. (1989), Characterization of diamond films by Raman-spectroscopy, *Journal of Materials Research* **4**(2), 385.

Knuth, E. L. (1995), Composition distortion in MBMS sampling, *Combustion and Flame* **103**(3), 171.

Kobashi, K., Nishimura, K., Kawate, Y., & Horiuchi, T. (1988), Synthesis of diamonds by use of microwave plasma chemical-vapor deposition - morphology and growth of diamond films, *Physical Review B* **38**(6), 4067.

Kociniewski, T., Barjon, J., Pinault, M. A., Jomard, F., Lusson, A., Ballutaud, D., Gorochov, O., Laroche, J. M., Rzepka, E., Chevallier, J., & Saguy, C. (2006), *n*-type CVD diamond doped with phosphorus using the MOCVD technology for dopant incorporation, *Physica Status Solidi A* **203**(12), 3136.

Kohn, E., Gluche, P., & Adamschik, M. (1999), Diamond MEMS - a new emerging technology, *Diamond and Related Materials* **8**, 934.

Kohse-Höinghaus, K., Löwe, A., & Atakan, B. (2000), Investigations of the gas phase mechanism of diamond deposition in combustion CVD, *Thin Solid Films* **368**(2), 185.

Koidl, P. & Klages, C.-P. (1992), Optical applications of polycrystalline diamond, *Diamond and Related Materials* **1**, 1065.

Koizumi, S., Kamo, M., Sato, Y., Ozaki, H., & Inuzuka, T. (1997), Growth and characterization of phosphorous doped 111 homoepitaxial diamond thin films, *Applied Physics Letters* **71**(8), 1065.

Konov, V. I., Smolin, A. A., Ralchenko, V. G., Pimenov, S. M., Obraztsova, E. D., Loubnin, E. N., Metev, S. M., & Sepold, G. (1995), DC-arc plasma deposition of smooth nanocrystalline diamond films, *Diamond and Related Materials* **4**(8), 1073.

Kováts, A. & Deák, P. (2005), Gas composition at the substrate in MWCVD diamond growth: An old problem revisited, *Diamond and Related Materials* **14**(9), 1517.

Krauss, A. R., Auciello, O., Gruen, D. M., Jayatissa, A., Sumant, A., Tucek, J., Mancini, D. C., Moldovan, N., Erdemir, A., Ersoy, D., Gardos, M. N., Busmann, H. G., Meyer, E. M., & Ding, M. Q. (2001), Ultrananocrystalline diamond thin films for MEMS and moving mechanical assembly devices, *Diamond and Related Materials* **10**(11), 1952.

Krüger, A., Kataoka, F., Ozawa, M., Fujino, T., Suzuki, Y., Aleksenskii, A. E., Vul', A. Y., & Osawa, E. (2005), Unusually tight aggregation in detonation nanodiamond: Identification and disintegration, *Carbon* **43**(8), 1722.

Krüger, A., Liang, Y. J., Jarre, G., & Stegk, J. (2006), Surface functionalisation of detonation diamond suitable for biological applications, *Journal of Materials Chemistry* **16**(24), 2322.

Krüger, A., Ozawa, M., Jarre, G., Liang, Y., Stegk, J., & Lu, L. (2007), Deagglomeration and functionalisation of detonation diamond, *Physica Status Solidi A* **204**(9), 2881.

Kronig, R. D. L. (1926), On the theory of dispersion of X-rays, *Journal of the Optical Society of America and Review of Scientific Instruments* **12**(6), 547.

Kulisch, W., Ackermann, L., & Sobisch, B. (1996), On the mechanisms of bias enhanced nucleation of diamond, *Physica Status Solidi A* **154**(1), 155.

Kulisch, W. & Popov, C. (2006), On the growth mechanisms of nanocrystalline diamond films, *Physica Status Solidi A* **203**(2), 203.

Laclare, J. L. (2001), Light source performance achievements, *Nuclear Instruments & Methods in Physics Research Section A - Accelerators Spectrometers Detectors and Associated Equipment* **467**, 1.

Leeds, S. (1999), Characterisation of the Gas-Phase Environment in a Microwave Plasma Enhanced Diamond Chemical Vapour Deposition Reactor using Molecular Beam Mass Spectrometry, PhD thesis, School of Chemistry, University of Bristol.

Leeds, S. M., May, P. W., Ashfold, M. N. R., & Rosser, K. N. (1999a), Molecular beam mass spectrometry studies of nitrogen additions to the gas phase during microwave-plasma-assisted chemical vapour deposition of diamond, *Diamond and Related Materials* **8**(2-5), 226.

Leeds, S. M., May, P. W., Bartlett, E., Ashfold, M. N. R., & Rosser, K. N. (1999b), Molecular beam mass spectrometry studies of the gas-phase chemistry occurring during microwave plasma assisted chemical vapour deposition of diamond, *Diamond and Related Materials* **8**(8-9), 1377.

Lee, S. S., Minsek, D. W., Vestyck, D. J., & Chen, P. (1994), Growth of diamond from atomic-hydrogen and a supersonic free jet of methyl radicals, *Science* **263**(5153), 1596.

Lee, S. T., Lin, Z. D., & Jiang, X. (1999), CVD diamond films: nucleation and growth, *Materials Science & Engineering R-Reports* **25**(4), 123.

Lengeler, B., Schroer, C. G., Richwin, M., Tummler, J., Drakopoulos, M., Snigirev, A., & Snigireva, I. (1999), A microscope for hard X-rays based on parabolic compound refractive lenses, *Applied Physics Letters* **74**(26), 3924.

Lengeler, B., Schroer, C. G., Kuhlmann, M., Benner, B., Gunzler, T. F., Kurapova, O., Zontone, F., Snigirev, A., & Snigireva, I. (2004), Beryllium parabolic refractive X-ray lenses, *Design and Microfabrication of Novel X-ray Optics II, SPIE* **5539**, 1.

Lespade, P., Marchand, A., Couzi, M., & Cruege, F. (1984), Characterization of carbon materials with Raman microspectrometry, *Carbon* **22**(4-5), 375.

Liang, Q., Chin, C. Y., Lai, J., Yan, C. S., Meng, Y., Mao, H. K., & Hemley, R. J. (2009), Enhanced growth of high quality single crystal diamond by microwave plasma assisted chemical vapor deposition at high gas pressures, *Applied Physics Letters* **94**(2), 024103.

Lias, S., Bartmess, J., Liebman, J., Holmes, J., Levin, R., & Mallard, W. (2011), Gas phase ion energetics data, *NIST Chemistry WebBook, National Institute of Standards and Technology, Gaithersburg* **69**. http://webbook.nist.gov/chemistry

Lifshitz, Y., Kasi, S. R., & Rabalais, J. W. (1989), Subplantation model for film growth from hyperthermal species - application to diamond, *Physical Review Letters* **62**(11), 1290.

Liu, Y. K., Liu, C., Chen, Y. C., Tzeng, Y., Tso, P., & Lin, I. (2004), Effects of hydrogen additive on microwave plasma CVD of nanocrystalline diamond in mixtures of argon and methane, *Diamond and Related Materials* **13**(4-8), 671.

Liu, Y. K., Tso, P. L., Lin, I. N., Tzeng, Y., & Chen, Y. C. (2006), Comparative study of nucleation processes for the growth of nanocrystalline diamond, *Diamond and Related Materials* **15**(2-3), 234.

Lloyd, G. M. & Ewart, P. (1999), High resolution spectroscopy and spectral simulation of C_2 using degenerate four-wave mixing, *Journal of Chemical Physics* **110**(1), 385.

Locher, R., Wild, C., Herres, N., Behr, D., & Koidl, P. (1994), Nitrogen stabilized (100) texture in chemical-vapor-deposited diamond films, *Applied Physics Letters* **65**(1), 34.

Locher, R., Wagner, J., Fuchs, F., Maier, M., Gonon, P., & Koidl, P. (1995), Optical and electrical characterization of boron-doped diamond films, *Diamond and Related Materials* **4**(5-6), 678.

Loh, K. P., Foord, J. S., Jackman, R. B., & Singh, N. K. (1996), Growth studies of thin film diamond using molecular beam techniques, *Diamond and Related Materials* **5**(3-5), 231.

Lombardi, G., Hassouni, K., Benedic, F., Mohasseb, F., Ropcke, J., & Gicquel, A. (2004), Spectroscopic diagnostics and modeling of $Ar/H_2/CH_4$ microwave discharges used for nanocrystalline diamond deposition, *Journal of Applied Physics* **96**(11), 6739.

Lombardi, G., Hassouni, K., Stancu, G. D., Mechold, L., Ropcke, J., & Gicquel, A. (2005a), Modeling of microwave discharges of H_2 admixed with CH_4 for diamond deposition, *Journal of Applied Physics* **98**(5), 053303.

Lombardi, G., Hassouni, K., Stancu, G. D., Mechold, L., Ropcke, J., & Gicquel, A. (2005b), Study of an H_2/CH_4 moderate pressure microwave plasma used for diamond deposition:

modelling and IR tuneable diode laser diagnostic, *Plasma Sources Science & Technology* **14**(3), 440.

Lommatzsch, U., Wahl, E. H., Owano, T. G., Kruger, C. H., & Zare, R. N. (2000), Spatial concentration and temperature distribution of CH radicals formed in a diamond thin-film hot-filament reactor, *Chemical Physics Letters* **320**(3-4), 339.

Löwe, A. G., Hartlieb, A. T., Brand, J., Atakan, B., & Kohse-Höinghaus, K. (1999), Diamond deposition in low-pressure acetylene flames: *In situ* temperature and species concentration measurements by laser diagnostics and molecular beam mass spectrometry, *Combustion and Flame* **118**(1-2), 37.

Lu, P. J., Yao, N., So, J. F., Harlow, G. E., Lu, J. F., Wang, G. F., & Chaikin, P. M. (2005), The earliest use of corundum and diamond, in prehistoric china, *Archaeometry* **47**, 1.

Ma, J. (2008), Exploration of the gas phase chemistry in microwave activated plasmas used for diamond chemical vapour deposition, PhD thesis, School of Chemistry, University of Bristol.

Ma, J., Richley, J. C., Ashfold, M. N. R., & Mankelevich, Yu. A. (2008), Probing the plasma chemistry in a microwave reactor used for diamond chemical vapor deposition by cavity ring down spectroscopy, *Journal of Applied Physics* **104**(10), 103305.

Ma, J., Cheesman, A., Ashfold, M. N. R., Hay, K. G., Wright, S., Langford, N., Duxbury, G., & Mankelevich, Yu. A. (2009a), Quantum cascade laser investigations of CH_4 and C_2H_2 interconversion in hydrocarbon/H_2 gas mixtures during microwave plasma enhanced chemical vapor deposition of diamond, *Journal of Applied Physics* **106**, 033305.

Ma, J., Ashfold, M. N. R., & Mankelevich, Yu. A. (2009b), Validating optical emission spectroscopy as a diagnostic of microwave activated CH_4/Ar/H_2 plasmas used for diamond chemical vapor deposition, *Journal of Applied Physics* **105**(4), 043302.

Ma, J., Richley, J. C., Davies, D. R. W., Cheesman, A., Ashfold, M. N. R., & Mankelevich, Yu. A. (2010a), Spectroscopic and modeling investigations of the gas-phase chemistry and composition in microwave plasma activated B_2H_6/Ar/H_2 mixtures, *Journal of Physical Chemistry A* **114**(7), 2447.

Ma, J., Richley, J. C., Davies, D. R. W., Ashfold, M. N. R., & Mankelevich, Yu. A. (2010b), Spectroscopic and modeling investigations of the gas phase chemistry and composition in microwave plasma activated B_2H_6/CH_4/Ar/H_2 mixtures, *Journal of Physical Chemistry A* **114**(37), 10076.

Malshe, A. P., Beera, R. A., Khanolkar, A. A., Brown, W. D., & Naseem, H. A. (1997), Initial results of a novel pre-deposition seeding technique for achieving an ultra-high nucleation density for CVD diamond growth, *Diamond and Related Materials* **6**(2-4), 430.

Malshe, A. P., Khanolkar, A. A., Brown, W. D., Yedave, S. N., Naseem, H. A., & Haque, M. S. (1998), Electrostatic seeding (ESS): A novel approach to seeding substrates for CVD-diamond growth, *Proceedings of the 5th International Symposium on Diamond Materials* **97**(32), 399.

Mankelevich, Yu. A., Ashfold, M. N. R., & Ma, J. (2008), Plasma-chemical processes in microwave plasma-enhanced chemical vapor deposition reactors operating with C/H/Ar gas mixtures, *Journal of Applied Physics* **104**(11), 113304.

Mankelevich, Yu. A. & May, P. W. (2008), New insights into the mechanism of CVD diamond growth: Single crystal diamond in MW PECVD reactors, *Diamond and Related Materials* **17**(7-10), 1021.

Martin, T. (2011), Lithium-oxygen termination as a negative electron affinity surface on diamond, PhD thesis, Department of Physics, University of Bristol.

Matsui, Y., Yabe, H., & Hirose, Y. (1990), The growth-mechanism of diamond crystals in acetylene flames, *Japanese Journal of Applied Physics* **29**(8), 1552.

Matsumoto, S., Sato, Y., Kamo, M., & Setaka, N. (1982), Vapor-deposition of diamond particles from methane, *Japanese Journal of Applied Physics* **21**(4), L183.

Matsumoto, O., Toshima, H., & Kanzaki, Y. (1985), Effect of dilution gases in methane on the deposition of diamond-like carbon in a microwave-discharge, *Thin Solid Films* **128**(3-4), 341.

May, P. W., Burridge, P. R., Rego, C. A., Tsang, R. S., Ashfold, M. N. R., Rosser, K. N., Tanner, R. E., Cherns, D., & Vincent, R. (1996), Investigation of the addition of nitrogen-containing gases to a hot filament diamond chemical vapour deposition reactor, *Diamond and Related Materials* **5**(3-5), 354.

May, P. W. (2000), Diamond thin films: a 21st-century material, *Philosophical Transactions of the Royal Society of London A* **358**(1766), 473.

May, P. W., Harvey, J. N., Smith, J. A., & Mankelevich, Yu. A. (2006), Re-evaluation of the mechanism for ultrananocrystalline diamond deposition from Ar/CH_4/H_2 gas mixtures, *Journal of Applied Physics* **99**(10), 104907.

May, P. W. & Mankelevich, Yu. A. (2006), Experiment and modeling of the deposition of ultrananocrystalline diamond films using hot filament chemical vapor deposition and Ar/CH_4/H_2 gas mixtures: A generalized mechanism for ultrananocrystalline diamond growth, *Journal of Applied Physics* **100**(2), 024301.

May, P. W., Ashfold, M. N. R., & Mankelevich, Yu. A. (2007), Microcrystalline, nanocrystalline, and ultrananocrystalline diamond chemical vapor deposition: Experiment and modeling of the factors controlling growth rate, nucleation, and crystal size, *Journal of Applied Physics* **101**(5), 053115.

May, P. W. & Mankelevich, Yu. A. (2008), From ultrananocrystalline diamond to single crystal diamond growth in hot filament and microwave plasma-enhanced CVD reactors: a unified model for growth rates and grain sizes, *Journal of Physical Chemistry C* **112**(32), 12432.

May, P. W., Allan, N. L., Ashfold, M. N. R., Richley, J. C., & Mankelevich, Yu. A. (2009), Simplified Monte Carlo simulations of chemical vapour deposition diamond growth, *Journal of Physics-Condensed Matter* **21**(36), 364203.

May, P. W., Allan, N. L., Ashfold, M. N. R., Richley, J. C., & Mankelevich, Yu. A. (2010), Simulations of polycrystalline CVD diamond film growth using a simplified Monte Carlo model, *Diamond and Related Materials* **19**(5-6), 389.

McGinnis, S. P., Kelly, M. A. & Hagstrom, S. B. (1995), Evidence of an energetic ion-bombardment mechanism for bias-enhanced nucleation of diamond, *Applied Physics Letters* **66**(23), 3117.

McMaster, M. C., Hsu, W. L., Coltrin, M. E., & Dandy, D. S. (1994), Experimental measurements and numerical simulations of the gas-composition in a hot-filament-assisted diamond chemical-vapor-deposition reactor, *Journal of Applied Physics* **76**(11), 7567.

McMaster, M. C., Hsu, W. L., Coltrin, M. E., Dandy, D. S., & Fox, C. (1995), Dependence of the gas-composition in a microwave plasma-assisted diamond chemical-vapor-deposition reactor on the inlet carbon source - CH_4 versus C_2H_2, *Diamond and Related Materials* **4**(7), 1000.

Meesters, G. M. H., Vercoulen, P. H. W., Marijnissen, J. C. M., & Scarlett, B. (1990), A monodisperse-aerosol-generator, using the Taylor cone, for the production of 1 μm droplets, *Journal Of Aerosol Science* **21**, S669.

Meesters, G. M. H., Vercoulen, P. H. W., Marijnissen, J. C. M., & Scarlett, B. (1992), Generation of micron-sized droplets from the Taylor cone, *Journal of Aerosol Science* **23**(1), 37.

Meier, U., Kohse-Höinghaus, K., Schafer, L., & Klages, C. P. (1990), 2-photon excited LIF determination of H-atom concentrations near a heated filament in a low-pressure H_2 environment, *Applied Optics* **29**(33), 4993.

Melendrez, R., Chernov, V., May, P. W., Castaneda, B., Pedroza-Montero, M., & Barboza-Flores, M. (2009), Thermoluminescence assessment of 0.5, 1.0 and 4.0 μm thick HFCVD undoped diamond films, *Physica Status Solidi A* **206**(9), 2103.

Meng, Y. F., Yan, C. S., Lai, J., Krasnicki, S., Shu, H., Yu, T., Liang, Q., Mao, H. K., & Hemley, R. J. (2008), Enhanced optical properties of chemical vapor deposited single crystal diamond by low-pressure/high-temperature annealing, *Proceedings of the National Academy of Sciences of the United States of America* **105**(46), 17620.

Met, C., de Persis, S., Vandenbulcke, L., Aubry, O., Delfau, J. L., Vovelle, C., & Lago, V. (2006), Emission spectroscopy, mass spectrometry, and kinetics in CH_4-CO_2 plasmas used for diamond deposition, *Journal of the Electrochemical Society* **153**(7), F127.

Michette, A. G. (1991), No X-ray lens, *Nature* **353**(6344), 510.

Mitsuda, Y., Kojima, Y., Yoshida, T., & Akashi, K. (1987), The growth of diamond in microwave plasma under low-pressure, *Journal of Materials Science* **22**(5), 1557.

Mohasseb, F., Hassouni, K., Benedic, F., Lombardi, G., & Gicquel, A. (2005), Modelling of Ar/H_2/CH_4 microwave discharges used for nanocrystalline diamond growth, in *Synthesis, properties and applications of ultrananocrystalline diamond*, Vol. 192, Springer.

Moran, D. A. J., Fox, O. J. L., McLelland, H., Russell, S., & May, P. W. (2011), Intrinsic scaling of hydrogen-terminated diamond FETs to sub-100 nm gate dimensions, *IEEE Electron Device Letters* **32**(5), 599.

Morrish, A. A. & Pehrsson, P. E. (1991), Effects of surface pretreatments on nucleation and growth of diamond films on a variety of substrates, *Applied Physics Letters* **59**(4), 417.

Moselhy, M., Petzenhauser, I., Frank, K., & Schoenbach, K. H. (2003), Excimer emission from microhollow cathode argon discharges, *Journal of Physics D - Applied Physics* **36**(23), 2922.

Müller-Sebert, W., Worner, E., Fuchs, F., Wild, C., & Koidl, P. (1996), Nitrogen induced increase of growth rate in chemical vapor deposition of diamond, *Applied Physics Letters* **68**(6), 759.

Musale, D. V., Pai, M. P., Sainkar, S. R., & Kshirsagar, S. T. (1999), Enhancement of nucleation and growth of diamond films using In-Sn-O buffer layer on si substrate, *Materials Letters* **39**(2), 86.

Nebel, C. E., Rezek, B., Shin, D., Uetsuka, H., & Yang, N. (2007), Diamond for bio-sensor applications, *Journal of Physics D - Applied Physics* **40**(20), 6443.

Netto, A. & Frenklach, M. (2005), Kinetic Monte Carlo simulations of CVD diamond growth - interlay among growth, etching, and migration, *Diamond and Related Materials* **14**(10), 1630.

Nöhammer, B., David, C., Rothuizen, H., Hoszowska, J., & Simionovici, A. (2003), Deep reactive ion etching of silicon and diamond for the fabrication of planar refractive hard X-ray lenses, *Microelectronic Engineering* **67-8**, 453.

Nishimori, T., Nakano, K., Sakamoto, H., Takakuwa, Y., & Kono, S. (1997), *n*-type high-conductive epitaxial diamond film prepared by gas source molecular beam epitaxy with methane and tri-*n*-butylphosphine, *Applied Physics Letters* **71**(7), 945.

O'Donnell, K. M., Martin, T. L., Fox, N. A., & Cherns, D. (2010), *Ab initio* investigation of lithium on the diamond C(100) surface, *Physical Review B* **82**(11), 115303.

Ohtake, N. & Yoshikawa, M. (1990), Diamond film preparation by arc-discharge plasma-jet chemical vapor-deposition in the methane atmosphere, *Journal of the Electrochemical Society* **137**(2), 717.

Ozawa, M., Inaguma, M., Takahashi, M., Kataoka, F., Krüger, A., & Osawa, E. (2007), Preparation and behavior of brownish, clear nanodiamond colloids, *Advanced Materials* **19**(9), 1201.

Pan, C. Y., Chu, C. J., Margrave, J. L., & Hauge, R. H. (1994), Chlorine-activated diamond chemical-vapor-deposition, *Journal of the Electrochemical Society* **141**(11), 3246.

Park, S., Liao, F., Larson, J. M., Girshick, S. L., & Zachariah, M. R. (2004), Molecular beam mass spectrometry system for characterization of thermal plasma chemical vapor deposition, *Plasma Chemistry and Plasma Processing* **24**(3), 353.

Paul, W. & Steinwedel, H. (1953), Ein neues massenspektrometer ohne magnetfeld, *Zeitschrift für Naturforschung A - A Journal of Physical Sciences* **8**(7), 448.

Paul, W. & Raether, M. (1955), Das elektrische massenfilter, *Zeitschrift für Physik* **140**(3), 262.

Petherbridge, J. R., May, P. W., Pearce, S. R. J., Rosser, K. N., & Ashfold, M. N. R. (2001a), Low temperature diamond growth using CO_2/CH_4 plasmas: Molecular beam mass spectrometry and computer simulation investigations, *Journal of Applied Physics* **89**(2), 1484.

Petherbridge, J., May, P. W., Pearce, S. R. J., Rosser, K. N., & Ashfold, M. N. R. (2001b), Molecular beam mass spectrometry investigations of low temperature diamond growth using CO_2/CH_4 plasmas, *Diamond and Related Materials* **10**(3-7), 393.

Petherbridge, J. R., May, P. W., & Ashfold, M. N. R. (2001c), Modeling of the gas-phase chemistry in C-H-O gas mixtures for diamond chemical vapor deposition, *Journal of Applied Physics* **89**(9), 5219.

Petherbridge, J. R., May, P. W., Fuge, G. M., Robertson, G. F., Rosser, K. N., & Ashfold, M. N. R. (2002a), Sulfur doping of diamond films: Spectroscopic, electronic, and gas-phase studies, *Journal of Applied Physics* **91**(6), 3605.

Petherbridge, J. R., May, P. W., Fuge, G. M., Rosser, K. N., & Ashfold, M. N. R. (2002b), In situ plasma diagnostics of the chemistry behind sulfur doping of CVD diamond films, *Diamond and Related Materials* **11**(3-6), 301.

Pilkington, G. A., Thormann, E., Claesson, P. M., Fuge, G. M., Fox, O. J. L., Ashfold, M. N. R., Leese, H., Mattia, D., & Briscoe, W. H. (2011), Amontonian frictional behaviour of nanostructured surfaces, *Physical Chemistry Chemical Physics* **13**(20), 9318.

Plessis, P., Marmet, P., & Dutil, R. (1983), Ionization and appearance potentials of CH_4 by electron-impact, *Journal of Physics B - Atomic Molecular and Optical Physics* **16**(7), 1283.

Plessis, P. & Marmet, P. (1986), Electroionization study of acetylene and fragment ions, *International Journal of Mass Spectrometry and Ion Processes* **70**(1), 23.

Popov, C., Bliznakov, S., & Kulisch, W. (2007), Influence of the substrate nature on the properties of nanocrystalline diamond films, *Diamond and Related Materials* **16**(4-7), 740.

Prawer, S. & Nemanich, R. J. (2004), Raman spectroscopy of diamond and doped diamond, *Philosophical Transactions of the Royal Society of London A* **362**(1824), 2537.

Prawer, S. & Greentree, A. D. (2008), Applied physics - diamond for quantum computing, *Science* **320**(5883), 1601.

Proffitt, S., Thompson, C. H. B., Gutierrez-Sosa, A., Paris, N., Singh, N. K., Jackman, R. B., & Foord, J. S. (2000), Understanding the chemistry of low temperature diamond growth: an investigation into the interaction of chlorine and atomic hydrogen at CVD diamond surfaces, *Diamond and Related Materials* **9**(3-6), 246.

Rabeau, J. R., John, P., Wilson, J. I. B., & Fan, Y. (2004), The role of C_2 in nanocrystalline diamond growth, *Journal of Applied Physics* **96**(11), 6724.

Railkar, T. A., Kang, W. P., Windischmann, H., Malshe, A. P., Naseem, H. A., Davidson, J. L., & Brown, W. D. (2000), A critical review of chemical vapor-deposited (CVD) diamond for electronic applications, *Critical Reviews in Solid State and Materials Sciences* **25**(3), 163.

Ralchenko, V. G., Smolin, A. A., Konov, V. I., Sergeichev, K. F., Sychov, I. A., Vlasov, I. I., Migulin, V. V., Voronina, S. V., & Khomich, A. V. (1997), Large-area diamond deposition by microwave plasma, *Diamond and Related Materials* **6**(2-4), 417.

Ralchenko, V. G., Saveliev, A., Voronina, S., Dementjev, A., Maslakov, K., Salerno, M., Podesta, A., & Milani, P. (2005), Nanodiamond seeding for nucleation and growth of CVD diamond films, in *Synthesis, properties and applications of ultrananocrystalline diamond*, Vol. 192, Springer.

Ramamurti, R., Becker, M., Schuelke, T., Grotjohn, T., Reinhard, D., Swain, G., & Asmussen, J. (2008), Boron doped diamond deposited by microwave plasma-assisted CVD at low and high pressures, *Diamond and Related Materials* **17**(4-5), 481.

Rapp, D. & Englander-Golden, P. (1965), Total cross sections for ionization and attachment in gases by electron impact: I. positive ionization, *Journal of Chemical Physics* **43**(5), 1464.

Rego, C. A., May, P. W, Henderson, C. R, Ashfold, M. N. R., & Everitt, N. M. (1994), Molecular beam mass spectrometric study of the spatial distribution of gas-phase species involved in the growth of HFCVD diamond films, *Advances in New Diamond Science and Technology* p. 485.

Rego, C. A., May, P. W., Henderson, C. R., Ashfold, M. N. R., Rosser, K. N., & Everitt, N. M. (1995), *In-situ* mass-spectrometric study of the gas-phase species involved in CVD of diamond as a function of filament temperature, *Diamond and Related Materials* **4**(5-6), 770.

Rego, C. A., Tsang, R. S., May, P. W., Ashfold, M. N. R., & Rosser, K. N. (1996), Gas-phase composition measurements during chlorine assisted chemical vapor deposition of diamond: A molecular beam mass spectrometric study, *Journal of Applied Physics* **79**(9), 7264.

Rennick, C. J., Smith, J. A., Ashfold, M. N. R., & Orr-Ewing, A. J. (2004), Cavity ring-down spectroscopy measurements of the concentrations of C_2 radicals in a DC arc-jet reactor used for chemical vapour deposition of diamond films, *Chemical Physics Letters* **383**(5-6), 518.

Ribbing, C., Cederstrom, B., & Lundqvist, M. (2003), Microstructured diamond X-ray source and refractive lens, *Diamond and Related Materials* **12**(10-11), 1793.

Richley, J. C., Harvey, J. N., & Ashfold, M. N. R. (2009), On the role of carbon radical insertion reactions in the growth of diamond by chemical vapor deposition methods, *Journal of Physical Chemistry A* **113**(42), 11416.

Richley, J. C., Fox, O. J. L., Ashfold, M. N. R., & Mankelevich, Yu. A. (2011), Combined experimental and modeling studies of microwave activated $CH_4/H_2/Ar$ plasmas for microcrystalline, nanocrystalline, and ultrananocrystalline diamond deposition, *Journal of Applied Physics* **109**(6), 063307.

Ristein, J., Riedel, M., Maier, F., Mantel, B. F., Stammler, M., & Ley, L. (2001), Surface doping: a special feature of diamond, *Journal of Physics - Condensed Matter* **13**(40), 8979.

Robertson, J. (1995), Mechanism of bias-enhanced nucleation and heteroepitaxy of diamond on Si, *Diamond and Related Materials* **4**(5-6), 549.

Sakaguchi, I., Gamo, M. N., Kikuchi, Y., Yasu, E., Haneda, H., Suzuki, T., & Ando, T. (1999), Sulfur: A donor dopant for *n*-type diamond semiconductors, *Physical Review B* **60**(4), R2139.

Sawabe, A. & Inuzuka, T. (1986), Growth of diamond thin-films by electron-assisted chemical vapor-deposition and their characterization, *Thin Solid Films* **137**(1), 89.

Schmidt, I. & Benndorf, C. (2001), Low temperature CVD diamond deposition using halogenated precursors - deposition on low melting materials: Al, Zn and glass, *Diamond and Related Materials* **10**(3-7), 347.

Schneider, A., Malik, A., Djakov, V., Yang, T. H. J., Reuben, R. L., Stevens, R., & McNeill, S. A. (2004), Optimisation of Si DRIE for perfect high sidewalls of microchannels and movable micropistons in hydraulic actuated device, *Proceedings of the European conference on Micro and Nano-systems* **1**, 19.

Schroer, C. G., Kuhlmann, M., Hunger, U. T., Gunzler, T. F., Kurapova, O., Feste, S., Frehse, F., Lengeler, B., Drakopoulos, M., Somogyi, A., Simionovici, A. S., Snigirev, A., Snigireva, I., Schug, C., & Schroder, W. H. (2003), Nanofocusing parabolic refractive X-ray lenses, *Applied Physics Letters* **82**(9), 1485.

Schroer, C. G., Kurapova, O., Patommel, J., Boye, P., Feldkamp, J., Lengeler, B., Burghammer, M., Riekel, C., Vincze, L., van der Hart, A., & Kuchler, M. (2005), Hard X-ray nanoprobe based on refractive X-ray lenses, *Applied Physics Letters* **87**(12), 124103.

Schroer, C. G. & Lengeler, B. (2005), Focusing hard X-rays to nanometer dimensions by adiabatically focusing lenses, *Physical Review Letters* **94**(5), 054802.

Shenderova, O. A., Zhirnov, V. V., & Brenner, D. W. (2002), Carbon nanostructures, *Critical Reviews in Solid State and Materials Sciences* **27**(3-4), 227.

Shiomi, H., Tanabe, K., Nishibayashi, Y., & Fujimori, N. (1990), Epitaxial-growth of high-quality diamond film by the microwave plasma-assisted chemical-vapor-deposition method, *Japanese Journal of Applied Physics* **29**(1), 34.

Shkurenkov, I. A., Mankelevich, Yu. A., & Rakhimova, T. V. (2008), Diffuse and constricted modes of a DC discharge in neon: Simulation of the hysteresis transition, *Plasma Physics Reports* **34**(9), 780.

Silva, F., Achard, J., Bonnin, X., Brinza, O., Michau, A., Secroun, A., De Corte, K., Felton, S., Newton, M., & Gicquel, A. (2008), Single crystal CVD diamond growth strategy by the use of a 3D geometrical model: Growth on (113) oriented substrates, *Diamond and Related Materials* **17**(7-10), 1067.

Simeonsson, J. B. & Miziolek, A. W. (1993), Time-resolved emission studies of ArF-laser-produced microplasmas, *Applied Optics* **32**(6), 939.

Singh, H., Coburn, J. W., & Graves, D. B. (1999), Mass spectrometric detection of reactive neutral species: Beam-to-background ratio, *Journal of Vacuum Science & Technology A* **17**(5), 2447.

Singh, H., Coburn, J. W., & Graves, D. B. (2000), Appearance potential mass spectrometry: Discrimination of dissociative ionization products, *Journal of Vacuum Science & Technology A* **18**(2), 299.

Smith, D. P. H. (1986), The electrohydrodynamic atomization of liquids, *IEEE Transactions on Industry Applications* **IA-22 (3)**, 527.

Smith, J. A., Cameron, E., Ashfold, M. N. R., Mankelevich, Yu. A., & Suetin, N. V. (2001), On the mechanism of CH_3 radical formation in hot filament activated CH_4/H_2 and C_2H_2/H_2 gas mixtures, *Diamond and Related Materials* **10**(3-7), 358.

Smith, J. A., Wills, J. B., Moores, H. S., Orr-Ewing, A. J., Ashfold, M. N. R., Mankelevich, Yu. A., & Suetin, N. V. (2002), Effects of NH_3 and N_2 additions to hot filament activated CH_4/H_2 gas mixtures, *Journal of Applied Physics* **92**(2), 672.

Smolin, A. A., Ralchenko, V. G., Pimenov, S. M., Kononenko, T. V., & Loubnin, E. N. (1993), Optical monitoring of nucleation and growth of diamond films, *Applied Physics Letters* **62**(26), 3449.

Snigirev, A., Kohn, V., Snigireva, I., & Lengeler, B. (1996), A compound refractive lens for focusing high-energy X-rays, *Nature* **384**(6604), 49.

Snigirev, A., Bjeoumikhov, A., Erko, A., Snigireva, I., Grigoriev, M., Yunkin, V., Erko, M., & Bjeoumikhova, S. (2007), Submicrometer hard X-ray focusing using a single-bounce ellipsoidal capillary combined with a Fresnel zone plate, *Journal of Synchrotron Radiation* **14**, 227.

Solin, S. A. & Ramdas, A. K. (1970), Raman spectrum of diamond, *Physical Review B* **1**(4), 1687.

Spitsyn, B. V., Bouilov, L. L., & Derjaguin, B. V. (1981), Vapor growth of diamond on diamond and other surfaces, *Journal of Crystal Growth* **52**, 219.

Stalder, K. R. & Sharpless, R. L. (1990), Plasma properties of a hydrocarbon arc-jet used in the plasma deposition of diamond thin-films, *Journal of Applied Physics* **68**(12), 6187.

Sternschulte, H., Schreck, M., & Stritzker, B. (2002), *In situ* characterisation of CVD diamond growth under H_2S addition by optical emission spectroscopy, mass spectroscopy and laser reflection interferometry, *Diamond and Related Materials* **11**(3-6), 296.

Stockel, R., Stammler, M., Janischowsky, K., Ley, L., Albrecht, M., & Strunk, H. P. (1998), Diamond nucleation under bias conditions, *Journal of Applied Physics* **83**(1), 531.

Stoner, B. R. & Glass, J. T. (1992), Textured diamond growth on (100) beta-SiC *via* microwave plasma chemical vapor-deposition, *Applied Physics Letters* **60**(6), 698.

Suehiro, S., Miyaji, H., & Hayashi, H. (1991), Refractive lens for X-ray focus, *Nature* **352**(6334), 385.

Swihart, M. T. & Girshick, S. L. (1999), An analysis of flow, temperature, and chemical composition distortion in gas sampling through an orifice during chemical vapor deposition, *Physics of Fluids* **11**(4), 821.

Talin, A. A., Dean, K. A., & Jaskie, J. E. (2001), Field emission displays: a critical review, *Solid-state Electronics* **45**(6), 963.

Tang, C. J., Neves, A. J., & Fernandes, A. J. S. (2004), Study the effect of O_2 addition on hydrogen incorporation in CVD diamond, *Diamond and Related Materials* **13**(1), 203.

Taylor, G. (1964), Disintegration of water drops in electric field, *Proceedings of the Royal Society of London Series A - Mathematical and Physical Sciences* **280**(1380), 383.

Tennant, S. (1797), On the nature of the diamond, *Philosophical Transactions of the Royal Society of London* **87**, 123.

Tomie, T. (2010), The birth of the X-ray refractive lens, *Spectrochimica Acta Part B - Atomic Spectroscopy* **65**(3), 192.

Tosi, P., Bassi, D., Brunetti, B., & Vecchiocattivi, F. (1995), Molecular processes in CH_4/H_2 plasmas diluted with rare-gases - reactions of X* atoms and X^+ ions (X = Ne and Ar) with methane molecules, *International Journal of Mass Spectrometry* **149**, 345.

Toyoda, H., Kojima, H., & Sugai, H. (1989), Mass spectroscopic investigation of the CH_3 radicals in a methane RF discharge, *Applied Physics Letters* **54**(16), 1507.

Tsang, R. S., Rego, C. A., May, P. W., Thumim, J., Ashfold, M. N. R., Rosser, K. N., Younes, C. M., & Holt, M. J. (1996), Gas-phase concentration measurements and diamond film composition from chlorine assisted CVD, *Diamond and Related Materials* **5**(3-5), 359.

Tsang, R. S., Rego, C. A., May, P. W., Ashfold, M. N. R., & Rosser, K. N. (1997), Examination of the effects of nitrogen on the CVD diamond growth mechanism using *in situ* molecular beam mass spectrometry, *Diamond and Related Materials* **6**(2-4), 247.

Tsang, R. (1997), Characterisation of the gas-phase environment in a hot filament diamond chemical vapour deposition chamber using molecular beam mass spectrometry, PhD thesis, School of Chemistry, University of Bristol.

Tsang, R. S., May, P. W., Ashfold, M. N. R., & Rosser, K. N. (1998), Influence of phosphine on the diamond growth mechanism: a molecular beam mass spectrometric investigation, *Diamond and Related Materials* **7**(11-12), 1651.

Tsang, R. S., May, P. W., & Ashfold, M. N. R. (1999), Modelling of the gas phase chemistry during diamond CVD: the role of different hydrocarbon species, *Diamond and Related Materials* **8**(2-5), 242.

Tserepi, A., Schwarzenbach, W., Derouard, J., & Sadeghi, N. (1997), Kinetics of F atoms and fluorocarbon radicals studied by threshold ionization mass spectrometry in a microwave CF_4 plasma, *Journal of Vacuum Science & Technology A* **15**(6), 3120.

Tsuda, M., Nakajima, M., & Oikawa, S. (1986), Epitaxial-growth mechanism of diamond crystal in CH_4/H_2 plasma, *Journal of the American Ceramic Society* **108**(19), 5780.

Tuinstra, F. & Koenig, J. L. (1970), Raman spectrum of graphite, *Journal of Chemical Physics* **53**(3), 1126.

Van Regemorter, T. & Larsson, K. (2008), Effect of coadsorbed dopants on diamond initial growth processes: CH_3 adsorption, *Journal of Physical Chemistry A* **112**(24), 5429.

Van Regemorter, T. & Larsson, K. (2009a), Effect of substitutional N on important chemical vapor deposition diamond growth steps, *Journal of Physical Chemistry A* **113**(13), 3274.

Van Regemorter, T. & Larsson, K. (2009b), Effect of a NH coadsorbate on the CH_3 (or CH_2) adsorption to a surface step on diamond (100), *Journal of Physical Chemistry C* **113**(46), 19891.

Vaz, R. (2011), personal communication.

Vonnegut, B. & Neubauer, R. L. (1952), Production of monodisperse liquid particles by electrical atomization, *Journal of Colloid Science* **7**(6), 616.

Wahl, E. H., Owano, T. G., Kruger, C. H., Zalicki, P., Ma, Y., & Zare, R. N. (1996), Measurement of absolute CH_3 concentration in a hot-filament reactor using cavity ring-down spectroscopy, *Diamond and Related Materials* **5**(3-5), 373.

Western, C. M. (2011), PGOPHER, a program for simulating rotational structure, University of Bristol. pgopher.chm.bris.ac.uk

Wetzel, R. C., Baiocchi, F. A., Hayes, T. R., & Freund, R. S. (1987), Absolute cross-sections for electron-impact ionization of the rare-gas atoms by the fast-neutral-beam method, *Physical Review A* **35**(2), 559.

Wheeler, M. D., Newman, S. M., Orr-Ewing, A. J., & Ashfold, M. N. R. (1998), Cavity ring-down spectroscopy, *Journal of the Chemical Society - Faraday Transactions* **94**(3), 337.

Wild, C., Herres, N., & Koidl, P. (1990), Texture formation in polycrystalline diamond films, *Journal of Applied Physics* **68**(3), 973.

Wild, C., Kohl, R., Herres, N., Müller-Sebert, W., & Koidl, P. (1994), Oriented CVD diamond films - twin formation, structure and morphology, *Diamond and Related Materials* **3**(4-6), 373.

Williams, O. A., Zimmermann, T., Kubovic, M., Denisenko, A., Kohn, E., Jackman, R. B., & Gruen, D. M. (2005), Electronic properties and applications of ultrananocrystalline diamond, in *Synthesis, properties and applications of ultrananocrystalline diamond*, Vol. 192, Springer.

Williams, O. A., Daenen, M., D'Haen, J., Haenen, K., Maes, J., Moshchalkov, V. V., Nesladek, M., & Gruen, D. M. (2006), Comparison of the growth and properties of ultrananocrystalline diamond and nanocrystalline diamond, *Diamond and Related Materials* **15**(4-8), 654.

Williams, O. A., Douheret, O., Daenen, M., Haenen, K., Osawa, E., & Takahashi, M. (2007a), Enhanced diamond nucleation on monodispersed nanocrystalline diamond, *Chemical Physics Letters* **445**(4-6), 255.

Williams, O. A., Daenen, M., & Haenen, K. (2007b), Biological applications of nanocrystalline diamond, *Diamond Electronics - Fundamentals to Applications* **956**, 121.

Williams, O. A., Nesladek, M., Daenen, M., Michaelson, S., Hoffman, A., Osawa, E., Haenen, K., & Jackman, R. B. (2008), Growth, electronic properties and applications of nanodiamond, *Diamond and Related Materials* **17**(7-10), 1080.

Williams, O. A., Hees, J., Dieker, C., Jaeger, W., Kirste, L., & Nebel, C. E. (2010), Size-dependent reactivity of diamond nanoparticles, *ACS NANO* **4**(8), 4824.

Wills, J. B., Smith, J. A., Boxford, W. E., Elks, J. M. F., Ashfold, M. N. R., & Orr-Ewing, A. J. (2002), Measurements of C_2 and CH concentrations and temperatures in a DC arc jet using cavity ring-down spectroscopy, *Journal of Applied Physics* **92**(8), 4213.

Wong, K. W., Wang, Y. M., Lee, S. T., & Kwok, R. W. M. (1999), Negative electron affinity on polycrystalline diamond surface induced by lithium fluoride deposition, *Diamond and Related Materials* **8**(10), 1885.

Xiao, X., Birrell, J., Gerbi, J. E., Auciello, O., & Carlisle, J. A. (2004), Low temperature growth of ultrananocrystalline diamond, *Journal of Applied Physics* **96**(4), 2232.

Yamada, H., Chayahara, A., & Mokuno, Y. (2007), Simplified description of microwave plasma discharge for chemical vapor deposition of diamond, *Journal of Applied Physics* **101**(6), 063302.

Yang, B. X. (1993), Fresnel and refractive lenses for X-rays, *Nuclear Instruments & Methods in Physics Research Section A - Accelerators, Spectrometers, Detectors and Associated Equipment* **328**(3), 578.

Yang, G. S. & Aslam, M. (1995), Ultrahigh nucleation density for growth of smooth diamond films, *Applied Physics Letters* **66**(3), 311.

Yang, G. S., Aslam, M., Kuo, K. P., Reinhard, D. K., & Asmussen, J. (1995), Effect of ultrahigh nucleation density on diamond growth at different growth-rates and temperatures, *Journal of Vacuum Science & Technology B* **13**(3), 1030.

Yarbrough, W. A. (1991), *Applications of Diamond Films and Related Materials*, Elsevier, Amsterdam.

Yarbrough, W. A., Tankala, K., Mecray, M., & Debroy, T. (1992), Hydrogen assisted heat-transfer during diamond growth using carbon and tantalum filaments, *Applied Physics Letters* **60**(17), 2068.

Yeap, W. S., Chen, S. M., & Loh, K. P. (2009), Detonation nanodiamond: An organic platform for the Suzuki coupling of organic molecules, *Langmuir* **25**(1), 185.

Yoshiki, H., Ikeda, K., Wakaki, A., Togashi, S., Taniguchi, K., & Horiike, Y. (2003), Localized plasma processing of materials using atmospheric-pressure microplasma jets, *Japanese Journal of Applied Physics* **42**(6B), 4000.

Yugo, S., Kanai, T., Kimura, T., & Muto, T. (1991), Generation of diamond nuclei by electric-field in plasma chemical vapor-deposition, *Applied Physics Letters* **58**(10), 1036.

Yugo, S., Kimura, T., & Kanai, T. (1993), Nucleation mechanisms of diamond in plasma chemical-vapor-deposition, *Diamond and Related Materials* **2**(2-4), 328.

Yugo, S., Semoto, K., & Kimura, T. (1996), The cause of suppression of the diamond nucleation density, *Diamond and Related Materials* **5**(1), 25.

Yumoto, H., Mimura, H., Matsuyama, S., Handa, S., Sano, Y., Yabashi, M., Nishino, Y., Tamasaku, K., Ishikawa, T., & Yamauchi, K. (2006), At-wavelength figure metrology of hard X-ray focusing mirrors, *Review of Scientific Instruments* **77**(6), 063712.

Zheng, S. H. & Srivastava, S. K. (1996), Electron-impact ionization and dissociative ionization of acetylene, *Journal of Physics B - Atomic Molecular and Optical Physics* **29**(14), 3235.

Zhou, D., Krauss, A. R., Qin, L. C., McCauley, T. G., Gruen, D. M., Corrigan, T. D., Chang, R. P. H., & Gnaser, H. (1997), Synthesis and electron field emission of nanocrystalline diamond thin films grown from N_2/CH_4 microwave plasmas, *Journal of Applied Physics* **82**(9), 4546.

Zhou, D., Gruen, D. M., Qin, L. C., McCauley, T. G., & Krauss, A. R. (1998a), Control of diamond film microstructure by Ar additions to CH_4/H_2 microwave plasmas, *Journal of Applied Physics* **84**(4), 1981.

Zhou, D., McCauley, T. G., Qin, L. C., Krauss, A. R., & Gruen, D. M. (1998b), Synthesis of nanocrystalline diamond thin films from an Ar-CH_4 microwave plasma, *Journal of Applied Physics* **83**(1), 540.

Zhu, W., Inspektor, A., Badzian, A. R., Mckenna, T., & Messier, R. (1990), Effects of noble-gases on diamond deposition from methane-hydrogen microwave plasmas, *Journal of Applied Physics* **68**(4), 1489.

9.0 Operational procedures

9.1.1 Diamond MWCVD SOP

The procedure below describes, in detail, the steps necessary for deposition of a diamond film in the MWCVD apparatus.

Initial Setup – adding the substrate

- Using protective gloves clean the substrate holder of diamond fragments, especially inside the recess to allow substrate to lie flat in the holder. Ensure no diamond/sooty shards emanate above the holder plate (they will get heated in the plasma).
- Use the nitrogen gas pipe fitted with a needle valve to blow away any diamond fragments inside the reaction cavity.
- Wipe the chamber surface and O-ring clean using methanol or IPA.
- Place the W wire on the base of the chamber (this separates the plasma heated Mo substrate holder from the Al reaction chamber base and comprises of a length of 250-µm thick W wire bent into ring with a 25 mm diameter), there is a ring scribed onto the surface to indicate the required position and make sure it lies flat.
- Put the substrate in its holder and place this on top of the tungsten wire, within the scribed ring.
- Lower the chamber by releasing the jack (turn the jack bolt anticlockwise) and gently lower chamber parallel to the base. This can be quite hard to align and should be done slowly guiding the apparatus with one hand on the back bar. Tighten jack bolt and jack up if chamber gets stuck/poorly aligned.
- Secure the chamber with the 4 bolts (3 at front (those either side of the window are handed) and one at back of the chamber) and exhaust manifold with O-rings and clamps.
- Return air blower to correct position (green tubing).

- Open valve above rotary pump.
- On the pressure control box (top left hand black panel), open the butterfly valve by setting the dial to the 'open' position. Then quickly alternate the adjacent flip switch between open and closed (NB. There are 3 switch positions, open is the highest) until the pressure reading is below 100 Torr. Then leave switch on 'open'. It is important to not flip the switch permanently to open from atmospheric pressure as the sudden decrease may dislodge the substrate.
- When low pressure is reached open the solenoid valve (mains plug labelled solenoid) and pump out gas inlet manifold.
- Leave for 15 minutes to ensure all gas is pumped out. Make note of the base vacuum value – should be in 10^{-2} Torr range, if not then there may be leak which requires investigation (commonly a poor seal on quartz window or base O-rings needing cleaning and checking).
- Adjust mass flow controller (MFC) set-points for gas flows required in experiment – Each gas has a labelled switch (1 of 4: H_2, CH_4, Ar, other), turn the dial to the number corresponding to the desired gas. The lower set of switches has the same labelling system. On the appropriate switch, hold to the "set pt" position and simultaneously use a small screw driver to obtain the desired value for the experiment.

Starting Deposition

- If running a long experiment, check that there is sufficient gas in the cylinders for the experiment to reach completion.
- Switch on water flow rate gauges if not already on (2 white mains plugs above reactor).
- Open cooling water valves fully – there are four black valves here, do not touch the two left hand valves which control the diff/turbo pump cooling water circuit). Secondly turn on the tap on the wall above the rotary pump.
- Check if pumped down to base pressure – if it is not there is a leak that needs to be detected and addressed.
- Ensure solenoid is open (mains plug).
- Open gas valves above and below MFC: there are 3 valves associated with each MFC, the one directly to the left of the MFC is the bypass, the other two are situated above and below the MFC. Gas valves are opened by opening the top and bottom valves only. Do not open all three valves simultaneously as this will fill the chamber with gas very fast.
- Turn on Hydrogen and Argon MFCs together (from middle to up position for the appropriate switches on the MFC control box). It may take a few minutes for the pressure reading to adjust.

- Set butterfly valve to 18-20 Torr – On the pressure control box (top left black panel) set the right hand dial to 'auto' first, then the pressure dial (left) can be tuned to the required value. The pressure display can take a while to respond so be patient when changing pressure.
- Turn on the MW power supply (beige control box is the MW control, the large switch turns the MW power supply on).
- Turn on air blower (blue box connected to chamber by green tubing)
- It should now be ready to strike a plasma: this is done by pressing "HV ON" on the MW controller (if "OVLD" shows press "HV OFF" and try again)
- Increase the power dial (MW controller) quite rapidly until the plasma lights (this will often occur for a power greater than 500 kW). (Infrequently the reflected power will get too high; in this case move the left-most MW tuner on the waveguide to decrease the reflected power and the plasma should light – occurs when previous plasma used significantly different gas mixture).
- As soon as the plasma strikes increase the pressure (dial on pressure control box) to 100 Torr (you will observe that as the pressure increases the reflected power value will decrease if the tuning is correct). Recall that it is necessary to watch the digital pressure display which will take a little longer to respond than the speed at which the dial is turned. Be careful not to increase the pressure too much too quickly as this can result in the plasma becoming unstable and going out. If this does occur, press "HV OFF", turn power down and decrease the pressure back to 18-20 Torr and start the process again.
- Observe the plasma through the window to check that it is in the correct place (should not be near or on the quartz window and is aligned centrally above the substrate holder.
- When the plasma is stable adjust to experimental variables (*i.e.* required pressure)
- Adjust up the MW power to the required value. Tune the waveguide to minimize the reflected power, if non-zero, add this quantity onto the required experimental power.
- Turn on Methane and note time (t_0).
- Move pyrometer to above the hole in the top of the chamber and ensure it is directed at the centre of the substrate. When in place, note the initial temperature (T_0) shown on screen at the base of the control panels.
- Enable interlock (flip the bottom-most switch to the right).
- Keep fine tuning to reduce reflected power and forward power until it has stabilised over the first 30 minutes of the experiment. The reflected power often drifts up during this time and need attention.
- Check pressure, power, reflected power, gas flows and plasma position etc every hour throughout the deposition.

End of Deposition

- Turn off the methane on the MFC control box by turning the switch to the central position.
- Note the final temperature (T_f) and length of deposition (t_f).
- Purge out the methane for about 2 min and allow the film surface to clean in a H_2 or H_2/Ar plasma.
- If running at high T_{sub}, turn down the pressure and MW power to prevent sample from overheating.
- To turn off the plasma, wind down the MW power and the pressure gradually. As soon as plasma goes out rapidly turn power down the minimum position and press "HV OFF". Turn butterfly valve to 'open' then turn pressure dial down to pump out gas.
- Turn off H_2 and Ar on the MFC control box.
- Turn off temperature measurement.
- Turn off air blower.
- Close valves above and below the MFCs – making sure all are turned off.
- Check that system has pumped down to 10^{-2} Torr region
- After 15 minutes turn off MW power supply.
- Disable interlock (bottommost switch to the left) and turn off cooling water (the tap on the back wall and the two flow valves). Switch off water flow gauges.
- If leaving pumped overnight etc. down close solenoid at mains switch. Also turn off butterfly valve control (as long as set to open) and MFC controller box to prevent overheating.
- Leave for an hour before dismantling the chamber.

Removing Substrate

- Check pressure is in 10^{-2} Torr region.
- Close butterfly (right hand switch and dial on pressure control box both to 'close' position).
- Close valve above rotary pump.
- Check the solenoid is open (mains plug).
- Use Argon line bypass valve to vent chamber: First open the bypass valve and then alternately opening (briefly) the remaining two (top and bottom) valves until you hear the interlock click as 350 Torr is reached. Once the click is heard close all valves. Never open all three valves at the same time.
- Turn off solenoid.
- Undo the 2 exhaust manifold clamps (silver tubing) and move manifold away.

- Undo the 4 bolts that clamp the chamber in place.
- Lock jack by turning the bolt clockwise then raise the entire chamber until at a height with which the support stand can fit underneath and hold it up.
- Using protective gloves, remove the substrate in Molybdenum holder and tungsten wire.
- Add new substrate and lower chamber as indicated above.

9.1.2 Electrospray seeding SOP

A general procedure for seeding a substrate with a nucleation layer of ND is given below:

i) Ensure substrate is well cleaned and de-greased in acid/acetone/methanol wash.

ii) Check voltage supply is off and apparatus is earthed (this can be done by filling the syringe with methanol and observing the solvent dripping down the syringe needle inside the box: indicating that no voltage is applied).

iii) Clean syringe and needle with methanol (if necessary flush through by removing from position).

iv) Stick the substrate onto the mount using conductive carbon sticking pads, making sure that the pads are strong enough to hold the sample depending on its weight. Ensure large substrates are located centrally.

v) Clamp mount into optimized position within box (optimization is crucial for homogeneous application onto large substrates and involves adjusting:

   a. mount position up/down on threaded bar within box
   b. mount position left/right on clamp within box
   c. mount position by changing to one of three positions on top of box

vi) Start substrate rotation on control box.

vii) Fill syringe with colloid solution (generally in methanol).

viii) Apply high voltage (between 35 and 50 kV) by switching on power supply, dialling in the required voltage, and pressing the red and green switches to apply the voltage.

ix) The suspension should now be pulled through the syringe and some arcing may be observed inside the box. While the voltage is applied the syringe, wiring and entire box should not be touched due to the build up of charge.

x) Once all the suspension has been pulled through, leave for another minute to allow any residue in the syringe to evaporate.

xi) Turn off voltage supply by pressing the green and red switches. Return dial to zero and switch off power.

xii) Check voltage is off by placing methanol in syringe and allowing solvent to drip down inside box (this will also clean the needle).

xiii) Open box and remove mount and substrate.

xiv) Clean syringe, mount and box thoroughly after use.